INTERFACIAL ELECTRON TRANSFER OF CYTOCHROME *C* AND CONJUGATED POLYELECTROLYTE/SURFACTANT COMPLEXES

by

Hongjun Yue

BS, Dalian Railway Institute, P. R. China, 1994

ME, East China University of Science and Technology, P. R. China, 2001

Submitted to the Graduate Faculty of Arts and Sciences
in partial fulfillment of
the requirements for the degree of Doctor of Philosophy

University of Pittsburgh
2007

UNIVERSITY OF PITTSBURGH

FACULTY OF ARTS AND SCIENCE

This dissertation was presented

by

Hongjun Yue

It was defended on

July 18th, 2007

and approved by

Prof. Sunil Saxena

Prof. Shigeru Amemiya

Prof. Rose A. Clark

Dissertation Director: Prof. David H. Waldeck

Dedicated to

My parents, my wife, my son and my family

INTERFACIAL ELECTRON TRANSFER OF CYTOCHROME *C* AND POLYELECTROLYTE/SURFACTANT COMPLEXES

Hongjun Yue, PhD

University of Pittsburgh, 2007

Abstract

Cytochrome *c* (cyt *c*) acts as an electron shuttle in biological respiration and photosynthesis. Although the understanding of this protein and its electron transfer (ET) reaction is relatively highly developed, many of its aspects remain unclear. We use supramolecular assemblies of cytochrome *c* to understand its ET at an interface in terms of how the ET depends on solution composition, SAM composition, temperature, immobilization methods and the nature of the electron tunneling pathway. From these studies we have learned: (1) the formal potential and the surface charge of cytochrome *c* are modified when binding to a negatively charged surface; (2) cytochrome *c* molecules assume a wide distribution of geometries when electrostatically binding to a negatively charged surface, which leads to a wide distribution of ET rate constants; (3) when the protein is within 14 Å of the electrode, the ET rate is controlled by local frictional motions rather than by electron tunneling; (4) the binding-inactive sites, the diluent molecules on the SAM can provide alternative electron tunneling pathways from electrode surface to the heme of cytochrome *c*, and in suitable conditions the diluent molecules dominate in the electron tunneling pathway.

Poly (phenylethynylene) (PPE) based conjugated polyelectrolytes are a class of polyions having rigid backbones. We present a fluorescence correlation spectroscopy (FCS) study on the

hydrodynamic properties of complexes formed by two PPE-SO_3^- polymers, having different charge density, with octadecyl trimethylammoniumbromide (OTAB) below the critical micelle concentration. The concentration ratio C_{OTAB} /$C_{monomer}$ ranges from 0.2 to 1800. The hydrodynamic radius of the complexes as a function of OTAB concentration has three regimes. In the low concentration regime, the complex has a comparable size with the polymer in deionized water. In the intermediate concentration regime the complexes have the largest size and substantial heterogeneity. In the high concentration regime, the complexes have a size that is about three times larger than that in the low concentration regime. The results significantly extend the understanding of the interaction between polyelectrolyte and ionic surfactant, and indicate that the rigidity of polymer backbone and C_{OTAB} /$C_{monomer}$ concentration ratio act to determine the composition of polyelectrolyte/surfactant complexes.

TABLE OF CONTENTS

LIST OF TABLES

LIST OF FIGURES

LIST OF SCHEMES

LIST OF CHARTS

ACKNOWLEDGEMENTS

I would like to express my sincerest gratitude to Dr. David H. Waldeck, my advisor for his patience, guidance, support, encouragement, trust and inspiration during my graduate research. He has provided a unique research environment with friendly and helpful colleagues throughout these years. It is the diversity of the research in his group that provided me with valuable opportunities to learn different principles and work on a wide range of research projects. His diligence and passion in science aspires me not only during my graduate research but in my future career as well.

I would like to thank Dr. Sunil Saxena, Dr. Shigeru Amemiya and Dr. Rose A. Clark for their constantly helps during my graduate study. They served on my committees and have helped me go through important events during these years. I learned a lot through conversations with them on a variety of scientific subjects.

I would like to thank Dr. Min Liu who kindly recommended me to Dave when I was still in China. I would like to thank Dr. Jianjun Wei. He trained me to carry out electrochemical experiments to study cytochrome *c* electron transfer when I just joined Professor Waldeck's group. I would also like to Thank Dr. Matthew Shtrahman for his generous help with the FCS instrument.

It has been a wonderful experience to working with my intelligent colleagues, Palwinder Kaur, Subhasis Chakrabarti, Lei Wang, Amit Paul, Mingyan Wu, Daniel Lemont, Kathy Davis and Matt Kofke. I learned a lot from them in group meeting and by discussing with them on

various experimental problems. I would like to thank Kathy Davis and Matt Kofke. They kindly provided proofreading to many of my written materials.

I would like to thank the support teams of our department. They are Tom Gasmire, Dennis Sicher, Jeff Sicher and Roy Watters in our Machine shop; Bob Muha, Chuck Fleishaker, Dave Emala, and Jim McNerney in electronic shop; Bob Greer in Glass shop, all the members of the main office and chemistry stockroom. Their expertise, skills and generous assistant have been indispensable for me to overcome difficulties and to finish my graduate research.

Finally, I would like to express my deepest affection for my wife Hongjuan Xu and my son Alan Wenyu Yue. They make my life real and enjoyable. I would like to thank my mother-in-law, Hanzhen Wang, who selflessly came from China to help us take care of Alan. I would like to thank my whole family for their support and understanding. They are always there when I needed them.

PART I INTERFACIAL ELECTRON TRANSFER OF CYTOCHROME C ON SELF-ASSEMBLED MONOLAYER

Abstract

Cytochrome *c* (cyt *c*) acts as an electron shuttle in biological respiration and photosynthesis. Although the understanding of this protein and its electron transfer (ET) reaction is relatively highly developed, many of its aspects remain unclear.

We have been exploring supramolecular assemblies of cytochrome *c* to understand its ET when immobilized at an interface. By binding cyt *c* to a self-assembled monolayer (SAM) deposited on a gold surface, its redox partner is replaced by a metallic electrode and the electron transfer process is simplified. On assemblies of pure carboxylic acid terminated SAM and mixed carboxyl/hydroxyl terminated SAM; cytochrome *c* is electrostatically bound to the films and these assemblies act as models for the biological system. Two reference assemblies have been used. One is the assemblies where cytochrome *c* is covalently attached to a mixed carboxyl/hydroxyl terminated SAM by an amide bond between a Lys residue of cytochrome *c* and a carboxyl group of the SAM. The other one is the assembly where cytochrome *c* is tethered by a pyridine group protruding above the SAM surface. With these assemblies, we studied how the ET depends on solution composition, SAM composition, temperature, immobilization methods and the nature of the electron tunneling pathway.

From these studies we have learned: (1) the formal potential and the surface charge of cytochrome *c* are modified when binding to a negatively charged surface; (2) cytochrome *c*

molecules assume a wide distribution of geometries when electrostatically binding to a negatively charged surface, which leads to a wide distribution of ET rate constants; (3) when the protein is within 14 Å of the electrode, the ET rate is controlled by local frictional motions rather than by electron tunneling; (4) the binding-inactive sites, the diluent molecules on the SAM can provide alternative electron tunneling pathways from electrode surface to the heme of cytochrome *c*, and in suitable conditions the diluent molecules dominate in the electron tunneling pathway.

CHAPTER 1 INTRODUCTION

1.1 Cytochrome *c* and its Role in Nature

Cytochrome *c*, a heme containing electron transfer protein, has been the subject of extensive studies because of its physiological, theoretical and practical importance.

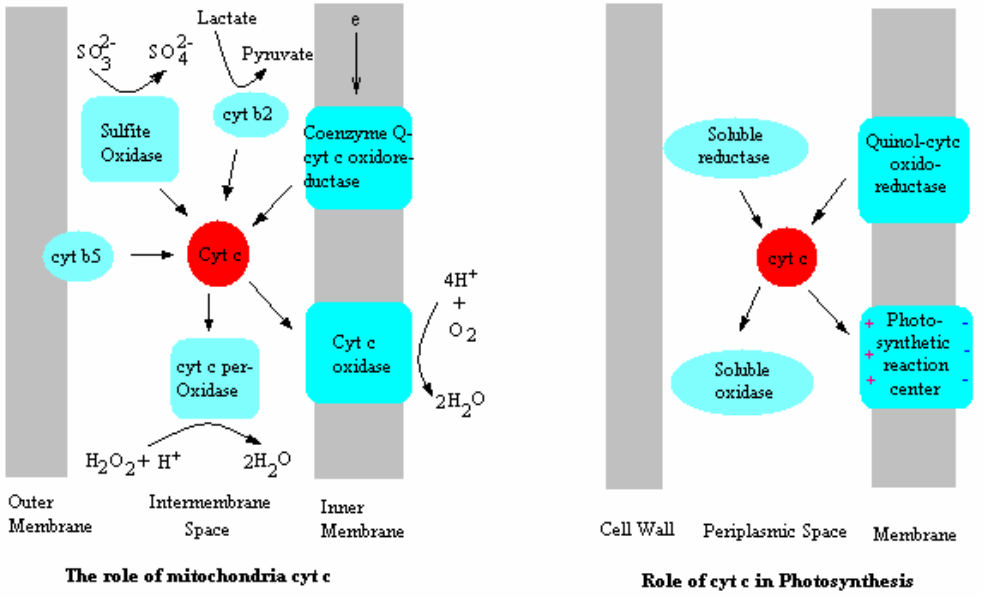

Figure 1. 1 Schematic diagram illustrations of the role of cytochrome *c* in the process of mitochondrial respiration and bacterial photosynthesis. This figure is taken from ref 1.

Cytochrome *c* plays an important role in biological energy conversion, both respiration and photosynthetic processes (see Figure 1.1). In mitochondria, cytochrome *c* diffuses in the intermembrane space, acting as an electron shuttle that transfers an electron from Coenzyme Q-Cytochrome *c* oxidoreductase (complex III) to cytochrome *c* oxidase (Cytochrome *cO*, complex

IV). Cytochrome *c* also plays key roles in three other electron transport processes having physiological importance, involving electron donors: cytochrome b_5, sulfite oxidase, cytochrome b_2, and the electron acceptor cytochrome *c* peroxidase. In photosynthesis, cytochrome *c* transports an electron to the photosynthetic center which is excited and in a charge-separated state.[1-3] Knowledge on the electron transfer reaction of cytochrome *c* is important for understanding these biological energy conversion reactions.

Mitochondrial cytochrome *c* is the most thoroughly characterized c-type cytochrome and belongs to the subset type 1, among four identified types. This type of cytochrome *c*, with a molecular weight of 8-12 kDa and 103-115 amino acid residues, is a small globular protein. The 3-D structure, both in the crystal and in solution, has been well characterized by X-ray crystallography, multidimensional NMR, and *ab-initio* methods.[4-8] In the sequence of cytochrome *c* from different species, 21 amino acids are invariant and only 14 amino acids are highly variable. The abundance of protein variants provides an avenue for studying the relationship between outer-sphere electron transfer (ET) properties and structural variations. In addition, cytochrome *c* is easy to obtain, to purify and to store. These properties make cytochrome *c* an ideal model for studying biological electron transfer.

A number of workers have explored the tunneling pathway, reorganization energy, and orientation dependence of the cytochrome *c* ET reaction, in both homogeneous and heterogeneous systems. Two electron transfer modes were suggested for cytochrome *c* and its redox partners, the edge-to-edge electron transfer and the axial ligand facilitated electron transfer. The edge-to-edge model assumes that the electron travels from one redox center to the other by way of the porphyrin ring; the axial ligand model suggests that the electron travels through Lys79-Met 80 to the redox center. NMR and X-ray data show that six water molecules spend a

long time in the heme pocket, and one of them changes position upon redox reaction. The structure of the heme and axial ligands were studied for different Fe oxidation states. It is concluded that the saddle-shaped porphyrin ring and axial ligands undergo a small change in bond length and bond angle, corresponding to a small value of inner reorganization energy, ca one-fourth of the outer-sphere reorganization. It is accepted that the ferric/ferrous cytochrome *c* has a reorganization energy of about 0.6eV.[9]

1.2 Self-Assembled Monolayer

A self-assembled monolayer (SAM) is a type of ordered single molecule film that is formed on a solid substrate through spontaneous chemical adsorption from solution (see Figure 1.2). Presently, SAMs are derived from three main systems: 1) alkyltrichlorosilanes on hydroxyloxide surfaces which can be SiO_2, Al_2O_3, and glass;[10-27] 2) organosulfur compounds on gold,[28-51] silver,[30-32,52] copper and other metals;[30,31] 3) carboxylic acid on oxide[29,53-55] and silver.[56] The following cartoon shows the SAM formed on a metal surface, as used in these studies. It is widely accepted that on metal surfaces, the molecular chain is not perpendicular to the metal surface but forms an angle with respect to the solid surface normal, e.g. alkanethiol molecules form SAMs on a gold surface and a tilt angle in the range from 20-30˚. Alkyl chains of the molecules pack closely through interchain van der Waals interaction.

The experimental procedure of forming a SAM is straightforward. Immerse a pretreated clean surface into a solution (commonly in ethanol) having a concentration of 0.01 – 1.0 mM of the thiol; a SAM forms on the surface spontaneously, and can be quite compact after 10 hours or so. By varying the chain lengths and the tail groups or by mixing compounds having various chain lengths and tail groups, an organic film that has the desired chemical and physical properties is formed. A range of techniques, including wetting,[27,33,44,57] X-ray photoelectron

spectroscopy (XPS),[11,12,27,30,32,33,38,41,49,50,58] polarized infrared external reflectance spectroscopy (PIERS),[21,28,30,53-55,59-61] optical ellipsometry,[10-12,27,28,33,36,41,49,56,62-65] and electrochemistry[28,66] have been employed to characterize both the SAM's surface properties and its influence on the substrate.

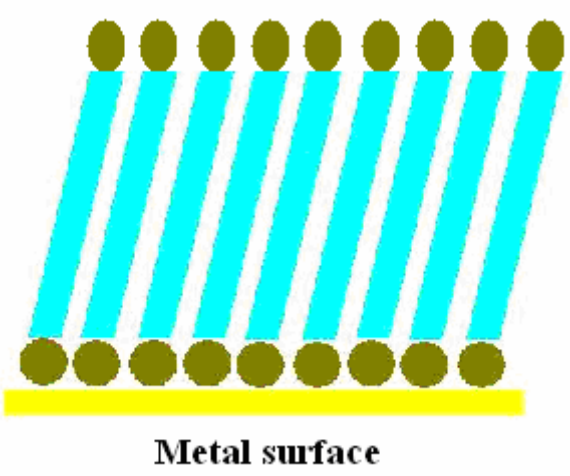

Figure 1. 2 Schematic structure of self-assembled monolayers grown from alkanethiol on a gold surface.

SAMs formed by adsorption of alkanethiols onto a gold surface have been explored most, for at least four reasons. First, gold is a relatively inert metal. Its oxide is not stable under common atmospheric conditions,[49,66] and it can be reduced by ethanol. It also has decent melting point about 1046 ˚C,[67] so several techniques, such as flame annealing or thermal evaporation, can be successfully applied to obtain a clean surface which is relatively smooth on both the microscopic and the macroscopic scale. Second, gold interacts strongly with sulfur.[35] It is accepted that a covalent bond with a bond strength of *ca* 40 kcal/mol forms between gold and sulfur. This specific interaction allows thiol molecules, having many different kinds of tail groups, to form a well packed SAM.[48] Third, thiol molecules with long methylene chain lengths (n>8, n is the number of methylene group in the molecule) can form densely packed, crystalline,

or pseudocrystalline monolayers on gold.[28,34] Furthermore, a thiol SAM on gold is a thermodynamically stable system, the free energy of adsorption of thiol and disulfide are -5.5 and -24 kcal/mol, respectively.[68] This system is more stable in aquous solution than in other solvents.[68] Hence it can be used directly in the study of biosystem using electrochemistry [69-75]as well as other techniques.[76]

Thiol and disulfide molecules in solution form SAMs, which cannot be distinguished by ellipsometry and XPS, on the surface of gold through adsorption as shown in scheme 1 of Chart 1.1.[77] The adsorption involves the cleavage of S-H bonds or S-S bonds and the formation of Au-S bonds, respectively. If thiol molecules are used, the balance of material requires that one half equivalent of hydrogen molecules be produced, however no direct experimental evidence is found for this.[47,77]

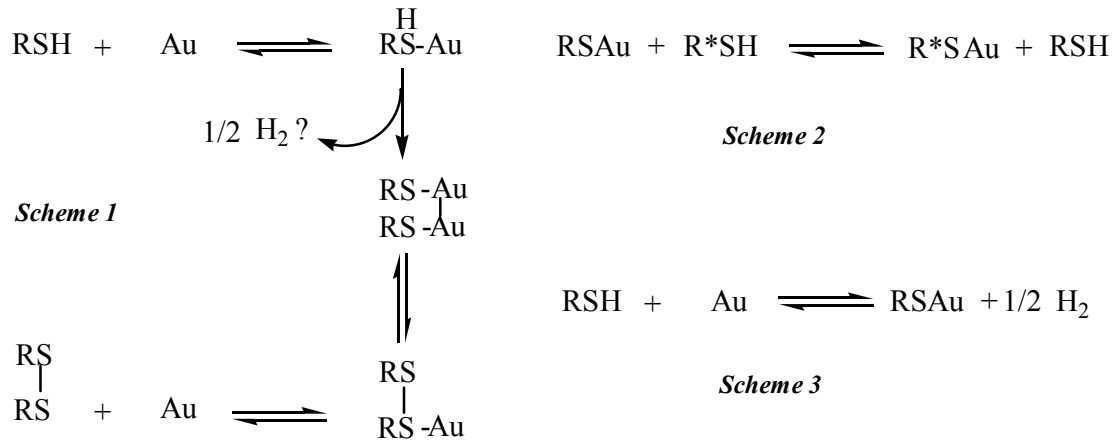

Chart 1. 1 The reactions between gold and thiol during the formation of a self-assembled monolayer.

The whole process proceeds in two steps. The first step is fast, during which the contact angle and ellipsometric thickness change sharply. In about two seconds a clean gold surface becomes hydrophobic if alkyl thiol is used and in 10 min the ellipsometric thickness reaches

80% of its maximum value.[49] This fast reaction is not affected by chain length. For the same chain length, thiol molecules adsorb faster than disulfides with a preference of 75:1,[50] or 10:1.[49] The second step is a slow one, during which the surface properties reach their maximum slowly, more than ten hours. The adsorption free energy is -5.5 and -24 kcal/mol for thiol and disulfide, respectively.

Desorption of thiol molecules from the SAM occurs in solvent. The more soluble the thiol is in the solvent, the more completely the desorption proceeds. Typically, however, 40% percent of the SAM is more stable, attributed to the stronger binding of sulfur to defects on the gold surface, and remain on the surface.[68] Whether the product is a disulfur, as suggested in Scheme 1 of Chart 1.1, or a thiol molecule, as suggested in Scheme 3, is not clear. The reaction rate depends on chain length. The free energy of desorption is 28 kcal/mol for an alkanethiol/gold SAM and increases by 0.2 kcal/mol when the thiol molecule has one more methylene group. If the SAM is put into a solution which contains a different type of thiol or disulfide molecules, an exchange reaction occurs as shown in Scheme 2 of Chart 1.1. The displacement reaction by thiol molecules is 50 times faster than by disulfide molecules.[47,77] Both exchange and desorption reactions are slow reactions having a rate constant of the order of 10^{-5} s^{-1}.[47,49,68,77]

On a clean and microscopically smooth gold surface, a compact monolayer forms spontaneously from thiol solution. In fact SAMs form on gold surfaces that are quite rough.[78] Thiol molecules are not perpendicular to the gold surface but assume a tilt angle of 20-30 ° with respect to the gold surface.[30,34,68,79] The thickness of a monolayer can be measured with ellipsometry and XPS. If a 30° tilt angle from the normal is assumed, the thickness will increase linearly with increase of the chain length, with a theoretically predict slope of 1.27 Å /CH_2 and

an intersection of 4.0 and 5.0Å for methyl and carboxyl group terminated SAM respectively. The reported experimental slopes range from 1.1 to 1.5 Å /CH_2 when there are more than 9 methylene groups in the molecular chain.[28,47,49,77] When n<5 the reported experimental slope is 0.56 Å /CH_2.[28] The SAM formed by long chain molecules is more ordered than by short chain molecules. In the case of mixed monolayers, no macroscopic phase segregation was found on the SAM formed directly from mixed solution.

1.3 Interfacial Electron Transfer of Cytochrome *c*

During the past few decades our knowledge about biological electron transfer processes has improved profoundly. In general, a protein regulates electron transfer by modulating the formal potentials of its redox moieties, defining the local environment to control the reorganization energy, and providing proper electron tunneling pathways between redox centers. Biological electron transfer occurs at protein-protein interfaces and many proteins or enzymes can only maintain their activity in biological membranes. For these reasons, electron transfer of proteins that are immobilized at chemically modified electrode surfaces provides a useful model system for addressing some fundamental aspects of protein electron transfer.

Other motivations for studying protein electron transfer at an electrode are the demands for clinic assays, drug screening, and biofuel cells.[80-86] Many supramolecular assemblies of proteins/enzymes, which maintain the necessary bio-activity and display Faradaic current, have been created. For example nanoparticle/nanotube arrays, hydrogels, molecular sieves, redox active polyions, oligonucleotide assemblies and others have been constructed. Table 1.1 provides some examples of strategies for immobilizing protein into redox active assemblies. The electron transfer in these systems occurs either directly between the target redox species and the electrode or is mediated by other redox species. Such systems require theoretical developments that

include the coupling of one or more diffusion and charge transfer steps to account for the multi-charge transfer dynamics.[84]

Effective electronic communication ('wiring') between proteins and electrodes is a key issue for immobilization of proteins into electroactive assemblies. Protein immobilized into a monolayer or submonolayer assembly provides a better platform for elucidating the redox properties and catalytic mechanism of enzymes, and it has been exploited extensively in fundamental studies to elucidate the mechanism and kinetics of protein electron transfer.[87,88] This protein immobilization provides better control of the protein's orientation and position, yielding a high level of homogeneity. Self-assembled monolayer (SAM) films and protein-metal junctions allow diffusion to be eliminated from the kinetic modeling and provide more transparent display of the fundamental charge transfer.[80,89,90] Recent work uses *in situ* STM to study individual protein molecules.[91,92] Such studies can provide important information on the heterogeneity of electron transfer rates and generate population distributions of protein activity.[91]

A straightforward way of 'wiring' a protein to an electrode is to attach it directly to the electrode surface. Whether a protein can be immobilized in this way and retain its function depends on its structure. For example, immobilization of horse heart cytochrome *c* directly to a gold electrode surface causes it to denature and lose its electroactivity, however yeast iso-1 cytochrome *c* can be immobilized on a gold surface by forming a Au-S bond with the Cys 102 amino acid on its surface. STM and cyclic voltammetry show that the yeast cytochrome *c* retains much of its structure and electrochemical activity in the assembly; in particular, the protein is well localized (covalently linked) and the redox potential is close to that for the native protein.[95,119] Heering et al reported that the electron transfer rate constant of this immobilized cytochrome *c* is 1.8×10^{3} s^{-1}, and it efficiently relays electrons to its natural partner cytochrome *c*

peroxidase, as well as two other enzymes, cd_1 nitrite reductase and NO-reductase from *Paraccocus denitrificans*. [94] Baymann reported on the immobilization of cytochrome c^{m}_{555} to Au by a thiol bond to cysteine 18, with an electron exchange rate constant of 1.4×10^{4} s^{-1}.[96] Not all proteins have surface accessible linking groups and can be immobilized directly like yeast iso-1 cytochrome *c* , hence other strategies are needed.

A number of workers have used protein engineering to create mutant proteins which can be directly linked to electrodes; *e.g.,* a cysteine group can be introduced on the protein surface by site directed mutagenesis. Davis *et al* reported introducing cysteine residues onto the surface of Azurin (two mutants, K27C and S118C, were studied) and compared their electron transfer behavior to that of the native protein, which can also be immobilized. The assemblies were characterized by fluid-phase AFM and cyclic voltammetry.[97] Andolfi et al reported introducing disulphide or surface cysteine residues to azurin and plastocyanin. The resulting proteins retain gross native structure and form well-defined and electroactive assemblies on polycrystalline gold electrodes.[98] A related approach incorporates into the protein a histidine tag [106,120,121] that forms a coordinative bond with a metal ion chelating to the organic film, e.g., Ni-ANTA (N_{α}, N_{α}-bis(carboxymethyl)-L-lysine). Johnson *et al* used this method to immobilize thioredoxin on a modified gold surface, creating a highly oriented monolayer that is capable of rapid electron exchange with the electrode.[121] Although nature limits the number of proteins which can be directly "wired" to an electrode, protein engineering provides an avenue for modifying native protein structures so that they can be directly bound to electrodes. By carefully choosing the site of mutagenesis, it may also be possible to make "tough" proteins, which can be used in harsher, non-physiological environments.

Self-assembled monolayer (SAM) films provide an attractive method to immobilize proteins into arrays, because of the ability to form organized films with diverse chemical functionality on their exposed surface. For Au electrodes these films commonly consist of a methylene chain which has a thiol functionality on one end that binds to the electrode and an organic functionality on the other end. SAM films have been used to immobilize proteins through covalent linkages[122], coordinative bonding,[70,120] electrostatic attraction[123] and hydrophobic interactions. [102,103] Recent studies have investigated how the electron transfer rate changes with the nature of the protein to surface binding, the thickness of the film, and the composition of the SAM molecules, e.g. replacing the methylene units with ether linkages or conjugated units, the electronic coupling strength can be modified.[73,102]

Cytochrome *c* has a net positive surface charge.[124] It is believed that cytochrome *c* fulfills its biochemical role by binding to its counterpart in the respiratory chain or photosynthetic center through complementary electrostatic interactions[124-128]. Immobilization of cytochrome *c* on self-assembled monolayer/metal assemblies has been used to mimic cytochrome *c* bound to its redox partner in a simple but effective way. A number of studies have been done with this model, for example, the distance dependence of ET rate constants,[74,129] research on the electron transfer mechanism,[75,129,130] and the impact of special surface sites on the electron transfer reaction.[131,132]

Table 1. 1 Examples of immobilized protein assemblies on electrodes.

Type	Promoters	Substrates	Proteins/enzymes	*References*
Direct		*Au*	*Yeast iso-1 cytochrome c*	*93 94,95*
			Cytochrome C^{m}_{555}	*96*
			Azurin mutants K27C, S118C	*97,98*
			Disulphide/cysteine tagged plastocyanin	*98*
		PG	*Cytochrome c*	*99*
		ITO	*Cytochrome c*	*100*
SAM	*Ni-NTA terminated thiol*	*Au*	*Poly-histidine tagged Photosynthetic center*	*101*
	OPV	*Au*	*Azurin*	*102*
	Alkanethiol/hydroxyl terminated thiol	*Au*	*Subunit II of Cytochrome c oxidase*	*103*
			Azurin	
	epoxysilane	*ITO*	E. Coli *O157:H7*	*104*
	MPA or cysteine	*Au(111)*	Pyrococcus furiousus *Terredoxin*	*92*
Lipid film		*PG*	*Redox cofactor of spinach photosystem 1*	*105*
		Ni-NTA coated Ag	*L-Cys tagged cytochrome c*	*106*
Nano material	*TiO2, SnO2 nanocrystalline*	*Conducting glass*	*Cytochrome b maquette*	*107,108*
			flavodoxin	*109*
	Ag Nanoparticle	*PG*	*Myoglobin*	*110*
	Carbon Nanotube	*GC*	*Glucose oxidase*	*111*
	Carbon Nanotubel arry	*SAM/Au*	*Microperoxidase-11*	*112*
DNA	*Thiol modified DNA*	*Au*	*photolyase*	*113*
			Glycosyslases	*114*
Gel	*Silica sol-gel*	*CP*	*Myoglobin*	*115*
	Agarose hydrogel	*EPG*	*Myoglobin, hemoglobin, horseradish peroxidase*	*116*
Polymer	*polyaniline*	*PG*	*hemoglobin*	*117*
		CP	*Horseradish peroxidase*	*118*

NTA: nitrilotriacetic acid; OPV: oligomeric phenylenevinylene; PG: pyrolytic graphite; GC: glassy carbon; CP: carbon paste

SAMs composed of carboxylic acid-terminated thiols present a negatively charged surface for cytochrome *c* adsorption and provide a direct model to study the ET reaction of cytochrome *c* when electrostatically immobilized.[133-135] [122] On carboxylic-acid terminated SAMs, the nonadiabatic ET rate constant k^0 of cytochrome *c* has an exponential dependence on distance, for methylene chain length larger than 6. The decay coefficient β is close to 1.1 per $-CH_2-$ when the number of methylene groups in the chain n is larger than 8. When $n < 6$, k^0 displays only a weak dependence on distance. This phenomenon indicates that the electron transfer mechanism is different for the thin and thick SAM film. The nature of this mechanism switching is currently under study.[129] [136-138]

Cytochrome *c* has a total of 19 lysyl residues on the surface. Some of these lysine residues seem to be more important than others in the ET between cytochrome *c* and an electrode modified by carboxylic acid film [131,132]. Niki, K. et. al. found that mutation at the Lys13 group has more effect on k^0 than mutation at Lys 72 and Lys79.[131] Recent work in our lab corroborates this finding for electrostatic immobilization.[132]

The rate constant of cytochrome *c* was found to be faster on mixed carboxyl/hydroxyl monolayers than on pure carboxylic monolayers, even though the carboxylic acid has the same chain length in both cases.[134,139] Because the hydroxyl diluent has a shorter chain length than the carboxylic terminated molecules, the increase of rate constant was interpreted as resulting from of enhancement of the electronic coupling; on a mixed monolayer, the interaction between the film and cytochrome *c* is weaker than on a pure monolayer, and the cytochrome *c* can arrange to a conformation in which the electronic coupling between cytochrome *c* and the electrode is more efficient. The experiments in Chapter 5 shows that electron can tunnel through the short chain diluent and increase the ET rate constant.

A second SAM system that has been reported in cytochrome *c* studies uses pyridine or imidazole receptors to bind the protein.[74,75] If a pyridyl or imidazole group sticks above the surface it can ligate to cytochrome *c* in place of Met-80, at the sixth coordination site. This binding strategy has the advantage of creating a narrow orientational distribution of cytochrome *c* on the surface and provides a direct connection to the heme. The formal potential of cytochrome *c* on this type of SAM shifts negatively because of the ligation of the nitrogen containing group. It was found that when the chain length is n>11 the k^0 depends exponentially on distance with a decay coefficient β around 1.1 per methylene group. In contrast, when n<11 the distance dependence is weak. This finding is similar to that observed for electrostatic immobilization. In the nonadiabatic region the rate constant for the pyridine system is larger than that on the carboxylic SAM having the same chain length. This difference was attributed to the 5 Å longer electron tunneling distance in the carboxylic acid terminated group.[140-142]

The formal potential of solution cytochrome *c* shifts upon binding to mitochondrial and lipid bilayer membranes,[143-145] cytochrome oxidase,[123,134,146] and different SAM films.[35, 36,147-149] Since cytochrome *c* is an electron transport protein that functions in different regions of the mitochondrion, and the cell, it is important to understand how changing the protein environment changes its redox characteristics.

1.4 Electron Transfer (ET) Theory

As illustrated by chart 1.2, we consider electron transfer as the charge separation process in a Donor (D) – Acceptor (A) complex. Based on the strength of the interaction between D and A, electron transfer reactions can be classified into two categories, *inner-sphere* ET and *outer-sphere* ET. In the *inner-sphere* ET, there is a strong interaction between D and A, and the properties of D and A in a DA complex differ from those of free precursors. In the *outer-sphere*

ET, only a weak interaction occurs between D and A, and the properties of D and A in DA complex can be treated as the same as those of their precursors.

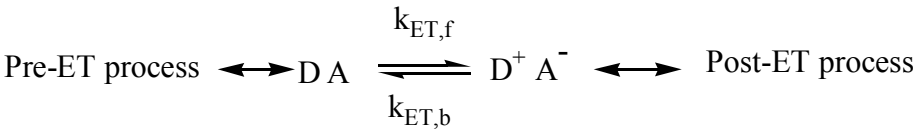

Chart 1. 2 The electron transfer process in electron Donor-Acceptor complex

1.4.1 Homogenous Electron Transfer

Classical Marcus Theory The kinetics of the homogeneous ET process can be understood by Marcus theory. Based on transition state theory, the classical Marcus theory assumes a reaction coordinate for the electron transfer reaction that corresponds to polarization changes in the medium. The polarization changes arise from the intermolecular responses, such as the orientation of the dipole of solvent molecules, and intramolecular responses, such as the length of certain chemical bonds and frequencies of some vibrational modes. In the Figure 1.3, the Gibbs free energy surfaces are assumed to have a quadratic shape with the same force constant and they cross each other at C. The displacements q_R and q_P refer to the equilibrium geometry of the reactant and the product respectively. By thermal fluctuation, reactant molecules reach point C, the transition state, and electron transfer can occur. The electron transfer rate constant $k_{ET}$is determine by the following expression,

$$k_{ET} = \kappa_{el} \nu_n \exp\left(- \Delta G^{\neq} \Big/ k_B T \right) \tag{1.1}$$

where κ_{el} is the electronic transmission coefficient, ν_n is the frequency of passage (nuclear motion) through the transition state corresponding to the point C, $\Delta G^{\neq}$ is the activation free energy, k_B is

the Boltzmann constant, and T is the temperature. It is useful to distinguish two types of ET reaction: 1) adiabatic ET reaction if $\kappa_{el} \approx 1$, which means that almost every passage through the transition state leads to electron transfer, and 2) nonadiabatic ET reaction when $\kappa_{el} << 1$, which means that just a small fraction of passage through the transition state leads to electron transfer.

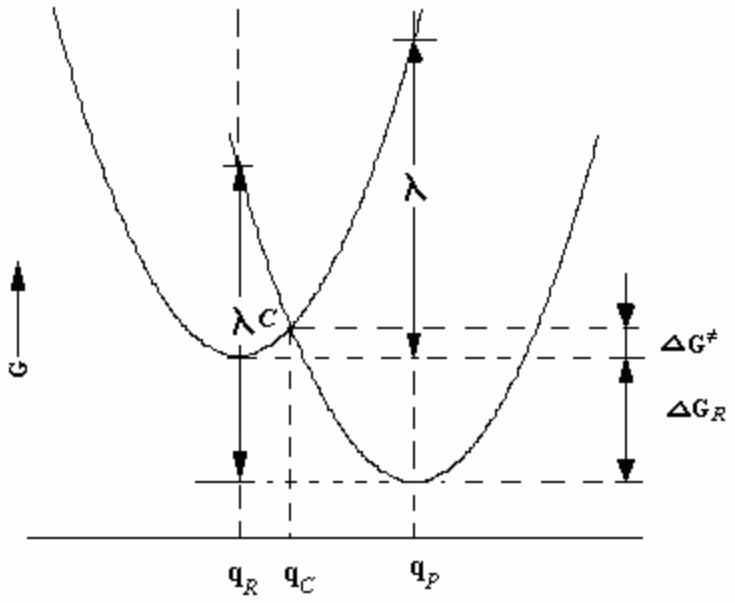

Figure 1. 3 Free energy surface of an electron transfer reaction

By assuming that the quadratic energy surfaces have the same force constant, the $\Delta G^{\neq}$ can be calculated from the free energy of reaction ΔG_R and reorganization energy λ with the following equation,

$$\Delta G^{\neq} = \frac{(\lambda + \Delta G_R)^2}{4\lambda} \tag{1.2}$$

The reorganization energy λ is defined as the energy given off when the reactant (product) molecule transmits from the state having product's (reactant's) equilibrium configuration to the

state having its own configuration. Both intramolecular factors λ_{in} and intermolecular factors λ_{out} contribute to λ, such that

$$\lambda = \lambda_{in} + \lambda_{out} \tag{1.3}$$

In the harmonic approximation, the inner reorganization energy λ_{in} is given by

$$\lambda_{in} = \frac{1}{2}\sum_i \overline{f_i}(r_R^{eq} - r_P^{eq})^2 \tag{1.4}$$

where r_R^{eq} and r_P^{eq} are the equilibrium bond lengths in the reactant and product states respectively. $\overline{f}_i$ is a reduced force constant of the i^{th} vibrational mode. The outer reorganization energy λ_{out} is correlated to the orientation and polarization of solvent molecules near the DA complex. In a two sphere dielectric continuum model, λ_{out} is given by

$$\lambda_{out} = \frac{(\Delta e)^2}{4\pi\varepsilon_0}\left[\frac{1}{2a_D} + \frac{1}{2a_A} - \frac{1}{r_{DA}}\right]\left[\frac{1}{\varepsilon_{op}} - \frac{1}{\varepsilon_s}\right] \tag{1.5}$$

where ε_0 is the permittivity of vacuum, r_{DA} is the distance between the electron donor center and the electron acceptor centor, a_D and a_A are the radii of the donor and acceptor respectively, ε_{op} and ε_s are the optical and static dielectric constants respectively.

Quantum Mechanical Aspects of Electron Transfer The classical Marcus theory works well in many cases, but the nonadiabatic region requires a quantum mechanical view to calculate the transmission coefficient κ_{el} and /or when high frequency modes contribute significantly to λ_{in}. In quantum mechanics, the electron donor and acceptor are treated as a whole system. It is common to use time-dependent perturbation theory, the Fermi "Golden rule" expression, to calculate the transmission rate constant ω_j from level j of the reactant state to a set product state:

$$\omega_j = \frac{2\pi}{\hbar}\left|V_{rp}\right|^2 \sum_i \left\langle \varphi_{p,i} \middle| \chi_{r,j} \right\rangle^2 \delta(\varepsilon_{p,i} - \varepsilon_{r,j}) \tag{1.6}$$

where $\left|V_{rp}\right|$ is the electronic coupling between reactant and product states(see Figure 1.4). $\varphi_{p,i}$ and $\chi_{r,j}$ are the vibrational wave functions for the equilibrium reactant level *i* and product level *j*, $\varepsilon_{p,i}$ and $\varepsilon_{r,j}$ are the corresponding energies, δ is the Dirac delta function that makes the transmission (electron tunneling) meet the requirement of energy conservation (Note: Assumes an "elastic tunneling"). The electronic coupling is commonly taken to have an exponential dependence on the distance between donor and acceptor,

$$\left|V_{rp}\right| = \left|V_{rp}^{0}\right| \exp\left(-\frac{\beta}{2} d\right) \tag{1.7}$$

Where β is the tunneling decay coefficienct, and d is the distance between donor and acceptor.

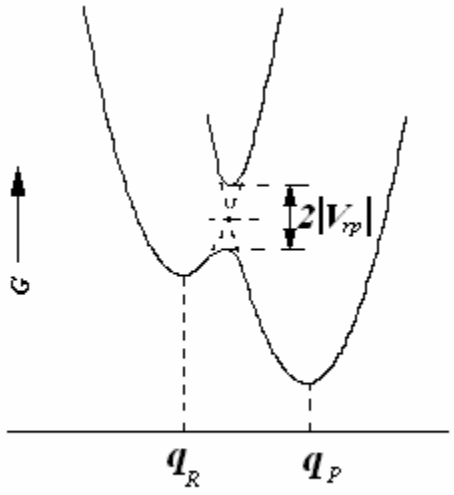

Figure 1. 4 Electron coupling and electron transfer energy surface

More than one reactant state can be the initial state of the transmission. So the overall rate constant is the sum over all reactant vibrational levels, weighted by some distribution law $\rho(\varepsilon_j)$, such as Boltzmann distribution.

$$k_{ET} = \frac{2\pi}{\hbar}\left|V_{rp}\right|^2 \sum_j \sum_i \left\langle \varphi_{p,i} \middle| \chi_{r,j} \right\rangle^2 \rho(\varepsilon_j)\delta(\varepsilon_{p,i} - \varepsilon_{r,j}) \tag{1.8a}$$

or more compactly

$$k_{ET} = \frac{2\pi}{\hbar}\left|V_{rp}\right|^2 FCWD \tag{1.8b}$$

where FCWD is named as Franck-Condon weighted density-of-states and defined by Equation 1.8a.

Several approximations are used in the treatment of FCWD and result in different expression for k_{ET}. One example is the "high-temperature limit" of the semiclassical Marcus, equation 1.9, which treats the solvent vibrational modes classically. In this limit, the rate constant is

$$k_{ET} = \frac{2\pi}{\hbar}\frac{\left|V_{rp}\right|^2}{\sqrt{4\pi\lambda\ k_B T}}\exp\left(-\frac{(\lambda + \Delta G_r)^2}{4\lambda k_B T}\right) \tag{1.9}$$

By introducing an "adiabaticity" factor g, an expression that changes smoothly between the adiabatic and nonadiabatic limits for the ET rate constant can be written as

$$k_{ET} = \frac{2\pi}{\hbar}\frac{\left|V_{rp}\right|^2}{\sqrt{4\pi\lambda\ k_B T}}\left(\frac{1}{1+g}\right)\exp\left(-\frac{(\lambda + \Delta G_r)^2}{4\lambda k_B T}\right) \tag{1.10}$$

and

$$g = \frac{\pi^2 k_B T\left|V_{rp}\right|^2 \tau_s}{\hbar\lambda} \tag{1.11}$$

where τ_s is the effective polarization relaxation time. When g<<1, the electron transfer is in the nonadiabatic limit and one obtains equation 1.9 for nonadiabatic ET rate constant. When g>>1, one finds

$$k_{ET} = \frac{1}{\tau_{eff}} \sqrt{\frac{\lambda}{\pi^3 k_B T}} \exp\left(- \frac{(\lambda + \Delta G_r)^2}{4 \lambda k_B T} \right) \tag{1.12}$$

for the adiabatic ET rate constant, which is the expected result.[70]

1.4.2 Electron Transfer on Electrode Surface

Zusman[150] used a master equation approach to elucidate how solvent frictional coupling can influence electron transfer reactions. For heterogeneous electron transfer between a redox species and a metal electrode, he found the following expression for the rate constant.[151]

$$k_{ET} = \frac{1}{\pi \tau_s} \sqrt{\frac{\lambda}{\pi k_B T}} \sin\left(\pi \sqrt{\frac{\Delta G^{\neq}}{\lambda}} \right) \exp\left(- \frac{\Delta G^{\neq}}{k_B T} \right) \cdot \ln\left[1 + \pi \tau_s k_{NA}^0 \sqrt{\frac{\pi k_B T}{\lambda}} \frac{\exp\left(\Delta G^{\neq} / k_B T \right)}{\sin\left(\pi \sqrt{\Delta G^{\neq} / \lambda} \right)} \right] \tag{1.13}$$

in which the activation free energy is

$$\Delta G^{\neq} = \frac{1}{4\lambda} \left(e\eta + \lambda + kT \cdot \ln \frac{C_{ox}}{C_{red}} \right)^2 ,$$

where the overpotential η is the difference between the applied potential and the equilibrium potential determined by Nernst equation. Another common expression for the activation free energy is

$$\Delta G^{\neq} = \frac{1}{4\lambda} \left(e\eta_0 + \lambda \right)^2$$

λ is the reorganization energy, η_0 is the formal overpotential, the difference between the applied potential and the formal potential. The rate constant k_{NA}^0, the nonadiabatic limit, is the rate constant processed by the redox molecules that is most close to the electrode surface. Equation 1.13 is general, and two limits are commonly applied in analyzing electron transfer rates at electrodes.

Nonadiabatic Limit In the limit of weak electronic interaction, where the following inequality is satisfied,

$$k_{NA} << \frac{1}{\pi\tau_s}\sqrt{\frac{\lambda_o}{\pi k_B T}}\sin\left(\pi\sqrt{\frac{\Delta G^{\neq}}{\lambda}}\right)\exp\left(-\frac{\Delta G^{\neq}}{k_B T}\right)$$

the electron transfer rate constant simplifies to the nonadiabatic limit, $k_{ET} = k_{NA}^{0}$. This limit applies to the electron transfer for thick monolayers where the rate constant appears to decreas exponentially with distance.

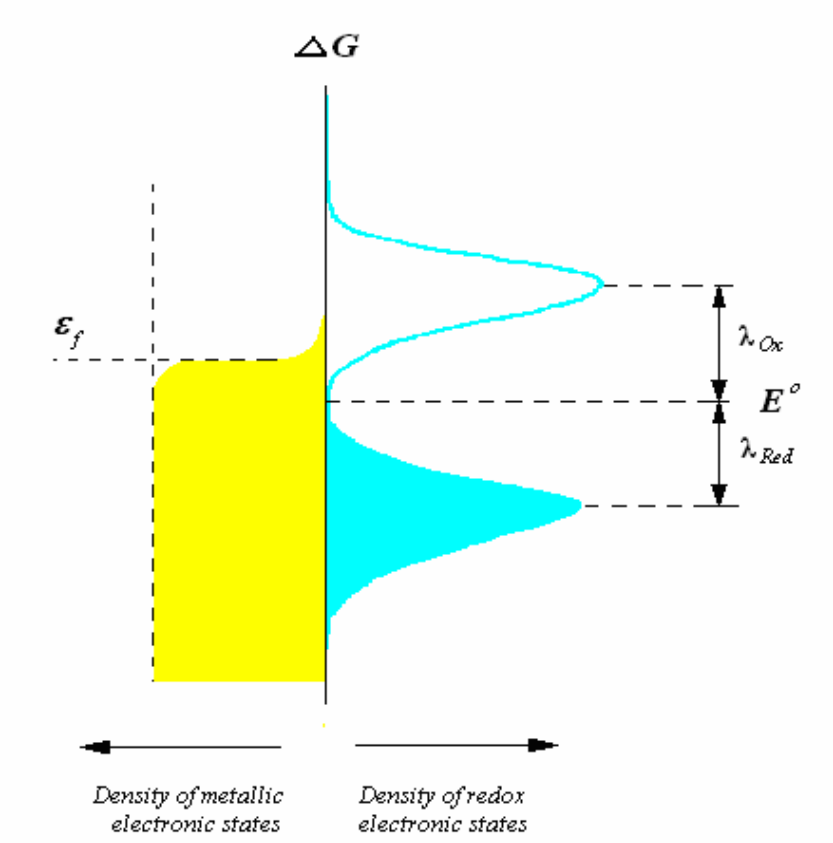

Figure 1. 5 Schematic presentation of the density of redox electronic states and the density of metal electronic states, ε_f is the Fermi energy, E0 is the free energy corresponding to the formal potential.

At conductive electrode surface, electrons can be exchanged between multiple redox electronic states and metallic electronic states meeting the requirement of conservation of energy. The rate constant may be obtained by taking the summation over these states, and be written as

$$k_{NA} = \int_{-\infty}^{\infty} k_{NA}^{0}(\varepsilon) f(\varepsilon)\ \rho(\varepsilon)\ d\varepsilon \tag{1.14}$$

$k(\varepsilon)$ is the nonadiabatic rate constant for electron transfer between redox state and electrode state having energy ε, and could be derived equation 1.9; ρ(ε) is the density of electronic states in the electrode; and *f(ε)* is distribution function describing the electron population over electrode states, the Fermi-Dirac distribution law for metallic electrodes.

In a cathodic reaction, the electrode is the donor and electron transfer proceeds from filled metallic states to oxidants (acceptors) whose population has a Gaussian distribution centered at $\varepsilon - E^0 = \lambda_{ox}$ (see Figure 1.5), and the molecule is reduced. For the anodic reaction, electron transfer proceeds from filled redox species' states which have a Gaussian distribution centered at $\varepsilon - E^0 = \lambda_{red}$, to vacant metallic states, and the molecule is oxidized. The free energy of this reduction reaction can be expressed as

$$\Delta G = (\varepsilon_f - \varepsilon) + e\eta \tag{1.15}$$

Combining equation 1.15 with equation 1.9, the electron transfer rate constant of transmission from one metallic level to redox states is given as

$$k(\varepsilon) = \frac{2\pi}{\hbar} \frac{\left|V_{rp}\right|^2}{\sqrt{4\pi\lambda\ k_B T}} \exp\left(- \frac{\left(\lambda + (\varepsilon_f - \varepsilon) + e\eta\right)^2}{4\lambda k_B T} \right) \tag{1.16}$$

By making the approximation that the electronic coupling and ρ(ε) vary weakly with energy, the rate constant (reducing half reaction) becomes

$$k_{\mathrm{Re}d} = \frac{2\pi}{\hbar}\frac{\left|V_{rp}\right|^2}{\sqrt{4\pi\lambda\ k_B T}}\int_{-\infty}^{\infty}\rho(\varepsilon)f(\varepsilon)\exp\left(-\frac{\left(\lambda+(\varepsilon_f-\varepsilon)+e\eta\right)^2}{4\lambda k_B T}\right) \tag{1.17}$$

where $\rho(\varepsilon)$ is the density of electronic states of the metallic electrode, and $f(\varepsilon)$ is the Fermi-Dirac distribution law.

$$f(\varepsilon) = \frac{1}{1+\exp\left[\dfrac{\varepsilon-\varepsilon_f}{k_B T}\right]} \tag{1.18}$$

The oxidation reaction can be obtained in similar way

$$k_{ox} = \frac{2\pi}{\hbar}\left|V_{rp}\right|^2\left(4\pi\lambda\ k_B T\right)^{-1/2}\int_{-\infty}^{\infty}\rho(\varepsilon)[1-f(\varepsilon)]\exp\left(-\frac{\left(-\lambda+(\varepsilon_f-\varepsilon)+e\eta\right)^2}{4\lambda k_B T}\right) \tag{1.19}$$

By approximating the Fermi distribution law as a step function ($f(\varepsilon) = 0$ for $\varepsilon > \varepsilon_f$ and $f(\varepsilon) = 1$ for $\varepsilon < \varepsilon_f$), Equation 1.17 becomes

$$k_{NA}^0 \approx \frac{\pi}{\hbar}|V|^2\ \rho\ erfc\left(\frac{\lambda+e\eta}{\sqrt{4\lambda\ k_B T}}\right) \tag{1.20}$$

where *erfc(z)* is the complimentary error function. This expression ignores contributions to the reorganization energy from quantized modes. At the special potential for which $\eta = 0$, the electron transfer rate constant is called the standard exchange rate constant, and can be approximated as

$$k^0 \approx \frac{\pi}{\hbar}|V|^2\ \rho\sqrt{\frac{\pi k_B T}{\lambda}}\exp\left(-\frac{\lambda}{4k_B T}\right) \tag{1.21}$$

where it is assume that and $\lambda >> k_B T$.

Solvent-Friction Limit In the case of strong interaction and/or large τ_s, the following relationship is satisfied,

$$k_{NA} >> \frac{1}{\pi\tau_s}\sqrt{\frac{\lambda}{\pi k_B T}}\sin\left(\pi\sqrt{\frac{\Delta G^{\neq}}{\lambda}}\right)\exp\left(-\frac{\Delta G^{\neq}}{k_B T}\right),$$

and the electron transfer rate constant is controlled by the rate of diffusing through the activation barrier. In this limit, equation 1.13 reduces to

$$k_{ET} = \frac{1}{\pi\tau_s}\sqrt{\frac{\lambda}{\pi k_B T}}\sin\left(\pi\sqrt{\frac{\Delta G^{\neq}}{\lambda}}\right)\exp\left(-\frac{\Delta G^{\neq}}{k_B T}\right)\cdot\ln\left[\pi\tau_s k_{NA}^{0}\sqrt{\frac{\pi k_B T}{\lambda}}\frac{\exp\left(\Delta G^{\neq}/k_B T\right)}{\sin\left(\pi\sqrt{\Delta G^{\neq}/\lambda}\right)}\right] \quad (1.22)$$

In this limit the rate constant is inversely proportional to the polarization relaxation time of the medium. If the reorganization can be approximated as classical and satisfies $\lambda >> k_B T$, equation 1.22 at zero overpotential ($\eta = 0$) can be simplified as

$$k_{red}(\eta = 0) = \frac{1}{\pi\tau_s}\sqrt{\frac{\lambda}{\pi k_B T}}\exp\left(-\frac{\lambda}{4k_B T}\right)\cdot\ln\left[\frac{\pi^3\tau_s}{\hbar}|V|^2\rho\frac{k_B T}{\lambda}\right] \quad (1.23)$$

where equation 1.21 was used as an approximation for k_{NA}^{0}, Often the solvent's relaxation time, τ_s, correlates with other properties of the solvent, such as the shear viscosity and/or the Debye relaxation time. Using a Debye model for τ_s, namely

$$\tau_s \approx \tau_L = \left(\frac{\varepsilon_\infty}{\varepsilon_s}\right)\left(\frac{3\eta_s V_m}{RT}\right) \quad (1.24)$$

illustrates this relationship. In equation 1.24, τ_s is approximated by the longitudinal dielectric relaxation time τ_L; ε_s is the static dielectric constant of solution; ε_∞ is the optical dielectric constant of solution; V_m is the molar volume of solution; and η_s is the shear viscosity of the medium, the temperature dependence of which is commonly rewritten as

$$\eta_s = A\exp\left(\frac{\Delta G_\eta}{k_B T}\right) \quad (1.25)$$

where ΔG_η is the activation free energy of viscosity. Using with equation 1.24 and 1.25, equation 1.23 simplifies to

$$k_{red}(\eta = 0) = \frac{B}{\pi\tau_s}\sqrt{\frac{\lambda}{\pi k_B T}}\exp\left(-\left(\frac{\lambda}{4} + \Delta G_\eta\right)\frac{1}{k_B T}\right) \tag{1.26}$$

where B is a combined constant written as

$$B = \left(\frac{\varepsilon_s}{\varepsilon_\infty}\right)\left(\frac{RT}{3V}\right)\ln\left(\frac{\pi^3\tau_s}{\hbar}|V|^2\rho\frac{k_B T}{\lambda}\right)$$

Equation 1.26 shows that temperature studies yield a larger activation energy in adiabatic ET than in nonadiabatic ET. This behavior was predicted by Zusman. [152]

For the solvent friction region, two limits should be considered. The first limit is $|V| << k_B T$, in which equation 1.26 is good enough to describe the reaction rate constant. When $|V| >> k_B T$, however, a value equal to $|V|$ has to be subtracted from the activation energy and the rate constant has the form

$$k_{red}(\eta = 0) = \frac{B}{\pi\tau_s}\sqrt{\frac{\lambda}{\pi k_B T}}\exp\left(-\left(\frac{\lambda}{4} + \Delta G_\eta - |V|\right)\frac{1}{k_B T}\right) \tag{1.27}$$

which accounts for the splitting of the energy surface.[70]

The relations presented for the reduction rate constant take a somewhat different form for the oxidation step, however they display the same dependency on solvent relaxation time, reorganization energy, and tunneling probability.

1.5 Research Strategies

For the interfacial electron transfer of horse heart cytochrome *c*, four different coupling methods were employed. A) Cytochrome *c* was absorbed electrostatically to a pure SAM composed of carboxylic acid-terminated alkanethiol molecules. B) Cytochrome *c* was absorbed electrostatically to a mixed SAM composed of hydroxyl-terminated and carboxylic acid terminated thiols. C) Cytochrome *c* was bound covalently to the mixed SAM (covalent attachment). D) Cytochrome *c* was tethered to a SAM by a pyridine terminus which replaces Met 80 as the sixth ligand.

The formal potential of cytochrome *c* was probed using cyclic voltammetry as a function of ionic strength. By comparing the four different SAM-based immobilization strategies (electrostatic binding on both pure and mixed monolayers, heme-ligated binding, and covalent attachment) and two different buffer types (one containing specifically binding ions and the other more weakly binding ions), the influence of ionic environment on formal potential is more fully elucidated.

The electron transfer kinetics of cytochrome *c* in these four systems were investigated electrochemically as a function of the ionic strength of the buffer solution. Comparisons among these systems allow ambiguities, originating from solution resistance and double layer effects, to be removed. The results suggest that the most stable binding geometry has the best electron transfer efficiency. The results also suggest that there exist a distribution of cytochrome *c* orientations, thus a distribution of electron transfer rates, at each ionic strength.

The temperature, distance and overpotential dependencies of the electron transfer rate constant of cytochrome *c* immobilized on pyridine terminated SAMs were studied by cyclic voltammetry and time-resolved surface-enhanced resonance Raman spectroelectrochemistry. The

results support a change of mechanism from a tunneling controlled reaction at long distances to a solvent / protein friction controlled reaction for the thinner films, rather than conformational gating.

The rate constant k^0 of cytochrome *c* immobilized with mixed C15-carboxylic acid/hydroxyl-terminated SAMs and C16-pyridine/alkane terminated SAMs, was investigated as a function of the surface composition of the mixed monolayer in the nonadiabatic electron tunneling region. It was found that by increasing the concentration of shorter-chain hydroxyl diluent thiol in the SAM the rate constant increased in a systematic way. When diluent composition is high, the k^0 increases exponentially with decreasing chain length of the diluent molecules until the chain length of the diluent molecule is eight methylene groups. These results indicate that the space occupied by the short chain diluent molecules is a part of the electron tunneling pathway, and electronic coupling between the protein and electrode is enhanced by shortening the tunneling distance.

References

(1) Pettigrew, G. W.; Moore, G. R. *cytochromes c: Biological Aspects*; Springer-Berlag: Berlin, Heidelberg, New York, London, Paris, Tokyo, 1987.

(2) Beissenhirts, M. K.; Scheller, F. W.; Lisdat, F. *Anal. Chem.* **2004**, *76*, 4665-4671.

(3) Dai, Z.; Liu, S.; Ju, H. *Electrochimica Acta* **2004**, *49* 2139-2144.

(4) Scott, R. A.; Mark, A. G. *Cytochrome c: a multidisciplinary approach*; University Science Books: Sausalito, california, 1996.

(5) Sanishvili, R.; Volz, K. W.; Westbrook, E. M.; Margoliash, E. *Structure* **1995**, *3*, 707-716.

(6) Brige, A.; Leys, D.; Meyer, T. E.; Cusanovich, M. A.; Van Beeumen, J. J. *J. Inorg. Biochem.* **2001**, *86*, 158-158.

(7) Banci, L.; Bertini, I.; Huber, J. G.; Spyroulias, G. A.; Turano, P. *J. Biol. Inorg. Chem.* **1999**, *4*, 21-31.

(8) Banci, L.; Bertini, I.; Gray, H. B.; Luchinat, C.; Reddig, T.; Rosato, A.; Turano, P. *Biochemistry* **1997**, *36*, 9867-9877.

(9) Fedurco, M. *Coord. Chem. Rev.* **2000**, *209*, 263-331.

(10) Tillman, N.; Ulman, A.; Schildkraut, J. S.; Penner, T. L. *J. Am. Chem. Soc.* **1988**, *110*, 6136-44.

(11) Tillman, N.; Ulman, A.; Elman, J. F. *Langmuir* **1990**, *6*, 1512-18.

(12) Tillman, N.; Ulman, A.; Elman, J. F. *Langmuir* **1989**, *5*, 1020-6.

(13) Sagiv, J. *J. Am. Chem. Soc.* **1980**, *102*, 92-8.

(14) Sagiv, J. *Israel J. Chem.* **1980**, *18*, 339-345.

(15) Sagiv, J. *Israel J. Chem.* **1980**, *18*, 346-353.

(16) Pomerantz, M.; Segmueller, A.; Netzer, L.; Sagiv, J. *Thin Solid Films* **1985**, *132*, 153-62.

(17) Netzer, L.; Sagiv, J. *J. Am. Chem. Soc.* **1983**, *105*, 674-6.

(18) Netzer, L.; Iscovici, R.; Sagiv, J. *Thin Solid Films* **1983**, *99*, 235-41.

(19) Netzer, L.; Iscovici, R.; Sagiv, J. *Thin Solid Films* **1983**, *100*, 67-76.

(20) Maoz, R.; Sagiv, J.; Degenhardt, D.; Moehwald, H.; Quint, P. *Supramol. Sci.* **1995**, *2*, 9-24.

(21) Maoz, R.; Sagiv, J. *Langmuir* **1987**, *3*, 1034-44.

(22) Maoz, R.; Sagiv, J. *Langmuir* **1987**, *3*, 1045-51.

(23) Maoz, R.; Sagiv, J. *Thin Solid Films* **1985**, *132*, 135-51.

(24) Gun, J.; Sagiv, J. *J. Coll. Interf. Sci.* **1986**, *112*, 457-72.

(25) Cohen, S. R.; Naaman, R.; Sagiv, J. *J. of Phys. Chem.* **1986**, *90*, 3054-6.

(26) Brolo, A. G.; Gordon, R.; Leathem, B.; Kavanagh, K. L. *Langmuir* **2004**, *20*, 4813-4815.

(27) Wasserman, S. R.; Whitesides, G. M.; Tidswell, I. M.; Ocko, B. M.; Pershan, P. S.; Axe, J. D. *J. Am. Chem. Soc.* **1989**, *111*, 5852-61.

(28) Porter, M. D.; Bright, T. B.; Allara, D. L.; Chidsey, C. E. D. *J. Am. Chem. Soc.* **1987**, *109*, 3559-68.

(29) Laibinis, P. E.; Hickman, J. J.; Wrighton, M. S.; Whitesides, G. M. *Science* **1989**, *245*, 845-7.

(30) Laibinis, P. E.; Whitesides, G. M.; Allara, D. L.; Tao, Y. T.; Parikh, A. N.; Nuzzo, R. G. *J. Am. Chem. Soc.* **1991**, *113*, 7152-67.

(31) Laibinis, P. E.; Whitesides, G. M. *Omega-terminated alkanethiolate monolayers on surfaces of copper, silver and gold have similar wettabilities*, Dep. Chem.,Harvard Univ.,Cambridge,MA,USA., 1991.

(32) Laibinis, P. E.; Bain, C. D.; Nuzzo, R. G.; Whitesides, G. M. *J. Phys. Chem.* **1995**, *99*, 7663-76.

(33) Troughton, E. B.; Bain, C. D.; Whitesides, G. M.; Nuzzo, R. G.; Allara, D. L.; Porter, M. D. *Langmuir* **1988**, *4*, 365-85.

(34) Strong, L.; Whitesides, G. M. *Langmuir* **1988**, *4*, 546-58.

(35) Nuzzo, R. G.; Fusco, F. A.; Allara, D. L. *J. Am. Chem. Soc.* **1987**, *109*, 2358-68.

(36) Nuzzo, R. G.; Allara, D. L. *J. Am. Chem. Soc.* **1983**, *105*, 4481-3.

(37) Lopez, G. P.; Biebuyck, H. A.; Harter, R.; Kumar, A.; Whitesides, G. M. *J. Am. Chem. Soc.* **1993**, *115*, 10774-81.

(38) Laibinis, P. E.; Whitesides, G. M. *J. Am. Chem. Soc.* **1992**, *114*, 9022-8.

(39) Laibinis, P. E.; Nuzzo, R. G.; Whitesides, G. M. *J.Phys. Chem.* **1992**, *96*, 5097-105.

(40) Folkers, J. P.; Laibinis, P. E.; Whitesides, G. M. *J. Adh. Sci. Techn.* **1992**, *6*, 1397-410.

(41) Folkers, J. P.; Laibinis, P. E.; Whitesides, G. M. *Langmuir* **1992**, *8*, 1330-41.

(42) Chidsey, C. E. D.; Loiacono, D. N. *Langmuir* **1990**, *6*, 682-91.

(43) Chidsey, C. E. D.; Liu, G. Y.; Scoles, G.; Wang, J. *Langmuir* **1990**, *6*, 1804-6.

(44) Chidsey, C. E. D.; Liu, G. Y.; Rowntree, P.; Scoles, G. *J. Chem. Phys.* **1989**, *91*, 4421-3.

(45) Chidsey, C. E. D.; Bertozzi, C. R.; Putvinski, T. M.; Mujsce, A. M. *J. Am. Chem. Soc.* **1990**, *112*, 4301-6.

(46) Carey, R. I.; Folkers, J. P.; Whitesides, G. M. *Langmuir* **1994**, *10*, 2228-34.

(47) Biebuyck, H. A.; Whitesides, G. M. *Langmuir* **1993**, *9*, 1766-70.

(48) Bain, C. D.; Whitesides, G. M. *Science* **1988**, *240*, 62-3.

(49) Bain, C. D.; Troughton, E. B.; Tao, Y. T.; Evall, J.; Whitesides, G. M.; Nuzzo, R. G. *J. Am. Chem. Soc.* **1989**, *111*, 321-35.

(50) Bain, C. D.; Biebuyck, H. A.; Whitesides, G. M. *Langmuir* **1989**, *5*, 723-7.

(51) Bain, C. D.; Biebuyck, H. A.; Whitesides, G. M. *Comparison of self-assembled monolayers on gold: coadsorption of thiols and disulfides*, Dep. Chem.,Harvard Univ.,Cambridge,MA,USA., 1989.

(52) Tao, Y.-T.; Pandiaraju, S.; Lin, W.-L.; Chen, L.-J. *Langmuir* **1998**, *14*, 145-150.

(53) Allara, D. L.; Nuzzo, R. G. *Langmuir* **1985**, *1*, 52-66.

(54) Allara, D. L.; Nuzzo, R. G. *Langmuir* **1985**, *1*, 45-52.

(55) Allara, D. L.; Nuzzo, R. G. *Polymer Preprints (ACS, Division of Polymer Chemistry)* **1984**, *25*, 185.

(56) Schlotter, N. E.; Porter, M. D.; Bright, T. B.; Allara, D. L. *Chem. Phys. Lett.* **1986**, *132*, 93-8.

(57) Whitesides, G. M.; Laibinis, P. E. *Langmuir* **1990**, *6*, 87-96.

(58) Patel, N.; Davies, M. C.; Hartshorne, M.; Heaton, R. J.; Roberts, C. J.; Tendler, S. J. B.; Williams, P. M. *Langmuir* **1997**, *13*, 6485-6490.

(59) Ahn, S. J.; Mirzakhojaev, D. A.; Kim, S. H.; Kim, K. *Molecular Crystals Liquid Crystals Sci. Techn., A:* **1995**, *267*, 205-10.

(60) Tao, Y. T.; Huang, C. Y.; Chiou, D. R.; Chen, L. J. *Langmuir* **2002**, *18*, 8400-8406.

(61) Tao, Y.-T.; Lin, W.-L.; Hietpas, G. D.; Allara, D. L. *J. Phys. Chem. B* **1997**, *101*, 9732-9740.

(62) Allara, D. L.; Atre, S. V.; Elliger, C. A.; Snyder, R. G. *J. Am. Chem. Soc.* **1991**, *113*, 1852-4.

(63) Tao, Y.-T. *Bulletin Institute Chem.* **1996**, *43*, 63-75.

(64) Tao, Y. T. *J. Am. Chem. Soc.* **1993**, *115*, 4350-8.

(65) Tao, Y. T.; Lee, M. T.; Chang, S. C. *J. Am. Chem. Soc.* **1993**, *115*, 9547-55.

(66) Finklea, H. O. *electroanal. Chem.*. **1996**, *19*, 109-335.

(67) Lide, D. R.; Frederikse, H. P. R. *CRC Handbook of chemistry and physics*; 75th edition 1913-1995 ed. Boca Raton, Ann Arbor,London,Tokyo.

(68) Schlenoff, J.; Li, M.; Ly, H. *J. Am. Chem. Soc.* **1995**, *117*, 12528-36.

(69) Khoshtariya, D. E.; Dolidze, T. D.; Zusman, L. D.; Waldeck, D. H. *J. Phys. Chem. A* **2001**, *105*, 1818-1829.

(70) Khoshtariya, D. E.; Wei, J.; Liu, H.; Yue, H.; Waldeck, D. H. *J. Am. Chem. Soc.* **2003**, *125*, 7704-7714.

(71) Kumar, K.; Kurnikov, I. V.; Beratan, D. N.; Waldeck, D. H.; Zimmt, M. B. *J. Phys. Chem. A* **1998**, *102*, 5529-5541.

(72) Liu, H.; Yamamoto, H.; Wei, J.; Waldeck, D. H. *Langmuir* **2003**, *19*, 2378-2387.

(73) Napper, A. M.; Liu, H.; Waldeck, D. H. *J. Phys. Chem. B* **2001**, *105*, 7699-7707.

(74) Wei, J.; Liu, H.; Dick Allison, R.; Yamamoto, H.; He, Y.; Waldeck David, H *J. Am. Chem. Soc.* **2002**, *124*, 9591-9.

(75) Wei, J.; Liu, H.; Khoshtariya, D. E.; Yamamoto, H.; Dick, A.; Waldeck, D. H. *Angewandte Chemie, International Edition* **2002**, *41*, 4700-4703.

(76) Yamamoto, H.; Waldeck, D. H. *J. Phys. Chem. B* **2002**, *106*, 7469-7473.

(77) Biebuyck, H. A.; Bain, C. D.; Whitesides, G. M. *Langmuir* **1994**.

(78) Creager, S. E.; Hockett, L. A.; Rowe, G. K. *Langmuir* **1992**, *8*.

(79) Ulman, A.; Eilers, J. E.; Tillman, N. *Langmuir* **1989**, *5*, 1147-52.

(80) Davis, J. J.; Morgan, D. A.; Wrathmell, C. L.; Axford, D. N.; Zhao, J.; Wang, N. *J. Materials Chem.* **2005**, *15*, 2160-2174.

(81) Vincent, K. A.; Armstrong, F. A. *Inorg. Chem.* **2005**, *44*, 798-809.

(82) Shleev, S.; Tkac, J.; Christenson, A.; Ruzgas, T.; Yaropolov Alexander, I.; Whittaker James, W.; Gorton, L. *Biosensors & bioelectronics* **2005**, *20*, 2517-54.

(83) Wong Tuck, S.; Schwaneberg, U. *Curr. opinion biotechn.* **2003**, *14*, 590-6.

(84) Rusling, J. F.; Forster, R. J. *J. Colloid Interf. Sci.e* **2003**, *262*, 1-15.

(85) Liu, S.; Leech, D.; Ju, H. *Anal.l Lett.* **2003**, *36*, 1-19.

(86) Katz, E.; Willner, I. *Electroanal.* **2003**, *15*, 913-947.

(87) Armstrong, F. A. *Russian J.Electrochem.* **2002**, *38*, 58-73.

(88) Leger, C.; Elliott, S. J.; Hoke, K. R.; Jeuken, L. J. C.; Jones, A. K.; Armstrong, F. A. *Biochemistry* **2003**, *42*, 8653-8662.

(89) Zhang, J.; Grubb, M.; Hansen, A. G.; Kuznetsov, A. M.; Boisen, A.; Wackerbarth, H.; Ulstrup, J. *J Physics: Cond. Matter* **2003**, *15*, S1873-S1890.

(90) Hansen, A. G.; Wackerbarth, H.; Nielsen, J. U.; Zhang, J.; Kuznetsov, A. M.; Ulstrup, J. *Russian J.Electrochem.* **2003**, *39*, 108-117.

(91) Zhang, J.; Kuznetsov, A. M.; Ulstrup, J. *J.Electroanal. Chem.* **2003**, *541*, 133-146.

(92) Zhang, J.; Christensen, H. E. M.; Ooi, B. L.; Ulstrup, J. *Langmuir* **2004**, *20*, 10200-10207.

(93) Bonanni, B.; Alliata, D.; Bizzarri, A. R.; Cannistraro, S. *ChemPhysChem* **2003**, *4*, 1183-1188.

(94) Heering, H. A.; Wiertz, F. G. M.; Dekker, C.; De Vries, S. *J. Am. Chem. Soc.* **2004**, *126*, 11103-11112.

(95) Hansen, A. G.; Boisen, A.; Nielsen, J. U.; Wackerbarth, H.; Chorkendorff, I.; Andersen, J. E. T.; Zhang, J.; Ulstrup, J. *Langmuir* **2003**, *19*, 3419-3427.

(96) Baymann, F.; Barlow, N. L.; Aubert, C.; Schoepp-Cothenet, B.; Leroy, G.; Armstrong, F. A. *FEBS Letters* **2003**, *539*, 91-94.

(97) Davis, J. J.; Bruce, D.; Canters, G. W.; Crozier, J.; Hill, H. A. O. *Chem. Comm.* **2003**, 576-577.

(98) Andolfi, L.; Bruce, D.; Cannistraro, S.; Canters, G. W.; Davis, J. J.; Hill, H. A. O.; Crozier, J.; Verbeet, M. P.; Wrathmell, C. L.; Astier, Y. *J. Electroanal. Chem.* **2004**, *565*, 21-28.

(99) Strauss, E.; Thomas, B.; Yu, S.-T. *Langmuir* **2004**, *20*, 8768-8772.

(100) Runge, A. F.; Saavedra, S. S. *Langmuir* **2003**, *19*, 9418-9424.

(101) Trammell, S. A.; Wang, L.; Zullo, J. M.; Shashidhar, R.; Lebedev, N. *Biosensors & Bioelectronics* **2004**, *19*, 1649-1655.

(102) Armstrong, F. A.; Barlow, N. L.; Burn, P. L.; Hoke, K. R.; Jeuken, L. J. C.; Shenton, C.; Webster, G. R. *Chem. Comm.* **2004**, 316-317.

(103) Fujita, K.; Nakamura, N.; Ohno, H.; Leigh, B. S.; Niki, K.; Gray, H. B.; Richards, J. H. *J. Am. Chem. Soc.* **2004**, *126*, 13954-13961.

(104) Yang, L.; Li, Y. *Biosensors & Bioelectronics* **2005**, *20*, 1407-1416.

(105) Munge, B.; Das, S. K.; Ilagan, R.; Pendon, Z.; Yang, J.; Frank, H. A.; Rusling, J. F. *J. Am. Chem. Soc.* **2003**, *125*, 12457-12463.

(106) Friedrich, M. G.; Geib, F.; Naumann, R.; Knoll, W.; Ataka, K.; Heberle, J.; Hrabakova, J.; Murgida, D., H.; Hildebrandt, P. *Chem. Comm.*. **2004**, 2376-2377.

(107) Topoglidis, E.; Astuti, Y.; Duriaux, F.; Graetzel, M.; Durrant, J. R. *Langmuir* **2003**, *19*, 6894-6900.

(108) Topoglidis, E.; Discher, B. M.; Moser, C. C.; Dutton, P. L.; Durrant, J. R. *ChemBioChem* **2003**, *4*, 1332-1339.

(109) Astuti, Y.; Topoglidis, E.; Briscoe, P. B.; Fantuzzi, A.; Gilardi, G.; Durrant, J. R. *J. Am. Chem. Soc.* **2004**, *126*, 8001-8009.

(110) Gan, X.; Liu, T.; Zhong, J.; Liu, X.; Li, G. *ChemBioChem* **2004**, *5*, 1686-1691.

(111) Cai, C.; Chen, J. *Analytical Biochemistry* **2004**, *332*, 75-83.

(112) Gooding, J. J.; Wibowo, R.; Liu, J.; Yang, W.; Losic, D.; Orbons, S.; Mearns, F. J.; Shapter, J. G.; Hibbert, D. B. *J. Am. Chem. Soc.* **2003**, *125*, 9006-9007.

(113) DeRosa Maria, C.; Sancar, A.; Barton Jacqueline, K. *PNAS* **2005**, *102*, 10788-92.

(114) Boal Amie, K.; Yavin, E.; Lukianova Olga, A.; O'Shea Valerie, L.; David Sheila, S.; Barton Jacqueline, K. *Biochemistry* **2005**, *44*, 8397-407.

(115) Wang, Q.; Lu, G.; Yang, B. *Langmuir* **2004**, *20*, 1342-1347.

(116) Liu, H.-H.; Tian, Z.-Q.; Lu, Z.-X.; Zhang, Z.-L.; Zhang, M.; Pang, D.-W. *Biosensors bioelectronics* **2004**, *20*, 294-304.

(117) Fan, C.; Zhong, J.; Guan, R.; Li, G. *Biochimica et biophysica acta* **2003**, *1649*, 123-6.

(118) Morrin, A.; Guzman, A.; Killard, A. J.; Pingarron, J. M.; Smyth, M. R. *Biosensors Bioelectronics* **2003**, *18*, 715-720.

(119) Bonanni, B.; Alliata, D.; Bizzarri Anna, R.; Cannistraro, S. *Chemphyschem : Eur. J. chem. Phys. Phys. Chem.* **2003**, *4*, 1183-8.

(120) Trammell Scott, A.; Wang, L.; Zullo Joseph, M.; Shashidhar, R.; Lebedev, N. *Biosensors bioelectronics* **2004**, *19*, 1649-55.

(121) Johnson, D. L.; Polyak, S. W.; Wallace, J. C.; Martin, L. L. *Lett. Peptide Sci.* **2004**, *10*, 495-500.

(122) Collinson, M.; Bowden, E. F.; Tarlow, M. J. *Langmuir* **1992**, *8*, 1274-50.

(123) Clark, R. A.; Bowden, E. F. *Langmuir* **1997**, *13*, 559-565.

(124) Barlow, G. H.; Margoliash, E. *J. Biol. Chem.***1966**, *241*, 1473-1477.

(125) Brautigan, D. L.; Ferguson-Miller, S.; Margoliash, E. *J. Biol. Chem.* **1978**, *253*, 130-139.

(126) Brautigan, D. L.; Ferguson-Miller, S.; Tarr, G. E.; Margoliash, E. *J. Biol. Chem.***1978**, *253*, 140-148.

(127) Ferguson-Miller, S.; Brautigan, D. L.; Margoliash, E. *J. Biol. Chem.* **1978**, *253*, 149-159.

(128) Kang, C. H.; Brautigan, D. L.; Osheroff, N.; Margoliash, E. *J. Biol. Chem.***1978**, *253* 6502-6510.

(129) Avila, A.; Gregory, B. W.; Niki, K.; Cotton, T. M. *J. Phys. Chem. B* **2000**, *104*, 2759-2766.

(130) Rivas, L.; Murgida, D. H.; Hildebrandt, P. *J. Inorg.c Biochem.* **2001**, *86*, 402-402.

(131) Niki, K.; Hardy, W. R.; Hill, M. G.; Li, H.; Sprinkle, J. R.; Margoliash, E.; Fujita, K.; Tanimura, R.; Nakamura, N.; Ohno, H.; Richards, J. H.; Gray, H. B. *J. Phys. Chem. B* **2003**, *107*, 9947-9949.

(132) Wei, J. J.; Liu, H. Y.; Niki, K.; Margolish, E.; Waldeck David, H. *J. Phys. Chem. B.* **2004**, *108* 16912-16917.

(133) Leopold, M. C.; Bowden, E. F. *Langmuir* **2002**, *18*, 2239-2245.

(134) El Kasmi, A.; Wallace, J. M.; Bowden, E. F.; Binet, S. M.; Linderman, R. J. *J. Am. Chem. Soc.* **1998**, *120*, 225-226.

(135) Chen, X.; Ferrigno, R.; Yang, J.; Whitesides, G. M. *Langmuir* **2002**, *18*, 7009-7015.

(136) Wackerbarth, H.; Hildebrandt, P. *Chemphyschem* **2003**, *4*, 714-724.

(137) Murgida, D. H.; Hildebrandt, P. *J.Phys. Chem. B* **2002**, *106*, 12814-12819.

(138) Hildebrandt, P.; Murgida, D. H. *Bioelectrochemistry* **2002**, *55*, 139-143.

(139) Arnold, S.; Feng, Z. Q.; Kakiuchi, T.; Knoll, W.; Niki, K. *J.Electroanal. Chem.* **1997**, *438*, 91-97.

(140) Khoshtariya, D. E.; Wei, J. J.; Liu, H. Y.; Yue, H. J.; Waldeck, D. H. *J. Am. Chem. Soc.* **2003**, *125*, 7704-7714.

(141) Wei, J. J.; Liu, H. Y.; Khoshtariya, D. E.; Yamamoto, H.; Dick, A.; Waldeck, D. H. *Angewandte Chemie-International Edition* **2002**, *41*, 4700-4703.

(142) Wei, J. J.; Liu, H. Y.; Dick, A. R.; Yamamoto, H.; He, Y. F.; Waldeck, D. H. *J. Am. Chem. Soc.* **2002**, *124*, 9591-9599.

(143) Dutton, P. L. W., D. F.; Lee, C.-P. *Biochemistry* **1970**, *9*, 5077-5082.

(144) Vanderkooi, J. E., M.; Chance, B. *Arch. Biochem. Biophys.* **1973**, *154*, 531-540.

(145) Salamon, Z. T., G. J. *Bioenerg. Biomem.* **1997**, *29*, 211-216.

(146) Vanderkooi, J. E., M. *Arch. Biochem. Biophys.* **1974**, *162*, 385-391.

(147) Prime, K. L. W., G. M. *J. Am. chem. Soc.* **1993**, *115*, 10714-10721.

(148) Chen, X. F., R.; whitesides, G. M. *Langmuir* **2002**, *18*, 7009-7015.

(149) Amador, S. M. P., J.M.; Fischetti, R.; McCauley, J. P.; Smith, III, A. B.; Blasie, J. K. *Langmuir* **1993**, *9*, 812-817.

(150) Zusman, L. D. *Zeitschrift fur Physikalische Chemie* **1994**, *186*, 1-29.

(151) Zusman, L. D. *Chem. Phys.* **1987**, *112*, 53-59.

(152) Zusman, L. D. *Chem. Phys.* **1980**, *49*, 295-304.

CHAPTER 2 IMPACT OF SURFACE IMMOBILIZATION AND SOLUTION IONIC STRENGTH ON THE FORMAL POTENTIAL OF IMMOBILIZED CYTOCHROME *C*

This work has been published as Petrovic, Jelena; Clark, Rose A.; Yue, Hongjun; Waldeck, David H. *Langmuir* **2005**, 21, 6308-6316

Abstract

Four different self-assembled monolayer (SAM) electrode systems were examined electrochemically in order to better understand surface charge effects on the redox thermodynamics of immobilized horse heart cytochrome *c*. Neutralization of protein surface charge upon adsorption on anionic COOH-terminated SAMs was found to cause substantial changes in the formal potential, as determined by cyclic voltammetry. For cytochrome *c* immobilized on negatively charged surfaces, the formal potential shifted to more negative values as the ionic strength was decreased, which is opposite the trend displayed by solution cytochrome *c*. In contrast, immobilization to uncharged interfaces results in an ionic strength dependence for cytochrome c that is similar to its solution behavior. The results provide insight into the importance of surface charge on the formal potential of cytochrome *c*.

2.1 Introduction

Proteins perform a variety of vital tasks in living cells, hence a better understanding of their function in vivo and in vitro is desirable. Because proteins and other cellular components typically adsorb strongly or irreversibly to metal electrodes, surface modification is often required to study them electrochemically. Self-assembled monolayer (SAM) films provide a useful method to modify metal electrodes1 for the investigation of biological molecules and assemblies. SAM-modified electrode surfaces currently available are chemically diverse and can be tailored to enhance, prevent, or control adsorption of biological molecules. SAMs of alkanethiol derivatives have been used to mimic membranes, in particular for incorporation of proteins,[2] to investigate adsorbed and datively bound proteins,3-9 and to study covalently tethered proteins.[10-12]

Cytochrome *c* (cyt *c*) remains a focal point for the protein electrochemistry community, as evidenced by the extensive studies found in the literature.[9-20] Cyt *c* plays an important role in cellular respiration. In a mitochondrion, cyt *c* transfers electrons between two inner-membrane bound proteins, cyt *c* reductase and cyt *c* oxidase, by docking at specific adsorption sites on these redox partners. Excess positive charge, in the form of lysine residues surrounding cyt *c*'s exposed heme edge, allows it to complex and transfer electrons with protein partners that display anionic surface domains. Many useful biocompatible surfaces for preparing stable cyt *c* monolayers have been developed on the basis of the protein's surface structure. [4,5,7-9,12] In addition, improvements in protein monolayer development have led to more ideal cyt *c* voltammetric behavior.[4,9,13]

Although immobilization of cyt *c* to electrode surfaces simplifies electrochemical analysis in key respects,[16] it also leads to changes in voltammetry, compared to the solution-

based protein. Shifts in formal potential relative to solution values have been reported for cyt *c* when bound to mitochondrial and lipid bilayer membranes,[21] cytochrome oxidase,[22] and different SAM films.[4,5,12,13] Because cyt *c* is an electron transport protein that functions in different regions of the mitochondrion and the cell, it is important to understand how changes in its environment affect its redox characteristics. In particular, if a protein is not at the appropriate potential in an electron transport chain, the cascade of steps may be interrupted and the process terminated. Alternatively, changes in redox properties could enable other reactions, either desirable or undesirable. Biological systems may optimize electron transfer by changing charge density on the surface of redox partners to tune formal potential. The current study investigates the impact of protein immobilization and ionic strength on the redox potential of cyt *c*.

Four different monolayer films were used to immobilize cyt *c* at submonolayer coverages to electrode surfaces. Carboxyl-terminated SAMs were used as electrode analogues of cyt *c*'s biological redox partners. Several investigations of the electrochemistry of strongly adsorbed [13-17] and covalently attached[11] horse heart cyt *c* on carboxyl-terminated SAM/Au electrodes have been published. These studies clearly demonstrate that cyt *c* can bind on this type of surface in an electroactive state under neutral pH conditions. Results from surface-enhanced resonance Raman spectroscopy (SERRS) experiments have corroborated the electrochemical findings, documenting that the cyt *c* structure remains largely unperturbed upon electrostatic adsorption to longer-chainCOOHSAMs.[18a-c] In addition to electrostatic immobilization at electrode surfaces, cyt *c* has been successfully immobilized on pyridyl-terminated SAMs [8,19] through dative bonding to the heme iron and on carboxyl-terminated SAMs through carbodiimide coupling to lysines.[11]

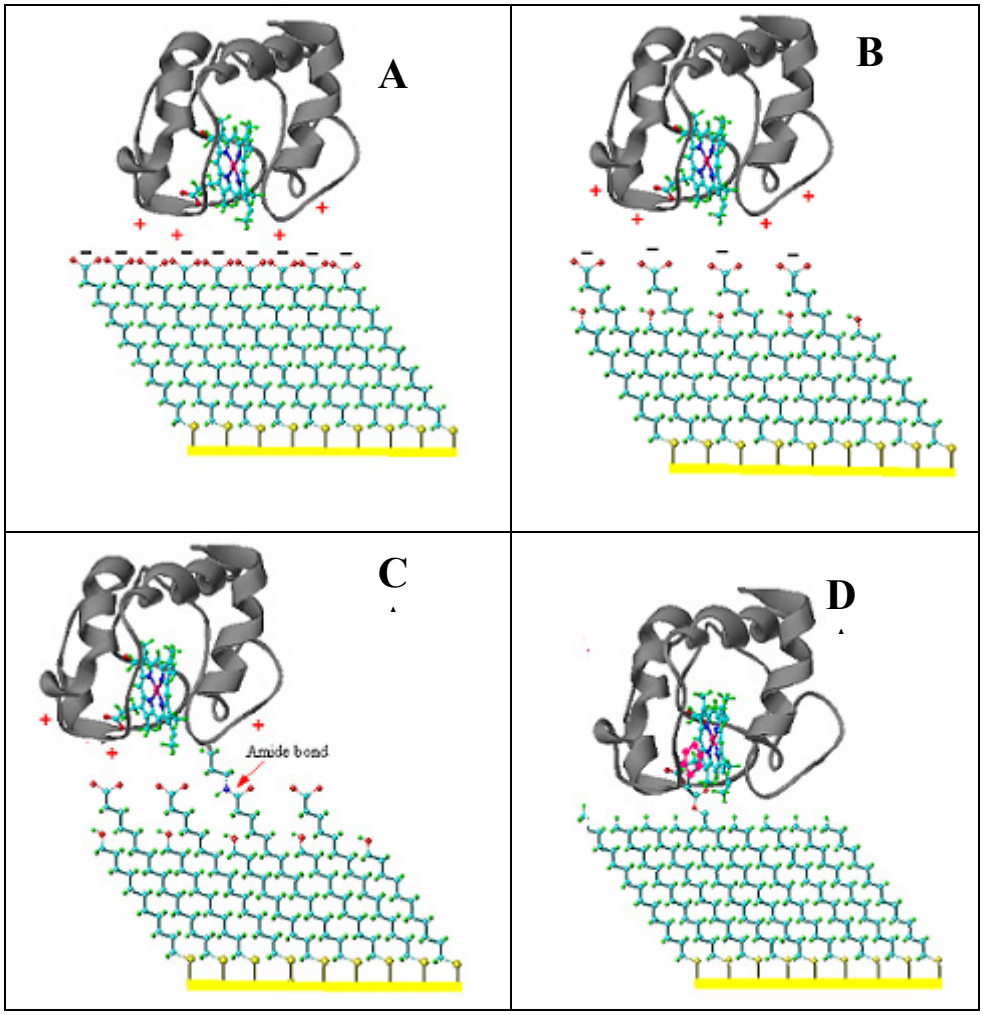

Figure 2. 1 Cartoon depicting idealized SAMs with cyt *c* immobilized on the surface. A) cyt *c* adsorbed to 100% COOH SAM, B) cyt *c* adsorbed to 50/50 COOH/OH SAM, C) cyt *c* covalently attached to 50/50 monolayer and D) cyt *c* datively bound to neutral PyC_{16}/C_{15} SAM.

A number of prior investigations of ionic strength effects on solution cyt *c* are available;[23-30] however, few studies have focused on the effect of ionic strength for the adsorbed protein.[4,9,31] Although a number of factors are known to be important for influencing the formal potential of cyt *c*, electrostatic forces are clearly significant. This work uses voltammetry to probe formal potential changes as a function of ionic strength. By comparing four different SAM-based immobilization strategies (electrostatic binding on both pure and mixed monolayers, heme-ligated binding,[19a] and covalent attachments see Figure 2.1) and two different buffer types (one containing specifically binding ions and the other more weakly binding ions), the influence of ionic environment on formal potential is probed and more fully elucidated.

2.2 Experimental

2.2.1 Reagents and Materials

Water was purified on a Milli-Q/ Organex-Q system (Millipore) or Barnstead-Nanopure water purification system (resistivity of 18 MΩ·cm at delivery). The alkanethiol derivatives 16-mercaptohexadecanoic acid ((HS-$(CH_2)_{15}$-COOH, 16-MHDA, 90%), 11-mercapto-1-undecanol (HS-$(CH_2)_{10}$-COOH, 97%), 1-entadecanethiol (HS-$(CH_2)_{14}$-CH_3, C_{15}), and the carbodiimide linker (*N*-cyclohexyl-*N*'-(2-morpholinoethyl) carbodiimide metho-*p*-toluenesulfonate, ($C_{14}H_{26}N_{30}$·$C_7H_7O_3S$, CMC were purchased from Aldrich and used without further purification. All other chemicals were reagent grade. Pyridine alkane thiol (4-pyridinyl-CO2-(CH2)16-SH, PyC16) was synthesized using published procedures.[19]

Cytochrome *c* (Sigma Type VI, horse heart) was purified on a cation exchange column (Whatman, CM-52, carboxymethylcellulose) and stored in 4.4 mM phosphate buffer.[4]

Purification and storage temperature was 4-5°C. In some cases, cyt *c* was frozen and dried at -80 °C. [26] Identical electrochemical results were obtained for both preparations.

2.2.2 Equipment

Cyclic voltammetry (CV) was performed using an EG&G PARC 263A potentiostat controlled by PARC Model 270 software in the ramp mode. Formal potentials were calculated from CV peak positions, i.e., $E^{\circ\prime} = (E_{p,a}+E_{p,c})/2$.

The three-electrode electrochemical cell[16b] used for collecting immobilized cyt *c* data utilized a platinum wire counter electrode, Ag/AgCl (1 M KCl) reference electrode, and SAM-modified gold working electrode. The Ag/AgCl reference electrode was compared to a standard saturated calomel electrode before experimentation. The measured values were used to convert the potentials to NHE for comparison to published results.

2.2.3 Electrode Preparation

Gold film electrodes (1000 Å Au/50 Å Ti on glass) were purchased from Evaporated Metal Films (Ithaca, NY). Electrodes were first heated in concentrated nitric acid until boiling, rinsed in room temperature with Millipore water followed by rinsing with absolute ethanol, and then immersed into an ethanolic alkanethiol solution. For carboxylic acid terminated SAMs, either pure 1 mM 16-mercaptohexadecanoic acid (16-MHDA) or a 1:1 mixture of 1 mM 16-MHDA and 11-mercapto-1-undecanol (11-MUDA) was used. To prepare mixed monolayers with pyridine terminated SAMs, an alkanethiol solution containing a 1:9 mixture of 1.0 mM 4-pyridinyl-COO-$(CH_2)_{16}$-SH (PyC16) and 1.0 mM HS-$(CH_2)_{15}$-CH_3 (C15) was used. Both carboxylic acid and pyridine terminated SAMs were allowed to self-assemble for 2-3 days.

Each electrode was rinsed with ethanol, mounted into the electrochemical cell, and rinsed with buffer. Background voltammograms were obtained prior to protein immobilization on SAMs.

2.2.4 Electrostatically Immobilized Cytochrome *c*

Cytochrome *c* was initially adsorbed at 4-5°C to carboxylic acid electrodes surface by 0.5 h immersion in low ionic strength phosphate buffer (4.4 mM, pH 7.0, μ = ~10 mM, 5-30 μM cyt *c*) and yielded approximately monolayer coverage (~15 pmol/cm^2). A partial desorption was then performed by rinsing with pH 7.0, 4.4 mM phosphate buffer (80 mM ionic strength) for 5-10 seconds, leaving behind a cyt *c* submonolayer of ca. 3 to 5 pmol/cm^2. Because the desorption step removes more weakly bound molecules, the resulting, more strongly bound, submonolayer proved suitable for use in ionic strengths up to 80 mM. A narrower E°′ distribution also was obtained, in agreement with prior findings.

Datively Bound Cytochrome c The protein was immobilized on a new electrode for each ionic strength buffer sequence. No additional rinsing with higher ionic strength buffer was performed prior to experimentation.

Covalently Attached Cytochrome c Following SAM preparation, the Au working electrode was assembled into the electrochemical cell and 5 mM CMC was placed in the cell for 0.5 hours. After activation of the carboxylic acid film with CMC, 30-40 μM cyt *c* at pH 8.0 was incubated for 1 hour. Any unbound protein was removed from the surface by rinsing with 200 mM ionic strength buffer.

2.2.5 Solution Conditions

Two different media were utilized to investigate the ionic strength dependence of the formal potential for cyt *c* in adsorbed, covalently attached, or datively bound states. The “binding”

electrolyte consisted of 4.4 mM potassium phosphate buffer (pH 7.0, I ≈10 mM) with KCl added to adjust the total ionic strength over a range of 10-80 mM (10-200 mM for covalently attached cyt *c*). Phosphate is known to strongly bind to cyt *c* in at least two sites[23,28, 32] Chloride is also know to strongly bind to cyt *c*.[21a] The "weakly binding" electrolyte was composed of 10 mM tris(hydroxymethyl)aminomethane (I ≈ 14 mM) with 1.0 M acetic acid added to adjust the pH of the buffer to pH 7.0 (referred to as tris/acetate buffer). Potassium nitrate was added to the tris/acetate buffer in order to vary the ionic strength.

During both buffer preparations, slight changes in the pH were observed with addition of inert electrolyte. To prevent pH changes, the electrolyte was added to one buffer component before the final pH adjustment with the second buffer component. In order to assure accurate ionic strength and pH values, final ionic strengths were calculated after combining the two buffer components.

Liquid junction potentials calculated for KCl/1M KCl and KNO_3/1M KCl junctions over the ionic strength range 0.01 M to 0.08 M, had values of $\leq$ 1.2 mV, which is within experimental error of the formal potential measurement.

2.3 Background

In solution phase, the electrochemical potential of a redox couple at fixed specie concentrations will shift if changes occur in the activities of the species because of ionic strength variation. This observation can be cast as a dependence of the formal potential on the activity coefficients,[33] by way of

$$E^{o'} = E^{o} + \frac{RT}{nF} \ln \frac{\gamma_{ox}}{\gamma_{red}}. \qquad (2.1)$$

where $E^{o'}$ is the formal potential, E^{o} is the standard potential (at zero ionic strength), and γ_{ox} and γ_{red} are the activity coefficients for the oxidized and reduced species, respectively. Previous studies on the ionic strength dependence of cyt *c*'s formal potential have used the extended Debye-Hückel model[23,25,28] to calculate activity coefficients:

$$\log \gamma = \frac{-Z^2 A\sqrt{I}}{1 + Ba_1\sqrt{I}} \tag{2.2}$$

where Z is the charge number of the ion and I is the ionic strength. The parameter A depends on the relative permittivity and temperature, and it has a value of 0.509 $(L/mol)^{1/2}/cm$ for an aqueous solution at 25°C. B is a constant for a specific temperature and has a value of 0.329×10^8 $(L/mol)^{1/2}/cm$ at 25°C.[23,28] The parameter a_1 corresponds to the effective radius of the ion (mean distance of closest approach). Previous authors have used a value of 18 Å for cyt *c*.[23,25,28] As previously shown[23,25,28], combining equations 2.1 and 2.2 gives:

$$E^{o'} = E^{o} - 0.059\frac{A\left(Z_{ox}^2 - Z_{red}^2\right)\sqrt{I}}{1 + Ba_1\sqrt{I}} \tag{2.3}$$

where Z_{ox} and Z_{red} are the charges on the oxidized and reduced species, respectively. For aqueous solutions at 25°C, equation 2.3 becomes

$$E^{o'} = E^{o} - 0.030(Z_{ox}^2 - Z_{red}^2)f(I) \tag{2.4}$$

where

$$f(I) = \frac{\sqrt{I}}{1 + 0.328a_1\sqrt{I}} \tag{2.5}$$

This simple model, which approximates the solvent by a continuum dielectric and the protein by a low dielectric spherical cavity with spherical surface charge distribution, has been used with success in prior studies of horse heart cyt *c*. In the present work we make use of this

model to facilitate comparison of our data for immobilized cyt *c* with previously published results for solution cyt *c*. The model does not account for structural perturbations or other effects arising from specific binding of ions to the protein. Gopal et al. [23] and Sun et al.[28] have described more detailed models that incorporate the stoichiometry and thermodynamics of specifically bound ions and have used them to fit data obtained for horse, bovine, and tuna cyt *c*.[23]

In adsorbed state, at equilibrium the chemical potential of the adsorbed protein and the bulk protein are equal and may be written as

$$\mu^{o}_{ads} + RT \ln a_{ads} = \mu^{o}_{so\ln} + RT \ln a_{so\ln}$$

or

$$a_{ads} = \exp\left(- (\mu^{o}_{ads} - \mu^{o}_{so\ln}) \Big/ RT \right) a_{so\ln} = \lambda\, a_{so\ln}$$

where λ accounts for the adsorption isotherm, and the activity for the adsorbed protein is directly proportional to the activity of the protein in solution. Hence if λ does not change significantly with the solution ionic strength then the activity of the adsorbed protein depends in the same way on the solution ionic strength as does the solvated protein. Thus, to the extent that the DH model is appropriate for the solution protein and λ is independent of ionic strength, the approximation is valid for comparison of the two systems.

When cyt *c* is adsorbed to an electrode surface, a number of factors can affect the observed ionic strength dependence of its $E^{o'}$. In addition to ions that specifically bind in the solution phase, the electrostatically bound protein's surface charge is affected by the negatively charged surface. This effect can be probed by comparing the datively bound protein to the electrostatically bound one. Second, desorption of cyt *c* becomes more of a factor with increasing ionic strength and can result in a shift in the apparent formal potential.[15] This issue

can be addressed by comparing results obtained for adsorbed cyt *c* to the covalently attached protein. Third, earlier studies identified an apparent distribution in $E^{o'}$ for adsorbed cyt *c* presumably arising from inhomogeneity of adsorption environments or protein geometries.[4] Clark and Bowden[4] have shown that $E^{o'}$ subpopulations correlate with the strength of adsorption, with more negative values corresponding to stronger binding. A practical solution to this difficulty has been realized in the present work by desorbing more weakly bound cyt *c* prior to measurements.

2.4 Results

Figure 2.2A shows typical cyclic voltammograms obtained for cyt *c* electrostatically bound on a $C_{15}COOH/C_{11}OH$ mixed SAM/Au electrode in tris/acetate buffers of several different ionic strengths. These data reflect the response of a 3-5 pmol/cm^2 submonolayer of adsorbed cyt *c* (see Experimental Section). The cyclic voltammograms (CVs) in Figure 2.2A are nearly reversible (ΔE_p = 10-30 mV) at 25 mV/s and have full-width-half at maximum (FWHM) values of 99 to 110 mV depending on ionic strength (vide infra). Readily apparent in Figure 2.2A is a positive shift in formal potential with increasing ionic strength, a dependence that was consistently observed with COOH-terminated films irrespective of the immobilization strategy, i.e., electrostatic (pure or mixed SAMs, Figures 2.1A and 2.1B) or covalent (mixed SAMs, Figure 2.1C, data not shown). Furthermore, positive shifts were observed for both phosphate (specific binding) and tris/acetate (weak binding) buffers that were of similar magnitude, a finding that excludes specific ion binding as the primary cause of the dependence. It was also found that the formal potential shifts were not related to desorption of the electrostatically adsorbed protein nor were they time-dependent. With extended exposure to ionic strength at the upper end of the 10-80 mM range, more extensive desorption of protein does occur, however, only a negligible

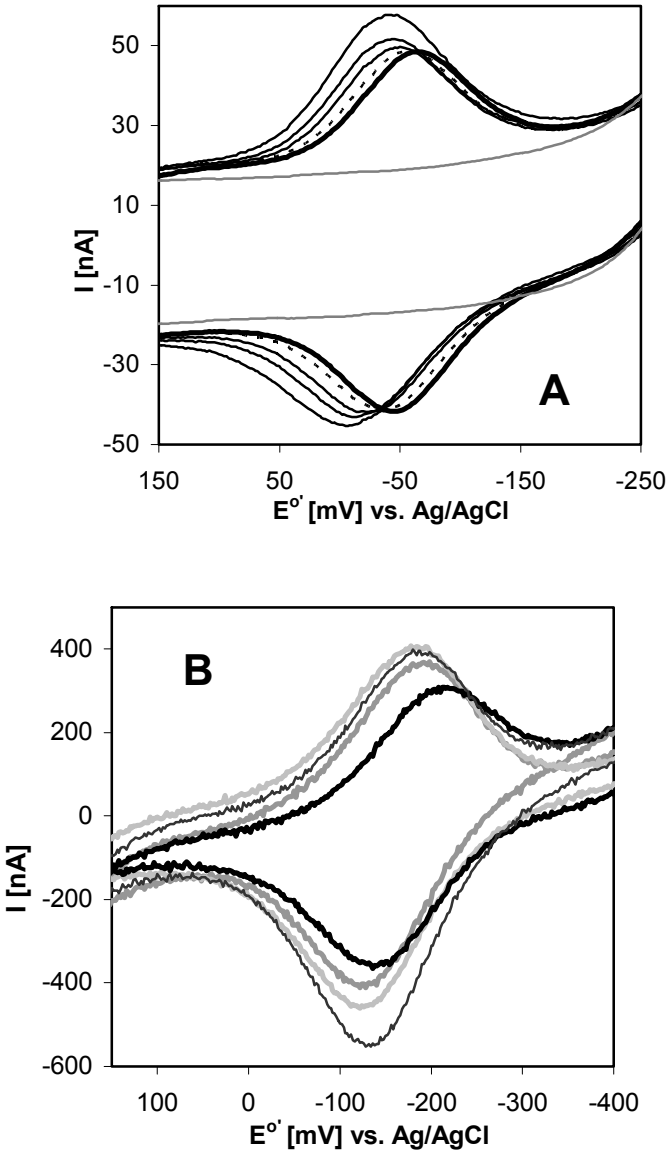

Figure 2. 2 Representative cyclic voltammograms for immobilized cyt *c*. Panel A shows CVs for cyt *c* electrostatically adsorbed to a $C_{15}COOH/C_{11}OH$ modified Au electrode in 20 mM tris/acetate buffer, and a background CV at 25 mV/s from left to right: 80, 60, 40, 20 and 14 mM ionic strength Tris/acetate buffer, pH 7.0. Panel B shows background subtracted CVs for cyt *c* datively bound to the PyC_{16}/C_{15} modified Au electrodes in varying ionic strength Tris/Acetate buffer at 1000 mV/s; light gray, 20 mM; darker gray, 40 mM; thin line, 60 mM; and black, 80 mM.

change in the formal potential was observed over a time scale of 1 hour (ample time to collect data for an ionic strength series).

The FWHM values for CVs of electrostatically bound cyt *c* were also monitored in desorption experiments. In 80 mM ionic strength buffer, a narrowing of the FWHM occurred over time and was correlated with slow desorption. For example, the FWHM of a 4 pmol/cm^2 submonolayer was found to decrease by 2 and 5 mV, respectively, after 1 and 2 hour exposures. At 23 hours exposure, FWHM had decreased to 90 mV, the ideal width, but surface coverage was low, ~1.5 pmol/cm^2. Surface coverage was calculated from electroactive protein using total charge and peak currents (no difference was found with either method). For short times (< hour), the ionic strength affected FWHM in a reversible manner. For example, changing the ionic strength of one sample from 80 to 10 mM caused a FWHM decrease from 105 to 95 mV. Upon reintroducing the 80 mM buffer into the cell, FWHM returned to its starting value of 105 mV. In part, the reversible dependence of FWHM on ionic strength may be caused by slowed electron transfer kinetics. [34]

Figure 2.2B shows four voltammograms for cyt *c* datively bound to PyC_{16}/C_{15} electrodes as a function of ionic strength. As reported earlier,[19a] dative bonding of cyt *c* causes a negative shift in formal potential due to direct pyridyl interaction with the heme iron, hence the current peaks in Figure 2.2B are positioned at ca. –150 mV vs. Ag/AgCl. In contrast to Figure 2.2A, the formal potential for cyt *c*-PyC_{16}/C_{15} shifts to more negative values with increasing ionic strength. Because cyt *c* binding is weaker on pyridyl-terminated thiols and the initial surface coverages were low (1-3 pmol/cm^2), data comprising a complete ionic strength series were collected on multiple electrodes (one electrode per ionic strength value). Electrode-to-electrode variability in cyt *c* surface coverage is reflected in the range of currents evident in Figure 2.2B. The

voltammetry of the cyt *c*-PyC16/C15 system was stable and nearly reversible over the time scale of the experiment (at 100 mV/s, FWHM ~100-120 mV, ΔE_p < 10 mV; at 500 mV/s, FWHM ~ 110-130 mV, ΔE_p = 55 mV).

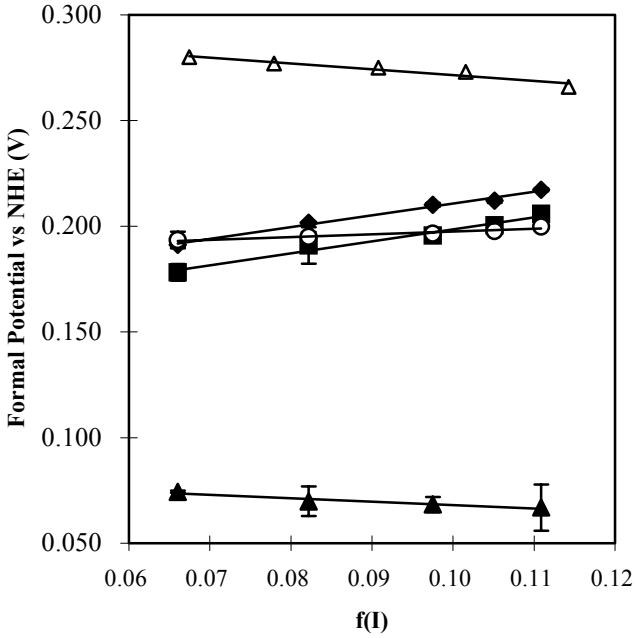

Figure 2. 3 Eo' is plotted versus f(I), for cyt c adsorbed on C15COOH SAMs (solid diamonds), mixed C15COOH/C11OH SAMs (solid squares), covalently attached to mixed C15COOH/C11OH monolayers (open circles), and datively bound (solid triangles) in Tris/Acetate buffer. Solution horse heart cyt *c* data from Gopal et al.[23] is plotted for comparison (open triangles). Error bars were determined from the standard deviation for 3 or more trials. The average values for all data with slopes and standard deviations are presented in Table 2.1.

Figure 2.3 shows the variation of formal potential with ionic strength for each immobilization strategy along with a representative data set from the solution cyt *c* literature. Fits of equation 2.4 to the data are shown in each case. The y-intercept of the regression line corresponds to the standard potential, E^o, and the slope is $-0.030(Z_{ox}^2-Z_{red}^2)$. The average slope

values reported in Table 2.1 represent 3-4 trials for each immobilization strategy. Positive slopes were obtained for cyt *c* interacting with anionic COOH SAM surfaces whereas negative slopes were obtained for cyt *c* immobilized on the uncharged pyridyl-terminated surface, similar to cyt *c* in solution. The apparent surface charge was calculated from the slope of the line, assuming $Z_{ox} - Z_{red} = 1$. In addition to standard potentials, Table 2.1 includes formal potentials calculated at 100 mM ionic strength, which is comparable to physiological conditions.

Because the observed shifts in formal potential were relatively small, care was taken to evaluate the acquired data for other possible contributions. The voltammetric responses were examined for any time dependence that might reveal changes in formal potential related to changes in coverage. For a typical ionic strength series collected from high ionic strength to low ionic strength, little change in coverage was observed over the one hour needed for data collection. To better characterize possible changes in cyt *c* coverage, a series of desorption studies were conducted on the mixed and pure carboxylic acid SAMs. Figure 2.4 displays the change in electroactive coverage over time for cyt *c* in 4.4 mM phosphate/KCl buffer (I=80 mM; pH 7.0) at applied potentials of -300 mV or +300 mV. Voltammograms were collected every 10 minutes for the first two and a half hours and then spaced more coarsely for the remainder of the experiment. As seen in Figure 2.4, desorption occurs faster if the potential is held at –300 mV compared to +300 mV. The inset in Figure 2.4 reports desorption data acquired over the first hour for oxidized cyt *c* in I = 80 mM buffer, the highest ionic strength used. An acceptably small loss of protein over the first hour was observed (time needed to complete ionic strength measurements, see Supplemental Information).

A comparison of $E^{o'}$ values for cyt *c,* in pH 7.0 and 10 - 20 mM ionic strength buffers, is presented in Table 2.2. For electrostatic adsorption on COOH-terminated films, the formal potential is shifted negative of the solution value by 70 to 90 mV. For cyt *c* adsorbed on SnO_2

Table 2. 1 Summary of Horse Heart Cyt *c* (pH 7.0) Formal Potential[a] vs. f(I) Data

Conditions	Slope (V)[b]	E^o (V vs. NHE)[b]	$E^{o'}$ I=100 mM (V vs. NHE)[b]	Apparent Surface Charge[e]
Immobilized cyt *c* (Phosphate buffer[c])				Cyt *c* (Oxd.)
Adsorbed on 100% $C_{15}COOH$	0.53 ± 0.04	0.163 ± 0.003	0.221 ± 0.007	-8 ± 1
Adsorbed on 50:50 $C_{15}COOH/C_{11}OH$	0.80 ± 0.06	0.119 ± 0.006	0.21 ± 0.02	-13 ± 1
Covalently Attached to Mixed COOH/OH	0.34 ± 0.08	0.167 ± 0.008	0.21 ± 0.02	-5 ± 1
Datively Bound to PyC16/C15 SAM	-0.12 ± 0.09	0.085 ± 0.010	0.07 ± 0.02	3 ± 1
Immobilized cyt *c* (Tris/Acetate buffer[d])				
Adsorbed on 100% $C_{15}COOH$	0.56 ± 0.06	0.158 ± 0.006	0.22 ± 0.01	-9 ± 1
Adsorbed on 50:50 $C_{15}COOH/C_{11}OH$	0.57 ± 0.09	0.145 ± 0.010	0.21 ± 0.02	-9 ± 1
Covalently Attached to Mixed COOH/OH	0.15 ± 0.04	0.184 ± 0.004	0.20 ± 0.02	-2 ± 1
Datively Bound to PyC16/C15 SAM	-0.16 ± 0.06	0.084 ± 0.006	0.07 ± 0.01	3 ± 1
Solution cyt *c*				
Tris/cacodylate[23]	-0.339	0.30	0.262	6
Tris/cacodylate[28]	-0.278	0.30	0.268	5
Maleylated cyt *c* (Tris/cacodylate)[26]				
# Lysines modified ΔZ				
13 -26	1.0	0.09	0.200	–16
6 -12	0.16	0.23	0.247	–2
4 -8	0	0.24	0.24	
0 0	-0.34	0.27	0.232	6

[a] $E^{o'} = E^o - 0.030\,(Z_{ox}^2 - Z_{red}^2)\,f(I)$

[b] All error values are based on the error in the regression analysis with 2σ.

[c] Phosphate buffer with KCl, cyt *c* initially adsorbed from 4.4 mM phosphate buffer.

[d] Tris/acetate buffer with KNO_3, cyt *c* initially adsorbed from 4.4 mM phosphate buffer.

[e] Apparent surface charge determined from the slope assuming $Z_{ox} - Z_{red} = 1$.

electrodes,[16b] cyt *c* oxidase,[22] and membranes,[30b] the negative shift is not quite as large; it lies in the range from 10 to 60 mV. Cyt *c* adsorbed on neutral hydroxyl-terminated thiols in phosphate buffer has a formal potential similar to solution values. The most positive $E^{o'}$ value in Table 2.2, 95 mV positive of the solution value, was reported for cyt *c* adsorbed on trimethylammonium-terminated SAMs.[5b]

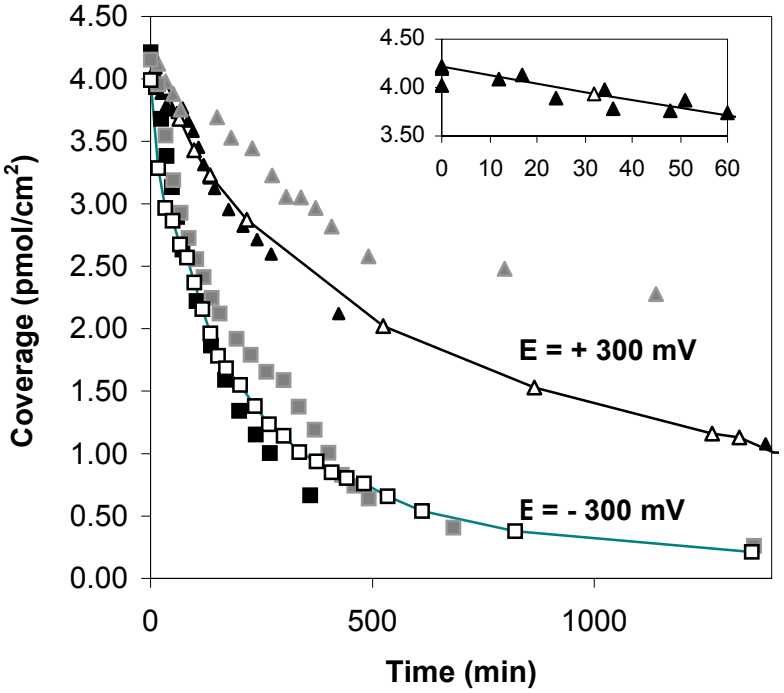

Figure 2. 4 Desorption of cytochrome *c* in 80 mM phosphate buffer with the potential held at +300 mV (triangles, 3 trials, black, grey, and white) and -300 mV (squares, 3 trials, black, grey, and white). An expanded view of the first hour's data for E = +300 mV is shown in the inset. Lines serve as a guide to the eye.

Table 2.2: Comparison of Horse Heart Cyt *c* Formal Potentials[a] vs. NHE

Substrate (with Cyt *c*)	$E^{o'}$ (V) Phos.	$E^{o'}$ (V) Tris	$\Delta E^{o'}$(V)[c] Phos.	reference
Adsorbed to 100% $C_{15}COOH$	0.204 ± 0.002	0.203 ± 0.002	-0.068	this work
Adsorbed to 50:50 $C_{15}COOH/C_{11}OH$	0.181 ± 0.006	0.183 ± 0.006	-0.091	"
Covalently Attached to Mixed COOH	0.192 ± 0.004	0.193 ± 0.005	-0.080	"
Datively Bound to PyC_{16}/C_{15} SAM	0.077 ± 0.008	0.070 ± 0.007		"
Adsorbed to $C_{15}COOH$ (monolayer)	0.215, 0.198		-0.057, -0.074	15, 4
Adsorbed to $C_{15}COOH$ (submonolayer)	0.178		-0.094	4
Adsorbed to 11-mercapto-1-undecanol	0.268		0.004	9
Adsorbed to SnO_2	0.239		-0.033	16b
Mitochondrial membranes, Cyt *c* oxidase[a]			-0.055, -0.035	21;22
Free in solution	0.264[d]	0.272[b]		23,25,28
Adsorbed to trimethylammonium	0.359		0.095	5b

[a] Various buffers pH 7-7.5 (I=10-20 mM)

[b] Average $E^{o'}$(solution cyt *c*) at 20 mM ionic strength.

[c] $\Delta E^{o'} = E^{o'}_{bound} - E^{o'}_{soln}$.

[d] Value calculated at 20 mM ionic strength for added phosphate from ref .23

2.5 Discussion

Many studies on cyt *c* demonstrate its interactions with other charged species in its environment. Cytochrome *c* not only interacts with small ions such as chloride and phosphate[23,27b,35] but it also binds to membranes,[21] protein partners,[22] and a variety of artificial surfaces, including SAM-modified electrodes. Numerous reports of negative shifts in formal potential due to specific anion binding or anionic surface binding can be found in the literature. Electrochemical probing of cyt *c* that has been surface-confined through the use of different immobilization strategies provides additional insight into the roles played by the binding surfaces and protein surface charge in cyt *c* activity.

2.5.1 Formal Potential of Immobilized Cytochrome *c*

The $E^{o'}$ value measured for adsorbed cyt *c* on $C_{15}COOH$/Au electrodes (Table 2.2) is similar to previously published values for this surface type.[4,14-15] A formal potential of +202 mV vs. NHE for cyt *c*/ $C_{15}COOH$ /Ag measured using surface-enhanced resonance Raman (SERR) spectroscopy[18b] also compares well with the 204 mV reported here.

Upon binding to anionic domains, cyt *c* undergoes thermodynamic changes that are typically evidenced by a negative shift in formal potential. The negative shift in formal potential occurs as a result of changes in the protein environment during immobilization. Previous studies have related the redox thermodynamics of cyt *c* to its adsorption thermodynamics using a square scheme to represent the immobilization process,[16b] namely:

$$\begin{array}{lcll} Fe(III)_{soln} + e^- & \rightleftharpoons & Fe(II)_{soln} & E^{o\prime} = 0.264 \text{ V vs NHE}^{23} \\ \beta_{ox} \uparrow\downarrow & & \uparrow\downarrow \beta_{red} & \\ Fe(III)_{surf} + e^- & \rightleftharpoons & Fe(II)_{surf} & E^{o\prime}_{surf} \neq E^{o\prime} \text{ if } \beta_{ox} \neq \beta_{red} \end{array}$$

where Fe(III) and Fe(II) denote ferri- and ferrocytochrome *c*, and β_{ox} and β_{red} are their respective adsorption equilibrium constants. In terms of the free energy of binding, ΔG_b:

$$\Delta G_b = -RT \ln \beta \qquad (2.6)$$

Denoting the solution and surface formal potentials by $E^{o\prime}$ and $E^{o\prime}_{surf}$, respectively, it follows that any change in formal potential upon immobilization can be described by:[15,16b,27b, 33]

$$\Delta E^{o\prime} = E^{o\prime}_{surf} - E^{o\prime} = - (RT/nF) \ln (\beta_{ox} / \beta_{red}) \qquad (2.7)$$

A change or shift in formal potential can only occur when there is differential binding of the two redox forms. Thus, in the special case of identical ΔG_b values for ferri- and ferrocytochrome *c*, no change in formal potential would be expected upon binding, regardless of the magnitude of ΔG_b. The negative shifts that are typically observed upon cytochrome *c* binding to anionic surfaces indicate that the oxidized form binds more strongly than the reduced form, as other authors have noted.[9,16b,21] This view is reinforced in the present work by the desorption data shown in Figure 2.4. In pH 7.0, I=80 mM, phosphate buffer, the two redox forms desorb at distinctly different rates with ferricytochrome *c* desorbing about threefold slower even though it is held at a potential that is +0.6 V (positive potentials are expected to repel cyt c) with respect to ferrocytochrome *c*. The desorption rates for the Fe^{3+} and Fe^{2+} forms were determined to be 7.0 ± 0.9 and 20 ± 2 fmol/cm^2-min, respectively.

In addition to the intrinsic chemical differences between the two redox species that impact their binding behavior, other factors can contribute to differential free energies including changes in surface charge, the potential drop across the SAM, and other microenvironmental factors. Surface charge can be a dominant contributing factor to changes in ΔG_b and formal potential. Pettigrew and Moore have summarized the extensive literature that has addressed the influence of surface charge on the formal potential of solution cyt *c*.[31a] One observes a 5-10 mV

change in formal potential for each unit change in Z at the protein surface; somewhat smaller than the 12 mV expected from a smeared charge model.[31a] Upon immobilization, it appears that cytochrome c can experience changes in |Z| of 15 or greater (Table 2.1), which would be consistent with a change in formal potential of 75 – 150 mV. Clearly, surface charge plays a major role in the redox thermodynamics of cyt *c* in solution as well as immobilized on SAM modified electrodes.

The impact of ionic surface charge on formal potential can be further appreciated by considering cytochrome c adsorption on differently charged SAM surfaces. Formal potentials for the COOH-terminated SAMs in Table 2.2 range from +178 to +215 mV vs. NHE, which translates to negative shifts of ca. 50-90 mV. These values tend to be somewhat more negative than those observed for horse heart cyt *c* bound to anionic biological surfaces such as mitochondrial membranes[21] and cytochrome oxidase,[22] for which negative $E^{o'}$ shifts of 35-55 mV have been reported. A reasonable inference from these data is that the density of negative charge is greater on the SAM surfaces. Horse heart cyt *c* adsorption to neutral hydroxyl-terminated SAMs give $E^{o'}$ values in phosphate buffer of 260 mV, which are comparable to solution values.[36] In addition, Haas et. al.[22c] reported a value of 241 mV for cyt *c* adsorbed on neutral OH-terminated SAMs but a shift to 225 mV when cyt *c* is complexed to the negative surface of cyt *c* oxidase before immobilization on the same SAMs. Although cyt *c* binding to cationic surfaces is not often considered, Chen et al. have reported its adsorption on trimethylammonium-terminated SAMs with a 100 mV *positive* shift.[5b]

In addition to surface charge variations, the SAM properties cause a potential drop between the metal-thiol boundary and the outer surface of the film. Murgida and Hildebrandt have explained the dependence of cytochrome c formal potential on chainlength, in COOH-

terminated SAMs on Ag electrodes, by electric field effects arising from potential drop across the SAM interface. As the methylene chain length was increased from C2 to C16, they observed that the formal potential of adsorbed cytochrome c shifted 41 mV negative in a monotonic fashion.[18b] Data were fit using an electrostatic model that places excess charge at three locations: the metal surface, the SAM/protein interface, and the redox center of the adsorbed cytochrome c. The potential drop through the layer does not explain the data reported here, however. If the potential drop through the layer dominated the behavior, the dependence of E°′ on chainlength should be significantly different on Au than on Ag because Au's potential of zero charge is about 1 V positive of the Ag pzc (bare silver, pzc -0.975 V vs. SCE[18b] and –S(CH2)14OH/Au, pzc -0.024V vs. SCE[18d]). In contrast, the observed E°′ change for adsorbed cyt *c* on COOH/OH SAMs on gold,-39 mV, is very similar to that found on Ag. The formal potential of C3 was found to be 220 ± 2 mV (n=7) [36] and C16 181 ± 6 mV (Table 2.1).

Since the observations of E°′ made on the two metals are essentially identical, other factors that are similar in the two systems must control the shift in E. In addition, a complete explanation should account for the small positive shift in formal potential with chain length that is observed for the dative attachment of cyt *c* on uncharged pyridyl-terminated.[37] It may be that both surface charge and electric field contributions to the formal potential shift are significant. If the pK_a of the COOH surface changes with methylene chain length, the charge density at the SAM/protein interface would be chain length dependent, and this may contribute in an important way to the shift. Although some workers have reported changes in COOH pKa with chain length in SAMs, others report no change.[38] Further work is warranted.

2.5.2 Standard Potential at I = 0

The E^o values follow the same pattern as formal potential. The study by Aviram et al.[26] supports the surface charge argument by showing that addition of negative charge to cyt *c* by lysine maleylation causes a significant decrease in E^o (Table 2.1). A negative shift of 40 mV was observed with the addition of 6 maleyic anhydrides ($\Delta Z = -12$), which provides a change in standard potential of 7 mV/charge change compared to the 12mV/charge predicted by the theoretical smeared charge model.

In addition to the standard potential at zero ionic strength, Table 2.1 reports the formal potential at 100 mM, E^{100}. E^{100} is a more relevant value for comparison of formal potential since physiological ionic strength is ~100 mM. Based on the calculated values in Table 2.1, changes in E^{100} between the different immobilization methods are small relative to changes in E^o for the same systems. The higher ionic strength in a cell environment should act to minimize changes in formal potential as cyt *c* binds to different substrates.

2.5.3 $E^{o'}$ vs. f(I)

The effect of ionic strength on the formal potential of cyt *c* immobilized on SAM/Au electrodes was evaluated using the extended Debye-Hückel model discussed above. Figure 2.3 plots the formal potential vs. the ionic strength function given in equation (2.5). The slopes and intercepts (E^o) (Eqn. 2.4) presented in Table 2.1 clearly change with solution conditions and immobilization strategy.

The formal potential for electrostatically adsorbed cyt *c* shifts to more negative values with decreasing ionic strength (positive slopes in Figure 2.3), which is opposite the behavior observed for the native protein in solution and for pyridine ligated cyt *c* (negative slopes in Figure 2.3). The inversion of slope can be explained in the context of the Debye-Hückel

description as arising from an inversion in the protein's apparent surface charge, caused by the negative charge from SAM carboxylates. This means that cyt *c*, a basic protein (net positive surface charge) is behaving as if it had become an acidic protein (net negative surface charge).

Table 2.1 reports apparent surface charges for the four immobilization strategies with both buffers, along with those calculated from several earlier studies. The surface charge obtained for oxidized solution cyt *c* is +5 to +6. The values obtained for adsorbed and covalently attached cyt *c* on carboxyl-terminated SAMs are negative, ranging from –2 to –13. For instance, a slope of 0.556 = -0.03 (Z_{ox}^2-Z_{red}^2) gives a surface charge of –8.7 if Z_{ox} - Z_{red} = 1. The most positive slope is found for cyt *c* electrostatically adsorbed on $C_{15}COOH/C_{11}OH$ mixed monolayers, yielding a surface charge of –13. In contrast the slope for cyt *c* immobilized on pyridine-terminated SAMs, which are neutral and hydrophobic, is negative and gives an apparent charge of +3. Negative slopes also characterize the proteins solution phase behavior (Table 2.1). These results support the contention that the apparent surface charge of cyt *c* becomes negative when electrostatically adsorbed on COOH SAMs.

The effect of protein surface charge is well illustrated in a study by Aviram et al.,[26] in which negative charge was systematically added to cyt *c* by modification of surface lysine residues with maleic anhydride. For each maleylation, the protein undergoes a net charge change of -2. Formal potential vs. f(I) plots were found to display increasingly positive slopes upon progressive addition of negative charge (see Table 2.1). When the protein was neutralized (4 maleylations corresponding to total charge change of -8), the formal potential was insensitive to ionic strength. As reported in Table 2.1, negatively charged versions of cyt *c*, resulting from charge changes of –12 and -26, yield positive slopes for the f(I) dependence as we have observed for electrostatically adsorbed cyt *c*.

The concept of converting the apparent net charge on cyt *c* from positive to negative is well supported by this work and prior literature. Is it possible, however, for a COOH SAM coated electrode to provide enough negative charge to accomplish this charge inversion? If solution cyt *c* has a net positive charge of +6, then a net charge change of –15 or greater is needed to obtain an apparent surface charge of -9. An estimate of the number of negative surface charges that interact with the protein can be obtained by comparing the size of the protein to the packing density in the monolayer film. Assuming cyt *c* is ~30 Å in diameter and each carboxylic acid / alcohol terminal group is 5Å in diameter, approximately 30 alkanethiols would be located under each protein molecule. Since *ca*. 50% of the mixed thiols are carboxylic acids (pK_a of 6.6 – 5.6, for the 0.01 M to 0.10 M buffer solutions),[38] 12 to 14 deprotonated acid groups can be expected to be in close proximity to the protein surface. If the distribution of terminal groups in the film is not homogeneous, then the partial monolayer of cyt c remaining after rinsing with 80 mM buffer is likely to adsorbed preferentially in regions that are rich in carboxyl functionalities, further supporting this estimation. This amount of charge is sufficient to counteract the net positive surface charge on cyt *c*, hence giving adsorbed cyt *c* an apparent net negative charge.

2.5.4 Immobilization Strategies

By modeling the effect of ionic strength on formal potential using the extended Debye-Hückel theory, one can calculate values of the apparent surface charge for cytochrome c in different situations. A comparison of cytochrome c's behavior while adsorbed, to its behavior when covalently attached reveals an interesting difference, as documented in Table 2.1. In phosphate buffer, the apparent surface charge determined for cyt *c* covalently attached to 50:50 $C_{15}COOH$:$C_{11}OH$ SAMs is –5 versus a value of –13 for electrostatic adsorption. In tris/acetate buffer, the corresponding charges were found to be –2 and –9, respectively, highlighting what

appears to be an increase in apparent protein surface charge of ~7 to 8 as a result of carbodiimide coupling. This increase seems initially strange since the electrode's surface charge for these two cases are expected to be similar. For C15COOH:C11OH SAMs, the carboxylic acid groups should display pKa values close to solution values and should therefore be mostly ionized at pH 7.0. In addition, any changes in the surface carboxylate groups upon carbodiimide treatment are expected to undergo hydrolysis upon removal of linking agent and protein from the buffer solution. In the case of purely electrostatic adsorption, neutralization of a unit positive charge on cyt *c* will occur whenever a lysine ammonium ion pairs to a SAM carboxylate. For the covalently attached cyt *c*, positive charge can be neutralized in two ways, namely, amide bond formation and the ammonium-carboxylate ion pairing. Based on these assumptions and that binding ions interact similarly with covalently attached and electrostatically immobilized proteins, the amount of surface charge neutralized on cyt *c* should be similar for the two cases. This assumes that the protein adsorbs in similar geometries and that changes in cyt *c* structure for the covalent attachment process are minimal, which is supported by SERRS studies.[18a]

The origin of the increase in apparent surface charge of ~7 to 8 that occurs as a result of covalent attachment remains unclear. It may be that the change in apparent surface charge results from differences in the protein's local environment. The voltammograms for the protein are significantly broader in the covalent case (*ca* 120 mV) than the electrostatic case (*ca* 95 mV) and this could reflect a broader distribution of protein geometries at the surface,[39] which may include orientations that neutralize less of the surface charge. In addition, the electrostatic immobilization may cause binding of the protein with resulting structural changes to both the oxidized and reduced forms. Because the oxidized form is more susceptible to structural change arising from external stress,[27a] it will undergo greater deformity and thus bind more strongly.

Upon reduction, the structure would relax to its more refractory ferrous form. However, if the oxidized form were tacked down with covalent linkages, the extent of structural relaxation upon reduction may be limited by the imposition of conformational restraints

The apparent surface charge of cyt *c* also varies between the two buffer systems. For the covalently attached system, it is –5e in phosphate buffer and –2e for the tris/acetate buffer. The difference in the apparent charge seen between the two buffer systems suggests that one or two phosphates are ion paired to the protein. Since Equations 2.4 and 2.5 assume that the only contribution to the slope is surface charge on the protein and do not account for the specifically binding ions, the surface charge values in Table 2.1 become artificially high. Both adsorbed and solution cyt *c* data show a general increase in the $E^{o'}$ vs. f(I) slope to more positive values upon addition of binding ions. The addition of binding ions plays a role because of the net change in the protein's surface charge upon specific binding of ions (Table 2.1, Tris/Acetate vs. Phosphate buffer system). For three of the four immobilized cyt *c* systems the slopes are more positive for the binding phosphate buffer. The cyt *c* on pure $C_{15}COOH$ SAMs shows no change for the two buffer systems which may be attributed to greater amount of heterogeneity (larger FWHM) in the response obtained on these SAM surfaces.

Previous literature supports this interpretation, Gopel et. al. reported changes in solution cyt *c* response with addition of chloride and phosphate to nonbinding tris/cacodylate buffers.[23] Solution cyt *c* results show a more positive slope under binding conditions with a slope of -0.34 reported for tris/cacodylate. If the data for chloride and phosphate are plotted using Equations 2.4 and 2.5, slopes of -0.274 for tris/cacodylate with added chloride and -0.214 for tris/cacodylate with added phosphate are obtained. A comparable change of 0.2 V is observed in the slopes of the binding (phosphate buffer) and weaker binding (tris acetate buffer) systems

in Table 2.1. Once again, the same trend is observed: the addition of strongly binding negative ions to cyt *c* causes the $E^{o'}$ vs. f(I) slope to become more positive because of the decreased apparent surface charge on the protein.

2.6 Conclusions

Surface interactions are involved in many biological phenomena including protein/protein docking. Since electrostatic interactions between proteins are essential for cyt *c* electron transfer, it is important to understand surface charge effects on the protein. Many studies have shown that electrostatically adsorbed cyt *c*/HOOC-SAM/Au electrodes appear to be a useful model system for illustrating how changes in protein binding affect its function. The investigations reported in this work show that adsorption of cyt *c* onto negatively charged surfaces alters the electrostatic and redox thermodynamic properties of the protein significantly. This change is illustrated by a shift in the formal potential and by an inversion in the slope of formal potential versus f(I) relative to solution cyt *c*. The inversion of slope, however, was not observed for cyt *c* immobilized on a neutral electrode surface through dative bonding of the protein to pyridine terminated SAMs. The major cause of the inverted slope appears to be a reversal in the apparent surface charge of the protein upon immobilization to highly negative surfaces. Specific binding of ions also contributes to the protein's effective charge. It seems that the Debye-Hückel model, which has been successfully used to account for ionic strength effects on solution cyt *c*, can be used for adsorbed cyt *c,* with the recognition that the protein's apparent charge can be converted from being net positive to net negative. The importance of this conclusion arises from cyt *c*'s function in the mitochondrion where it electrostatically binds to the inner mitochondrial membrane and subsequently participates in electron transfer. Further investigations that better establish the correspondence between SAM modified electrodes and

physiological binding environments, in particular the dependence of differential adsorption free energy on ionic strength, are warranted.

2.7 Acknowledgments

We gratefully acknowledge support of this work by the NSF through CHE-9307257, CHE-9814410, CHE-0111435, CHE-0353856, and the Society of Analytical Chemists of Pittsburgh - Undergraduate Analytical Research Program Grant.

References

(1) a) Ulman, A. *An Introduction to Ultrathin Organic Films From Langmuir Blodgett to Self Assembly*; Academic Press: San Diego, 1991. b) Finklea, H. Electrochemistry of Organized Monolayers of Thiols and Related Molecules on Electrodes., In *Electroanalytical Chemistry*. Bard. A.J., Rubenstein, I., Eds.; Marcel Dekker: New York, 1996; Vol. 19, pp 110-337.

(2) a) Prime, K. L.; Whitesides, G. M. *Science* **1991**, *252*, 1164-1167. b)Cullison, J. K.; Hawkridge, F. M. *Langmuir* **1994**, *10*, 877-882. c) Rhoten, M. C.; Hawkridge, F. M. *J. Electroanal. Chem*. **2002**, *535*, 97-106.

(3) a)Willner, I.; Katz, E.; Riklin, A.; Kasher, R. *J. Am. Chem. Soc.* **1992**, *114*, 10965-10966. b) Kinnear, K. T.; Monbouquette, H. G. *Langmuir* **1993**, *9*, 2255.

(4) Clark, Rose A; Bowden, Edmond F. *Langmuir* **1997**, *13*, 559-565.

(5) a)Prime, K. L.; Whitesides, G. M. *J. Am. Chem. Soc.* **1993**, *115*, 10714-10721. b) Chen, X.; Ferrigno, R.; Yang, J.; Whitesides, G.M. *Langmuir*, **2002**, *18*, 7009-7015.

(6) Margel, S.; Vogler, E. A.; Firment, L.; Watt, T.; Haynie, S.; Sogah, D. Y. *J. Biomedical Materials Res.* **1993**, *27*, 1463-1476.

(7) Maeda, Y.; Yamamoto, H.; Kitano, H. *J. Phys. Chem*. **1995**, *99*, 4837-4841

(8) Murgida, D. H.; Hildebrandt, P.; Wei, J.; He, Y.-F.; Liu, H.; Waldeck, D. H. *J.Phys. Chem*. **2004**, *108*, 2261-2269.

(9) Gavioli, Giovanna; Borsari, Marco; Cannio, Maria; Ranieri, Antonio; Volponi, G. J. Electroanal. Chem. **2004**, 564, 45-52.

(10) Jiang, L.; McNeil, C. J.; Cooper, J. M. *J. Chem. Soc., Chem. Comm*. **1995**, 1293-1295.

(11) Collinson, M.; Bowden, E. F. *Langmuir* **1992**, *8*, 1247-1250.

(12) Amador, S.M.; Pachence, J. M.; Fischetti, R.; McCauley, J. P. Jr.; Smith, III, A. B.; Blasie, J. K.; *Langmuir* **1993**, *9*, 812-817.

(13) Kasmi, A. E.; Wallace, J. M.; Bowden, E. F.; Binet, S. M.; Linderman, R. J. *J. Am. Chem. Soc*. **1998**, *120*, 225-226.

(14) Tarlov, M. J.; Bowden, E. F. *J. Am. Chem. Soc.* **1991**, *113*, 1847-1849.

(15) Song, S.; Clark, R. A.; Bowden, E. F.; Tarlov, M. J. *J. Phys. Chem.* **1993**, *97*, 6564-6572.

(16) a)Bowden, E. F.; Clark, R. A.; Willit, J. L.; Song, S. *Proceedings of the Fifth International Symposium on Redox Mechanisms and Interfacial Properties of Biological Molecules.* 1993, F. Schultz and I. Taniguchi (editors) , 34-45. b) Willit, J. L.; Bowden, E. F. *J. Phys. Chem.* **1990**, *94*, 8241-8246.

(17) Nahir, T. M.; Clark, R. A.; Bowden, E. F. *Anal. Chem.* **1994**, *66*, 2595-2598.

(18) a) Murgida, D. H.; Hildebrandt, P. *J. Mole. Struct.* **2001**, *565*, 97-100. b) Murgida, D. H.; Hildebrandt, P. *J. Phys. Chem. B* **2001**, *105*, 1578-1586. c) Murgida, D. H.; Hildebrandt, P. Acc. Chem. Res. **2004,** 37, 854-861. d) Sinniah, K.; Cheng, J.; Terrettaz, S.; Reutt-Robey, J. E.; Miller, C. J. J. Phys. Chem. 1995, 99, 14500-14505.

(19) a) J. Wei, J.; Liu, H; Dick, A; Yamamoto, H.; He, Y.; Waldeck, D. H. *J. Am. Chem. Soc.* **2002**, *124*, 9591. b) Khoshtariya, D. E.; Wei, J.; Yamamoto, H.; Liu, H.; Dick, A.; Waldeck, D. H. *J. Am. Chem. Soc*. **2003**, *125*, 7704. c) Yamamoto, H.; Liu, H.; Waldeck, D. H. *Chem. Commun*. **2001**, 1032-1033.

(20) Fedurco, M. *Coord. Chem. Rev*. **2000**, *209*, 263-331.

(21) a) Dutton, P. L.; Wilson, D. F.; Lee, C.-P. *Biochemistry* **1970**, *9*, 5077-5082. b) Vanderkooi, J.; Erecinska, M.; Chance, B. *Arch. Biochem. Biophys*. **1973**, *154*, 531-540. c) Salamon, Z.; Tollin, G. J. *Bioenerg. Biomemb*. **1997**, *29*, 211-216.

(22) a) Vanderkooi, J.; Erecinska, M. *Arch. Biochem. Biophys.* **1974**, *162*, 385-391. b) Moser, C.C; Dutton, P. L. *Biochemistry* **1988**, *27*, 2450-2461. c) Haas, A. S.; Pilloud, K. S.; Babcock, G. T.; Moser, C. C.; Blasie, J. K.; Dutton, P. L. *J. Phys. Chem. B* **2001**, *105*, 11351-11362.

(23) Gopal, D.; Wilson, G. S.; Earl, R. A.; Cusanovich, M. A. *J. Biol. Chem.* **1988**, *263*, 11652-11656.

(24) Peterman, B. F.; Morton, R. A. *Can. J. Biochem*. **1979**, *57*, 372-377.

(25) Margalit, R.; Schejter, A. *Eur. J. Biochem.* **1973**, *32*, 492-499.

(26) Aviram, I.; Myer, Y. P.; Schejter, A. *J. Biol. Chem.* **1981**, *256*, 5540-5544.

(27) a) Koller, K. B.; Hawkridge, F. M. *J. Am. Chem. Soc*. **1985**, *107*, 7412-7417. b) Koller, K. B.; Hawkridge, F. M. *J. Electroanal. Chem*. **1988**, *239*, 291-306.

(28) Sun, S.; Reed, D. E.; Hawkridge, F. M. *Redox Chem. and Interfacial Behavior of Biological Molecules* **1988**, 47-61.

(29) a) Battistuzzi, G.; Borsari, M.; Dallari, D.; Lancellotti, I.; Sola, M. Eur. J. Biochemistry. **1996**, 241, 208-214. b) Battistuzzi, G.; Loschi, L.; Borsari, M.; Sola, M. JBIC **1999**, 4, 601-607. c) Battistuzzi, G.; Borsari, M.; Cowan, J. A.; Ranieri, A.; Sola, M. J. Am. Chem. Soc. **2002**, 124, 5315-5324.

(31) a) Moore, G. R.; Pettigrew, G. W. *Cytochromes c : Evolutionary, Structural and Physicochemical Aspects,* Springer-Verlag: Heidelberg, 1990. b) Pettigrew, G. W.; Moore, G. R. *Cytochromes c : Biological Aspects,* Springer-Verlag: Heidelberg, 1990. c) Scott, Robert A.; Mauk, A. Grant. *Cytochromes c A Multidisciplinary Approach*. University Science Books: Sausalito, CA, 1996.

(31) Avila, A.; Gregory, B. W.; Niki, K.; Cotton, T. M. *J. Phys. Chem. B*. **2000**, *104*, 2759-2766.

(32) Osheroff, N.; Brautigan, D. L.; Margoliash, E. *Proc. Natl. Acad. Sci. USA* **1980**, *77*, 4439-4443.

(33) Bard, A. J.; Faulkner, L. R. *Electrochemical Methods*, Wiley: New York, 1980, p. 52.

(34) Yue, H.; Waldeck, D. H.; Petrović, J.; Clark, R.A. *Manuscript in preparation*.

(35) Margalit, R.; Schejter, A. *Eur. J. Biochem.* **1973**, *32*, 500-505.

(36) Clark, R. A.; Unpublished Data.

(37) E°′ values of -159 mV and -147 mV vs. Ag/AgCl were found for cyt *c* /$PyCO_2(CH_2)_6S$/Au and cyt *c*/$PyCO_2(CH_2)_{16}S$/Au, respectively. See reference 19.

(38) a) Creager, S. E; Clarke, J. *Langmuir* **1994**, *10*, 3675-3683. b) Smalley, J. F. *Langmuir* **2003**, *19*, 9284-9289.

(39) a) Zhou, J.; Zheng, J.; Jiang, S. *J. Phys. Chem. B* **2004**, *108*, 17418-17424; b) Dick, L. A.; Haes, A. J.; Van Duyne, R. P. *J. Phys. Chem B* **2000**, *104*, 11752-11762.

CHAPTER 3 THE EFFECT OF IONIC STRENGTH ON THE ELECTRON TRANSFER RATE OF SURFACE IMMOBILIZED CYTOCHROME *C*

This work has been published as Yue, Hongjun; Waldeck, David H.; Petrovic, Jelena; Clark, Rose A. *J. Phys. Chem. B* **2006**, 110 5062-5072

Abstract

Horse heart cytochrome *c* was immobilized on four different self-assembled monolayers (SAM). The electron tunneling kinetics were studied in the different assemblies as a function of ionic strength of buffer solution using cyclic voltammetry. When cytochrome *c* is electrostatically immobilized, the standard electron exchange rate constant k^0 decreases with increase of the solution ionic strength. In contrast the protein covalently attached or ligated has a rate constant independent of the ionic strength. The inhomogeneity of electrostatically immobilized cytochrome *c* increases with increase of the solution ionic strength, while that of the covalently attached protein is independent of the ionic strength. Comparison of these different electron transfer behaviors suggests that the thermodynamically stable geometry of cytochrome *c* in the electrostatic assemblies is also an electron transfer favorable one. It suggests that the surface charges of cytochrome *c* are capable of guiding it into geometries in which its front surface faces the electron transfer partner. The inhomogeneity observed in this study indicates that a distribution of cytochrome *c* orientations and thus a distribution of electron transfer rate constants exists.

3.1 Introduction

Cytochrome *c* acts as an electron shuttle in biological respiration and photosynthetic processes.[1-3] During electron transfer cytochrome *c* forms a reversible electron transfer complex with its redox counterpart.[4-13] Complementary electrostatic interactions between the oppositely charged protein surfaces draw the redox centers together,[14-18]which can facilitate the protein-protein binding, or docking.[19, 20] Van der Waals forces and hydrophobic interactions are also important in the electron transfer complex. A molecular dynamics calculation shows that van der Waals interactions and protein solvation energy help stabilize of the protein complexes, whereas electrostatic forces play a guiding role in the initial stage of complex formation.[21]

An important question concerning the electron transfer is whether a correlation exists between the most stable complex geometry and the most efficient electron transfer geometry. Two-dimensional NMR combined with theoretical calculations and kinetic studies have been employed to investigate the dependence of electron transfer on complex conformation,[13, 22-24] however little information is available about the conformational distribution of cytochrome *c* in the electron transfer complex. Although studies of the electron transfer rate as a function of ionic strength have been used to address this question, contradictory results have been reported for cytochrome *c*. Some studies conclude that the most stable cytochrome *c* electron transfer complex is also the most proficient electron transfer complex,[21, 25] whereas others suggest not.[7, 8, 10] Differences in the charge distribution of both cytochrome *c* and its redox partner could be the reason for the observed differences, also. Hence it is desirable to know the contribution from each partner, which requires a simplified model system for studying them separately.

Several supramolecular models exist for elucidating the electron transfer of cytochrome *c*, including cytochrome *c* immobilized on electrodes which are coated with self-assembled

monolayer (SAM) films. SAM films have received extensive interest because of their simplicity. By replacing the protein redox partner with a chemically modified electrode, it is possible to address fundamental features in a systematic way. Studies on the distance dependence of electron transfer rate constants,[26, 27] the electron transfer mechanism,[27-29] the impact of special surface sites on the electron transfer reaction[30, 31] and others have been performed using this model.

SAMs composed of carboxylic acid-terminated thiols,[32-34] which provide a negatively charged surface for cytochrome *c* adsorption, are used as a model to understand the electron transfer properties of electrostatically complexed cytochrome *c* and draw analogies to its physiological redox partners. On carboxylic-acid terminated SAMs, the nonadiabatic electron transfer rate constant k^0 of cytochrome *c* has an exponential dependence on distance, for methylene chain lengths larger than six. The decay coefficient β is close to 1.1 per -CH_2- when the number of methylene groups (n) in the chain is larger than eight. For $n < 6$, k^0 displays only a weak dependence on distance and is referred to as the plateau region. This phenomenon indicates that the electron transfer mechanism is different for the thin and thick SAM film. The nature of this mechanism switching is currently under study.[27, 35-37] This work addresses electron transfer in the large distance regime, in which the rate constant decreases exponentially with distance.

A second SAM system that has been reported in cytochrome *c* studies uses pyridine or imidazole receptors to bind the protein.[26, 29] If a pyridyl or imidazole group protrudes above the surface it ligates to cytochrome *c* by displacing Met-80 at the sixth coordination site. This binding strategy is expected to narrow the orientational distribution of cytochrome *c* on the surface and provide a direct connection of the electrode to the heme. The formal potential of cytochrome *c* on this type of SAM shifts negatively, because of the ligation with the nitrogen receptor containing group. It was found that when the chain length is longer than eleven

methylene groups, the k^0 depends exponentially on distance with a decay coefficient β around 1.1 per methylene group. In contrast, when $n<11$ the distance dependence is weak. Although shifted to higher n values, this finding is similar to that observed for electrostatic immobilization. In the nonadiabatic region the rate constant for the pyridine system is larger than that on the carboxylic SAM having the same chain length. This difference was attributed to the 5 Å longer electron tunneling distance for cytochrome *c* on the carboxylic acid terminated film. This conclusion is corroborated by studies of cytochrome *c* mutants.[26, 29, 38] This assembly is a good reference system because of the absence of electrostatic binding.

Oftentimes, the electron transfer complex is pictured as having a single geometry, however computational studies show that this view is not accurate .[9, 21, 39] Rather, simulations produce a distribution of protein-protein binding complexes with similar stability for a certain ionic strength, and these different geometries may have different electron transfer efficiencies, as calculated through electron tunneling pathways. Clark *et al* observed the heterogeneity of cytochrome *c* on gold electrodes modified with carboxylic acid terminated SAM.[40] This result suggests that electrochemical methods might be a sensitive way to experimentally probe the variety of absorption geometries and rate constant distributions.

In the current work, four different coupling methods were employed to immobilize cytochrome *c*. Diagrams of these methods are shown in the Figure 3.1. The first two (panels A and B) were employed as models for the naturally occurring electron transfer complexes and the last two (panels C and D) served as reference systems. The alkanethiol molecules that contact the protein were chosen to have the same length, and all the electron transfer reactions occur in the electron tunneling regime. The electron transfer properties of cytochrome *c* in these four systems were investigated electrochemically as a function of the ionic strength of the buffer solution.

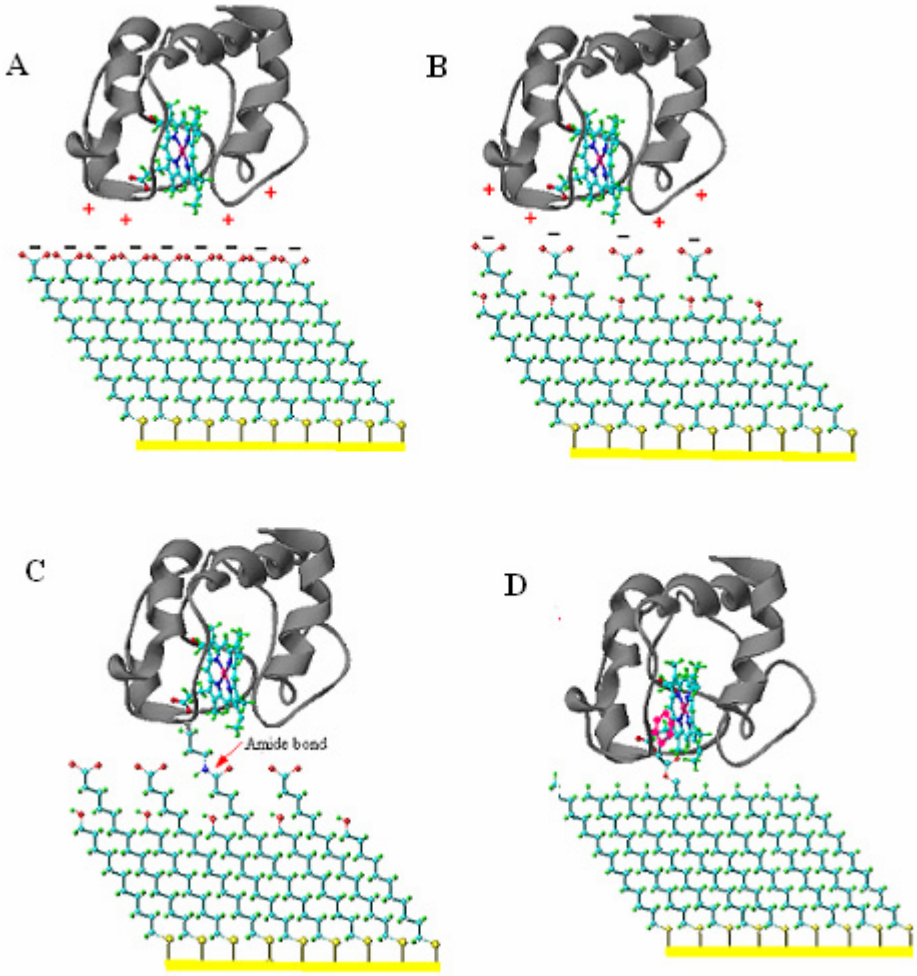

Figure 3. 1 Cartoon depicting cytochrome *c* immobilizations. A) Cytochrome *c* adsorbed electrostatically to a pure SAM composed of carboxylic acid-terminated alkanethiol molecules with fifteen methylene groups and one carboxyl group (pure C15COOH).B) Cytochrome *c* adsorbed electrostatically to a mixed SAM composed of hydroxyl-terminated and carboxylic acid terminated thiols (C15COOH/C11OH). The hydroxyl-terminated thiol has eleven methylene groups and the acid-terminated has fifteen methylenes. C) Cytochrome *c* bound covalently to the mixed SAM C15COOH/C11OH through an amide bond between cyt *c* surface lysine groups and the carboxyl group of the SAM (covalent attachment). D) Cytochrome *c* tethered to a SAM by a pyridyl group which replaces Met 80 as the sixth ligand (PyC16/C15), in which PyC16 represents a thiol molecule having sixteen methylene groups and one pyridyl group and C15 represents a thiol molecule having fourteen methylene groups and one methyl terminus.[26]

Comparisons among these systems allow ambiguities, originating from solution resistance and double layer effects, to be removed. The results suggest that the most stable binding geometry has the best electron transfer efficiency. The results also suggest that a distribution of cytochrome *c* orientations, thus a distribution of electron transfer rates, exist at each ionic strength.

3.2 Experimental Methods

3.2.1 Reagents and Material

Water used in all experiments was purified by a Barnstead-Nanopure system and the resistance was ≥18 MΩ. Horse heart cytochrome *c* was purchased from Sigma and was purified chromatographically on a CM-52 column as described before. [26] 16-mecaptohexadecanoic acid (C15COOH), 11-mecaptoundecanol (C11OH), Bis[16-((4-pyridinylcarbony)oxy)hexadecyl] disulfide (PyC16) were synthesized as reported before[26]. All other chemicals were bought from Sigma and used as received. Electrodes used in all experiments were gold test slides (EMF Corp.), 1000 Å gold film on float glass with 50 Å Titanium to promote adhesion.

Phosphate buffer solution was made by mixing 4.4 mM potassium phosphate dibasic (GR) aqueous solution and 4.4 mM potassium phosphate monobasic monohydrate (GR) aqueous solution until pH 7. The ionic strength was adjusted with suitable amount of solid potassium chloride. Commonly KCl contains an acidic impurity and adding KCl solid decreased pH, so KCl solid was added before the pH was adjusted to desired values.

Tris/acetate (Tris buffer with pH adjusted by acetic acid is referred to as Tris/Acetate buffer) buffer was made from 10mM aqueous solution of tris(hydroxymethyl) amino methane and adjusting the pH with 1M acetic acid until pH 7. The ionic strength was adjusted with a

suitable amount of solid potassium nitrate during mixing of the two buffer components. KNO_3 was added before adjusting the pH to the desired values. All the buffer solutions were stored below 5 ˚C to prevent bacterial growth and kept at ambient temperature for 1hr before use.

3.2.2 Electrode Preparation

Gold film electrodes were pretreated chemically in boiling concentrated nitric acid for 1 min as previously reported, [41] and then were rinsed with water and absolute ethanol before immersion into the SAM solution. Gold films were allowed to stay in the SAM solution for 48 hours to form well organized monolayers. The quality of the SAMs was monitored by contact angle measurements with deionized water. The contact angle of the SAM formed under the condition applied in this study are 13˚ for pure carboxylic SAM, 35˚ for mixed carboxylic SAM, and 93˚ for pyridine mixed SAM.

SAM Solutions For pure carboxylic acid-terminated SAMs, the solution was 2mM C15COOH ethanol solution. For mixed carboxylic acid SAMs, the solution had a total thiol concentration of 2mM in absolute ethyl alcohol and 50% of the thiol was C15COOH and 50% C11OH. For the pyridine-terminated SAM, the solution was 1mM total thiol concentration in dry THF, and the thiol composition was 90% $HS(CH_2)_{14}CH_3$ and 10% $HS(CH_2)_{16}OCOC_5H_4N$.

Incubation of Cytochrome c Cytochrome *c* was incubated by bringing the SAMs into contact with a 0.1 mL cytochrome *c* solution (30-40 μM, in 4.4 mM phosphate buffer, pH 7). For the experiments on pure carboxylic SAM, mixed carboxylic acid SAM and pyridine terminated SAM, the gold film electrode was taken out of the SAM solution, was rinsed gently but thoroughly with ethanol to remove excess thiol solution, and then was rinsed with water to remove ethanol. After drying in an argon flow, the SAM/Au film electrode was assembled into an electrochemical cell. Subsequently 0.1 mL of the cytochrome *c* solution was added into the

cell and allowed to sit at room temperature for 45-60 mins. The design of the cell has been previously published.[42]

Covalent Attachment of the Cytochrome c onto the Mixed Carboxylic SAM This was accomplished by following a previously reported procedure with a slight modification. A gold film electrode was assembled into the electrochemical cell as described above, and then 0.5 mL 5mM CMC (1-cyclohexyl-3-(2-morpholinoethyl) carbodiimide meth-p-toluenesulfonate) solution, with CMC dissolved in 100 mM pH 7 phosphate buffer, was added to activate the surface carboxyl group of SAM. After 30 min the CMC solution was poured out and 0.1 ml cytochrome *c* solution (In 4.4 mM phosphate buffer, pH 8) was added immediately into the cell to let the amide bond form between the activated carboxyl group on the SAM surface and surface lysine residue on cytochrome *c*'s surface. This solution was allowed to react for 30 min, after which the solution was poured out and the electrode was rinsed with the buffer solution.

3.2.3 Electrochemistry Measurements

Cyclic voltammetry was carried out on an EG&G PARC 273 potentiostat controlled by PARC Model 270 software in the ramp mode and CH Instrument Electrochemical Analyzer 618B. The three-electrode electrochemical cell was used, with an Ag/AgCl (1 M KCl) reference electrode and a platinum wire as counter electrode. The Ag/AgCl reference electrode was calibrated against a standard SCE reference electrode.

After cytochrome *c* incubation or covalent attachment and before the voltammetric measurement, the extra cytochrome *c* solution was removed from the electrochemical cell and the cell was rinsed with phosphate buffer solution having a higher ionic strength, e.g. I = 100 mM, to remove any weakly bound cytochrome *c* from the electrode. For the carboxylic acid-terminated SAM system, including pure, mixed SAM and covalent attachment cases, buffer

solution was added to the cell and voltammograms were collected. Typically, the scan was run from 300 mV to -300 mV with the scan rate changing from 25 mV/s to 800 mV/s, or faster depending on the observed behavior. For the pyridine system, voltammograms were collected by scanning primarily from -500mV to 100mV, with scan rates of 1 mV/s to 30 V/s. For each SAM/Au sample, voltammograms were run first in phosphate buffer, from high ionic strength buffer (I = 80mM) to low ionic strength buffer (I = 10mM), and then in tris/acetic buffer, also from high ionic strength to low ionic strength. Kinetic data were extracted from these voltammograms. Peak separations of the voltammogram, the difference between cathodic peak potential and anodic peak potential, is a function of scan rate and increases with increasing scan rate. The electron transfer rate constant k^0 can be determined by fitting the experimental peak separation/ scan rate data to Marcus theory.

For each voltammogram, the cathodic peak potential, the total cathodic peak current, the anodic peak potential, and the total anodic peak current were determined. Both kinetic and ohmic drop (iR_u) contributions to the shift of peak potential were analyzed. iR_u is harmful and unavoidable in electrochemistry measurements. It makes the measured electron transfer rate constant smaller than the actual rate constant. Correction of iR_u must be made to the raw peak potentials. R_u can be measured with AC impedance, and the value of the current i is the total peak current. Subsequently the correction is accomplished by subtracting the product iR_u from the raw peak potential data.[31] The peak potentials after iR_u correction were fit to Marcus theory for the electron transfer rate constant, instead of the raw peak potentials. For systems A, B and C, the rate constant is low, so the applied scan rate does not exceed 1 V/s, and the largest peak current is of the order of μA. The largest R_u is 2-3 kΩ when using the buffer solution of I = 10 mM. Because of the small current, the largest iR_u at a scan rate less than 1 V/s is < 3 mV.

Consequently the iR_u was neglected in the three carboxylic systems. In the pyridine SAM systems, the scan rate was much higher from 1 – 30 V/s, and therefore an iR_u correction was made in data analysis. See reference 31 for details[31].

3.3 Results

The standard electron transfer rate constant k^0 of cytochrome *c* immobilized with the four strategies was studied using cyclic voltammetry. Figure 3.2 shows a voltammogram for each case. Panel A is for pure carboxylic acid-terminated (C15COOH) thiol SAM; panel B is for mixed carboxylic acid and hydroxyl terminated (C15COOH/C11OH) thiol SAM; panel C is for covalent attachment of cytochrome *c* on C15COOH/C11OH SAM and panel D is for pyridine (PyC16/C15) SAM. The voltammograms in Figure 3.2A, 3.2B and 3.2C were collected at a scan rate of 25 mV/s, whereas the one in Figure 3.2D was collected at 1000 mV/s because of its faster electron transfer rate.

These voltammograms are consistent with a one-electron redox reaction of cytochrome *c* immobilized on these surfaces. An ideally reversible one-electron redox reaction of adsorbed species gives a symmetric voltammogram with a zero peak separation (ΔEp) and a full width at half height (*FWHH*) of 90.6 mV.[42] In this study, the voltammograms are nearly symmetric, and the *FWHH* and ΔEp correspond to quasireversible electrochemical behavior. For C15COOH SAM and PyC16/C15, the voltammograms have broader peaks and larger peak separations because the potential sweep rate is fast compared to the rate constant.

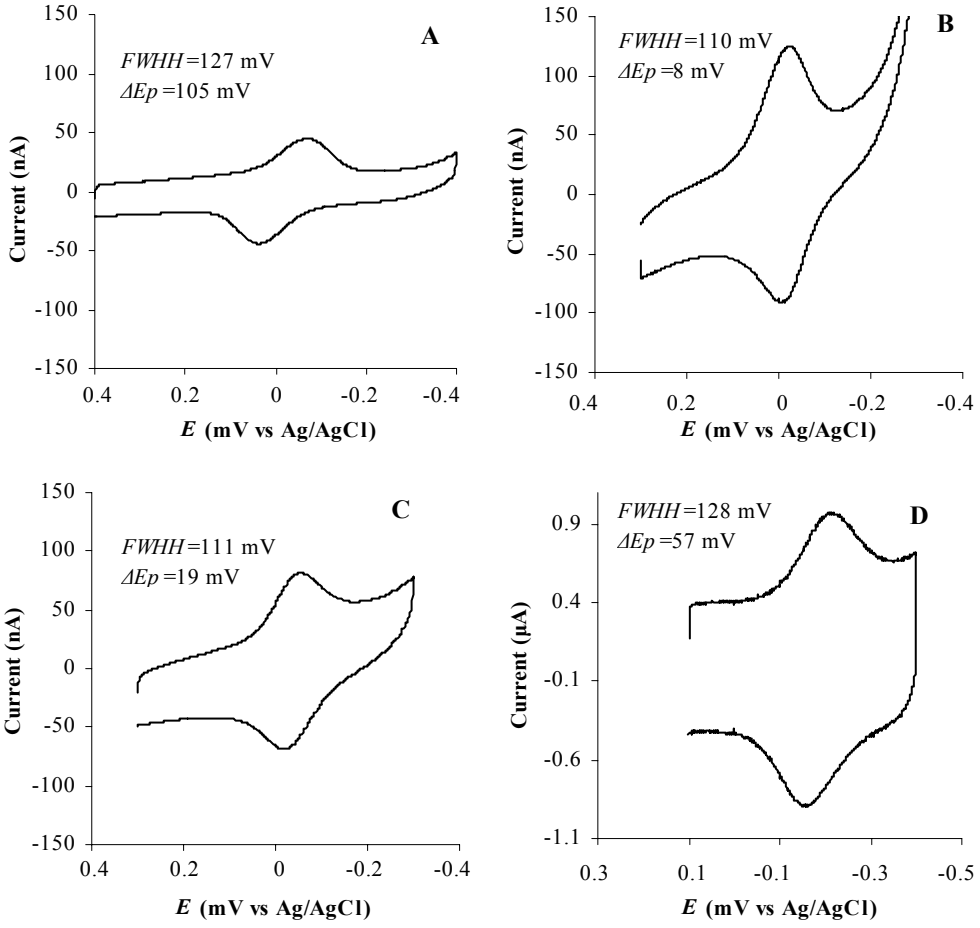

Figure 3. 2 Sample voltammograms of cytochrome *c* with the four different immobilization strategies. The voltammograms were collected in phosphate buffer solutions with ionic strength of 40 mM. A) pure C15COOH SAM, at a scan rate of 25 mV/s; B) C15COOH/C11OH SAM, at a scan rate of 25 mV/s; C) covalently attached to C15COOH/C11OH SAM, at a scan rate of 25 mV/s; D) ligated to PyC16/C15 SAM, at a scan rate of 1000 mV/s. *FWHH* is the full with at half height and *ΔEp* is the peak separation.

The voltammograms in Figure 3.2 show different background current. Both non-faradaic and faradaic processes could contribute to these backgrounds. The large background currents appearing in the voltammograms in the negative potential region, as compared to their positive regions, may be caused by the tail of the reduction of the Au-S bond.[43, 44] The assemblies in these studies are different in hydrophilicity, charge density and cytochrome *c* coverage, which causes variations not only in the non-faradaic current but also in the potential drop across the monolayer, and contribute to this background, as well.[45, 46]

3.3.1 Scan Rate Dependence of Voltammograms

To measure the standard rate constant of electron transfer, voltammograms were collected at a series of potential scan rates. The separation between the cathodic peak and the anodic peak of the voltammogram increases with increase of the scan rate. By fitting the peak separation as a function of scan rate to a theoretical model, based on Marcus theory, the standard electron exchange rate constant k^0 can be extracted.

To perform the fitting, a value of the reorganization energy of electron transfer was assumed.[47-49] The reorganization energy of cytochrome *c* has been studied extensively. A value of 0.8 eV was reported for cytochrome *c* self exchange reactions in aqueous solution.[50] For immobilized cytochrome *c*, values in the range of 0.2 eV to 0.8 eV have been reported, depending on the composition of the SAM and the substrate.[36, 37, 51-53] For cytochrome *c* immobilized by pyridine SAM, a value of 0.58 eV was reached in this lab.[26] For these reasons, 0.6 eV was used to obtain k^0 for cytochrome *c* immobilized with the four different SAMs. It is noteworthy that the analysis is not highly sensitive to the choice of reorganization energy, a change of 25% in the reorganization energy does not lead to a significant difference in k^0 value obtained from the fitting.[55] Figure 3.3 shows representative plots of the peak potential as a

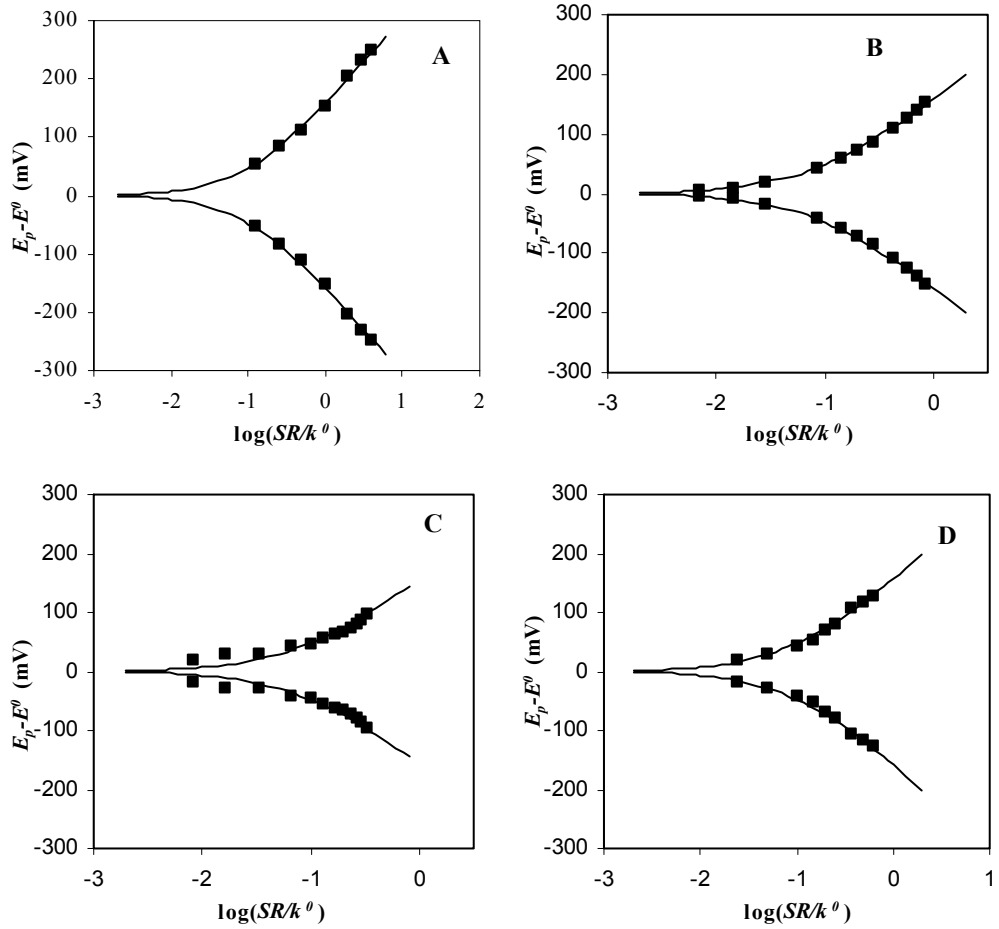

Figure 3. 3 Example of fitting of the experimental peak separation as a function of scan rate to the Marcus model when the buffer is 40mM phosphate buffer pH=7. The solid curves are theoretical calculations, and the black squares(■) are experimental points. A) pure C15COOH SAM, k^0 = 0.2 s^{-1}; B) C15COOH/C11OH SAM, k^0 = 3.5 s^{-1}; C) covalently attached C15COOH/C11OH, k^0 =3.1 s^{-1}; D) tethered to PyC16/C15 SAM, k^0 = 41 s^{-1}.

function of the scan rate and an example of the fitting for each SAM. The good quality of fitting suggests that the electron transfer of cytochrome *c* in those systems is well described by Marcus theory.

Figure 3.3A shows a fit for cytochrome *c* immobilized on pure C15COOH SAM, with a standard rate constant k^0 of 0.2 s^{-1}. This value is comparable to that reported by Avila[27] and larger than that reported by Hildebrandt for SERR on SAM/Ag electrodes 0.073 s^{-1}.[54] Because of the small rate constant, the voltammograms deviate more from the reversible expectation at the experimental scan rate 25 mV/s (see Figure 3.2A) yielding a peak separation of 100mV, whereas a reversible reaction has a peak separation of 0 mV. The fitting between experimental data and theory is good for all the scan rates applied, from a peak separation of below 110 mV to a peak separation of more than 500 mV.

Figure 3.3B shows a fit for cytochrome *c* on C15COOH/C11OH SAM, the rate constant obtained from this fitting is 3.5 s^{-1}, which is more than ten times larger than that on a pure C15COOH SAM. The fitting is good for all the peak separations from 8 mV to 300 mV, and the reaction, at 25 mV/s, has a very small separation, indicating that a more reversible reaction occurs.

Figure 3.3C fits the data for cytochrome *c* covalently bound to a mixed carboxylic acid/hydroxyl SAM, like that used in panel 3 B. For scan rates ranging from 25 mV/s to 300 mV/s, the experimental peak-separations can not be fit with a single theoretical curve. A fit to each of these data points of slow scan rate yields different rate constants. If all the points in figure 3.3C are independently fit and averaged, the rate constant is 2.6 s^{-1} with a range of 1.0 s^{-1} to 3.1 s^{-1}. For higher scan rates (> 300 mV/s), the peak separation fits to the same theoretical curve yielding a single value of k^0, 3.1 s^{-1}. The values of k^0 obtained from the two strategies are

closer to each other than the observed changes of k^0 under different solution conditions. Electron transfer rate constants reported for covalently attached cytochrome *c* in the following plots and tables were obtained by fitting the high scan rate data.

For the PyC16/C15 SAM system, voltammograms were collected from 1 to 30 V/s. Shown in panel D is a fit yielding a rate constant of 41 s^{-1}, which is comparable to the previously reported value 43 s^{-1} measured in 50 mM phosphate buffer.[29] In general, on the SAM/protein assemblies used in this study, the electron transfer rate constant is well characterized by Marcus' theory.

3.3.2 Impact of Ionic Strength on the k^0 of Cytochrome *c*

The standard electron exchange rate constant k^0 of cytochrome *c* was studied as a function of ionic strength of the buffer solution, varying from 10 mM to 80 mM. As the ionic strength exceeds 80 mM, cytochrome *c* starts to desorb from the carboxylic-terminated SAM. For the purpose of comparison, the same range of ionic strength was applied in the case of covalent attachment and PyC16/C15 even though cytochrome *c* is stable at much higher ionic strength. Figure 3.4 shows the dependence of k^0 on the ionic strength.

On pure C15COOH SAM, the rate constant k^0 of cytochrome *c* (Fig 3.4 A) shows a systematic decrease from 0.34 s^{-1} to 0.11 s^{-1} in phosphate buffer and from 0.30 s^{-1} to 0.15 s^{-1} in tris/acetate buffer solution as the ionic strength increases from 10 mM to 80 mM. A t-test at a significance level of 0.05 shows that each data point in Fig 3.4 A is different from the others. A similar trend was observed on the C15COOH/C11OH SAM, shown in Fig 3.4 B; k^0 decreases systematically from 4.8 s^{-1} to 2.8 s^{-1} for the phosphate buffer, and from 4.6 s^{-1} to 2.8 s^{-1} for the tris/acetate buffer, as the ionic strength of the buffer solution is increased. The change is

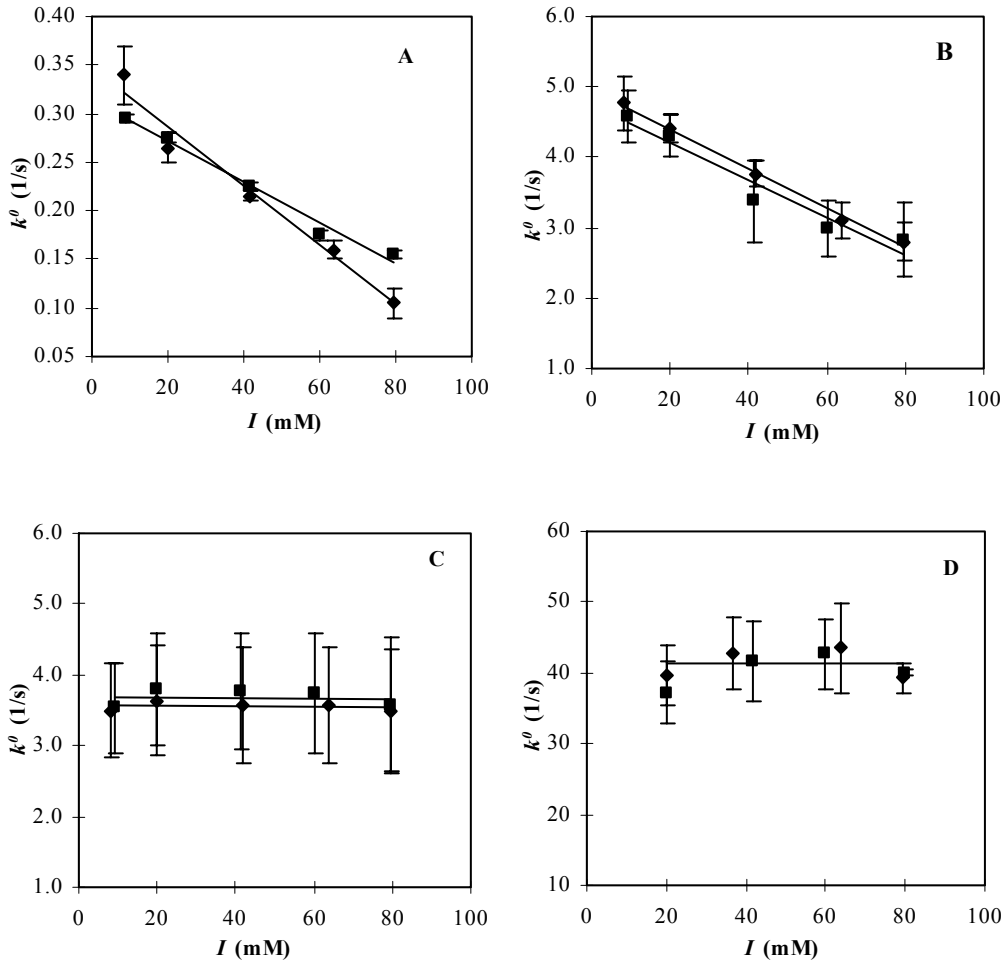

Figure 3. 4 The dependence of the standard electron transfer rate constant k^0 of cytochrome *c* on different SAMs. Black diamonds (♦) are data from phosphate buffer solutions at pH 7, and black squares (■) are data from tris-acetate buffer solutions at pH 7.The solid curves are a linear fitting of experimental data. A) cytochrome *c* on pure C15COOH SAM; B) on C15COOH/C11OH SAM; C) covalently attached to C15COOH/C11OH SAM; D) tethered to PyC16/C15 SAM

comparatively small (less than a factor of two). Any two successive data points are not significantly different under a t-test at a significance level of 0.05. However any two non-successive data points are significantly different under the same statistical test. Taking into account the experimental procedure, the similarity of the trend in the two buffers suggests that the observed behavior of k^0 occurs because of the ionic strength variation, rather than some uncontrolled effect of the SAM structure.

Figure 3.4C shows data for the covalent attachment case, in which cytochrome *c* was immobilized by amide bond formation between its surface lysine groups and carboxylic termini of the C15COOH/C11OH SAM. The rate constant k^0 is independent of ionic strength, and has a value of 3.5 s^{-1}. The data shown in figure 3.4C have a large standard deviation because of deviations in the rate constant between electrodes. On a single electrode the rate constant k^0 of cytochrome *c* displayed no dependence on ionic strength. This was true for every trial. In contrast, the k^0 measured on different electrodes varied significantly from 3.0 s^{-1} to 5.0 s^{-1}, hence the variation of the data points is large but the difference of their averages is small. In the experiment, extra precautions were taken to make sure cytochrome *c* was covalently attached on the surface. After the covalent attachment procedure was complete, the electrode was rinsed several times with a buffer having an ionic strength of 200 mM. Control experiments show that cytochrome *c* electrostatically adsorbed will be totally removed from the C15COOH/C11OH surface under the same conditions, *i.e.* Faradaic current would not be observed. During electrochemical measurement, the surface coverage of cytochrome *c* was monitored by the integral charge under the peaks of the voltammograms. Less than a 5% change in the surface coverage of cytochrome *c* was observed throughout the whole process of the experiment (*ca*. 2

hours), whereas a loss of 25% surface bound cytochrome *c* is unavoidable in the electrostatic case of C15COOH/C11OH SAM.

The pyridine group of the PyC16/C15 SAM displaces the axial ligand Met-80 and ligates to the heme iron of cytochrome *c*, thereby binding cytochrome *c* to the film.[26] Figure 3.4D shows the ionic strength dependence of k^0 in this case, namely no significant change in the k^0 upon increase in the ionic strength of the buffer solution from 20 mM to 80 mM. The k^0 has a value around 40 s^{-1}. The rate constant is a hundred times larger for the ligated system than that of pure carboxylic acid because of the direct coupling of the SAM terminal group to the redox center.[26]

Table 3. 1 Rate constant k^0 (1/s)of cytochrome *c* at I = 40 Mm

	Pure C15COOH	Mixed C15COOH/C11OH	Covalent attachment	PyC16/C15
Phosphate Buffer	0.22 ± 0.01	3.6 ± 0.4	3.4 ± 0.8	43 ± 5
Tris/Acetic	0.23 ± 0.01	3.7 ± 0.6	3.5 ± 0.8	42 ± 4

Cytochrome *c* standard rate constants for the different immobilization strategies under the same ionic strength conditions I = 40mM are summarized in Table 3.1. These values are close to those reported previously.[26, 29, 54]

3.3.3 Broadening of the Voltammograms

The preceding analysis addressed the dependence of the peak potential on the scan rate by assuming that the voltammograms are ideal. If this assumption is valid, the peak width and the k^0

are related in a well-defined manner. Hence it is interesting to compare the full width at half height (*FWHH*) of the cathodic peak and anodic peak of the voltammograms for the different immobilization strategies and compare them to the expected value. Voltammograms collected at a potential sweep rate of 25 mV/s are used in this analysis because they are closer to reversible. The values of the *FWHH* are shown as a function of the ionic strength in Figure 3.5. The theoretical *FWHH* is predicted from simulations using Marcus theory and the experimental k^0 values extracted from analyzing the peak potential shifts. Each panel of Figure 3.5 shows theoretical *FWHH* values as well.

For the C15COOH SAM, the voltammetric peaks become narrower as the ionic strength decreases, both in phosphate buffer and in tris/acetic buffer, (see Figure 3.5A). Accounting for the experimental procedure, the similarity of the trend in the two buffers suggests that the observed behavior results from the changing ionic strength, and not some artificial effect of the experimental procedure. The theoretical *FWHH* displays the same trend, indicating that the electron transfer reaction of cytochrome *c* on this pure carboxylic acid film is not electrochemically reversible at a scan rate of 25 mV/s. The effect of changing the ionic strength on the *FWHH* can be analyzed by comparing the experimental *FWHH* and the corresponding theoretical one. In 80 mM buffer, the experimental voltammogram peaks had a *FWHH* of 136 mV, which is 9% larger than the theoretical *FWHH* of 125 mV, predicted for the rate constant of 0.07 s^{-1}. With the 10 mM buffer solution, the difference between the experimental *FWHH* and theoretical ones is 7 mV.

The dependence of *FWHH* on ionic strength for the C15COOH/C11OH monolayer is shown in Figure 3.5B. The calculation shows that the ideal voltammogram under experimental conditions should have a *FWHH* of 91 mV. The experimental voltammograms are consistently

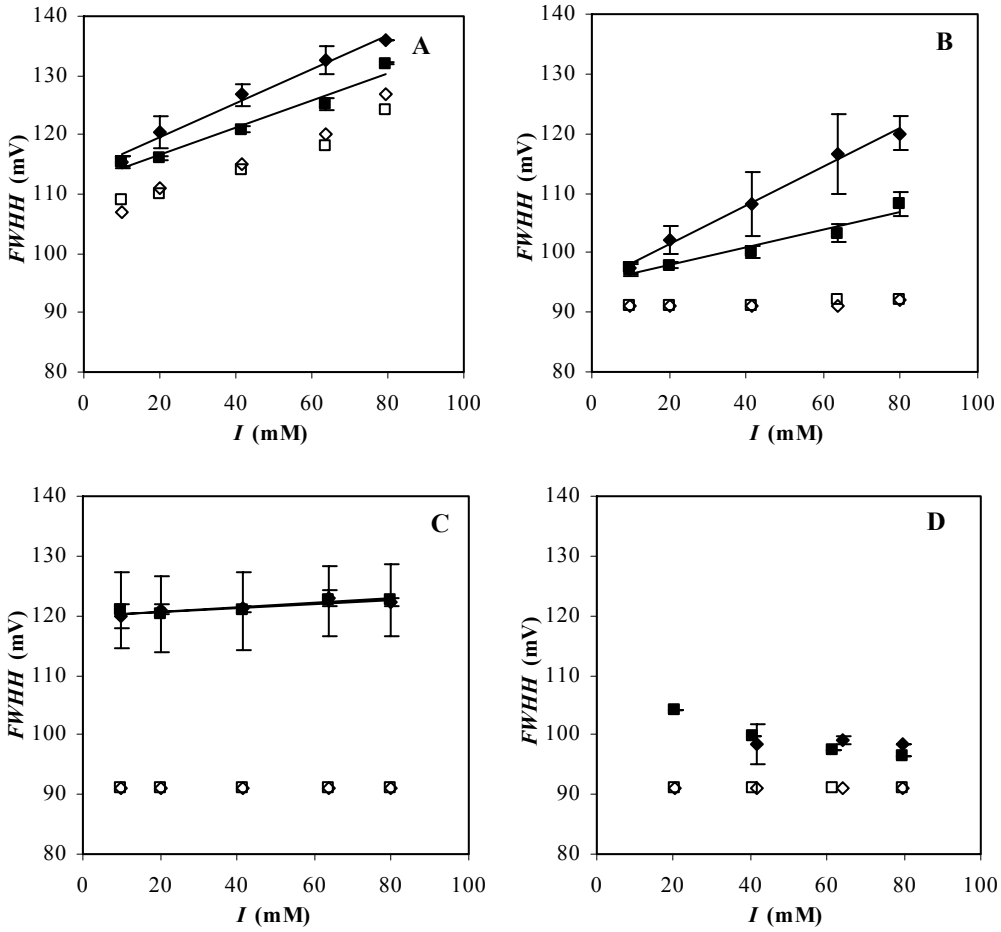

Figure 3. 5 The dependence of Full Width at Half Height (*FWHH*)of the voltammograms on the ionic strength of buffer solution. Black diamonds (♦) are data from phosphate buffer solutions at pH 7, and black squares (■) are data from tris-acetate buffer solutions at pH 7. Theoretical data predicted from Marcus theory are shown in unfilled diamonds(◊) for phosphate buffer solutions and unfilled squares (□) for tris-acetate buffer solutions. The solid curves are linear fitting of experiment data. A) Cytochrome *c* on pure C15COOH SAM, scan rate: 25 mV/s; B) on C15COOH/C11OH SAM, scan rate: 25mV/s; C) covalently attached C15COOH/C11OH SAM, scan rate: 25mV/s; D) tethered to PyC16/C15 SAM, scan rate: 100 mV/s

broader and broaden more with increasing ionic strength. Although the peak widths are smaller than that of the pure monolayers, they still deviate from the theoretical prediction. The broadness cannot be attributed solely to the change of rate constant with ionic strength.

In Figure 3.5C, the ionic strength dependence of the *FWHH* for the covalent attachment case is shown. The peak broadening is larger than the adsorbed case and the ionic strength dependence is weak. In the case C, the cytochrome *c* is bound covalently and constrained on the film, whereas the electrostatic assemblies (cases A and B) allow large amplitude motion and displacement of the cytochrome *c*. The different *FWHH* behavior of these three systems clearly shows that changing ionic strength perturbs the geometry of cytochrome *c* on the film.

Panel D shows the case of pyridine ligated cytochrome *c*. In this case, the *FWHH* is much smaller than in the other immobilization schemes. Note that the value at 20 mM may reflect the importance of solution resistance. At 40 mM electrolyte and higher the *FWHH* does not change with ionic strength; a behavior similar to that observed for the covalent attachment.

The experimental *FWHH* values are much larger than theoretical ones in all of these immobilization cases. Comparisons between the systems suggest that the broadening (above the 90 mV ideal limit) results from differences in the immobilization procedures, implying that protein geometry and heme proximity affects the distribution of electron transfer rates.

3.3.4 Annealing of Cytochrome *c* on Pure C15COOH SAM

For the pure C15COOH assemblies the *FWHH* is large and changes significantly with ionic strength. To understand this feature, another experiment was carried out to study the electron transfer kinetics of cytochrome *c* at different surface coverages. On a single pure carboxylic acid modified electrode, cytochrome *c* was electrostatically absorbed. Different surface coverages were obtained by stripping a fraction of the cytochrome *c* off the surface, by washing the

electrode with a 100 mM buffer solution. Between each wash, electrochemical measurements were performed. The surface coverage was obtained from the integral of the total charge under the voltammetric peaks. The standard rate constant k^0, *FWHH*, and theoretical *FWHH* are plotted versus the percentage of the cytochrome *c* coverage, in Figure 3.6. The percentage refers to the ratio of experimental coverage to the full coverage of cytochrome *c*, which was approximated by the number of cytochrome *c* molecules that would be required to cover the whole electrode surface. In this calculation the effective radius of a cytochrome *c* molecule was taken as 18 Å.[55] Figure 3.6 shows that the surface coverage of cytochrome *c* is well below a full monolayer, even on a pure carboxylic acid SAM which has a higher charge density. As the number of surface cytochrome *c* molecules decreases, the rate constant shows a systematic increase, and simultaneously the *FWHH* decreases. Most interestingly, the experimental value of the *FWHH* better approaches the predicted value. At low surface coverage, a very nearly ideal voltammogram was observed.

These data indicate that cytochrome *c* molecules on the surface of the electrode have a non-uniform distribution, leading to a non-uniform distribution of electron transfer rate constants. It appears that the highly concentrated buffer solution strips off cytochrome *c* of lower electron transfer rate constant first, and it is likely that these are the less strongly bound molecules. The washing narrows the distribution of the rate constant and hence the voltammogram. After several washes only the most strongly bound cytochrome *c* are left, and they possess the largest rate constant.

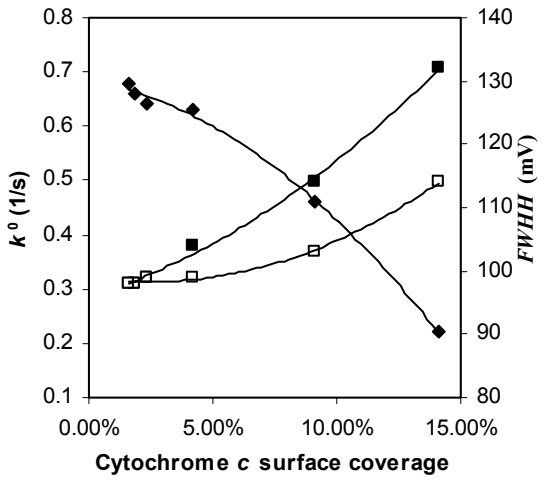

Figure 3. 6 k^0 and *FWHH* of cytochrome *c* electrostatically immobilized on pure carboxylic acid surface. The buffer solution is phosphate buffer with an ionic strength of 20 mM. Data in solid diamonds is for the k^0. The solid square represents the experimental *FWHH*s of the voltammograms at scan rate of 25 mV/s. The unfilled square is the *FWHH* predicted from the corresponding k^0 with Marcus theory.

3.4 Discussion

In this study, cytochrome *c* was immobilized by various strategies: electrostatic interaction, covalent attachment, and ligation. Use of these four systems allows ambiguities, such as the role of solution resistance and double layer effects to be eliminated. The effect of ionic strength on the electron transfer kinetics of cytochrome *c* in these systems was studied and compared.

Ionic strength is known to affect protein electron transfer rates. Goldkorn and Schejter studied the ionic strength dependence of the second order rate constant of cytochrome *c* with ascorbate.[6] The rate constant was found to decrease with the increase of solution ionic strength. The observation was successfully explained using a Brønsted-Debye-Hückel (BDH) model in which the ionic strength affects the activity coefficient of the reactants and the activated complex

differently.[6, 56] For the SAM assemblies, cytochrome *c* molecules are immobilized and form a "unimolecular" electron transfer system, for which the BDH model predicts no ionic strength dependence. The dependence "disappears" because the activity coefficients of the activated complex and the reactant change in a similar way with the ionic strength.[56] For surface bound cytochrome *c*, this model does not explain the experimental findings.

3.4.1 Pure $C_{15}COOH$ SAM versus Mixed $C_{15}COOH/C_{11}OH$ SAM

Cytochrome *c* has positively charged surface lysine groups. A large percentage of the carboxylic termini of the carboxylic SAM ionize in aqueous buffer at pH~7, producing a negatively charged surface.[57, 58] The electrostatic attraction between the opposite charges (SAM and lysines of the protein) accounts for the binding of cytochrome *c* to this type of surface. In the C15COOH/C11OH SAM, the short chain hydroxyl terminated thiol acts as a diluent to reduce the charge density of the film without altering the nature of the interaction. Dramatically, the electron transfer rate constant k^0 is ten times larger on the mixed monolayer than that on the pure carboxylic acid film (Table 3.1). This phenomenon was observed before by El Kasmi *et al*.[33] Despite the difference in the k^0 values, the two assemblies display a similar ionic strength dependence. Increasing the ionic strength slows down the electron transfer, by 200% to 300% for the pure C15COOH SAM and by a factor of 160% for the mixed C15COOH/C11OH SAM.

3.4.2 Electrostatic Binding versus Covalent Attachment and Pyridine Coordination

In the covalent attachment case and C15COOH/C11OH case, the monolayer has the same surface composition, even though the cytochrome *c* is bound differently. This change does not affect the magnitude of k^0, suggesting that the covalent attachment does not perturb the system substantially. However, the ionic strength dependence of the k^0 observed for the electrostatic

cases is not present for the covalent attachment case. In addition k^0 does not depend on the ionic strength for the pyridine SAM, in which cytochrome *c* coordinates to the heme iron. Together, these observations suggest that the ionic strength changes the effective distance between the electrode and the protein for the electrostatic assemblies but not the covalent attachment and ligated assemblies.

Electron tunneling through an alkane chain can be understood by a superexchange mechanism.[48] In the mixed monolayer, the diluent molecule is four methylene groups shorter than the carboxylic acid-terminated molecule, exposing part of the carboxylic chain to the solution. The ionic strength independent k^0 for the covalent attachment case suggests that the electron tunneling probability through the alkane chain is not affected by the medium ions. In the other words, the electronic coupling strength of the alkane chain exposed to solution is not affected significantly by its immediate ionic atmosphere. Hence the ionic strength must affect the interaction between the cytochrome *c* and the negatively charged surface rather than the alkane chain of the SAM. If small buffer ions lodge between the protein and the electrode, then increasing the ionic strength will increase the percentage of cytochrome *c* molecules that have ions lodged between them and the negatively charged monolayer. Such ions could screen the electrostatic interaction and decrease the electronic coupling between cytochrome *c* and the SAM by increasing the effective distance. The ionic strength effect observed in the two electrostatic cases is small; however, its obvious contrast to that observed in the reference cases suggests that increasing the ionic strength of the buffer solution weakens the interaction between the positive charges of cytochrome *c* and the negative charge of the SAM.

When cytochrome *c* is immobilized by carboxylic acid-terminated SAMs, the electron transfer rate constant decreases monotonically with increase in the ionic strength, both for long

chain SAMs as in this study and for short chain SAMs as in Niki's study.[27] This observation stands in contrast to the behavior found for protein-protein complexes. Hazzard *et al* found that the electron transfer between yeast ferrous cytochrome *c* and yeast cytochrome *c* peroxidase at low ionic strength (8 mM) is almost 10 times slower than that at high ionic strength (260 mM).[7] The intermolecular electron transfer rate constant of *Anabaena* Ferredoxin : $NADP^+$ Reductase, reported by Hurley *et al*, shows a bell shaped ionic strength dependence.[59] The same ionic strength effect was also observed by Sadeghi *et al* for the second order electron transfer rate constant for reaction between flavodoxin and *D. vulgaris* cytochrome c_{553}.[60] In all these cases, the redox partners form a stable electron transfer complex whose geometry is not favorable for electron transfer so that a conformational gating step is a prerequisite for the electron transfer. In this model, the gating step becomes easier as the ionic strength increases, because it weakens their electrostatic attraction, however very high ionic strengths prevent the formation of the electron transfer complex and slows down the overall rate.[60] The monotonic ionic strength dependence (see Figure 3.4) observed for the carboxylic acid-terminated SAMs suggests that the stable binding geometry of cytochrome *c* on the surface is also the favorable electron transfer geometry. The results of the annealing experiment, in which the more strongly adsorbed cytochrome *c* molecules have the larger electron transfer rate constant, corroborate this interpretation.

The negative charge on the carboxylic acid surface does not follow a specific pattern as in natural protein partners. The overlap of the optimal electron transfer geometry and the thermodynamically stable geometry of cytochrome *c* formed in these assemblies suggests that the positive charges on cytochrome *c* surface are capable of guiding the molecule into an orientation in which cytochrome *c* faces the electrode with its front heme surface. In contrast,

whether a stable protein-protein complex is optimal for electron transfer largely depends as much on the charge distribution of the redox partner as cytochrome *c*.

The decrease in k^0 with the increase of ionic strength likely results from increasing the effective distance between the cytochrome *c* and the film. If the distance change causes a decrease in the rate because of the increased tunneling distance, the distance would need to increase by about 1.5 Å for an increase in ionic strength from 10 mM to 80 mM, assuming that the tunneling probability decreases as exp(-1.1*n*), where *n* is the number of methylene groups. Comparable tunneling distance changes were found for two homogeneous electron transfer systems. A 1.3 Å increase of tunneling distance could be inferred from the decrease of the second order rate constant of electron transfer between horse heart cytochrome *c* and flavodoxin when the ionic strength increased from 40 mM to 90 mM;[60] a 2.4 Å increase of electron tunneling distance could be inferred for cytochrome b_5 and methaemoglobin when the ionic strength increased from 10 mM to 150 mM.[61] For these two cases the electron transfer coefficient β was 1.6 Å as suggested in reference 63. It should be clear that the distance changes calculated in this way are only approximate and their accuracy depends on how well the model describes the real system.

3.4.3 Distribution of k^0 Values

A number of factors can cause cyclic voltammograms to deviate from the ideal behavior, and non-ideal voltammetric behavior for cytochrome *c* has been reported.[40] One manifestation of nonideality is a cyclic voltammogram that is broader than 90.2 mV. Factors such as the double layer and the solution resistance can distort the actual E versus time function, making it nonlinear and broadening the voltammetric peaks.[45, 46, 62-65] More commonly the peaks broaden when the potential sweep rate is high compared to k^0, *vide supra*. The faster the scan rate, the broader the

peaks. A third origin for peak broadening arises from cytochrome *c* molecules in the film that have different environments leading to a range of k^0 values.

The effect of ionic strength on the broadening of the voltammogram was analyzed by comparison to the predicted value of *FWHH*. As shown in Figure 3.5, on pure C15COOH SAMs, part of the broadening of the voltammogram arises from the fast scan rate as compared to the electron transfer rate. As the ionic strength increases, the k^0 decreases and the *FWHH* increases systematically.

For a mixed monolayer (case B and C), the electron transfer rate is faster than the pure carboxylic acid-terminated films. Even though k^0 depends on the ionic strength, the consequent change in k^0 is not so prominent as to affect the *FWHH* of the voltammogram. The difference between the experimental *FWHH* and the theoretical value must be caused by other effects such as solution resistance, double layer, a distribution of rate constants, and defects in the SAM. Technically it is possible to estimate the effect of the solution resistance on *FWHH* by numerical simulation with the actual *E-t* curve in which the iR_u is compensated. Without knowing the detailed structure of the double layer, it is impossible to calculate the effects of the charging process on the *FWHH* of the voltammograms. However, comparing the ionic strength effect of *FWHH* for the C15COOH/C11OH case and the covalent attachment case circumvents the need for cumbersome numerical simulations and removes the ambiguity caused by double layer effects. In the electrostatic case, the *FWHH* displays a dependence on ionic strength. In fact, the dependence is weak for pure C15COOH SAM, and strong for the mixed C15COOH/C11OH case. For the covalent attachment assembly, essentially no ionic strength dependence of *FWHH* is seen. If the ionic strength dependence observed in the mixed C15COOH/C11OH case arises from the effects of double layer or solution resistance, the same trend should appear in the case

of covalent attachment. The contrast between the experimental data for these two cases suggests that double layer effects and solution resistance are not important for voltammogram broadening under the conditions of this study. The striking difference of the ionic strength dependence of *FWHH* is associated with the binding stability of cytochrome *c* in the two cases. Unlike the electrostatic case, the binding of cytochrome *c* by covalent attachment is not likely to be perturbed by simply increasing the ionic strength. The covalently attached cytochrome *c* voltammograms are broadened to the same extent during the whole process of the experiment. In the electrostatic case, however, changing the buffer solution can desorb loosely bound cytochrome *c* leaving cytochrome *c* with a more uniform binding geometry. The net effect is a higher electron transfer rate constant and a narrower voltammetric peak.

The *FWHH* for the covalently attached protein is broad, and this width is interpreted as a distribution of protein geometry and covalent linkages. Because the protein is electrostatically adsorbed initially, it should have a distribution of geometries that is similar to that for case B (Figure 3.5). A major difference arises in the amide bond formation, however. Because the cytochrome *c* has a number of lysine groups on the surface, a covalent linkage could be formed at a number of different sites and one could form more than one bond between the surface and protein. These features could create a broad distribution of rates and account for the larger *FWHH* over the ionic strength range (Figure 3.5C). The observations of the pyridine ligated *FWHH* provide circumstantial evidence in support of this interpretation. For the pyridine system, which ligates to the heme iron, the global geometry of the adsorbed protein is well defined and any variation are likely linked to differences in the heme pocket.[66] The *FWHH*s measured for the pyridine system reflect the more uniform distribution (Figure 3.5D).

3.4.4 Evolution of Cytochrome *c* on the Electrode Surface

The annealing experiment data verified the hypothesis that a range of k^0 values exist for cytochrome *c* on the carboxylic surface. The impact of removing part of the cytochrome *c* was studied directly in this experiment, whereas changes in the double layer and solution resistance were mitigated using the same SAM and buffer solution with the same ionic strength. The strong correlation of k^0 and *FWHH* with the surface coverage, as shown in Figure 3.6, indicates that cytochrome *c* on the surface is far from homogeneous.

The presence of inhomogeneity in the cytochrome *c* layers is reasonable. Cytochrome *c* has 19 lysine groups, and most of them are positively charged. About 8 lysines are distributed unevenly around the heme crevice. Each of the positively charged groups can act individually or in concert with others to bind with the negatively charged surface. Consequently, cytochrome *c* molecules that approach the SAM film in different ways can assume different geometries, therefore different binding free energies. Although an optimal binding geometry exists, whether the protein molecule is bound in this geometry is also determined by the availability of the right local distribution of the negative charge at the binding site and the ability to fluctuate and access other geometries. The binding constant of cytochrome *c* on carboxylic acid-terminated SAM is *ca*. 10^6 M^{-1} in a 4.4 mM phosphate buffer (ionic strength 10 mM, pH 7). The binding free energy calculated from this constant is fourteen times larger than the thermal energy k_BT at room temperature.[67] Therefore, at low ionic strength the probability of a spontaneous conformational change for cytochrome *c* is low at room temperature. Because the electrostatic interaction is non-specific, it is likely that cytochrome *c* is trapped in a conformation having a local minimum of binding free energy. It is reasonable to propose that cytochrome *c* has a distribution of binding geometries and binding strengths. The observed rate constant is an average over the range of rate

constants in the distribution of cytochrome *c* geometries. During the stripping, less strongly bound molecules desorb from the surface, and it is also possible that some of the molecules left on the surface might be perturbed and adjust their binding state--- an annealing process. These two processes could lead to a more uniform geometric distribution of the remaining cytochrome *c* (*FWHH* decreases, Figure 3.6).

The results from this study are consistent with the theoretical calculations[21, 39, 61] and the dynamic docking model of protein-protein electron transfer complexes.[19, 20, 68] Brownian motion simulations of the cytochrome b_5: hemoglobin system shows that at each ionic strength an ensemble of similarly weakly docked complexes exist. In the ensemble the heme edge- heme edge distance varies from 3.2Å to 9Å and leads to a 400 times difference in the electron tunneling rate constant.[62] Similar results were found for the cytochrome b_5: cytochrome *c* system with Brownian motion simulation and for the flavodoxin : cytochrome *c* (or cytochrome c_{553}) system with Monte Carlo simulation followed by a MD refinement.[21] Although cytochrome *c* is irreversibly adsorbed in our case, the non-specific nature of electrostatic interaction suggests an ensemble of binding orientations. The difference in binding orientation does not necessarily cut off the electron transfer between the gold electrode and the heme of cytochrome *c*; however it may cause a large difference in electron tunneling rate. The validity of this statement is not only supported by theoretical calculations, but also by experimental results previously reported by Pan *et al*.[11] They showed that the electron transfer between Plastocyanin and ruthenium-bisbipyridine-dicarboxybipyridine cytochrome *c* derivatives has a rate constant dependent on the position where the cytochrome *c* was modified. The chemical modification at different lysine groups caused the cytochrome *c* derivatives to bind plastocyanin with different orientation, resulting in a variation of the electron transfer rate from 530 s^{-1} to 1920 s^{-1}. The electrochemical

measurement samples the electron transfer for the whole ensemble, and an average k^0 is obtained from the analysis.

3.5 Conclusion

The interaction between cytochrome *c* and the negatively charged surface of carboxylic acid-terminated SAMs has an electrostatic nature. On this surface, the thermodynamically stable geometry of cytochrome *c* is also an electron transfer favorable one, which results in an electron transfer rate that monotonically decreases with increase of the ionic strength. The inhomogeneities observed in these studies experimentally support the notion that a range of adsorbate geometries are being probed, analogous to the dynamic docking model for generic protein-protein interactions.

3.6 Acknowledgement

We thank Professor Shigeru Amemiya for his generous support and advice, and we thank Professor Haiying Liu who prepared the alkyl pyridine compound used in case D. The work was supported by NSF CHE-0415457 and NSF-REU CHE-0353856.

References

(1) Pettigrew, G. W.; Moore, G. R., *cytochromes c: Biological Aspects*. ed.; Springer-Verlag: Berlin, Heidelberg, New York, London, Paris, Tokyo, 1987

(2) Beissenhirts, M. K.; Scheller, F. W.; Lisdat, F. *Anal. Chem.* **2004,** 76, 4665-4671.

(3) Dai, Z.; Liu, S.; Ju, H. *Electrochim. Acta* **2004,** 49, 2139-2144.

(4) Cheddar, G.; Meyer, T. E.; Cusanovich, M. A.; Stout, C. D.; Tollin, G. *Biochemistry* **1986,** 25, (21), 6502-7.

(5) Cheddar, G.; Meyer, T. E.; Cusanovich, M. A.; Stout, C. D.; Tollin, G. *Biochemistry* **1989,** 28, (15), 6318-22.

(6) Goldkorn, T.; Schejter, A. *J. Biol. Chem.* **1979,** 254, (24), 12562-12566.

(7) Hazzard, J. T.; McLendon, G.; Cusanovich, M. A.; Tollin, G. *Biochem. Biophys. Res. Comm.* **1988,** 151, (1), 429-34.

(8) Meyer, T. E.; Rivera, M.; Walker, F. A.; Mauk, M. R.; Mauk, A. G.; Cusanovich, M. A.; Tollin, G. *Biochemistry* **1993,** 32, (2), 622-7.

(9) Northrup, S. H.; Thomasson, K. A.; Miller, C. M.; Barker, P. D.; Eltis, L. D.; Guillemette, J. G.; Mauk, A. G.; Inglis, S. C. *Biochemistry* **1993,** 32, (26), 6613-23.

(10) Nuevo, M. R.; Chu, H. H.; Vitello, L. B.; Erman, J. E. *J. Am. Chem. Soc.***1993,** 115, (13), 5873-4.

(11) Pan, L. P.; Frame, M.; Durham, B.; Davis, D.; Millett, F. *Biochemistry* **1990,** 29, (13), 3231-6.

(12) Pan, L. P.; Hibdon, S.; Liu, R. Q.; Durham, B.; Millett, F. *Biochemistry* **1993,** 32, (33), 8492-8.

(13) Prudencio, M.; Ubbink, M. *J. Mo. Recognit.* **2004,** 17, (6), 524-539.

(14) Brautigan, D. L.; Ferguson-Miller, S.; Margoliash, E. *J. Biol. Chem.* **1978,** 253, (1), 130-139.

(15) Brautigan, D. L.; Ferguson-Miller, S.; Tarr, G. E.; Margoliash, E. *J. Biol. Chem.* **1978,** 253, (1), 140-148.

(16) Ferguson-Miller, S.; Brautigan, D. L.; Margoliash, E. *J. Biol. Chem.* **1978,** 253, (1), 149-159.

(17) Barlow, G. H.; Margoliash, E. *J. Biol. Chem.* **1966,** 241, (7), 1473-1477.

(18) Kang, C. H.; Brautigan, D. L.; Osheroff, N.; Margoliash, E. *J. Biol. Chem.* **1978,** 253, (18), 6502-6510.

(19) Liang, Z. X.; Nocek, J. M.; Huang, K.; Hayes, R. T.; Kurnikov, I. V.; Beratan, D. N.; Hoffman, B. M. *J. Am. Chem. Soc.* **2002,** 124, (24), 6849-6859.

(20) Liang, Z. X.; Jiang, M.; Ning, Q.; Hoffman, B. M. *J. Biol. Inorg. Chem.* **2002,** 7, (6), 580-588.

(21) Cunha, C. A.; Romao, M. J.; Sadeghi, S. J.; Valetti, F.; Gilardi, G.; Soares, C. M. *J. Biol. Inorg. Chem.* **1999,** 4, (3), 360-374.

(22) Shao, W. P.; Im, S. C.; Zuiderweg, E. R. P.; Waskell, L. *Biochemistry* **2003,** 42, (50), 14774-14784.

(23) Maneg, O.; Malatesta, F.; Ludwig, B.; Drosou, V. *Biochim. Biophys. Acta* **2004,** 1655, (1-3), 274-281.

(24) Banci, L.; Bertini, I.; Felli, I. C.; Krippahl, L.; Kubicek, K.; Moura, J. J. G.; Rosato, A. *J. Biol. Inorg. Chem.* **2003,** 8, (7), 777-786.

(25) Simondsen, R. P.; Weber, P. C.; Salemme, F. R.; Tollin, G. *Biochemistry* **1982,** 21, (25), 6366-75.

(26) Wei, J.; Liu, H.; Dick A., R.; Yamamoto, H.; He, Y.; Waldeck D.H. *J. Am. Chem. Soc.* **2002,** 124, (32), 9591-9599.

(27) Avila, A.; Gregory, B. W.; Niki, K.; Cotton, T. M. *J. Phys. Chem. B* **2000,** 104, (12), 2759-2766.

(28) Rivas, L.; Murgida, D. H.; Hildebrandt, P. *J. Inorg. Biochem.* **2001,** 86, (1), 402-402.

(29) Wei, J.; Liu, H.; Khoshtariya, D. E.; Yamamoto, H.; Dick, A.; Waldeck, D. H. *Angew. Chem., Int. Ed. Engl.* **2002,** 41, (24), 4700-4703.

(30) Niki, K.; Hardy, W. R.; Hill, M. G.; Li, H.; Sprinkle, J. R.; Margoliash, E.; Fujita, K.; Tanimura, R.; Nakamura, N.; Ohno, H.; Richards, J. H.; Gray, H. B. *J. Phys. Chem. B* **2003,** 107, (37), 9947-9949.

(31) Wei, J. J.; Liu, H. Y.; Niki, K.; Margolish, E.; Waldeck David, H. *J. Phys. Chem. B* **2004,** 108, (43), 16912-16917.

(32) Leopold, M. C.; Bowden, E. F. *Langmuir* **2002,** 18, (6), 2239-2245.

(33) El Kasmi, A.; Wallace, J. M.; Bowden, E. F.; Binet, S. M.; Linderman, R. J. *J. Am. Chem. Soc.* **1998,** 120, (1), 225-226.

(34) Collinson, M.; Bowden, E. F.; Tarlow, M. J. *Langmuir* **1992,** 8, 1274-50.

(35) Wackerbarth, H.; Hildebrandt, P. *Chemphyschem* **2003,** 4, (7), 714-724.

(36) Murgida, D. H.; Hildebrandt, P. *J. Phys. Chem. B* **2002,** 106, (49), 12814-12819.

(37) Hildebrandt, P.; Murgida, D. H. *Bioelectrochem.* **2002,** 55, (1-2), 139-143.

(38) Khoshtariya, D. E.; Wei, J.; Liu, H.; Yue, H.; Waldeck, D. H. *J. Am. Chem. Soc.* **2003,** 125, (25), 7704-7714.

(39) Ren, Y.; Wang, W.-H.; Yun-Hua, W.; Case, M.; Qian, W.; Mclendon, G.; Huang, Z.-X. *Biochemistry* **2004,** 43, (12), 3527-3536.

(40) Clark, R. A.; Bowden, E. F. *Langmuir* **1997,** 13, (3), 559-565.

(41) Willit, J. L.; Bowden, E. F. *J. Phys. Chem.* **1990,** 94, 8241-8246.

(42) Bard, A. J.; Faulkner, L. R., *Electrochemical Methods*. 2nd Edition ed.; John Wiley & Sons, Inc.: New York, Chichester, Weiheim, Brisbane, Singapore, Toronto, 2001

(43) Munakata, H.; Oyamatsu, D.; Kuwabata, S. *Langmuir* **2004,** 20, 10123-10128.

(44) Munakata, H.; Kuwabata, S. *Chem. Commun.* **2001**, 1338-1339.

(45) Smith, C. P.; White, H. S. *Anal. Chem.* **1992,** 64, 2398-2405.

(46) Smith, C. P.; White, H. S. *Langmuir* **1993,** 9, 1-3.

(47) Chidsey, C. E. D. *Science* **1991,** 252, 919-922.

(48) Napper, A. M.; Liu, H. Y.; Waldeck, D. H. *J. Phys. Chem. B* **2001,** 105, 7699-7707.

(49) Weber, K.; Creager, S. E. *Anal. Chem.* **1994,** 66 (19), 3164-72.

(50) Gary, H. B.; Winkler, J. R. *Q. Rev. Biophys.* **2003,** 36, (3), 341-372.

(51) Terrettaz, S.; Cheng, J.; Miller, C. J.; Guiles, R. D. *J. Am. Chem. Soc.* **1996,** 118, (33), 7857-7858.

(52) Song, S.; Clark, R. A.; Bowden, E. F.; Tarlov, M. J. *J. Phys. Chem.* **1993,** 97, (24), 6564-72.

(53) Fedurco, M. *Coord. Chem. Rev.* **2000,** 209, 263-331.

(54) Murgida, D. H.; Hildebrandt, P. *J. Am. Chem. Soc.***2001,** 123, (17), 4062-4068.

(55) Dickerson, R. E.; Kopka, M. L.; Weinzierl, J. E.; Varnum, J. C.; Eisenberg, D.; Margoliash, E. *J. Biol. Chem.* **1967,** 242, (12), 3015-18.

(56) Frost, A. A.; Pearson, R. G., *Kinetics and mechanism*. 2nd Ed ed.; John Wiley and Sons: New York, 1961

(57) Hu, K.; Bard, A. J. *Langmuir* **1997,** 13, (19), 5114-5119.

(58) Sugihara, K.; Shimazu, K.; Uosaki, K. *Langmuir* **2000,** 16, (18), 7101-7105.

(59) Hurley, J. K.; Faro, M.; Brodie, T. B.; Hazzard, J. T.; Medina, M.; Gomez-Moreno, C.; Tollin, G. *Biochemistry* **2000,** 39, (45), 13695-13702.

(60) Sadeghi, S. J.; Valetti, F.; Cunha, C. A.; Romao, M. J.; Soares, C. M.; Gilardi, G. *J. Biol. Inorg. Chem.* **2000,** 5, (6), 730-737.

(61) Brittain, T.; Kidd, R. D.; Baker, E. N. *J. Inorg. Biochem.* **2002,** 88, (3-4), 328-334.

(62) Aberg, S. *Journal of Electroanal. Chem.* **1996,** 419, 99-103.

(63) Britz, D. *Journal of Electroanal. Chem.* **1978,** 88, 309-352.

(64) Creager, S. E.; Weber, K. *Langmuir* **1993,** 9, 844-850.

(65) Fawcett, W. R.; Fedurco, M.; Kovacova, Z. *Langmuir* **1994,** 10, 2403-2408.

(66) Murgida, D. H.; Hildebrandt, P.; Wei, J.; He, Y. F.; Liu, H. Y.; Waldeck, D. H. *J. Phys. Chem. B* **2004,** 108, (7), 2261-2269.

(67) Dick, L. A.; Haes, A. J.; Van_Duyne, R. P. *J. Phys. Chem. B* **2000,** 104, 11752-11762.

(68) Liang, Z. X.; Kurnikov, I. V.; Nocek, J. M.; Mauk, A. G.; Beratan, D. N.; Hoffman, B. M. *J. Am. Chem. Soc.* **2004,** 126, (9), 2785-2798.

CHAPTER 4 ON THE ELECTRON TRANSFER MECHANISM BETWEEN CYTOCHROME *C* AND METAL ELECTRODES. EVIDENCE FOR DYNAMIC CONTROL AT SHORT DISTANCES.

This work has been published as Yue, Hongjun; Khoshtariya, D.; Waldeck, David H. *Grouched, J.; Hildebrandt, P.; Murgida, D. H. J. Phys. Chem. B* ***2006****, 110, 19906-19913*

Abstract

Cytochrome *c* was coordinatively bound to self-assembled monolayers of pyridine-terminated alkanethiols on Au and Ag electrodes. The mechanism of heterogeneous electron transfer of the immobilized protein was investigated by cyclic voltammetry and time-resolved surface-enhanced resonance Raman spectroelectrochemistry. The temperature, distance and overpotential dependencies of the electron transfer rates indicate a change of mechanism from a tunneling controlled reaction at long distances (thicker films) to a solvent / protein friction control at smaller distances (thinner films).

4.1 Introduction

This work reports on the electron transfer behavior of the redox protein cytochrome *c* (Cyt-*c*) on modified metal electrodes. The electrochemistry of Cyt-*c* immobilized on metals coated with monolayers of organic molecules has attracted the attention of several groups over the past few years because these simple systems allow for a systematic study of the parameters that control the electron transfer kinetics. Through manipulation of the organic film's properties and terminal functionality it is possible to change the redox behavior, ranging from conditions that mimic biological systems to those far removed from that situation.[1-3] The knowledge gained from these studies contribute to a better understanding of biological redox reactions and may enable new technologies in bioelectronics and biosensors.

Most studies on Cyt-*c* electrochemistry have tried to mimic biological systems by presenting an anionic surface (typically carboxylate moieties) that electrostatically binds the positively charged binding domain of the protein (Scheme 4.1). Under these conditions the electron transfer between the protein and the electrode is facile but displays an unusual dependence on the protein-electrode distance. For ω-carboxylalkanethiols with alkyl chains of ten or more methylene units, the electron transfer rate falls exponentially with the number of methylenes, exhibits an overpotential dependence and is not influenced by solvent viscosity.[2,4-6] These findings are consistent with a nonadiabatic (electron tunneling) long-range electron transfer model. At shorter film thicknesses (less than or equal to nine methylenes) the electron transfer rate becomes nearly distance and overpotential independent and it is sensitive to the solvent viscosity.[2,4-7] A conformationally gated mechanism, i.e., a nuclear rearrangement to a 'redox active' state, has been used to explain these observations.[1,4,8]

Similar "unusual" distance dependencies of the electron transfer rate have been observed for other heme and non-heme proteins immobilized on different self-assembled monolayers (SAMs). Some examples are azurin[9,10] and the Cu_A domain of cytochrome *c* oxidase on hydrophobic surfaces[10], cytochrome c_6 on mixed CH_3/OH-terminated SAMs[11] and cytochrome b_{562} on NH_2-terminated SAMs[12].

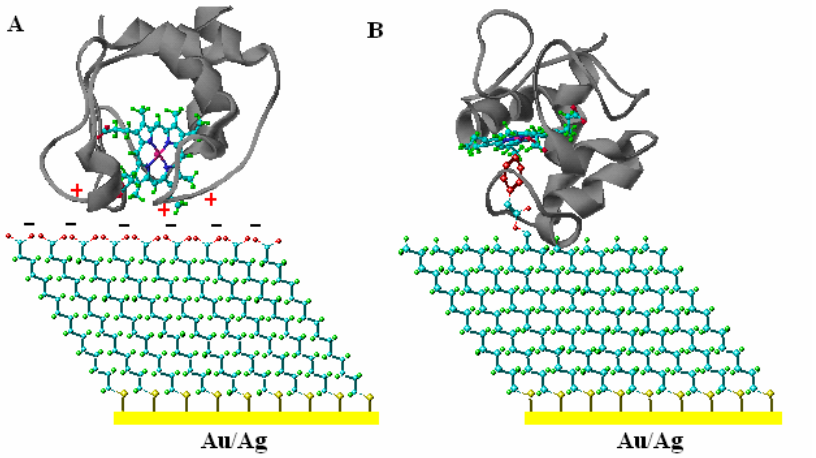

Scheme 4. 1 Immobilization of Cyt-*c* on SAM-coated electrodes. Left: electrostatic adsorption on ω-carboxylalkanethiols. Right: coordinative binding to pyridine-terminated alkanethiols.

An alternative immobilization scheme that has been applied to Cyt-*c* uses alkanethiols with a nitrogen containing terminal group (e.g., pyridine) that displaces the native methionine ligand and wires the Fe to the metal electrode (Scheme 4.1).[13] The distance dependence of the electron transfer rate for those systems is qualitatively similar to that found for the electrostatic immobilization, however the transition between the long range, electron tunneling mechanism and the short range mechanism occurs at a methylene chain length of twelve rather than nine.[14,15] A detailed analysis reveals that this difference results from a change in the dominant electron tunneling pathway for the two cases. For the electrostatic case the electron tunnels through the

methylene chain across the protein/SAM interface and through the peptide to the Fe site.[16] In contrast, for the ligated protein the electron tunnels through the methylene chain, across the pyridine ring and directly on the Fe site. By accounting for this difference in the tunneling pathway, the distance dependence of the rate data fall on a single curve.[13,14]

In the short distance regime, the electron transfer rate constant for the pyridinal immobilization has a weak dependence on the film thickness and decreases with the viscosity,[14] much like the electrostatically adsorbed protein. In this work, the temperature, distance and overpotential dependencies of the electron transfer rate constant of Cyt-*c* immobilized on pyridine terminated SAMs were studied by cyclic voltammetry and time-resolved surface-enhanced resonance Raman spectroelectrochemistry. The results support a change of mechanism from a tunneling controlled reaction at long distances to a solvent / protein friction controlled reaction for the thinner films, rather than conformational gating.

Theoretical Background

Zusman[17] used a master equation approach to elucidate how solvent frictional coupling can influence electron transfer reactions. For the rate of heterogeneous electron transfer at a metal electrode he found the following expression:[18]

$$k_{red} = \frac{1}{\pi\tau_s}\sqrt{\frac{\lambda}{\pi k_B T}}\sin\left(\pi\sqrt{\frac{\Delta G^{\ddagger}}{\lambda}}\right)\exp\left(-\frac{\Delta G^{\ddagger}}{k_B T}\right)\cdot\ln\left[1+\pi\tau_s k_{NA}\sqrt{\frac{\pi k_B T}{\lambda}}\frac{\exp\left(\Delta G^{\ddagger}/k_B T\right)}{\sin\left(\pi\sqrt{\Delta G^{\ddagger}/\lambda}\right)}\right] \quad (4.1)$$

in which the activation free energy is $\Delta G^{\ddagger} = \left(e\eta^0 + \lambda\right)^2 / 4\lambda$. λ is the reorganization energy, $\eta^0 = (E - E^0)$ is the standard overpotential, E is the actual electrode potential, E^0 is the standard potential for the redox couple, and τ_s is a characteristic polarization relaxation time for the surrounding medium (typically the solvent). k_{NA} is the electron transfer rate constant in the limit

of weak electronic interaction between the redox molecule and the electrode, i.e. in the nonadiabatic limit, and can be expressed in terms of the high temperature limit of the Marcus semiclassical equation. After proper integration to account for all the electronic levels of the metal, ε, contributing to the process, the rate constant is[19]

$$k_{NA} = \frac{\pi}{\hbar}\frac{|V|^2 \rho}{\sqrt{\pi\lambda k_B T}} \int_{-\infty}^{\infty} \exp\left[-\left(\frac{\left(\lambda + (\varepsilon_F - \varepsilon) + e\eta^0\right)^2}{4\lambda k_B T}\right)\right] \frac{1}{1+\exp\left[(\varepsilon - \varepsilon_F)/k_B T\right]} d\varepsilon \quad (4.2)$$

Here ρ(ε) is the density of electronic states in the electrode; f(ε) is the Fermi-Dirac distribution law, |V| is the magnitude of the electronic coupling and ε_F is the energy of the Fermi level.

In the limit where $k_{NA} << \frac{1}{\pi\tau_s}\sqrt{\frac{\lambda}{\pi k_B T}}\sin\left(\pi\sqrt{\frac{\Delta G^{\ddagger}}{\lambda}}\right)\exp\left(-\frac{\Delta G^{\ddagger}}{k_B T}\right)$, the electron transfer rate is limited by the electron tunneling event and Eqn. 4.1 reduces to $k_{red} = k_{NA}$, given by Eqn. 4.2. Equation 4.2 can be cast in a more conventional form by approximating the Fermi distribution law as a step function (f(ε)=0 for ε>ε_F and f(ε)=1 for ε<ε_F):

$$k_{NA} \approx \frac{\pi}{\hbar}|V|^2 \rho \; erfc\left(\frac{\lambda + e\eta^0}{\sqrt{4\lambda_o k_B T}}\right) \quad (4.3)$$

where erfc(z) is the complementary error function.[20] |V| decreases exponentially with the protein-to-electrode separation and accounts for the distance dependence of the electron transfer rate in this nonadiabatic limit. This expression ignores contributions to the reorganization energy from quantized modes. Numerical studies suggest that this approximation is reasonable for the case of Cyt-*c* at moderate driving forces.[21,22]

In the limit that $k_{NA} >> \frac{1}{\pi\tau_s}\sqrt{\frac{\lambda}{\pi k_B T}}\sin\left(\pi\sqrt{\frac{\Delta G^{\ddagger}}{\lambda}}\right)\exp\left(-\frac{\Delta G^{\ddagger}}{k_B T}\right)$, the rate is independent of the electronic coupling and is inversely proportional to the polarization relaxation time of the medium:

$$k_{red} = \frac{1}{\pi\tau_s}\sqrt{\frac{\lambda}{\pi k_B T}}\sin\left(\pi\sqrt{\frac{\Delta G^{\ddagger}}{\lambda}}\right)\exp\left(-\frac{\Delta G^{\ddagger}}{k_B T}\right)\cdot\ln\left[\pi\tau_s k_{NA}\sqrt{\frac{\pi k_B T}{\lambda}}\frac{\exp\left(\Delta G^{\ddagger}/k_B T\right)}{\sin\left(\pi\sqrt{\Delta G^{\ddagger}/\lambda}\right)}\right] \quad (4.4)$$

Equation 4.4 simplifies somewhat if the reorganization energy can be approximated as classical and $\eta^0 = 0$:

$$k_{red}^{0} = \frac{1}{\pi\tau_s}\sqrt{\frac{\lambda}{\pi k_B T}}\exp\left(-\frac{\lambda}{4k_B T}\right)\cdot\ln\left[\frac{\pi^3\tau_s}{\hbar}|V|^2\ \rho\frac{k_B T}{\lambda}\right] \quad (4.5)$$

The relations presented for the reduction reaction take a somewhat different form for oxidation but they display the same dependence on solvent relaxation time, reorganization energy, and tunneling probability.

4.2 Experimental Section

4.2.1 Reagents and Materials

Water used in all experiments was purified by a Barnstead-Nanopure system and its resistivity was more than 18 MΩ. The preparation procedure for bis [6-((4-pyridinylcarbony)oxy) hexadecyl] disulfide (PyC6), bis[11-((4-pyridinylcarbonyloxy) hexadecyl] disulfide (PyC11), bis [12-((4-pyridinylcarbony) oxy) hexadecyl] disulfide (PyC12), bis[16-((4-pyridinylcarbony) oxy) hexadecyl] disulfide (PyC16), bis(1-pentanly) disulfide (C6), bis(1-decanyl) disulfide (C10), bis(1-undecanyl) disulfide (C11), and bis (1- pentadecanyl) disulfide have been reported previously.[13] All other chemicals were bought from Sigma and were used as received.

Horse heart cytochrome *c* (Sigma) was purified to remove deamidated forms of the protein by passing through a cation exchange column (CM-52, carboxymethyl-cellulose, Whatman).

4.2.2 Electrode Preparation

A gold wire (0.5 mm diameter, 99.995%) was refluxed in nitric acid (67%) for 2 hrs and then was rinsed with deionized water. The tip of the gold wire was heated to form a ball of ca 1 mm diameter. The area of the gold ball was around 0.07 cm^2 characterized electrochemically in 0.5 M KCl solution containing 2 mM $K_3[Fe(CN)_6]/K_4[Fe(CN)_6]$ (molar ratio 1:1). The gold ball was annealed in a flame to obtain a smooth surface. The other part of the gold wire was sealed in a glass capillary tube. Then the electrode's ball tip was annealed again and cooled under Ar gas. The cooled electrode was immersed into a thiol solution for 12 hrs to allow a self-assembled monolayer to form on the gold surface. The solutions for PyC_n/C_{n-1} self assembly were 0.1 mM in PyC_n and 0.9 mM in C_{n-1}, in ethanol or tetrahydrofuran.

After thoroughly rinsing with ethanol and deionized water, the SAM-coated electrodes were immersed in a 30 μl Cyt-*c* solution (30-40 μM, in 20 mM phosphate buffer, pH 7) for 30 minutes. Subsequently, the electrode was rinsed with 20 mM sodium phosphate buffer and assembled into an electrochemical cell.

4.2.3 Cyclic Voltammetry

Cyclic voltammetry (CV) was carried out using a CH Instrument Electrochemical Analyzer 618B. A three-electrode electrochemical cell was used, with a Ag/AgCl (1 M KCl) reference electrode and a platinum wire counter electrode. The electrolyte was 20 mM sodium phosphate

buffer. The temperature of the electrochemical cell was controlled by a circulating water bath (Neslab RTE-221) and monitored with a homemade T-type thermocouple.

CV measurements of Cyt-*c* were performed at several temperatures, which were selected in random fashion from 2 ºC to 40 ºC with an interval of ca 8 ºC. For each temperature the measurements were repeated several times using freshly prepared electrodes. The voltammograms were collected with the scan rates increasing from 10 V/s to 500V/s for PyC6/C5, PyC11/C10, PyC12/C11 system, and from 1V/s to 100 V/s for the PyC16/C11 system.

Kinetic data were extracted from the peak separation in the voltammograms as a function of scan rate. The electron transfer rate constants k_{ET}^{0} were determined by fitting the experimental peak separation/scan rate data to Marcus theory. The peak separation of an experimental voltammogram arises from two factors, a kinetic factor and an uncompensated solution resistance R_u. The effect of R_u was removed by applying a "post-factum" correction in the data analysis; see an earlier report for details.[16]

4.2.4 Time-Resolved Surface-Enhanced Resonance Raman (TR-SERR)

The electrochemical cell has been described elsewhere.[23] A Pt wire and a Ag/AgCl electrode (WPI, Dri-Ref) are used as counter and reference electrodes respectively. The working electrode is a silver ring (8 mm in diameter and 2.5 mm high) mounted on a shaft that was rotated at ca. 5 Hz to avoid sample degradation due to long laser exposure. After mechanical polishing and electrochemical roughening to produce a SER active surface,[23] the Ag electrodes were coated following the same procedure as for Au (see above). The electrolyte solution (20 mM phosphate buffer pH = 7.0) was bubbled prior and during the measurements with a continuous stream of catalytically purified oxygen-free Ar.

SERR spectra were measured in back-scattering geometry using a confocal microscope coupled to a single stage spectrograph (Jobin Yvon, LabRam 800 HR) equipped with a 2400 l/mm grating and liquid nitrogen cooled back illuminated CCD detector. Elastic scattering was rejected with two Notch filters. The 413-nm line of a cw krypton ion laser (Coherent Innova 300) was focused onto the surface of the Ag rotating electrode by means of a long working distance objective (20x; N.A. 0.35).

Typically, experiments were performed with laser powers of ca. 5 mW at the sample, effective acquisition times of 4 seconds and increment per data point of 0.57 cm^{-1} and a spectral resolution of 2 cm^{-1}. For TR-SERR experiments, potential jumps of variable height (overpotential) and duration were applied to trigger the redox reaction. The SERR spectra were measured at variable delay times after each jump.[24,25] Synchronization of potential jumps and measuring laser pulses was achieved with a home made four channel pulse-delay generator. The measuring laser pulses were generated by passing the cw laser beam through two consecutive laser intensity modulators (Linos) which give a total extinction better than 1:25000 and a time response of ca. 20 ns.

After background subtraction the spectra were treated with home-made component analysis software. In this analysis the full spectra of the individual species are fitted to the measured spectra by using the relative contributions as the only adjustable parameters.[26,27] Each data point used for the kinetic analysis represents the average of at least three independent TR-SERR experiments.

4.3 Results

The mechanism for heterogeneous electron transfer between a metal electrode Cyt-*c* immobilized by PyC_n/C_{n-1} SAM films was investigated by measuring the distance, temperature, and overpotential dependence of the electrochemical rate constant.

4.3.1 Distance and Temperature Dependence of the Electron Transfer Rate

Standard electron transfer rate constants, k_{ET}^0, of Cyt-*c* bound to PyC_n/C_{n-1}-SAM modified Au electrodes were determined by cyclic voltammetry from the separation of the anodic and cathodic peaks as a function of the scan rate and subsequent numerical fitting to the Marcus-DOS equation.[28-31] For each SAM thickness (n = 6, 11, 12 and 16) the temperature was varied from 2ºC, slightly above the freezing point, to 40ºC, before the protein starts to denature.[32-34]

A typical data set is shown in Figure 4.1 for Cyt-*c* on a PyC_{11}/C_{10}-Au electrode at 24.4°C and scan rates ranging from 10 V/s to 500 V/s. The peak currents increase linearly with the scan rate, as expected for a surface-confined redox species. The voltammetric waves are symmetric (α ranges from 0.47 to 0.50) and indicative of a quasireversible electrochemical reaction. For example, at a scan rate of 10 V/s, the full width at half height is 96 mV and the peak separation is 8 mV. The experimentally determined formal potential, -148 mV, is in good agreement with previous determinations[27] and exhibits the characteristic negative shift, with respect to the native protein in solution, that indicates the substitution of the natural axial ligand Met 80 by a pyridine group of the SAM.[35,36] The curve in Figure 4.1C shows a best fit of the peak separation as a function of scan rate to Marcus theory with a $k_{ET}^0 = 2800 \pm 50\ s^{-1}$ and $\lambda = 0.4 \pm 0.1$ eV. Note that the average value obtained for three trials is $2500 \pm 100\ s^{-1}$, see Table 4.1.

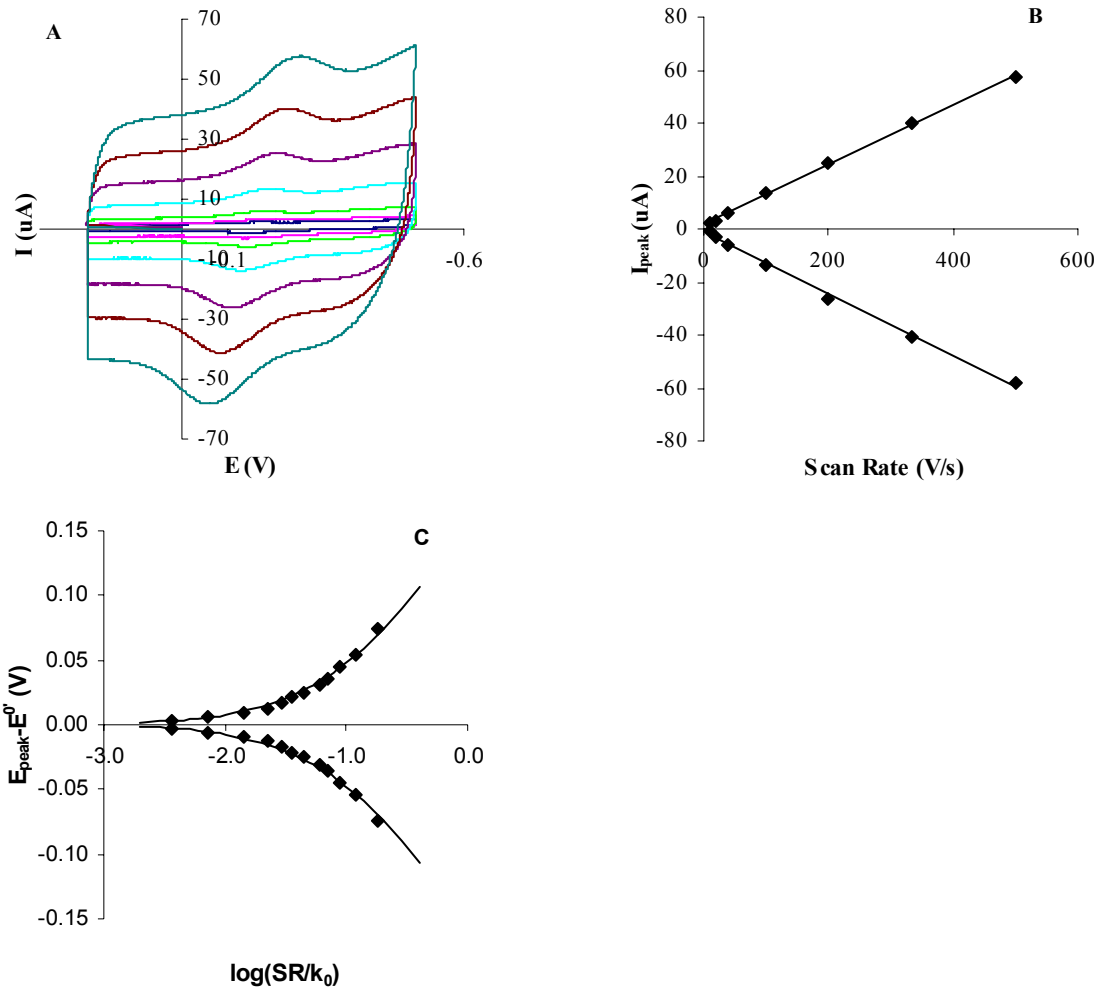

Figure 4. 1 (a) Cyclic voltammograms of Cyt-*c* on a PyC_{11}/C_{10} SAM at scan rates of 10, 20, 40, 100, 200, 300 and 500 V/s. The temperature is 298 K. (b) Linear dependence of the peak current on the scan rate. (c) Peak potentials (black diamonds) as a function of the scan rate. The solid curve is a fit to the Marcus model with $k_{ET}^{0} = 2800\ s^{-1}$ and $\lambda = 0.4$ eV.

Table 4. 1 Formal potential and standard electron transfer rate constant of Cyt-*c* on the different SAMs at 24.4ºC.

	PyC_{16}/C_{15}	PyC_{12}/C_{11}	PyC_{11}/C_{10}	PyC_6/C_5
E^0(mV)	-142 ±2	-144 ±2	-148 ±6	-162 ±2
k_{ET}^0 (s^{-1})	42 ± 3	1700 ± 150	2500 ± 300	2400 ± 500

Table 4. 2 Activation energies, reorganization energies, and viscosity parameters for Cyt-*c* on the different SAMs.

	Arrhenius	Classical analysis[a]		Correction for viscous flow[b]		
SAM	$\Delta G^{\ddagger}$ (eV)	$\Delta G_C^{\ddagger}$ (eV)	λ_C (eV)	γ	$\gamma\Delta G_{\eta_s}^{\ddagger}$ (eV)	λ (eV)
PyC_6/C_5	0.225	0.21	0.84	0.58[c]	0.112	0.48
PyC_{11}/C_{10}	0.205	0.19	0.76	0.36	0.065	0.56
PyC_{12}/C_{11}	0.15	0.14	0.56	0.22	0.040	0.44
PyC_{16}/C_{15}	0.082	0.095	0.38	0[c]	0	0.38

[a]Data treatment according to Eqn. 4.5 neglecting the logarithmic term, except for n = 16 that is treated as nonadiabatic. [b]Data treatment according to Eqn.4.8, except for n = 16 that is treated as nonadiabatic. [c]Values taken from reference 14.

A similar procedure was followed for the different temperatures and SAM compositions. For PyC_n/C_{n-1} coatings with n = 6, 11 and 12, the voltammetric response of the immobilized Cyt-*c* was qualitatively similar to the one shown in Figure 4.1 for the entire range of temperatures. The voltammetry of the PyC_{16}/C_{15} coated electrodes shows a broadening of the voltammetric waves and larger peak separations. For example, at a scan rate of 1 V/s the voltammogram has a full width at half height of 124 mV and a peak separation of 78 mV. This difference reflects the significantly smaller k_{ET}^0 compared to the shorter tethers.

The values of k_{ET}^0 and E^0 determined at room temperature for the different coatings are summarized in Table 4.1. In each case, λ was chosen to be 0.4 eV. The k_{ET}^0 obtained from this analysis is not strongly sensitive to the choice of λ in the range of 0.3 eV to 0.5 eV.[37] The standard rate constants in Table 4.1 are in good agreement with previous determinations[13] and are significantly higher than those observed for Cyt-*c* electrostatically adsorbed on carboxyl-terminated SAMs of comparable thickness.[4] In part, the faster electron transfer for the pyridine immobilized protein can be attributed to the direct connection of the heme iron to the electrode that provides a more efficient tunneling pathway, although the tunneling decay factors are similar.[15]

The temperature and distance dependence of k_{ET}^0 for Cyt-*c* on the different PyC_n/C_{n-1}-SAMs is shown in Figure 4.2 in a three-dimensional representation. The data display a substantial increase of the rate from n = 16 to n = 12 that is consistent with a nonadiabatic reaction, but it remains approximately constant for shorter chains, n<12. The Arrhenius

activation energy E_a, however, shows a monotonic increase with decreasing film thickness (Table 4.2).

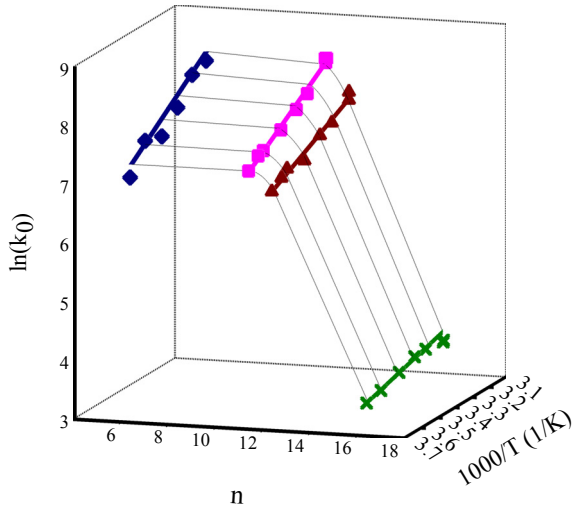

Figure 4. 2 The graph shows the distance and temperature dependence of k_{ET}^{0} for Cyt-*c* on SAMs of different composition on Au. Green crosses: PyC_{16}/C_{15}. Purple triangles: PyC_{12}/C_{11}.Pink squares: PyC_{11}/C_{10}. Blue diamonds: PyC_6/C_5.

4.3.2 Overpotential Dependence of the Electron Transfer Rate

Previous work employed stationary potential-dependent SERR for characterizing Cyt-*c* bound to PyC_{11}/C_{10}-coated Ag electrodes.[27] It was observed that the immobilized protein is in equilibrium between two forms that lack the natural axial ligand Met 80. The dominant form has a six coordinate, low spin heme (6cLS), in which the sixth ligand is the pyridine group of the monolayer. The second form has a five coordinate, high spin heme (5cHS) in which the protein remains attached to the mixed monolayer, presumably through hydrophobic interactions. The coordination equilibrium was shown to be potential dependent with the ferric form displaced towards the 6cLS state, reflecting the larger affinity of Fe^{3+} for pyridine as compared to Fe^{2+}.

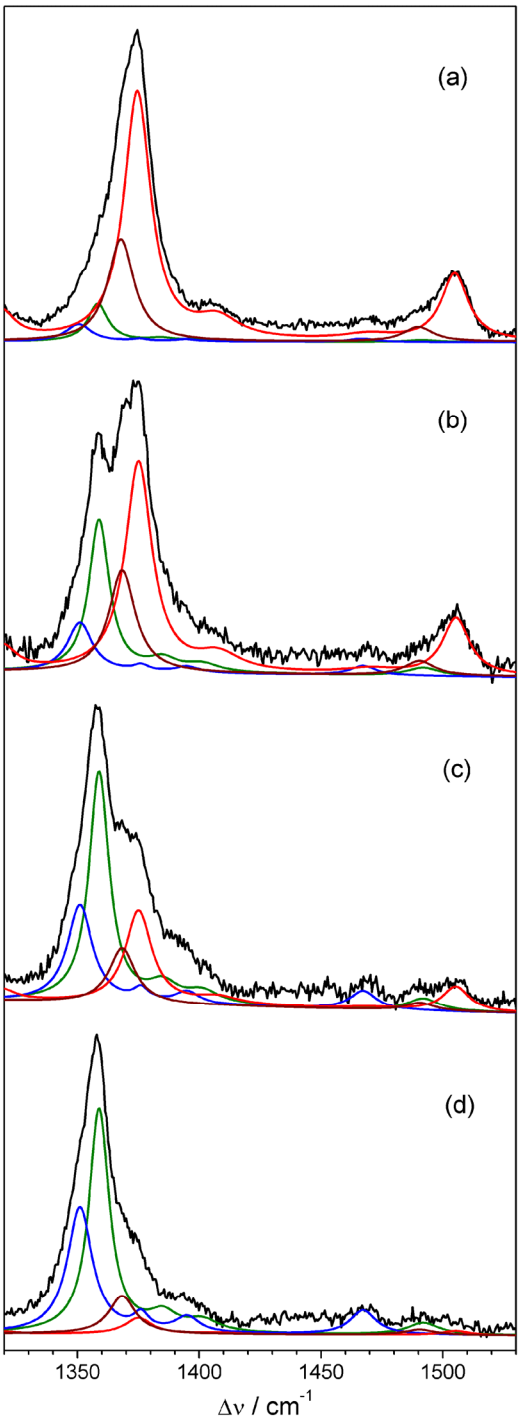

Figure 4. 3 TR-SERR spectra of Cyt-*c* bound to PyC_6/C_5 coated Ag electrodes, measured as a function of the delay time δ for a potential jump from 0.1 to -0.5 V (ΔE = -0.32 V). (a) δ = 0; (b) δ = 165 μs; (c) δ = 800 μs and (d) δ = 11 ms. Red: $6cLS^{Ox}$. Green: $6cLS^{red}$. Dark red: $5cHS^{ox}$. Blue: $5cHS^{red}$.

The present work investigates the overpotential dependence of the electron transfer kinetics of Cyt-*c* bound to PyC_6/C_5 coated Ag electrodes by time-resolved surface-enhanced resonance Raman (TR-SERR) spectroscopy. The spectra were measured at variable delay times following potential jumps from a fixed initial potential of 0.1 V to different final values (E_f) that correspond to standard overpotentials ($\eta_0 = E_f - E^0$) from ca. 0.0 V to -0.5 V. Significantly more negative jumps lead to a drastic drop of the SERR signal presumably due to disruption and /or reductive desorption of the SAM. Potential jumps in the opposite direction (oxidation) were not possible because of the relatively low oxidation potential of Ag.

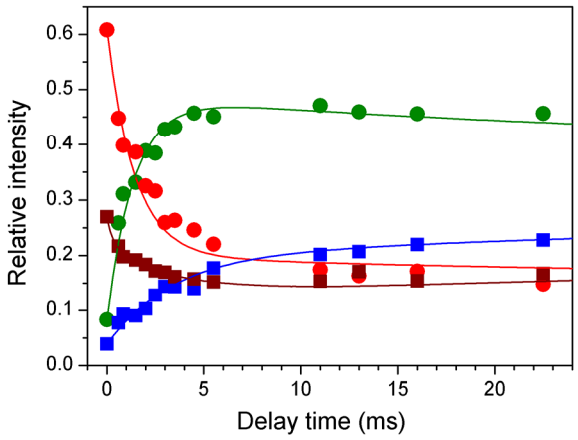

Figure 4. 4 SERR relative intensities of the different spectral species as a function of the delay time after a potential jump from 0.1 to -0.4 V. Green: $6cLS^{red}$. Red: $6cLS^{ox}$. Dark red: $5cHS^{ox}$. Blue: $5cHS^{red}$.

The TR-SERR spectra (Figure 4.3) include the same four spectral components that were found in the stationary SERR studies, i.e. $6cLS^{red}$, $6cLS^{ox}$, $5cHS^{red}$ and $5cHS^{ox}$.[27] As shown in Figure 4.4, within a time window of milliseconds after a potential jump, the total ratio 6cLS/5cHS remains approximately constant such that the two species can be regarded as nearly

independent redox couples. Indeed, the coordination equilibrium was observed to proceed on a time scale of seconds (data not shown). Consistent with these observations, fits of the TR-SERR data to a redox/coordination square equilibrium model[27] or to two independent redox couples yield similar reduction rate constants. In both cases the measured electron transfer rate constants sensitively respond to the applied standard overpotential (Figure 4.5).

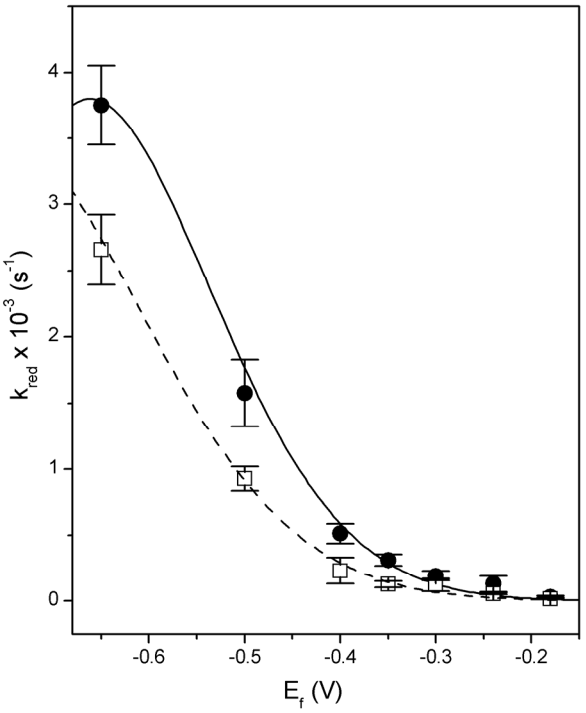

Figure 4. 5 Rate constant of reduction of Cyt-*c* on PyC_6/C_5 SAMs as a function of the final potential in the TR-SERR experiments (see text for details). Circles: 6cLS redox couple. Squares: 5cHS redox couple. The lines in each case represent the best fit to Eqn. 4.4.

Note that in the voltammetric studies on Au only the 6cLS redox couple is detected. The origin for this difference has already been addressed elsewhere.[27] Most of the discussion, however, is dedicated to the 6cLS couple for which a complete data set is available.The overpotential dependence of the reduction rate for the pyridine-coordinated Cyt-*c* (6cLS) gives

equally good fits to either a nonadiabatic model (Eqn. 3) or to a solvent-friction control model (Eqn. 4.4) with reorganization energies that are 0.30 and 0.58 eV, respectively. The value of k_{ET}^0 for the PyC_6/C_5 SAMs, i.e. in the plateau region, is substantially smaller on Ag compared to Au (146 s^{-1} *vs*. 2400 s^{-1}). A similar effect has been observed for electrostatically adsorbed Cyt-*c* on carboxyl-terminated SAMs.[5,38]

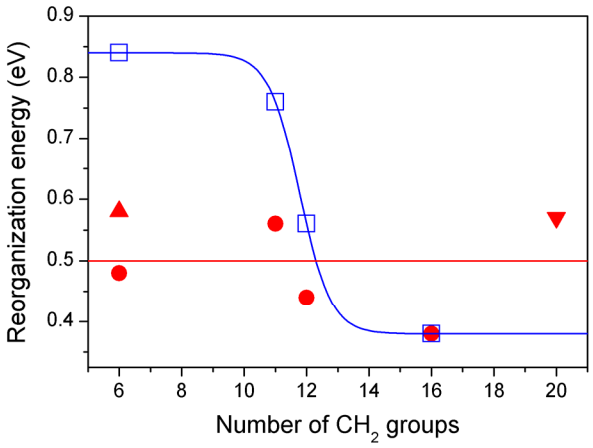

Figure 4. 6 Reorganization energy of Cyt-*c* on PyC_n/C_{n-1} SAMs as a function of the chain length n. Blue squares: λ_c determined by the temperature dependence of k_{ET}^0 using Eqn.4.5. Red circles: λ determined by CV from the temperature dependence of k_{ET}^0 using Eqn. 4.8 (except n = 16 that is treated as nonadiabatic). Red up triangle: λ determined by TR-SERR from the overpotential dependence of k_{ET}. Red down triangle: λ determined by fitting the voltammetric peak separation *vs*. scan rate to the nonadiabatic model.[16] The lines are included to guide the eye.

4.4 Discussion

4.4.1 Gated Mechanism or Frictional Control?

The experimentally determined electron transfer rate of Cyt-*c* immobilized on PyC_n/C_{n-1}-SAMs shows an exponential distance dependence for long tethers ($n \geq 12$), which is consistent with a

long range nonadiabatic reaction, but remains nearly constant at the thinner films (Figure 4.2).[14,15] The near distance-independence of the rate in this region, as well as its sensitivity to the viscosity, can be rationalized in different ways. For a gated mechanism, in which the nonadiabatic electron transfer process is preceded by protein rearrangement or reorientation, the nuclear rearrangement should become rate limiting at sufficiently short distances because of the exponential increase of the electronic coupling with decreasing thickness. Provided that the gating step involves some sort of nuclear motion, this mechanism accounts for the viscosity dependence of the rate at short distances and its insensitivity to viscosity at large distances. Alternatively, the experimental data can be explained in terms of a transition from a nonadiabatic reaction at long distances, in which the rate is controlled by the tunneling probability, to a friction controlled mechanism at short distances where the rate is determined by overdamped relaxation processes of the solvent and protein matrix.

These two mechanisms can be distinguished by measuring the dependence of the electron transfer rate constant on the overpotential. The gated mechanism should not depend on the overpotential, because the rate is limited by a nuclear rearrangement rather than electron transfer, whereas the friction controlled mechanism should change with overpotential, see Eqn. 4.4. The TR-SERR overpotential measurements provide clear evidence for a friction controlled electron transfer mechanism. These experiments show that for a thin PyC_6/C_5-SAM, which is clearly in the region where k_{ET}^0 is distance-independent, the rate of reduction of Cyt-*c* sensitively responds to the applied driving force for electron transfer. Furthermore, the reorganization energy obtained from analyzing these data with a frictional mechanism falls within the range expected for a heme protein[3] and shows excellent agreement with the value reported for Cyt-*c* on a PyC_{20}/C_{19}-Au electrode[16], i.e. well in the nonadiabatic regime. Hence, the data imply that the electron transfer

rate of Cyt-*c* coordinatively bound to short PyC_n/C_{n-1}-SAMs is not limited by a major gating step but by frictional effects related to polarization relaxation processes of the solvent and/or protein matrix.

4.4.2 The Effect of Friction on the Activation Energy

If the measured rate constants correspond to pure electron transfer processes, then the temperature dependence of k_{ET}^0 can be used to determine the reorganization energy of Cyt-*c* on the different PyC_n/C_{n-1} SAMs. In the nonadiabatic limit (n = 16) Eqn. 4.3 applies and in the solvent friction limit (n = 12, 11 and 6) Eqn. 4.5 applies. In each case the voltammetry analysis gives the standard electrochemical rate constant, for which $\Delta G^{\ddagger} = \lambda/4$. The reorganization energies found in this way are summarized in Table 4.2 and are denoted as λ_C to distinguish them from a subsequent analysis. We observe a systematic increase of λ_C from 0.38 eV to 0.84 eV as the thickness of the SAM decreases Note that this analysis assumes that the relaxation time τ_S is temperature independent, which is certainly not the case. A continuum model, which accounts for the image charge in the metal, predicts that the reorganization energy should decrease with film thickness, in direct contrast to the finding here.[39]

Detailed modeling of the relaxation time for the assembly, metal/SAM/protein/solution, is beyond the scope of this work. Instead we use a phenomenological approach for rationalizing the influence of the temperature on the friction controlled electron transfer reaction. In a first approximation, τ_S can be expressed as the longitudinal relaxation time τ_L from Debye's model:[17,40]

$$\tau_s \approx \tau_L = \left(\frac{\varepsilon_\infty}{\varepsilon_s}\right)\left(\frac{3\eta_s V_m}{RT}\right) \tag{4.6}$$

where ε_s is the solution's static dielectric constant, ε_∞ is the solution's high frequency dielectric constant, V_m is the solution's molar volume and η_s is its shear viscosity. Upon replacement of Eqn. 4.6 by Eqn. 4.5, and neglecting the logarithmic term, which is not expected to vary significantly, the frictional control model predicts a linear variation of k_{ET}^0 with the reciprocal viscosity of the medium, $k_{ET}^0 \propto \eta_s^{-1}$. In some experimental studies, however, a different power law of the form $k_{ET}^0 \propto \eta_s^{-\gamma}$ was found, where $0 \leq \gamma \leq 1$ is an empirical parameter.[15] For Cyt-*c* immobilized on PyC_n/C_{n-1}-Au electrodes we have characterized this power law for the different chain lengths by measuring k_{ET}^0 as a function of the viscosity, which is varied by additions of sucrose to the electrolyte solution. The values of γ obtained in that way are summarized in Table 4.2.

In the solvent friction limit, the electron transfer rate constant will depend on the temperature dependence of the friction. The temperature dependence of the viscosity can be expressed through Andrade's empirical equation[41]

$$\eta_s = A \exp\left(\Delta G^{\ddagger}_{\eta_s} \Big/ RT \right) \tag{4.7}$$

where A is an empirical parameter for the solution, and $\Delta G^{\ddagger}_{\eta_s}$ is the activation free energy for viscous flow. For diluted solutions, as those employed in the present work, one can reasonably adopt the parameter for pure water $\Delta G^{\ddagger}_{\eta_s}$ = 17.48 kJ/mol (0.18 eV).[42,43] By combining Eqns 4.5, 4.6 and 4.7 with the empirical power law for the viscosity dependence, the electron transfer rate constant at zero driving force can be written as

$$k_{ET}^{0} = \frac{\varepsilon_{\infty}}{3AV_m\varepsilon_s}\sqrt{\frac{RT}{4\pi\lambda_0}}\exp\left(-\frac{\Delta G^{\ddagger} + \gamma\Delta G_{\eta_s}^{\ddagger}}{RT}\right) \quad (4.8)$$

Equation 4.8 predicts that, for a friction controlled reaction, the activation Gibbs free energy extracted from temperature dependence measurements contains two contributions: (i) a term arising from the intrinsic reorganization energy of the system, $\Delta G^{\ddagger} = \lambda/4$ and, (ii) a term $\gamma\Delta G_{\eta_s}^{\ddagger}$ that accounts for the temperature dependence of the relaxation dynamics of the medium (combination of the solvent, protein matrix, and the film). Correcting the experimentally determined Gibbs activation energies for the friction contribution produces a consistent data set of reorganization energies that does not exhibit a distance dependence, despite the experimental scattering (Table 4.2 and Figure 4.6). Furthermore, the λ values determined in this way are in reasonable agreement with the overpotential determinations for a PyC_6/C_5 and PyC_{20}/C_{19} SAMs (0.58 and 0.57 eV respectively). As shown in Figure 4.6, a common plot of the λ values determined by the different methods points to an average value of *ca.* 0.5 ± 0.1 eV.

4.4.3 Distance Dependence of the Relaxation Dynamics

The parameter γ gives an empirical measure of the importance of the solvent/protein relaxation on the electron transfer reaction, and is known to change with the magnitude of the electronic coupling. In the fully nonadiabatic regime ($n \geq 12$ for the present case), the residence time within the intersection region is short compared to the characteristic time for curve 'hopping', so that the reaction is only controlled by the electronic coupling and becomes independent of the viscosity ($\gamma = 0$). In contrast, if the residence time is long compared to the characteristic time for 'hopping' from the reactant surface to the product surface (a slow nuclear relaxation and/or strong electronic coupling), then the reaction rate is directly proportional to τ_s^{-1} or η^{-1}, i.e. $\gamma = 1$,

and can be approximated by Eqn. 4.5. The fact that we find $0 < \gamma < 1$ may indicate that the reaction lies in an intermediate regime and is better described by Eqn. 4.8, however it could also arise from the approximation that τ_s is proportional to η (Eqn. 4.6).[44]

The observed decrease of γ with increasing film thickness (Table 4.2) can be ascribed to the decrease in the electronic coupling and possibly to changes in the polarization relaxation dynamics. Although the decrease in the electronic coupling with film thickness is widely appreciated, changes in the polarization relaxation are not so well recognized. Local electric fields, which arise from the potential drop across the interface, are expected to decrease with increasing chain length of the SAMs.[5] At sufficiently high field strengths, nuclear motion in the interfacial region is restricted and slowed; in some cases dielectric saturation can occur.[45,46] Therefore, one anticipates an increase in τ_s for the thinner films. The increase in activation energy with decreasing film thickness (see Table 4.2) is consistent with this expectation. Because of the slowed relaxation, this interpretation suggests that k_{ET}^0 should actually decrease for thinner films, however, this effect is counteracted by an increasing electronic coupling. Note that the measured k_{ET}^0 for Cyt-*c* on PyC_6/C_5 is slightly lower than on PyC_{11}/C_{10} SAMs, although the differences are certainly inside the experimental error and, therefore, this region has always been regarded as distance independent. The drop becomes more evident at higher viscosities, however.[14] A similar effect has been observed for the K13A mutant of rat heart Cyt-*c*.[16]

The finding that k_{ET}^0 for Cyt-*c* on PyC_6/C_5 is about fifteen times slower on Ag as compared to Au could result also from differences in the electric field, at least in part. The magnitude of the electric field at the SAM/solution interface scales with the charge density at the metal surface, i.e. with the difference between the actual potential and the potential of zero charge of the electrode.[6] At the standard potential for coordinatively bound Cyt-*c* this difference

is ca. 0.4 V larger for Ag, as compared to Au,[47,48] and one can expect an electric field induced increase of τ_s on Ag. The difference of density of states around the Fermi levels of the two metals is relatively small and should not have a big impact on the reaction rate, as shown by Marcus[49] and Finklea.[50]

The stronger electric field at the Ag surfaces may also explain the fact that we observe a relatively large population of 5cHS species on this metal but not on Au. Ligand exchange reactions of Cyt-*c* have been extensively characterized and shown to be strongly dependent on the electric field strength.[1,2]

4.5 Conclusions

The temperature, overpotential, distance and viscosity dependencies of the electron transfer rate of Cyt-*c* immobilized on PyC_n/C_{n-1} SAMs give a uniform picture consistent with a nonadiabatic reaction at long distances and an increasingly solvent / protein friction controlled mechanism for the thinner films. The mechanism change can be understood using the Zusman formulation and is linked to the increase in electronic coupling and the slowing of the polarization relaxation with the decreasing film thickness. The overpotential dependence of the rate constant at short distances is consistent with this interpretation and discounts conformational gating as a possible mechanism. In contrast, the measured rates on short carboxyl-terminated monolayers show no variation with the increasing driving force,[6,7] and can be regarded as a typical signature of a gated mechanism. The present results and interpretation suggest that the "unusual" distance dependence of the heterogeneous electron transfer rate that has been found for different proteins immobilized on metals by a variety of methods is in fact not unusual and may occur generally – driven by the large electronic couplings and large electric field strengths.

4.6 Acknowledgements

This work has been supported by the DFG (Sfb 498-A8) and the U.S. National Science Foundation (CHE-0415457). We also thank Professor Haiying Liu (Michigan Technological University) for preparing the pyridine terminated alkanethiols.

References

1. Murgida, D. H.; Hildebrandt, P. *PCCP* **2005**, *7*, 3773-3784.
2. Murgida, D. H.; Hildebrandt, P. *Acc. Chem. Res.* **2004**, *37*, 854-861.
3. Fedurco, M. *Coord. Chem. Rev.* **2000**, *209*, 263-331.
4. Avila, A.; Gregory, B. W.; Niki, K.; Cotton, T. M. *J. Phys. Chem. B* **2000**, *104*, 2759-2766.
5. Murgida, D. H.; Hildebrandt, P. *J. Am. Chem. Soc.* **2001**, *123*, 4062-4068.
6. Murgida, D. H.; Hildebrandt, P. *J. Phys. Chem. B* **2002**, *106*, 12814-12819.
7. Hildebrandt, P.; Murgida, D. H. *Bioelectrochemistry* **2002**, *55*, 139-143.
8. Jeuken, L. J. C. *Biochim. Biophys. Acta, Bioenerg.* **2003**, *1604*, 67-76.
9. Chi, Q. J.; Zhang, J. D.; Andersen, J. E. T.; Ulstrup, J. *J. Phys. Chem. B* **2001**, *105*, 4669-4679.
10. Fujita, K.; Nakamura, N.; Ohno, H.; Leigh, B. S.; Niki, K.; Gray, H. B.; Richards, J. H. *J. Am. Chem. Soc.* **2004**, *126*, 13954-13961.

11. Kranich, A.; De la Rosa, M. A.; Hildebrandt, P.; Murgida, D. H. unpublished work.

12. Albrecht, T.; Barker, P. D.; Murgida, D. H.; Hildebrandt, P. unpublished work.

13. Wei, J. J.; Liu, H. Y.; Dick, A. R.; Yamamoto, H.; He, Y. F.; Waldeck, D. H. *J. Am. Chem. Soc.* **2002**, *124*, 9591-9599.

14. Khoshtariya, D. E.; Wei, J. J.; Liu, H. Y.; Yue, H. J.; Waldeck, D. H. *J. Am. Chem. Soc.* **2003**, *125*, 7704-7714.

15. Wei, J. J.; Liu, H. Y.; Khoshtariya, D. E.; Yamamoto, H.; Dick, A.; Waldeck, D. H. *Angew. Chem. Int. Ed.* **2002**, *41*, 4700-4703.

16. Wei, J. J.; Liu, H. Y.; Niki, K.; Margoliash, E.; Waldeck, D. H. *J. Phys. Chem. B* **2004**, *108*, 16912-16917.

17. Zusman, L. D. *Z. Phys. Chem.* **1994**, *186*, 1-29.

18. Zusman, L. D. *Chem. Phys.* **1987**, *112*, 53-59.

19. Marcus, R. A. *J. Chem. Phys.* **1965**, *43*, 679-&.

20. Abramovitz, M.; Stegun, I. A. *Handbook of Mathematical Functions with Formulas, Graphs, and Mathematical Tables*, Dover Publications, Inc.: New York, 1972.

21. Muegge, I.; Qi, P. X.; Wand, A. J.; Chu, Z. T.; Warshel, A. *J. Phys. Chem. B* **1997**, *101*, 825-836.

22. Churg, A. K.; Weiss, R. M.; Warshel, A.; Takano, T. *J. Phys. Chem.* **1983**, *87*, 1683-1694.

23. Murgida, D. H.; Hildebrandt, P. *J. Phys. Chem. B* **2001**, *105*, 1578-1586.

24. Wackerbarth, H.; Klar, U.; Gunther, W.; Hildebrandt, P. *Appl. Spectrosc.* **1999**, *53*, 283-291.

25. Murgida, D. H.; Hildebrandt, P. *Angew. Chem. Int. Ed.* **2001**, *40*, 728-731.

26. Döpner, S.; Hildebrandt, P.; Mauk, A. G.; Lenk, H.; Stempfle, W. *Spectrochim. Acta, Part A* **1996**, *52*, 573-584.

27. Murgida, D. H.; Hildebrandt, P.; Wei, J.; He, Y. F.; Liu, H. Y.; Waldeck, D. H. *J. Phys. Chem. B* **2004**, *108*, 2261-2269.

28. Bard, A. J.; Faulkner, L. R. *Electrochemical Methods*, 2nd ed.; John Wiley & Sons, Inc.: New York, 2001.

29. Weber, K.; Creager, S. E. *Anal. Chem.* **1994**, *66*, 3164-3172.

30. Nahir, T. M.; Clark, R. A.; Bowden, E. F. *Anal. Chem.* **1994**, *66*, 2595-2598.

31. Chidsey, C. E. D. *Science* **1991**, *251*, 919-922.

32. Kreishman, G. P.; Simone, M. J.; Hines, R. M.; Brooks, E. E. *Anal. Biochem.* **1984**, *138*, 360-364.

33. Pascher, T. *Biochemistry* **2001**, *40*, 5812-5820.

34. Taniguchi, I.; Iseki, M.; Eto, T.; Toyosawa, K.; Yamaguchi, H.; Yasukouchi, K. *Bioelectrochemistry and Bioenergetics* **1984**, *13*, 373-383.

35. Fan, C. H.; Gillespie, B.; Wang, G. M.; Heeger, A. J.; Plaxco, K. W. *J. Phys. Chem. B* **2002**, *106*, 11375-11383.

36. Viola, F.; Aime, S.; Coletta, M.; Desideri, A.; Fasano, M.; Paoletti, S.; Tarricone, C.; Ascenzi, P. *J. Inorg. Biochem.* **1996**, *62*, 213-222.

37. Napper, A. M.; Liu, H. Y.; Waldeck, D. H. *J. Phys. Chem. B* **2001**, *105*, 7699-7707.

38. Niki, K.; Sprinkle, J. R.; Margoliash, E. *Bioelectrochemistry* **2002**, *55*, 37-40.

39. Liu, Y. P.; Newton, M. D. *J. Phys. Chem.* **1994**, *98*, 7162-7169.

40. Zusman, L. D. *Chem. Phys.* **1980**, *49*, 295-304.

41. Qadeer, R. *Journal of Zhejiang University SCIENCE* **2004**, *5*, 457-461.

42. Lide, D. R.; Frederikse, H. P. R. *CRC Handbook of chemistry and physics*, 75th ed.; CRC Press: Boca Raton, 1995.

43. Chenlo, F.; Moreira, R.; Pereira, G.; Vazquez, M. J. *J. Chem. Eng. Data* **1996**, *41*, 906-909.

44. Waldeck, D. H. *Chem. Rev.* **1991**, *91*, 415-436.

45. Adrian, R. H.; Almers, W. *J. Physiol.* **1976**, *254*, 317-338.

46. Debye, P. *Physik. Z.* **1935**, *36*, 193-194.

47. Sondag-Huethorst, J. A. M.; Fokkink, L. G. J. *J. Electroanal. Chem.* **1994**, *367*, 49-57.

48. Valette, G.; Hamelin, A. *J. Electroanal. Chem.* **1973**, *45*, 301-319.

49. Gosavi, S.; Marcus, R. A. *J. Phys. Chem. B* **2000**, *104*, 2067-2072.

50. Finklea, H. O.; Yoon, K.; Chamberlain, E.; Allen, J.; Haddox, R. *J. Phys. Chem. B* **2001**, *105*, 3088-3092.

CHAPTER 5 MULTIPLE SITES FOR ELECTRON TUNNELING BETWEEN CYTOCHROME C AND MIXED SELF-ASSEMBLED MONOLAYERS (SAM)

Abstract

The electron tunneling pathway between an electrode and the protein, cytochrome *c*, was studied on mixed C15-carboxylic acid/hydroxyl-terminated SAMs and C16-pyridine/alkane terminated SAMs as a function of the length of the diluent alkanethiol. It was found that by increasing the concentration of shorter-chain hydroxyl diluent thiol in the SAM the rate constant increased in a systematic way. When the diluent composition is high, the k^0 increases exponentially with decreasing chain length of the diluent molecules until the chain length of the diluent molecule reaches a length of about eight methylene groups. These results indicate that the space occupied by the short chain diluent molecules is a part of the electron tunneling pathway, and electronic coupling between the protein and electrode can be enhanced by shortening the tunneling distance in this way.

5.1 Introduction

Cytochrome *c* is an electron transfer protein that acts as an electron shuttle in biological respiratory and photosynthetic processes.[1-3] Many structural, thermal dynamic, and kinetic aspects of its electron transfer are understood. In biological processes, cytochrome *c* forms a reversible electron transfer complex with its redox counterparts,[4-13] which is realized by complementary electrostatic interaction.[14-19] and supported hydrophobic forces on the binding, or docking.[20,21] Hence a distribution in redox complex geometries exist for cytochrome *c*.[20,21] For these reasons cytochrome *c* provides a useful model system for addressing fundamental questions concerning the electron transfer at the protein electrode interface and for improving our understanding of how to adsorb proteins without denaturing or otherwise destroying their function.[22,23]

A number of studies have addressed the electrochemistry of cytochrome *c* immobilized on electrodes coated with self- assembled monolayer (SAM) films. The distance dependence of the electron transfer rate constants[24,25], the electron transfer mechanism,[25-27] the impact of special surface sites on the electron transfer reaction,[28,29] and others have been studied systematically. Two such assemblies are of particular interest here. One is the electrostatic adsorption of cytochrome *c* on carboxylic acid-terminated SAMs, which is used as a mimic of physiological redox complexes.[30-32] The second is immobilization of cytochrome *c* on to SAM systems using pyridine or imidazole receptors protruding above the surface to bind the protein by ligation to the heme iron.[27,33] This binding strategy is expected to narrow the orientational distribution of cytochrome *c* on the surface and directly links the redox center of the heme to the electrode.

In these two supramolecular assemblies, the dependence of the electron transfer rate constant k^0 on the distance between the protein and the electrode shows two regions. One is the

nonadiabatic tunneling region for which the k^0 decays exponentially with increasing SAM thickness; this region starts when n, the methylene chain lengths, is larger than six -CH_2- groups for carboxylic-acid terminated SAMs[25,34] and for pyridine SAM it starts when $n > 11$.[33,35] The decay coefficient β is close to 1.1 per -CH_2- group. When $n < 6$ for the carboxylic acid system and $n < 11$ for pyridine system, the k^0 displays only a weak dependence on distance; sometimes referred to as the plateau region. In this region the electron transfer depends on the protein's environment, in particular the viscosity of the medium.[35] The switching of the cytochrome *c* electron transfer mechanism is currently under study.[25,36-38]

In the nonadiabatic electron tunneling region for the electron transfer, the nature of the electron tunneling pathway inside the protein has evoked both theoretical[39-42] and experimental studies.[43,44] Two major models are commonly applied, the tunneling pathway model that identifies connectivity pathways with the strongest electronic coupling between redox cofactors and the average packing density model that calculates the electron coupling by "line-of-sight" by electron density. Beratan *et. al.*[39] has shown that these two models are mathematically isomorphic and is able to make comparable predictions of the electronic coupling if all possible pathways including water molecules are considered. Based on these two models, the electron tunnels through an arrangement of covalent bonds, hydrogen bonds, and vacuum spaces; typically the coupling is dominated by one pathway or a small number of pathways.

The electron tunneling pathway, in supramolecular assemblies, is less well studied even though it is important to a series of applications of interfacial electron transfer.[23] Napper *et. al.* [45] found that the electronic coupling between ferrocene and electrode occurs primarily through alkanethiol tether to the ferrocene but may have some contribution from the diluent thiol in the SAM. Mutation studies show that Lys 13 play an important role in coupling cytochrome *c* to a

carboxylic acid-terminated SAM [28] but not in the case when a pyridine receptor is used.[29] In addition to these studies, addressing how the binding site/redox tether influences the rate constant is important, a number of authors have found that the diluent molecule, the component of a mixed SAM that is not active in binding the redox species, affects the electron transfer rate constant.[31,46-48] An earlier study on the electron transfer between a metal electrode and ferrocene showed that changing the chain length of the alkanethiol diluent, lead to a change in the electron transfer rate constant.[47] On carboxylic acid terminated self-assembled monolayers diluted with hydroxyl thiols, cytochrome *c* has a faster electron transfer rate constant than on a pure carboxylic acid-terminated monolayers,[31,46,48] and mixed CH_3/COOH terminated SAMs show a slight increase in the k^0 compared to pure COOH monolayers.[49] Whitesides et al. have investigated a variety of self-assembled monolayer surfaces including terminal groups of trimethylammonium, sulfonate, amine, carboxylic acid and others. Cytochrome *c* electron transfer *c* kinetics were shown to decrease substantially in mixed monolayers of trimethylammonium/sulfonate with increasing negative character of the monolayer.[50] Surface charge seems to play a role in electron transfer rate; however, the diluent thiol in the monolayers also offer an alternate electron transfer pathway.

The recent work of Yue[22] and the earlier studies of Saavedra [51] show that cytochrome *c* molecules are bound in a distribution of orientations on both pure and mixed negatively charged monolayers giving rise to a distribution of electron transfer rate constants k^0. For cytochrome *c* it remains unclear whether the rate changes are caused by a change in protein orientation (enhanced electronic coupling), change in SAM charge density or whether it arises from electron tunneling through diluent molecules in the SAM.

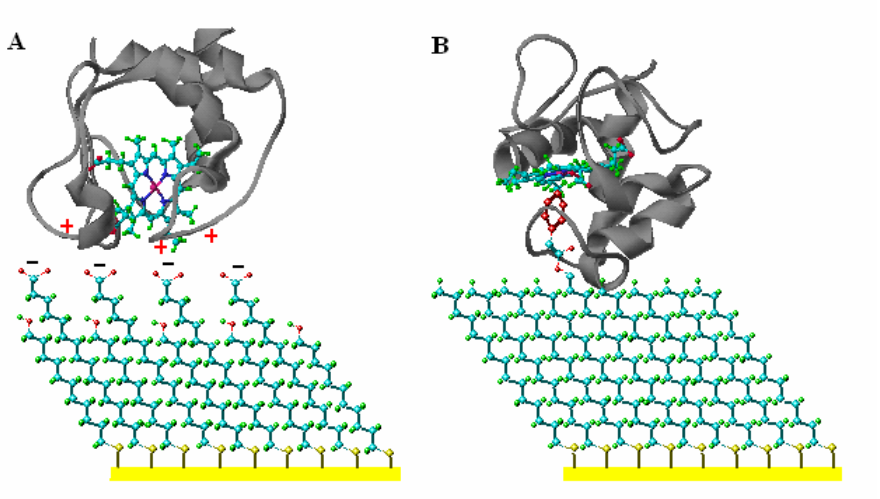

Figure 5. 1 Cartoon depicting the immobilization of cytochrome *c* onto self-assembled monolayers. A) cytochrome *c* electrostatically bound to negatively charged carboxylic acid/hydroxyl-terminated SAM. B) cytochrome *c* forming a complex with pyridine receptor on the SAM surface.

The current study examines the electron transfer for horse heart cytochrome *c* immobilized on mixed C15-carboxylic acid/hydroxyl-terminated SAMs and C16-pyridine/alkane terminated SAMs, as shown in Figure 5.1. The rate constant k^0 is investigated as a function of the surface composition of the mixed SAM in the nonadiabatic tunneling region. It is shown that by increasing the concentration of shorter-chain hydroxyl diluent thiol in the SAM the rate constant increases in a systematic way. When the diluent composition is high, the k^0 increases exponentially with decreasing chain length of the diluent molecules until the chain length of the diluent molecule is eight methylene groups. These results indicate that the space occupied by the short chain diluent molecules is a part of the electron tunneling pathway, and electronic coupling between the protein and electrode is enhanced by shortening the tunneling distance.

5.2 Experimental Section

5.2.1 Reagents and Materials

Water was purified on a Milli-Q/Organex-Q system (Millipore) or Barnstead-Nanopure water purification systems (resistance of 18 MΩ at delivery). Horse heart cytochrome *c* was purchased from Sigma-Aldrich and was purified chromatographically on a CM-52 column.[52] The bis[16-((4-pyridinylcarbony)oxy)hexadecyl] disulfide (PyC16) was synthesized as previously described[52] and 14-mercaptotetradecanol (14-MTOH) was synthesized from 1,12-dodecanedicarboxylic acid (ACROS ORGANIC). The 16-mercapto-hexadecanoic acid (16-MHDA, $C_{15}COOH$), 16-mercapto-1-hexadecanol ($C_{16}OH$), 11-mercapto-1-undecanol ($C_{11}OH$), 8-mercapto-1-octanol (C_8OH), dodecanethiol ($C_{11}CH_3$) and all other chemicals were bought from Sigma-Aldrich and were used as received.

The phosphate buffer solutions were made by mixing 4.4 mM potassium phosphate diabase (GR) aqueous solution and 4.4 mM potassium phosphate monobase monohydrate (GR) aqueous solution to obtain a pH of 7. All buffer solutions were stored below 5 ˚C to prevent bacteria from growing, and equilbrated to ambient temperature one hour before use.

5.2.2 Electrode Preparation

Gold film electrodes (1000 Å Au/50 Å Ti on glass) were purchased from Evaporated Metal Films (Ithaca, NY). Electrodes were first heated in concentrated nitric acid until boiling, rinsed in room temperature water, rinsed with ethanol, and then immersed into an ethanolic alkanethiol solution.[53] Gold films were allowed to stand in the SAM solution for 24 hrs to form well organized monolayers. The quality of SAMs were monitored by contact angle. The contact angle of a water droplet on the SAM formed under the condition applied in this study are 13˚ for pure

carboxylic SAM, 35˚ for mixed carboxylic/hydroxyl terminated (50/50) SAM, and 93˚ for the mixed pyridine/methyl SAM.

SAM Solutions For pure carboxylic acid-terminated SAMs, the solution was 2 mM 16-MHDA ethanol solution. For mixed carboxylic acid SAMs, the solution had a total thiol concentration of 2 mM in absolute ethyl alcohol and the thiols were $C_{15}COOH$ and one of the dydroxyl terminated ones: $C_{16}OH$, $C_{14}OH$, $C_{11}OH$ and C_8OH. For pyridine-terminated SAMs, the solution had a total thiol concentration of 1mM in dry THF and 90% of the thiol was $HS(CH_2)_{14}CH_3$ and 10% PyC_{16}.

Incubation of Cytochrome c was carried out by bringing the SAM coated electrodes into contact with a 0.1 ml cytochrome *c* solution (30-40 μM, in 4.4 phosphate buffer, pH 7). After standing in the SAM solution for 24 hrs, the gold electrode was taken out of the SAM solution and rinsed gently and thoroughly, first with ethanol to remove excess thiol solution and then with water to remove ethanol. After drying in an argon flow, the SAM/Au coated electrode was placed into the cell where 0.1 ml of the cytochrome *c* solution for 30-60 mins. The design of cell has been previously published.[54] After cytochrome *c* incubation and before the voltammetry measurement, the electrodes were rinsed with phosphate buffer solution having a high ionic strength, e.g. I=100 mM, to remove weakly bound cytochrome *c*.

5.2.3 Electrochemistry Measurements

Cyclic voltammetry (CV) was carried out on CH Instrument Electrochemical Analyzer model 600C and 618B. A three-electrode electrochemical cell was used, with an Ag/AgCl (1 M KCl) reference electrode and a platinum wire as the counter electrode. The Ag/AgCl reference electrode was calibrated against a standard SCE reference electrode.

For the carboxylic acid-terminated SAM system, including pure SAM, and mixed SAMs, 20 mM (I = 40 mM) buffer solution (pH 7) was added to the electrochemical cell and cyclic voltammograms were collected by scanning from 300 mV to -300 mV with scan rates changing from 25 mV/s to 800 mV/s, or faster, depending on the electron transfer rate. For the pyridine system, voltammograms were collected by scanning from -500 mV to 100 mV, with scan rates of 1 mV/s to 30 V/s in 20 mM (I = 40 mM) buffer solution. Kinetic data was extracted from these voltammograms. The peak separation, the difference between cathodic peak potential and anodic peak potential, is a function of scan rate and increases with an increase of scan rate. The electron transfer rate constant, k^0, and the reorganization energy can be determined by fitting the experimental peak separation/scan rate to the Marcus theory. The peak separation of an experimental voltammogram comes from two factors, a kinetic factor and an uncompensated solution resistance, R_u. Although the latter can distort kinetic studies, it is negligible when the scan rate is low, e.g. < 1 V/s. In our system, it caused an error of several mV out of a total peak separation of 200-300 mV, which is acceptable. When a higher scan rate is applied, the contribution of R_u to the peak separation can cause a significant error, however this effect can be removed by applying a "post-factum" correction in the data analysis. In each case the peak separation was corrected for R_u by the method reported in a previous paper.[29]

5.2.4 Synthesis of $HS(CH_2)_{14}OH$

The 14-mercapto-tetradecanol was synthesized according to scheme 5.1, which was designed by combining the procedures previously published.[55,56]

1,14-tetradecanediol (1). 1,12-dodecanedioic acid (98%, 4.5 g, 17.42 mmol, 1 eq) dissolved in dry THF (225 ml) was added to a suspension of $LiAlH_4$ (>97%, 1.9 g 52.26 mmol, 3 eq) in dry

THF (90 ml) at 0 ˚C under argon. The solution was stirred at room temperature for 2hrs, poured into a solution of sodium potassium tartrate at 0 ˚C and extracted with ether. The organic layer was washed with brine, dried with $MgSO_4$ and concentrated *in vacuo* to give a white 3.6 g solid. TLC: (hexane-AcOEt: 7-2) $R_f = 0.17$.

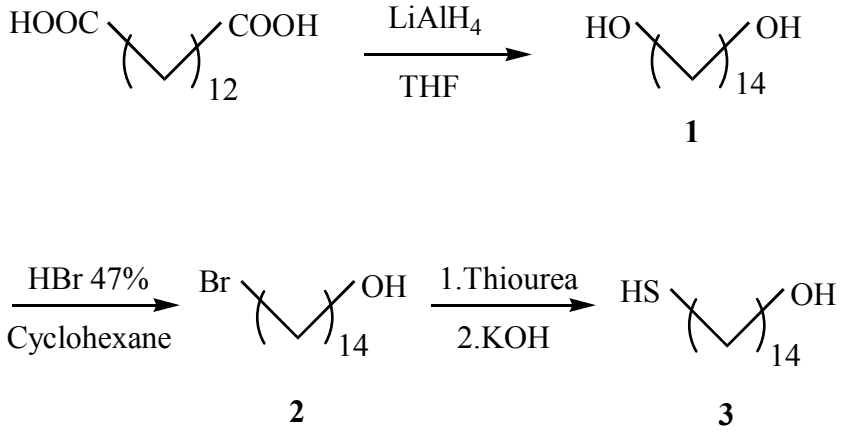

Scheme 5. 1 Synthetic route for 14-mercapto-1-tetradecanol

14-Bromo-tetradecan-1-ol (2). HBr (47% in water, 80 ml) was added to a solution of 1,14-tetradecanediol (3.6 g, 15.62 mmol) in cyclohexane (80 ml). After stirring at reflux for 6 hrs the reaction solution was extracted with 150 ml hexane 3 times, washed with saturated $NaHCO_3$ and brine for three times each, dried with $MgSO_4$ and concentrated *in vacuo*. The residue was purified by chromatography on silica-gel, eluting with hexane-AcOEt (70-20 to 50-50) to give a pale yellow solid 3.92 g. TCL:(hexane-AcOEt: 7-2) $R_f = 0.44$. 1H NMR (300 MHz) δ: ($CDCl_3$) 1.27-1.44 (m, 20 H); 1.57 (q, J = 6.9 Hz, 2 H); 1.86 (q, J =7.2 Hz, 2 H); 3.42 (t, J = 6.9 Hz, 2 H); 3.65 (t, J = 6.6 Hz, 2 H).

14-Mercapto-1-tetradecanol (3). 14-Bromo-tetradecan-1-ol (2.0 g, 7.167 mmol) and thiourea (1.636 g, 21.50 mmol) was dissolved in 60ml absolute ethanol. The mixture was bubbled with Ar for 20 min and then was kept at reflux overnight. After drying *in vacuo*, 20 ml KOH (1.206 g,

21.50 mmol) solution was added and refluxed for 6hrs. The resulting solution was cooled to ambient temperature, extracted with methylene chloride, washed with water and concentrated *in vacuo*. The residue was purified by chromatography on silica-gel, eluting with methylene chloride to obtain a white solid (1.1 g). TLC: (Hexane-AcOEt: 8-2) R_f =0.45. 1H NMR (300 MHz) δ: ($CDCl_3$) 1.27-1.36 (m, 20 H), 1.55-1.64 (m, 4 H), 2.52 (td, J = 7.5 Hz, J = 7.2 Hz, 2 H); 3.65 (t, J = 6.6 Hz, 2 H). MS ESI: 269.3 (MNa^+, 65)

5.3 Result and Discussion

5.3.1 Electrochemical Charaterization of Immobilized Cytochrome *c*

Characteristic cyclic voltammograms for cytochrome *c* immobilized on a mixed $C_{15}COOH/C_{14}OH$ (50/50) SAM are shown in Figure 5.2A. At the scan rate (SR) of 25 mV/s, the voltammogram has a Full Width at Half Maximum (FWHM) of 96 mV, which is close to the value for a reversible redox couple is 90.6 mV. At this scan rate, the voltammogram is symmetric with a peak-to-peak separation ($E_{p,a} - E_{p,c}$) of 12 mV. These results indicate that the electron transfer reaction of cytochrome *c* on this type of surface is quasi-reversible. From Figure 5.2A, it is evident that the peak separation in the voltammograms increases with the increase of the scan rate. The peak separation as a function of scan rate can be predicted by Marcus theory,[56,57] or by the Butler-Volmer model.[58] By fitting these models to the experimental peak separations, the standard electron transfer rate constant k^0 can be extracted. Figure 5.2B shows a fit of the Marcus theory to the peak-to-peak separation as a function of scan rate for the same system shown in Figure 5.2A, where the E^0 represents the formal potential of the redox species.

The theory reproduces the data for a reorganization energy of 0.4 eV, a literature value,[33,35] and a k^0 of 2.5 s^{-1}.

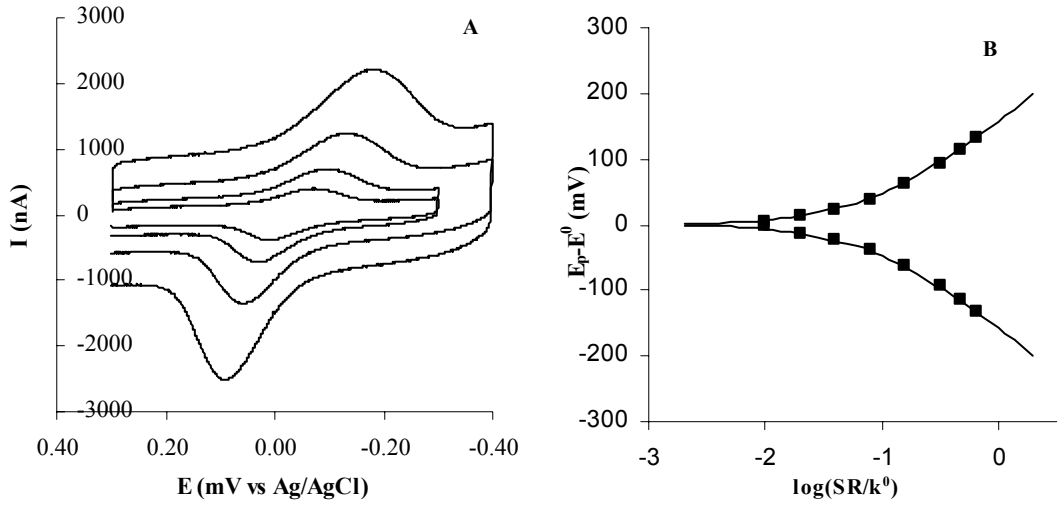

Figure 5. 2 A) Cyclic voltammograms of cytochrome *c* on mixed $C_{15}COOH/C_{14}OH$ (50/50) SAM, collected at scan rates of 25, 200, 400, 800, 1600 mV/s. B) Fitting of experimental peak separations (squares) by the Marcus theory (solid curves). The fitting yields a rate constant k^O of 2.5 s^{-1}.

The electron transfer of cytochrome *c* on other mixed carboxyl/hydroxyl SAM films was studied in the same way. The range of scan rate used for collecting cyclic voltammograms was adjusted according to the k^0 of that assembly, which is suggested by plotting the ratio of scan rate to k^0 in the abscissa of Figure 5.2B. A larger value of k^0 requires a faster scan rate to obtain a peak-to-peak separation larger that 300 mV. The consistently good fit of the theory to experimental data indicates the reliability of the measured k^0.

Characteristic cyclic voltammograms for cytochrome *c* immobilized on a mixed PyC_{16}/C_{11} SAM are shown in Figure 5.3A. The cyclic voltammograms at the lowest measured scan rate of 1 V/s are broadened. The voltammogram at 1 V/s is slightly asymmetric with a

FWHM of 102 mV and a peak separation of 50 mV. The experimental data at different scan rates does not fit simultaneously to one theoretical curve as shown in Figure 5.3B. In this case, each scan rate was fitted to generate a k^0 value, and the average rate constant was taken over all scan rates and reported. The typical relative standard deviation was around 40%. The k^0 for voltammograms shown in Figure 5.3A by the fitting is 300 ± 120 s^{-1}.

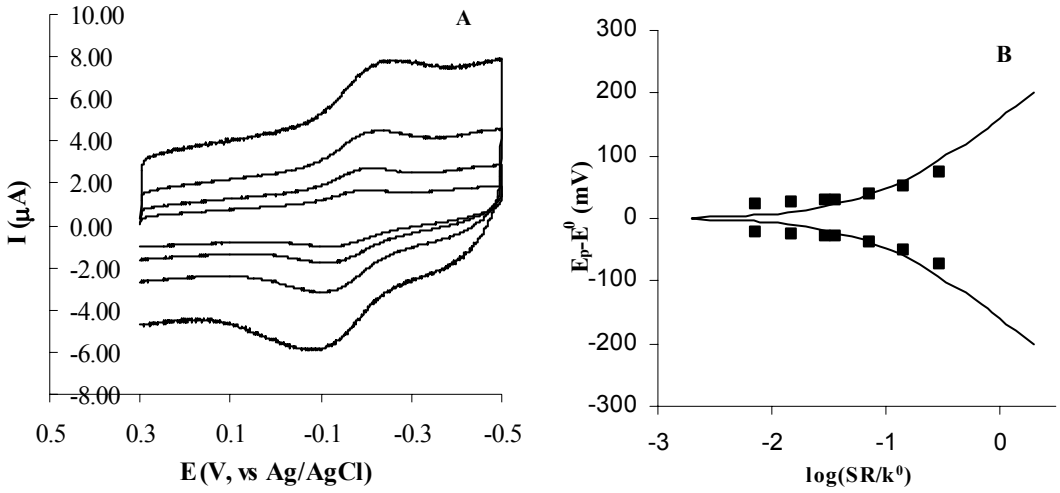

Figure 5. 3 A) Cyclic voltammograms of cytochrome *c* on on $PyC_{16}/C_{11}OH$ SAM, collected at scan rates of 1, 10, 20, 40, 80 V/s. B) Fitting of experimental peak separation (squares) by the Marcus theory (solid curves). The fitting yields a rate constant k^O of 300 s^{-1}.

The broad voltammogram and the reduced quality of fitting for this system should be contrasted with the really ideal behavior of PyC16/C15 voltammetry reported earlier.[33,35] It may be that the large difference in the chain length of the two components of PyC_{16}/C_{11} SAM causes a poorly defined or broad distribution of cytochrome *c* on the surface. Assuming that the SAM contains 10% long chain pyridine thiol and 90% short chain alkanethiol, it is reasonable to expect that cytochrome *c* molecules exist in a wide distribution of geometries with respect to the SAM/electrode surface. Even though the rate constants have a large uncertainty, they compare

well to the values obtained earlier from mixed SAMs of pyridine thiol and a diluent thiol that is only one methylene group shorter.[33,35]

5.3.2 The Formal Potential of Cytochrome *c* versus SAM Charge Density

The electrochemical reaction of cytochrome *c* on the mixed carboxyl/hydroxyl SAMs is quasireversible at a slow scan rate, 25 mV/s, and the voltammogram is symmetric with a small peak separation. Hence the apparent formal potential of cytochrome *c* was determined by taking the average of the anodic and cathodic peak potentials of the voltammogram at the slow scan rate. The SAMs were deposited onto gold electrodes from thiol solutions in which the $C_{15}COOH$ content was systematically increased form 10 % to 100%, while the total thiol content was kept constant. The monolayer modified gold electrodes were used to immobilize cytochrome *c* and the formal potential of the protein was studied as a function of the SAM composition using the cyclic voltammetry.

Figure 5.4 shows the dependence of the formal potential of cytochrome *c* on the surface composition of the mixed carboxyl/hydroxyl SAM films. The actual surface composition of the mixed SAM is difficult to measure, as is its morphology. Although some surface characterization methods have been tried, they have not succeeded yet. Consequently, the SAM composition in Figure 5.4 is given as that in the thiol solution used for the SAM deposition, similar to an earlier work.[46] For convenience the term SAM composition or surface content is used instead of "the thiol composition of the solution used for SAM growth" in the following text.

As shown in Figure 5.4, the formal potential of cytochrome *c* decreases systematically with increase of the surface content of $C_{15}COOH$, for the mixed $C_{15}COOH/C_{14}OH$, $C_{15}COOH/C_{11}OH$ and $C_{15}COOH/C_8OH$ SAM films. Taking into account the experimental error,

the three curves overlap with each other. For the pure $C_{15}COOH$ SAM, the formal potential is about 190 mV vs NHE comparable to the value reported earlier.[22] When the surface content of $C_{15}COOH$ decreases to 10% and the surface content of C_nOH increase to 90%, no matter what the value of n, the formal potential of cytochrome *c* systematically increases to a value of 240 mV. Hence it approaches the value 265 mV vs. NHE for cytochrome *c* in solution at pH 7.[59] The formal potential varies faster when the content of $C_{15}COOH$ is below 50%.

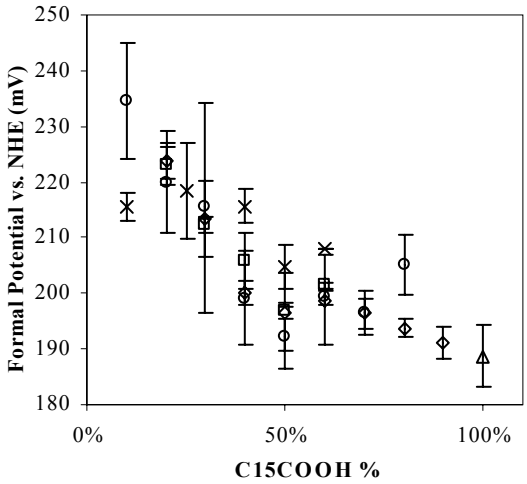

Figure 5. 4 The formal potential of cytochrome *c* plotted as a function composition of the solution used for SAM growth. Circles represent the data for mixed $C_{15}COOH/C_8OH$ SAM, diamonds for mixed $C_{15}COOH/C_{11}OH$ SAM, squares for mixed $C_{15}COOH/C_{14}OH$, crosses for mixed $C_{15}COOH/C_{16}OH$ and the triangle represent data on pure $C_{15}COOH$ SAM.[22]

For mixed $C_{15}COOH/C_{16}OH$, the trend is similar but the formal potentials are more positive and the increase in not as noticeable (curve is shallower). The formal potentials for this mixed SAM were obtained from voltammograms collected at 20 mV/s because of the slow electron transfer rate. A smaller change in formal potential is reasonable considering that the OH groups can H-bond with the COOH groups at the long chain lengths therefore decreasing the net

negative charge at the electrode surface. This would be supported by the more positive formal potentials as well.

Horse heart cytochrome *c* adsorbs weakly (or not at all) on pure hydroxyl-terminated SAM and coatings rich in hydroxyl groups are employed to prevent the adsorption of proteins.[59] Although some reports of the immobilization of cytochrome *c* with pure hydroxyl-terminated SAM exist in literature,[60] other reports indicate that it inhibits adsorption.[61,62] For the protocol used here (see the experimental section) no signal from cytochrome *c* could be detected on pure hydroxyl-terminated SAMs after rinsing with buffer. Therefore, the binding of cytochrome *c* in the current study can be unambiguously attributed to the electrostatic interactions, which originate from the carboxylic acid-terminated portion of surface.

The negative shift of the cytochrome *c* formal potential upon binding to a negatively charged surface has been experimentally established in mitochondria[1,63,64] and in SAM systems.[65-67] It has been attributed to the the differential adsorption strength of the two redox forms of cytochrome *c*.[65-67] A qualitative relationship between the formal potential shift and the difference of adsorption free energy is shown in Scheme 5.2. The formal potential difference for cytochrome *c* in solution versus in the adsorbed state is related to the Gibbs energy difference by $\Delta G_s - \Delta G_b = -nF(E_s^0 - E_b^0)$, where the subscripts *s* and *b* represent the quantity for solution phase and the adsorbed (bound) state respectively. This relation can be written as $-nF(E_s^0 - E_b^0) = \Delta G_o - \Delta G_r$, where ΔG_o is the Gibbs energy for adsorption of the oxidized form and ΔG_r is the Gibbs energy for adsorption of the reduced form. According to the latter equation, a negative shift of the formal potential for the surface bound state indicates a more negative ΔG_o than ΔG_r i.e. stronger adsorption strength for the oxidized state than the reduced state. This conclusion has been supported by a recent desorption study of cytochrome *c*

immobilized on a carboxylic acid-terminated SAM. It was found that it takes much longer for the oxidized cytochrome *c* to desorb from the negatively charged surface.[68]

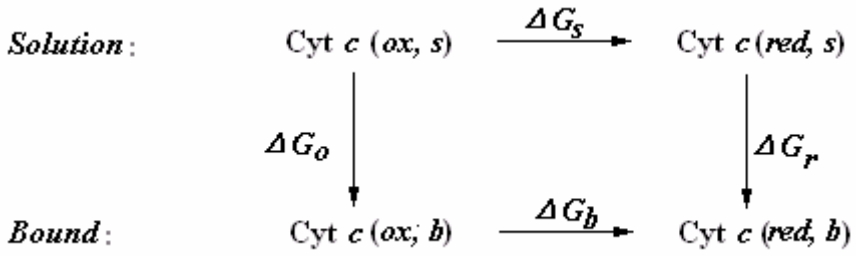

Scheme 5. 2 The thermodynamic cycle shows the relationship between the redox Gibbs energies and the binding Gibbs energies of the oxidized and reduced cytochrome *c*.

From the above reasoning, it follows that a lower negative charge density leads to a weaker oxidized cytochrome *c*/ SAM interaction and a less negative shift in the formal potential because of the electrostatic nature of the interaction. This prediction is consistent with the observed formal potential as a function of surface $C_{15}COOH$ content shown in Figure 5.4. A lower surface content of $C_{15}COOH$ gives rise to a lower negative charge density and hence a formal potential closer to that found in the solution phase. The carboxylic acid group (–COOH) is a weak acid, so that decreasing the surface content of –COOH does not initially lead to a dramatic decrease of surface charge density, if the surface content is high, because a large fraction of the –COOH groups are not ionized because of hydrogen bonding networks.[69] When the surface content of $C_{15}COOH$ is comparatively low, the fraction of –COOH group that are ionized is higher. Under these lower –COOH coverage conditions (less than 50%), the decrease in charge density caused by reducing the amount of acid content cannot be compensated by increasing the fraction of ionization, therefore a fast change of formal potential appears on the left half of the plot (Figure 5.4). For the case of $C_{15}COOH/C_{16}OH$, the two SAM components have similar chain length. The –OH terminal groups may hydrogen bond with the –COOH

decreasing the surface negative charge density. The more positive formal potentials and attenuated change over the varying percentage of COOH support this interpretation.

In summary, the observed dependence of cytochrome *c* formal potential on the surface carboxylic acid content is consistent with the protein adsorption depending on the negative charge density on the electrode surface. Two important implications of this analysis are a) the cytochrome *c* molecule is bound by multiple carboxylate groups, otherwise the absorption strength would be independent of the charge density of the surface (calculated ~15 COOH for 50/50 mixture); b) although no direct characterization of the mixed carboxylic/hydroxyl SAM was successfully performed, the solution $C_{15}COOH$ content appears to correlate roughly with the surface $C_{15}COOH$ content of the SAM grown in the solution.

5.3.3 Impact of SAM Composition on k^0 of Cytochrome *c*

As a comparison, k^0 of cytochrome *c* on $C_{15}COOH/C_{11}CH_3$ was measured at varying percentages of $C_{15}COOH$ surface content (data not shown) and only a slight enhancement of the electron transfer was found (0.22 s^{-1} for pure COOH compared to 0.44 s^{-1} for 50% and 0.41 s^{-1} for 30% COOH). No cytochrome *c* response was obtained for $–CH_3$ diluent monolayers with 20 and 10% -COOH. This data is comparable to the enhancements published by Holt[49] where a slight increase was observed with 50/50 films of $C_{11}COOH/C_9CH_3$ compared to pure COOH films. The enhancement rate constant for $C_{15}COOH/C_{11}OH$ in Figure 5.5 is much more dramatic increasing from 0.2 to over 20 s^{-1}. The methyl terminated films seem to have less enhancement of the electron transfer; however, if the changes in electron transfer rate constant were due solely to charge density changes, the CH_3 terminated and OH terminated diluent thiols should behavior similarly. Since the methyl group produces more of a blocking SAM for electron transfer the tunneling of electrons through the –OH terminated thiols is supported.

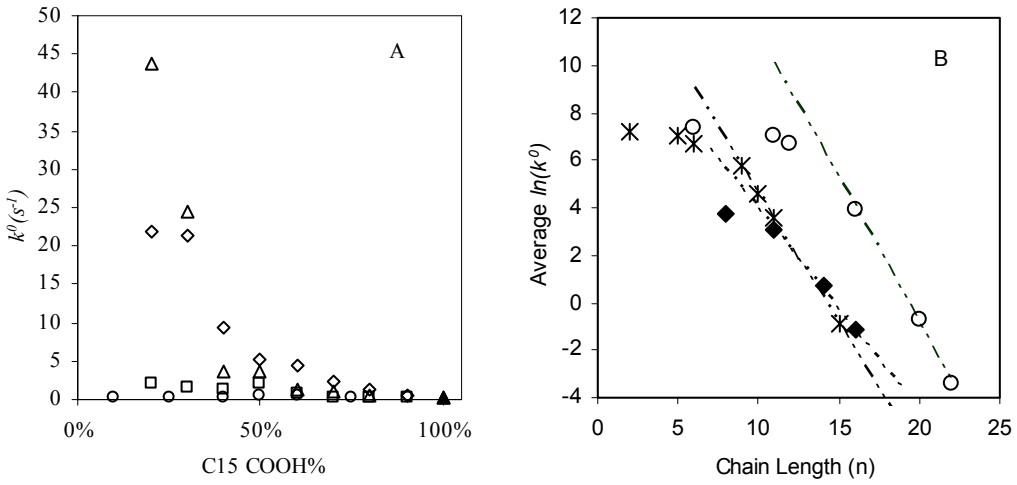

Figure 5. 5 A) Rate constant k^0 of cytochrome *c* as a function of monolayer composition. Circles are data for mixed $C_{15}COOH/C_8OH$ SAM, diamonds for mixed $C_{15}COOH/C_{11}OH$ SAM, squares for mixed $C_{15}COOH/C_{14}OH$ SAM, stars for mixed $C_{15}COOH/C_{16}OH$ SAM and the triangle represent data on pure $C_{15}COOH$ SAM.[22] B) $\ln(k^0)$ of cytochrome *c* versus the number of methylene groups. Diamonds are for mixed SAM containing 20% $C_{15}COOH$ as a function of the diluent chain length from this work; crosses are from [25] and [34] for pure COOH, Circles are from [27,33] for PyC_n/C_{n-1}.

For the same surface content of diluent molecule, the rate constant increases as the chain length of the diluent decreases. As show in Figure 4.4B, the value of k^0 decays exponentially as the diluent chain length increases with a decay constant $\beta = 0.85$ per $-CH_2-$ group, in the case where the surface content of diluent is 20%. In the same figure, the rate constant of cytochrome *c* on pure COOH SAM is also plotted versus the chain length of carboxylic acid-terminated SAM. The decay constant in this plot has a value of 1.1 per$-CH_2-$ group in this case.[25,34] The two lines cross each other with a slight variation in their slopes, indicating that the electron tunneling distance through the mixed SAM is very close to the chain length of the diluent molecules; i.e. the diluent molecule is part of the electron tunneling pathway. When the methylene chain length

is eight, the k^0 is below the line. The lower k^0 value most likely indicates a longer electron tunneling distance because n = 8 is still in the tunneling region.[25,34]

5.3.4 Dependence of k^0 on the Chain Length of the Diluent Thiol Molecule for PyC_{16}/C_{11} System

To see whether the same effect appears in the pyridine SAM system, cytochrome *c* was immobilized with PyC_{16}/C_{11} SAM and the electron transfer reaction was studied. The experimental k^0 values are listed in Table 5.1 with the k^0 of cytochrome *c* immobilized on PyC_{16}/C_{15} SAM and PyC_{12}/C_{11} SAMs.[22,35] Decreasing the chain length of diluent thiol from 15 methylene groups to 11 methylene groups, increases the rate constant almost 20 times. The average experimental rate constant for PyC_{16}/C_{11} SAM approaches the value on a PyC_{12}/C_{11} SAM coated surface, but is a factor of two lower

The experimental k^0 data for the PyC_{16}/C_{11}system has a large standard deviation of 460 s^{-1}. In contrast, the formal potential measured simultaneously shows a small standard deviation of 4 mV, with an average of - 0.157 V vs. Ag/AgCl 1M KCl (Table 5.1), which is comparable to that reported for the other pyridine systems.[22,35] This precision for the formal potential measurement indicates that the heme environment of cytochrome *c* is not significantly different in the two cases. If the large standard deviation in k^0 cannot be attributed to the variation of cytochrome *c* structure, then it must result from variation in the heme distance from the surface. In the PyC_{16}/C_{11} SAM, PyC_{16} is much longer than the C_{11} molecule. This might cause a rearrangement of the PyC_{16} molecule and the cytochrome *c* on the film to shorten the tunneling distance. In this case the tunneling proceeds mostly through the diluent thiol, giving a rate constant that is comparable to that on PyC_{12}/C_{11} SAM. The broad distribution of orientations and distances of cytochrome *c* molecules with respect to the SAM surface causes a broad range of k^0

values, hence a large uncertainty in k^0. It appears that the electron transfer kinetics falls into the turnover region that connects the tunneling region to a friction controlled one.[33,35]

Table 5. 1 The k^0 on Pyridine SAM

	k^0 (s^{-1})	σ_{k0} (s^{-1})	$E^{0'}$ (mV) (vs Ag/AgCl)	$\sigma_{E0'}$ (mV)
PyC_{16}/C_{11}	800	460	-157	4
* PyC_{16}/C_{15}	40	2	-165	13
# PyC_{12}/C_{11}	1700	100	-162	2

*: from reference 22, #: from reference 35; σ: the standard deviation of the measurements.

5.4 Conclusion

The consistent increase of k^0 as the diluent chain length decreases in mixed $C_{15}COOH/C_nOH$ SAM and mixed PyC_{16}/C_{11} SAM indicates an electron transfer pathway that is comprised of the diluent chain and spacer between cytochrome *c*, as schematically shown in Figure 5.6. The possibility of this kind of pathway is supported by studies on the electronic coupling mechanism inside the protein,[39,40,43,44] namely that the tunneling proceeds by multiple pathway and should be computed by an appropriate average over all possible tunneling pathways.[39] Even though the negatively charged carboxylic group interacts strongly with the protein, the electron transfer proceeds through the diluent thiol if a shorter tunneling distance is accessible.

On mixed carboxyl/hydroxyl SAM surfaces, cytochrome *c* has a faster electron transfer rate constant than on pure carboxylic acid SAMs. In both the carboxylic acid system and pyridine system, the rate constant of cytochrome *c* depends on the chain length of the thiol molecule that is believed to bind with cytochrome *c*, but may also depends on that of the diluent

molecules. This study shows that under the right condition (much shorter diluent), the diluent molecule can play an important part in the electron tunneling pathway.

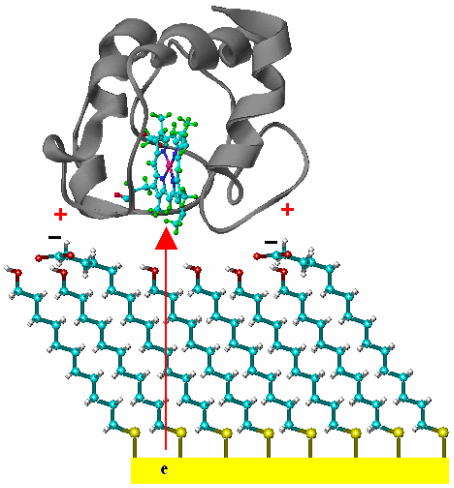

Figure 5. 6 The cartoon depicts an electron transfer pathway that proceeds through the diluent thiols.

5.5 Acknowledgements

This work has been supported by the U.S. National Science Foundation (CHE-0415457).

References

(1) Pettigrew, G. W.; Moore, G. R. *cytochromes c: Biological Aspects*; Springer-Berlag: Berlin, Heidelberg, New York, London, Paris, Tokyo, 1987.

(2) Beissenhirts, M. K.; Scheller, F. W.; Lisdat, F. *Anal. Chem.* **2004**, *76*, 4665-4671.

(3) Dai, Z.; Liu, S.; Ju, H. *Electrochimica Acta* **2004**, *49* 2139-2144.

(4) Cheddar, G.; Meyer, T. E.; Cusanovich, M. A.; Stout, C. D.; Tollin, G. *Biochemistry* **1986**, *25*, 6502-7.

(5) Cheddar, G.; Meyer, T. E.; Cusanovich, M. A.; Stout, C. D.; Tollin, G. *Biochemistry* **1989**, *28*, 6318-22.

(6) Goldkorn, T.; Schejter, A. *J. Biol. Chem.* **1979**, *254*, 12562-12566.

(7) Hazzard, J. T.; McLendon, G.; Cusanovich, M. A.; Tollin, G. *Biochem. & Biophys. Res. Comm.* **1988**, *151*, 429-34.

(8) Meyer, T. E.; Rivera, M.; Walker, F. A.; Mauk, M. R.; Mauk, A. G.; Cusanovich, M. A.; Tollin, G. *Biochemistry* **1993**, *32*, 622-7.

(9) Northrup, S. H.; Thomasson, K. A.; Miller, C. M.; Barker, P. D.; Eltis, L. D.; Guillemette, J. G.; Mauk, A. G.; Inglis, S. C. *Biochemistry* **1993**, *32*, 6613-23.

(10) Nuevo, M. R.; Chu, H. H.; Vitello, L. B.; Erman, J. E. *J. Am. Chem. Soc.* **1993**, *115*, 5873-4.

(11) Pan, L. P.; Frame, M.; Durham, B.; Davis, D.; Millett, F. *Biochemistry* **1990**, *29*, 3231-6.

(12) Pan, L. P.; Hibdon, S.; Liu, R. Q.; Durham, B.; Millett, F. *Biochemistry* **1993**, *32*, 8492-8.

(13) Prudencio, M.; Ubbink, M. *J. Mol. Recog.* **2004**, *17*, 524-539.

(14) Cunha, C. A.; Romao, M. J.; Sadeghi, S. J.; Valetti, F.; Gilardi, G.; Soares, C. M. *J. Biol. Inorg. Chem.* **1999**, *4*, 360-374.

(15) Brautigan, D. L.; Ferguson-Miller, S.; Margoliash, E. *J. Biol. Chem.* **1978**, *253*, 130-139.

(16) Brautigan, D. L.; Ferguson-Miller, S.; Tarr, G. E.; Margoliash, E. *J. Biol. Chem.* **1978**, *253*, 140-148.

(17) Ferguson-Miller, S.; Brautigan, D. L.; Margoliash, E. *J. Biol. Chem.* **1978**, *253*, 149-159.

(18) Barlow, G. H.; Margoliash, E. *J. Biol. Chem.* **1966**, *241*, 1473-1477.

(19) Kang, C. H.; Brautigan, D. L.; Osheroff, N.; Margoliash, E. *J. Biol. Chem.* **1978**, *253* 6502-6510.

(20) Liang, Z. X.; Nocek, J. M.; Huang, K.; Hayes, R. T.; Kurnikov, I. V.; Beratan, D. N.; Hoffman, B. M. *J. Am. Chem. Soc.* **2002**, *124*, 6849-6859.

(21) Liang, Z. X.; Jiang, M.; Ning, Q.; Hoffman, B. M. *J. Biol. Inorg. Chem.* **2002**, *7*, 580-588.

(22) Yue, H.; Waldeck, D. H.; Petrovic, J.; Clark, R. A. *J. Phys. Chem. B* **2006**, *110*, 5062-5072.

(23) Yue, H.; Waldeck, D. H. *Curr.t Opinion Solid State & Mater. Sci.* **2006**, *9*, 28-36.

(24) Wei, J.; Liu, H.; Dick Allison, R.; Yamamoto, H.; He, Y.; Waldeck David, H. *J. Am. Chem. Soc.* **2002**, *124*, 9591-9.

(25) Avila, A.; Gregory, B. W.; Niki, K.; Cotton, T. M. *J. phys. Chem. B* **2000**, *104*, 2759-2766.

(26) Rivas, L.; Murgida, D. H.; Hildebrandt, P. *J. Biol. Inorg. Chem.***2001**, *86*, 402-402.

(27) Wei, J.; Liu, H.; Khoshtariya, D. E.; Yamamoto, H.; Dick, A.; Waldeck, D. H. *Angewandte Chemie, Internatl. Ed.* **2002**, *41*, 4700-4703.

(28) Niki, K.; Hardy, W. R.; Hill, M. G.; Li, H.; Sprinkle, J. R.; Margoliash, E.; Fujita, K.; Tanimura, R.; Nakamura, N.; Ohno, H.; Richards, J. H.; Gray, H. B. *J. phys. Chem. B* **2003**, *107*, 9947-9949.

(29) Wei, J. J.; Liu, H. Y.; Niki, K.; Margolish, E.; Waldeck David, H. *J. phys. Chem., B.* **2004**, *108* 16912-16917.

(30) Leopold, M. C.; Bowden, E. F. *Langmuir* **2002**, *18*, 2239-2245.

(31) El Kasmi, A.; Wallace, J. M.; Bowden, E. F.; Binet, S. M.; Linderman, R. J. *J. Am. Chem. Soc.* **1998**, *120*, 225-226.

(32) Collinson, M.; Bowden, E. F.; Tarlow, M. J. *Langmuir* **1992**, *8*, 1274-50.

(33) Wei, J.; Liu, H.; Dick Allison, R.; Yamamoto, H.; He, Y.; Waldeck David, H. *J. Am. Chem. Soc.* **2002**, *124*, 9591-9599.

(34) Song, S.; Clark, R. A.; Bowden, E. F.; Tarlov, M. J. *J. phys. Chem.* **1993**, *97*, 6564-6572.

(35) Yue, H.; Khoshtariya, D.; Waldeck, D. H.; Grochol, J.; Hildebrandt, P.; Murgida, D. H. *J. phys. Chem. B* **2006**, *110*, 19906-19913.

(36) Wackerbarth, H.; Hildebrandt, P. *Chemphyschem* **2003**, *4*, 714-724.

(37) Murgida, D. H.; Hildebrandt, P. *J. phys. Chem. B* **2002**, *106*, 12814-12819.

(38) Hildebrandt, P.; Murgida, D. H. *Bioelectrochem.* **2002**, *55*, 139-143.

(39) Jones, M. L.; Kurnikov, I. V.; Beratan, D. N. *J. Phys. Chem. A* **2002**, *106*, 2002-2006.

(40) Lin, J.; Balabin, I.; Beratan, D. N. *Science* **2005**, *310*, 1311-1313.

(41) Newton, M. D. *Chem.l Rev.s* **1991**, *91*, 767-792.

(42) Ratner *J. Phys. Chem.* **1990**, *94*, 4877-4883.

(43) Winkler, J. R.; Di Bilio, A. J.; Farrow, N. A.; Richards, J. H.; Gray, H. B. *Pure Appl. Chem.* **1999**, *71*, 1753-1764.

(44) Gray, H. B.; Winkler, J. R. *Annu. Rev. Biochem.* **1996**, *65*, 537-561.

(45) Napper, A. M.; Liu, H.; Waldeck, D. H. *J. phys. Chem. B* **2001**, *105*, 7699-7707.

(46) Arnold, S.; Feng, Z. Q.; Kakiuchi, T.; Knoll, W.; Niki, K. *J. Electroanal. Chem.y* **1997**, *438*, 91-97.

(47) Summer, J. J.; Creager, S. E. *J. Am. Chem. Soc.* **2000**, *122*, 11914-11920.

(48) Dolidze, T. D.; Rondinini, S.; Vertova, A.; Waldeck, D., H. **2007**.

(49) Holt, K. B. *Langmuir* **2006**, *22*, 4298-4304.

(50) Chen, X.; Ferrigno, R.; Yang, J.; Whitesides, G. M. *Langmuir* **2002**, *18*, 7009-7015.

(51) Du, Y.-Z.; Saavedra, S. S. *Langmuir* **2003**, *19*, 6443-6448.

(52) Wei, J. J.; Liu, H. Y.; Dick, A. R.; Yamamoto, H.; He, Y. F.; Waldeck, D. H. *J. Am. Chem. Soc.* **2002**, *124*, 9591-9599.

(53) Clark, R. A.; Bowden, E. F. *Abstracts Of Papers Of ACS* **1994**, *208*, 132-COLL.

(54) Willit, J. L.; Bowden, E. F. *J.Phys.Chem.* **1990**, *94*, 8241-46.

(55) Girlanda-Junges, C.; Keyling-Bilger, F.; Schmitt, G.; Luu, B. *Tetrahedron* **1998**, *54*, 7735-7748.

(56) Napper, A. M.; Liu, H. Y.; Waldeck, D. H. *J. phys. Chem. B* **2001**, *105*, 7699-7707.

(57) Chidsey, C. E. D. *Science* **1991**, *252*, 919-922.

(58) Laviron, E. *J. Electroanal. Chem.* **1979**, *101*, 19-28.

(59) Fedurco, M. *Coord. Chem.. Rev.* **2000**, *209*, 263-331.

(60) Gavioli, G.; Borsari, M.; Cannio, M.; Ranieri, A.; Volponi, G. *J. Electroanal. Chem.* **2004**, *564*, 45-52.

(61) Terrettaz, S.; Cheng, J.; Miller, C. J.; Guiles, R. D. *J. Am. Chem. Soc.* **1996**, *118*, 7857-7858.

(62) Murgida, D. H.; Hildebrandt, P. *J. phys. Chem. B* **2001**, *105*, 1578-1586.

(63) Osheroff, N.; Brautigan, D. L.; Margoliash, E. *Proc. Natl. Acad. Sci* **1980**, *77*, 4439-4443.

(64) Margalit, R.; Schejter, A. *European Journal of Biochemistry* **1973**, *32*.

(65) Kasmi, E. A.; Wallace, J. M.; Bowden, E. F.; Binet, S. M.; Linderman, R. J. *J. Am. Chem. Soc.* **1998**, *120*, 225-226.

(66) Dick, L. A.; Haes, A. J.; Van Duyne, R. P. *J. phys. Chem. B* **2000**, *104*.

(67) Bard, A. J.; Faulkner, L. R. *Electrochemical Methods*; 2nd Edition ed.; John Wiley & Sons, Inc.: New York, Chichester, Weiheim, Brisbane, Singapore, Toronto, 2001.

(68) Petrovic, J.; Clark, R. A.; Yue, H.; Waldeck, D. H.; Bowden, E. F. *Langmuir* **2005**, *21*, 6308-6316.

(69) Creager, S. E.; Clarke, J. *Langmuir* **1994**, *10*, 3675-3683.

PART II CONJUGATED POLYELECTROLYTE/SURFACTANT COMPLEXES STUDIED BY FLUORESCENCE CORRELATION SPECTROSCOPY

Abstract

Poly (phenylethynylene) (PPE) based conjugated polyelectrolytes are a class of polyions having rigid backbones. We present an fluorescence correlation spectroscopy (FCS) study on the hydrodynamic properties of complexes formed by two PPE-SO_3^- polymers, having different charge density, with octadecyl trimethylammoniumbromide (OTAB) below the critical micelle concentration. The concentration ratio C_{OTAB} /$C_{monomer}$ ranges from 0.2 to 1800 in this work. The hydrodynamic radius of the complexes as a function of OTAB concentration has three regimes. In the low concentration regime, (C_{OTAB} /$C_{monomer}$ < 6), the complex has a comparable size with the polymer in deionized water. In the intermediate concentration regime (6 <C_{OTAB} /$C_{monomer}$ < 400) the complexes have the largest size and substantial heterogeneity. In the high concentration regime (400 <C_{OTAB} /$C_{monomer}$ < 1800), the complexes have a size that is about three times larger than that in the low concentration regime. The results significantly extend the understanding of the interaction between polyelectrolyte and ionic surfactant, and indicate that the rigidity of polymer backbone and C_{OTAB} /$C_{monomer}$ concentration ratio act to determine the composition of polyelectrolyte/surfactant complexes.

CHAPTER 6 INTRODUCTION

Fluorescence Correlation Spectroscopy (FCS) is a non-invasive method that provides dynamic and kinetic information by following the fluorescence fluctuation trajectory of fluorescence near the equilibrium state.[1-4] The autocorrelation function or cross-correlation function of the fluctuations contains information about the diffusion and photophysical and photochemical processes.[4]

6.1 The General Formulism of Autocorrelation Function for FCS

In steady state fluorescence measurements, the size of the excitation volume is typically of milliliter scale, and the fluorphore concentration is of micromolar scale. In the excitation volume, the average number of fluorophore molecules is on the order of 10^{14}. From this large number of molecules, the measurement yields an ensemble average of the system. However in FCS, the excitation volume is of femtoliter scale and the concentration of the fluorophore is of nanomolar scale. Under these conditions, the average number of fluorophore in the excitation volume is from 1 to a few tens. At equilibrium, the analyte molecules constantly diffuse into and out of the excitation volume, which causes a fluctuation in the instantaneous molecule number in the illumination volume. In addition, it is also possible that there is chemical reaction at equilibrium which changes the fluorescence properties of the fluorophore, such as singlet-triplet conversion and isomerization. The chemical reactions and diffusion cause the fluctuation in the instantaneous fluorescence photon counts *n(t)* as shown in Figure 6.1. The kinetic properties of

these physical and chemical processes can be revealed by the autocorrelation function calculated form the fluctuation. In what follows the general analytical form of the autocorrelation function is deduced based on the work of Krichevsky *et. al.*[4] to draw a relationship between the fluctuations and the kinetic properties of the chemical and physical processes.

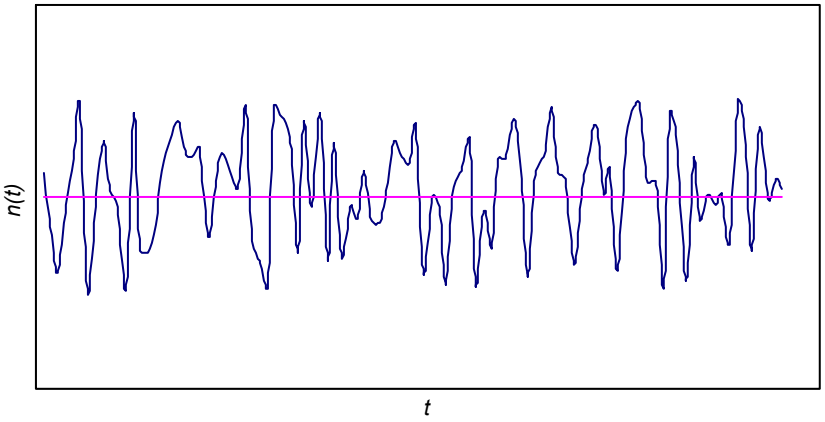

Figure 6. 1 Fluctuation of fluorescence photon counts generated from a small number of molecules. The pink line is the average photon counts.

The autocorrelation function is defined as $G(\tau)=\frac{1}{\bar{n}^2}\langle \delta n(0)\cdot \delta n(\tau)\rangle$, where n is the photon counts. $\delta n(t)=n(t)-\bar{n}=\Delta t\int d^3r\left[I(r)\cdot\sum_{k=1}^{m}Q_k\cdot\delta C_k(r,t)\right]$ is the fluctuation in the photon counts for a system comprised of multiple components; Q_k is the product of the absorption cross section with the fluorescence quantum yield and the efficiency of fluorescence detection for the component k; and $n(t)=\Delta t\int d^3r\left[I(r)\cdot\sum_{k=1}^{m}Q_k\cdot C_k(r,t)\right]$. $C_j(r,t)$ is the local concentration at time t, which have an ensemble average concentration of $\bar{C}_j=\langle C_j(r,t)\rangle$. The local concentration deviation is defined as $\delta C_j=C_j(r,t)-\bar{C}_j$.

$$G(\tau)=\frac{(\Delta t)^2}{\bar{n}^2}\int d^3r\int d^3r'\left[I(r)\cdot I(r')\cdot\sum_{j,k}Q_j\cdot Q_l\cdot\left\langle\delta C_j(r,0)\delta C_k(r',\tau)\right\rangle\right] \tag{6.1}$$

where $\delta C_j(r,0)$ is the initial condition; $\delta C_j(r,t)$ is the local fluctuation; *I(r)* is the spatial distribution of the excitation light; and $\left\langle\delta C_j(r,0)\delta C_l(r',t)\right\rangle$ is the concentration correlation function.

$\delta C_j(r,t)$ is obtained by solving the relaxation equation for δC_j

$$\frac{\partial\delta C_j(r,t)}{\partial t}=D_j\nabla^2\delta C_j(r,t)+\sum_{k=1}^{m}K_{jk}\cdot\delta C_j(r,t) \tag{6.2}$$

where the first term describes isotropic diffusion of component *j*; the second term describes equilibrium between component *j* and other components that have different fluorescence properties than *j*. Applying a Fourier transform to equation 6.2 yields

$$\frac{d\widetilde{C}_j(q,t)}{dt}=\sum_{k=1}^{m}M_{jk}\cdot\widetilde{C}_k(q,t) \tag{6.3}$$

where $\widetilde{C}_j(q,t)=\frac{1}{(2\pi)^{3/2}}\int d^3r\left[e^{iqr}\delta C_j(r,t)\right]$ is the Fourier transform of $\delta C_j(r,t)$; and $M_{jk}=K_{jk}-D_jq^2\delta_{jk}$. Knowing the eigenvalues $\lambda^{(s)}$ and eigenvectors $X^{(s)}$ of matrix *M*, the standard form of the solution is

$$\widetilde{C}_j(q,t)=\sum_{s=1}^{m}X_j^{(s)}h_s\exp(\lambda^{(s)}t) \tag{6.4}$$

The expression for the coefficient $h_s=\sum_{s=1}^{m}\left(X^{-1}\right)_k^{(s)}\overline{C}_k(q,0)$ can be obtained from the initial condition $\widetilde{C}_j(q,0)=\sum_{s=1}^{m}X_j^{(s)}h_s$, So that equation 6.4 may be written as

$$\widetilde{C}_j(q,t) = \sum_{s=1}^{m} X_j^{(s)} \exp(\lambda^{(s)} t) \sum_{s=1}^{m} \left(X^{-1}\right)_k^{(s)} \widetilde{C}_k(q,0) \tag{6.5}$$

From the initial condition and equation 6.5, the concentration correlation function can be derived as

$$\begin{aligned}
\left\langle \delta C_j(r,0)\delta C_l(r',t)\right\rangle &= \frac{1}{(2\pi)^{3/2}} \int d^3 q e^{-iqr'} \left\langle \delta C_j(r,0)\widetilde{C}_k(q,t)\right\rangle \\
&= \frac{1}{(2\pi)^{3/2}} \int d^3 q e^{-iqr'} \sum_{s=1}^{m} X_l^{(s)} \exp(\lambda^{(s)} t) \sum_{s=1}^{m} \left(X^{-1}\right)_k^{s} \left\langle \delta C_j(r,0)\widetilde{C}_k(q,0)\right\rangle \\
&= \frac{1}{(2\pi)^{3}} \int d^3 q e^{-iqr'} \sum_{s=1}^{m} X_{lj}^{(s)} \exp(\lambda^{(s)} t) \sum_{s=1}^{m} \left(X^{-1}\right)_k^{s} \int d^3 r'' e^{iqr''} \left\langle \delta C_j(r,0)\widetilde{C}_k(r'',0)\right\rangle \\
&= \frac{\overline{C}_j}{(2\pi)^{3}} \int d^3 q e^{-iqr'} \sum_{s=1}^{m} X_l^{(s)} \exp(\lambda^{(s)} t) \left(X^{-1}\right)_j^{s}
\end{aligned} \tag{6.6}$$

in which we applied the condition that $\left\langle \delta C_j(r,0)\delta C_l(r',t)\right\rangle = \overline{C}_j \delta_{jl} \delta(r-r')$, which means that the correlation length is much smaller that the distances between molecules; i.e. the positions of the different molecules of the same species as well as those of different species are not correlated.

Substituting equation 6.6 into 6.1, the autocorrelation function can be written as

$$G(\tau) = \frac{(\Delta t)^2}{\overline{n}^2} \int d^3 q \left[|I(q)|^2 \sum_{j,l} Q_j \cdot Q_l \cdot \overline{C}_j \cdot \sum_{s=1}^{m} X_l^{(s)} \cdot \exp(\lambda^{(s)} t) \left(X^{-1}\right)_j^{(s)} \right] \tag{6.7}$$

in which $\widetilde{I}(q) = \frac{1}{(2\pi)^{3/2}} \int d^3 r \left[e^{-iqr} I(r)\right]$ is the Fourier transform of the spatial intensity distribution, and $\overline{n} = \Delta t \int d^3 r \left[I(r) \cdot \sum_{k=1}^{m} Q_k \left\langle C_k(r,t)\right\rangle \right] = (2\pi)^{3/2} \widetilde{I}(0) \Delta t \sum_{k=1}^{m} Q_k \overline{C}_j$. For the confocal setup (see experimental section of Chapter 7) with a pinhole, the spatial illumination function can be approximated as

$$I(r) = I_0 \exp\left(-\frac{2\left(x^2 + y^2\right)}{\omega_{xy}^2} - \frac{2z^2}{\omega_z^2} \right) \tag{6.8}$$

The Fourier transform of equation 6.8 is

$$\begin{aligned} \tilde{I}(q) &= \frac{1}{(2\pi)^{3/2}} \int d^3 r \left\{ e^{-iqr} I_0 \exp\left(-\frac{2\left(x^2 + y^2\right)}{\omega_{xy}^2} - \frac{2z^2}{\omega_z^2} \right) \right\} \\ &= \frac{I_0 \omega_{xy}^2 \omega_z}{8} \exp\left(-\frac{\omega_{xy}^2}{8}\left(q_x^2 + q_y^2\right) - \frac{\omega_z^2}{8} q_z^2 \right) \end{aligned} \tag{6.9}$$

Combining equation 6.7 and 6.9, the autocorrelation function has the form

$$\begin{aligned} G(\tau) = & \frac{(2\pi)^{-3}}{\left(\sum Q_j \overline{C}_j\right)^2} \int d^3 q \left\{ \exp\left(-\frac{\omega_{xy}^2}{4}\left(q_x^2 + q_y^2\right) - \frac{\omega_z^2}{4} q_z^2 \right) \right\} \\ & \times \sum_{j,l} Q_j Q_l \overline{C}_j \sum_{s=1}^{m} X_l^{(s)} \exp(\lambda^{(s)} t) \left(X^{-1}\right)_j^{(s)} \end{aligned} \tag{6.10}$$

Equation 6.10 is the most general form of the autocorrelation function. It indicates that finding the autocorrelation function is equivalent to obtaining the M matrix, its eigenvalues and eigenvectors. In what follows, equation 6.10 is applied to two situations that are most common in the lab.

6.2 Diffusion of Single Species

A system containing only one diffusing species is the simplest FCS application. The relaxation function can be written as

$$\frac{\partial \delta C(r,t)}{\partial t} = D \nabla^2 \delta C(r,t) \tag{6.11}$$

The M matrix corresponding to equation 6.11 has only one element $M = -Dq^2$. The eigenvalue is $\lambda = -Dq^2$, and have the eigenvector is $X = 1$. By directly applying equation 6.10, the autocorrelation function can be written as

$$G(\tau)=\frac{(2\pi)^{-3}}{(Q\overline{C})^2}\int d^3q\left[Q^2\overline{C}\exp\left(-\frac{\omega_{xy}^2}{4}\left(q_x^2+q_y^2\right)-\frac{\omega_z^2}{4}q_z^2-Dt\left(q_x^2+q_y^2+q_z^2\right)\right)\right]$$
$$=\frac{1}{\overline{C}V}\left(1+\frac{\tau}{\tau_D}\right)^{-1}\left(1+\frac{\tau}{\omega^2\tau_D}\right)^{-1/2} \qquad (6.12)$$

where $\tau_D=\frac{\omega_{xy}^2}{4D}$ and $\omega=\frac{\omega_z}{\omega_{xy}}$.

From the very definition of the autocorrelation function, the multi-component autocorrelation function can be directly written as

$$G(\tau)=\frac{\left\langle\left(\sum n_i(0)\right)\left(\sum n_i(\tau)\right)\right\rangle}{\left(\sum n_i\right)^2}=\frac{\sum\langle n_i(0)n_i(\tau)\rangle}{\left(\sum n_i\right)^2}=\sum_i\frac{n_i^2}{\left(\sum n_i\right)^2}G_i(\tau) \qquad (6.13)$$

which is a linear combination of the autocorrelation function for single component diffusion

6.3 Isomerization

For a system that contains a fluorescent species in equilibrium with a non fluorescent species that has the same diffusion constant , the relaxation equation is written as

$$\frac{\partial\delta C_A}{\partial t}=D_A\nabla^2\delta C_A-k_{AB}\delta C_A+k_{BA}\delta C_B$$
$$\frac{\partial\delta C_B}{\partial t}=D_A\nabla^2\delta C_B+k_{AB}\delta C_A-k_{BA}\delta C_B \qquad 6.14)$$

The M matrix for equation 6.14 is written as

$$M=\begin{bmatrix}-\left(Dq^2-k_{AB}\right) & k_{BA}\\ k_{AB} & -\left(Dq^2-k_{BA}\right)\end{bmatrix} \qquad (6.15)$$

The eigenvalues for equation 6.15 are $-q^2D$ and $-q^2D-k_{AB}-k_{BA}$; the corresponding eigenvectors are $\begin{pmatrix}1\\K\end{pmatrix}$ and $\begin{pmatrix}1\\-1\end{pmatrix}$ respectively where $K=\frac{k_{AB}}{k_{BA}}$. The final autocorrelation function has the form

$$G(\tau) = \frac{1}{\overline{N}}\left(1+\frac{\tau}{\tau_D}\right)^{-1}\left(1+\frac{\tau}{\omega^2\tau_D}\right)^{-1/2}\left(1+K\exp\left(-\frac{\tau}{\tau_i}\right)\right) \quad (6.16)$$

where $\tau_i = \frac{1}{k_{AB}+k_{BA}}$. By fitting experimental autocorrelation function to equation 6.12, 6.13 and 6.16 the diffusion constant and chemical reaction rate constant can be determined.

6.4 Research Strategies

An FCS instrument was built from components and a used Zeiss IM35 microscope (the detail setup was described in the experimental section of Chapter 7), and it was used to study the hydrodynamic properties of complexes formed by two PPE-SO_3^- polymers, of different charge density, with OTAB below. The ratio C_{OTAB} /$C_{monomer}$ (C is in unit of M) ranges from 0.2 to 1800. The hydrodynamic radius of the complexes as a function of OTAB concentration shows three regimes. When C_{OTAB} /$C_{monomer}$ < 6, the complexes have comparable size with the polymer in DI water and are single strand substoichiometric complexes. When 6 <C_{OTAB} /$C_{monomer}$ < 400, a variety of complexes sizes are observed. These large complexes are comprised of multiple strands of stoichiometric complexes held together by the hydrophobic interactions of the alkyl chains in OTAB molecules. When 400 <C_{OTAB} /$C_{monomer}$ < 1800, the complexes are highly soluble and well defined in size, about three time larger than that in low concentration regime and much smaller than that in the intermediate regime. These complexes appear to have a single polymer chain binding with two layers of OTAB. The inner layer of OTAB interacts with PPE-SO_3^- through electrostatic forces and with the second layer of OTAB through the hydrophobic interactions. The outer layer of OTAB contacts the water with the ionic head groups. The complexes formed between PPE-SO_3^- and OTAB below the Critical Micelle Concentration (CMC) and the Critical Aggregation Concentration (CAC) as revealed by FCS, significantly

extends the understanding of the interaction between polyelectrolyte and ionic surfactant. The fact that the complex containing two layers of OTAB exists below the CMC indicates that the ratio C_{OTAB} /$C_{monomer}$ might be the controlling factor that determines the composition of polyelectrolyte/surfactant complexes.

References

(1) Koppel, D. E. *phys. Rev. A* **1974**, *10*, 1938-1945.

(2) Magde, D.; Elson, E.; Webb, W. W. *Phys. Rev. Lett.* **1972**, *29*, 705-708.

(3) *Fluorescence Correlation Spectroscopy, Theory and Applications*; Rigler, R.; Elson, E. S., Eds.; Springer, 2001.

(4) Krichevsky, O.; Bonnet, G. *Rep. Prog. Phys.* **2002**, *65*, 251-297.

CHAPTER 7 EVOLUTION IN THE COMPLEXES BETWEEN POLY (PHENYLETHYNYLENE) BASED POLYELECTROLYTES AND OCTADECYL TRIMETHYLAMMONIUMBROMIDE AS REVEALED BY FLUORESCENCE CORRELATION SPECTROSCOPY

Abstract

Poly (phenylethynylene) (PPE) based conjugated polyelectrolytes are a class of polyions having rigid backbones. We present an fluorescence correlation spectroscopy (FCS) study on the hydrodynamic properties of complexes formed by two PPE-SO_3^- polymers, having different charge density, with octadecyl trimethylammoniumbromide (OTAB) below the critical micelle concentration. The concentration ratio C_{OTAB} /$C_{monomer}$ ranges from 0.2 to 1800 in this work. The hydrodynamic radius of the complexes as a function of OTAB concentration has three regimes. In the low concentration regime, (C_{OTAB} /$C_{monomer}$ < 6), the complex has a comparable size with the polymer in deionized water. In the intermediate concentration regime (6 <C_{OTAB} /$C_{monomer}$ < 400) the complexes have the largest size and substantial heterogeneity. In the high concentration regime (400 <C_{OTAB} /$C_{monomer}$ < 1800), the complexes have a size that is about three times larger than that in the low concentration regime. The results significantly extend the understanding of the interaction between polyelectrolyte and ionic surfactant, and indicate that the rigidity of polymer backbone and C_{OTAB} /$C_{monomer}$ concentration ratio act to determine the composition of polyelectrolyte/surfactant complexes.

7.1 Introduction

Conjugated polymers have attracted extensive research interest because of their unique optical and electronic properties.[1-8] Poly (phenylethynylene) (PPE) responds to other solutes by a change of their fluorescence intensity and have been investigated as fluorescent sensory materials.[9-17] By side chain functionalization, their properties (hydrophobicity, polarity of charge, charge density, and the solubility) can be tailored for a particular purpose.[18-22] PPE is a linear semiflexible conjugated polymer,[23,24] which has a persistence length of 10 ~ 15 monomer units (consisting of one phenyl ring and one carbon-carbon triple bond),[25] and displays absorption and emission in the visible range.[8,19,20] The photophysical properties of functionalized PPE depends on the side chain configuration and the different solution conditions.[19,20,26,27] With certain hydrophobicity and charge properties of the side chain, the propensity of polymers to stay in single strands or aggregate in a particular solvent can be manipulated.[28]

This work reports on the hydrodynamic properties of two PPE-SO_3^- polymers with different charge densities in the presence of a cationic surfactant octadecyl trimethylammoniumbromide (OTAB). In particular, the high sensitivity of fluorescence correlation spectroscopy (FCS) is used to obtain hydrodynamic information about the complexes over a wide range of charge ratio of surfactant to polymer from 0.1 to 900. The interaction between polyelectrolytes and surfactants are an essential self-assembly motif and are important to industrial and biomedical applications.[29-36] Depending on the polyelectrolyte and surfactant properties, their concentrations, and solvent type, polyelectrolyte/surfactant complexes take a variety of morphologies, including single molecular substoichiometric complexes in aqueous solution,[37] stoichiometic complexes in nonaqueous solution,[31,37] polymer/micelle complexes,[34,38] vesicles, and liquid crystals.[29,32,34]

The effects of ionic surfactant on the photophysics of conjugated polyelectrolytes based on poly (phenylenevinylene),[39-43] polythiophene,[44] and others[45,46] have been studied. A substoichiometric amount of ionic surfactant with opposite charge to that of the conjugated polyelectrolyte is able to significantly increase its photoluminescence quantum yield and shift the emission spectra by either preventing interchain aggregation or extending the polymer's conjugation length.

PPE based polyelectrolytes have a rigid backbone structure with a long persistence length that spans 10 to 15 repeated units.[25] PPE complexes have been explored for a variety of applications, such as optoelectronic devices,[47,48] structure-directing agents,[49] and biosensors.[50-52] The solid state structure of stoichiometric complexes was studied using wide- and small-angle X-ray scattering.[47,48] A lamellar structure made up of alternative polymer rich layers (1.16 nm) and surfactant alkyl layers (1.86 nm) were found.[48] Literature reports of the effects of surfactant on the fluorescence of PPE [50-52] shows that the interactions between PPE and surfactant is complicated. The structure of complexes with stoichiometric ratio other than 1:1 is not well addressed, and the composition of the complexes as a function of surfactant concentration is not fully understood. PPE polyanions resemble double stranded DNAs in their rigidity of the polymer chain; dsDNA has a persistence length of 60 nm.[53,54] An in-depth understanding of the interaction between negatively charged PPE polyanions with charged and uncharged amphiphilic molecules has significant biological implications, especially in nonviral gene delivery realized by the complexes of DNA with cationic lipids[55-59]

A variety of techniques, such as fluorescence spectroscopy,[28] wide- and small-angle X-ray scattering,[47,48] small angle neutron scattering,[43,46] light scattering,[60] zeta potential measurements,[28] isothermal calorimetry,[61,62] and FCS[46,63] have been used to study

polyelectrolyte/surfactant interactions. FCS is a non-invasive method that provides dynamic and kinetic information by following the fluorescence fluctuation trajectory near the equilibrium state.[64,65] Analysis of the fluctuations yields information about the diffusion and photophysical and photochemical processes. The FCS technique has been widely employed in the life sciences[66] and to study chromophore labeled polymers.[67,68] PPE polymers are intrinsically fluorescent, FCS can be directly applied to it, however such applications are rare in the literature.

This work presents an FCS study on the hydrodynamic properties of complexes formed by OTAB with two PPE-SO_3^- polymers having different charge density and below the critical micelle concentration. The ratio C_{OTAB} /$C_{monomer}$ (C is in unit of M) ranges from 0.2 to 1800. The hydrodynamic radius of the complexes as a function of OTAB concentration shows three regimes. When C_{OTAB} /$C_{monomer}$ < 6, the complexes have comparable size with the polymer in deionized water and are single strand substoichiometric complexes. When 6 <C_{OTAB} /$C_{monomer}$ < 400, a variety of complex sizes are measured. These large complexes are likely comprised of multiple strands of complexes held together by the hydrophobic interactions of the alkyl chains in OTAB molecules. When 400 <C_{OTAB} /$C_{monomer}$ < 1800, the complexes are highly soluble, well defined, and have a size that is about three times larger than that in the low concentration regime and much smaller than that in the intermediate regime. These complexes appear to have a single polymer chain binding with two layers of OTAB. The inner layer of OTAB interacts with PPE-SO_3^- through electrostatic forces and with the second layer of OTAB through the hydrophobic interactions. The outer layer of OTAB contacts the water with the ionic head groups. The complexes formed between PPE-SO_3^- and OTAB below the critical micelle concentration (CMC)[69] and the critical aggregation concentration (CAC)[29] revealed by FCS significantly extends the understanding of the interaction between polyelectrolytes and ionic surfactants. The

observation that the complex containing two layers of OTAB exists below the CMC indicates that the ratio C_{OTAB} /$C_{monomer}$ might be a controlling factor in determining the composition of polyelectrolyte/surfactant complexes.

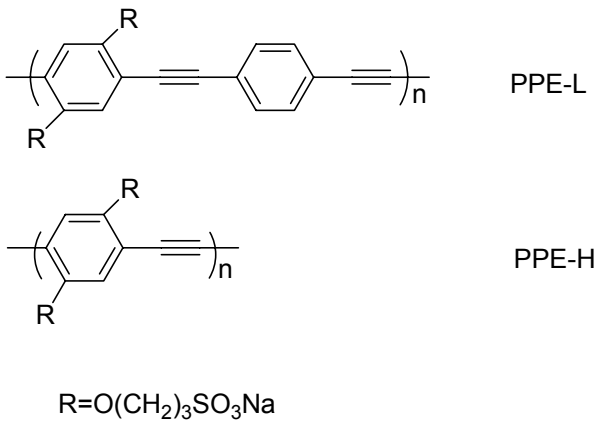

Scheme 7. 1 Molecular structure of the functionalized conjugated poly(phenylethylnylene)

7.2 Experimental

7.2.1 Materials

Water used in all experiments was purified by Barnstead-Nanopure system and its resistance was 18.2 MΩ. Two PPEs, labeled as **PPE-L**, **PPE-H**, having structures as shown in Scheme 7.1, were synthesized at Michigan Technological University. The synthesis procedures for these polymers were previously report.[9-12] Octadecyl trimethylammoniumbromide (OTAB), Octadecyl Sulfate Sodium Salt (ODSS) and all other chemicals were bought from Sigma and were used as received.

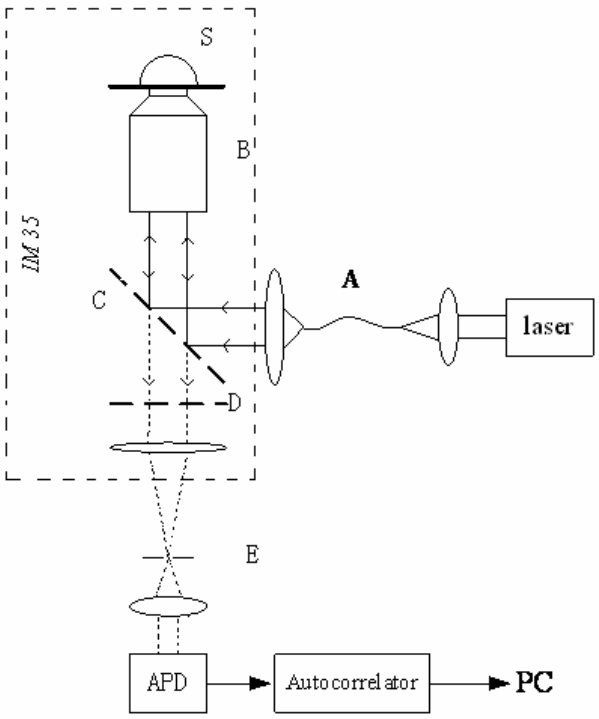

Scheme 7. 2 Schematic representation of the FCS instrument (see text for details).

7.2.2 Instrumentation

A home made FCS instrument was constructed by modifying a Zeiss IM 35 inverted microscope (See Scheme 7.2). The excitation source is a single wavelength (438 ± 3 nm) solid state diode laser (iBeam 440). The laser beam was coupled to the microscope by a single-mode optical fiber (A) which acts as a spatial filter and a beam expander. The dichroic mirror(C) reflects the laser beam and allows fluorescence to pass through. The laser beam is then focused by an objective lens (B) (Olympus UPlanfluor 40X/1.30 oil) into a volume of femtoliter size in the sample (S). By the same objective, the fluorescence was collected. The scattered laser light was blocked by an emission filter (D). At the other port of the microscope, the fluorescence was focused and coupled to a photon counting Avalanche Photodiode (APD) through a pinhole (of 100 μm in diameter) (E). In this confocal arrangement only the fluorescence from the objective's focal

point is detected by the APD. The signal form the APD provides a fluorescence versus time trajectory and is processed by an autocorrelator (BI-9000, Brookhaven Instrument Co.) to generate an autocorrelation function. The autocorrelation function is fit by a model to provide a correlation time for the dynamic or kinetic process.

7.2.3 FCS Theory

At the objective focal point, the intensity of the excitation light has a Gaussian distribution, and the illumination profile defined by a confocal configuration is approximately expressed as

$$I = I_0 \exp\left(-\frac{2\left(x^2 + y^2\right)}{\omega_{xy}^2}\right)\exp\left(-\frac{2z^2}{\omega_z}\right) \tag{7.1}$$

where I_0 is the intensity at the geometric center of the illumination spot; x and y are displacements perpendicular to the optical axis, z is the displacement along the optical axis; ω_{xy} and ω_z characterize the illumination volume of the excitation light.

The normalized autocorrelation function $G(\tau)$ is defined as

$$G(\tau) = \frac{1}{\overline{I}^2 T}\int_0^T \delta I(t)\delta I(t+\tau)dt = \frac{\langle \delta I(0)\delta I(\tau)\rangle}{\langle I(0)\rangle^2} \tag{7.2}$$

where I is the fluorescence intensity, δI is fluorescence fluctuation, t is the experimental time coordinate, τ is a delay time, and T is the total experimental time. In the limit that diffusion is the only cause of fluorescence fluctuations, the correlation function may be written as

$$G(\tau) = \frac{1}{\overline{N}}\left(1 + \frac{\tau}{\tau_D}\right)^{-1}\left(1 + \frac{\tau}{\omega^2 \tau_D}\right)^{-1/2} \tag{7.3}$$

where $\overline{N}$ is the average number of fluorescent molecules in the illuminated volume, τ_D is the correlation time, and ω is defined as

$$\omega = \frac{\omega_z}{\omega_{xy}} \tag{7.4}$$

The correlation time τ_D is given by

$$\tau_D = \frac{\omega_{xy}^2}{4D} \tag{7.5}$$

where D is the diffusion coefficient. The diffusion coefficient of a spherical particle can be estimated by Stokes-Einstein equation.

$$D = \frac{k_B T}{6\pi\eta R} \tag{7.6}$$

where k_B is the Boltzmann constant, T is the temperature, η is the viscosity of solution, and R is the hydrodynamic radius of the molecule.

The time average of the fluorescence intensity is determined by

$$\bar{I} = \frac{1}{T}\int dr^3 I(r)\int dt\left[Q \cdot C(r,t)\right] \tag{7.7}$$

where T is the experiment duration; $I(r)$ is the spatial distribution of the illumination intensity, which can be approximated by Equation 7.1; Q is the effective fluorescence efficiency determined by the absorbance cross section, the fluorescence quantum yield, instrument setup and the detection efficiency. $C(r,t)$, the instantaneous concentration at the point r, can be written as a constant concentration C plus a fluctuation term $C(r,t) = C + \delta C(r,t)$. If the experimental time is long enough, the time average of the fluctuation term dies out.

7.2.4 FCS Experiments

The instrument was calibrated with dyes whose diffusion coefficients are known. 10 nM Rhodamine 6G (D = 4.27×10^{-6} cm^2 s^{-1})[70] and 10 nM fluorescein (D = 4.14×10^{-6} cm^2 s^{-1})[70] were

used. The ω_{xy} was measured to be 0.39 μm and ω was 15. The concentrations of the polymer solutions were controlled to be 10^{-4} mg/ml or lower depending on the quantum efficiency of the fluorescence. To avoid photobleaching and optical trapping, the laser power was kept as low as 24 μW. The autocorrelation function was collected for 2 to 5 min. The time trajectory of fluorescence was monitored and was fitted by Equation 7.3 using a Levenberg-Marquardt algorithm.

7.3 Result

At high concentrations, PPE-SO_3^- aggregates in aqueous solution, hence the concentration of **PPE-L** and **PPE-H** were maintained as low as 2.8×10^{-5} mg/ml and 2.1×10^{-5} mg/ml respectively. The solutions are 1~2 nM in polymers, or 0.050 μM monomer units and 0.10 μM in negative charges, assuming that all of the sulfonate groups on the side chains are ionized. At such low concentrations, the polymers are in a single strand state, i.e. not aggregated.[28] The emission spectra show features belonging to unaggregated polymer in "good" solvent, and the hydrodynamic radius R_H measured with FCS are significantly smaller than that of polymer at a higher concentration.[28] For **PPE-L** the molecular weight M_w is around 20 kDa and R_H is 2.6 ± 0.3 nm calculated from a correlation time of 498 ± 51 μs and a diffusion coefficient of $(7.9 \pm 0.8) \times 10^{-7}$ cm^2 s^{-1}. For **PPE-H** the molecular weight M_w is around 10 kDa. and R_H is 1.6 ± 0.2 nm calculated from a correlation time of 299 ± 39 μs and a diffusion coefficient of $(1.3 \pm 0.2) \times 10^{-6}$ cm^2 s^{-1}.

7.3.1 FCS Measurement

When photophysical and photochemical processes, such as photobleaching, singlet-triplet transitions and photoinduced isomerization are negligible, the autocorrelation function measured by FCS for a single fluorescent species can be described by Equation 7.3. The fluctuation of the fluorescence intensity is approximately attributed to the polymer's diffusion into and out of the illumination volume. Fitting of the autocorrelation function to a diffusion model yields the correlation time that is determined by the diffusion constant of the fluorescent molecules. **PPE-L** has ca. 80 monomer units and **PPE-H** is ca. 50 monomer units estimated from the molecular weight of these polymer and corresponding monomers. PPE polymers have a persistence length of 10 to 15 monomer units (containing a phenyl ring and a carbon-carbon triple bond).[25] The contour length of **PPE-L** and **PPE-H** are much longer than persistence length, and they have semiflexible structures. In this work, the Stokes-Einstein equation is used to calculate a hydrodynamic radius for **PPE-L** and **PPE-H** in solution, which can then be compared in a relative way for different OTAB concentrations or compared to a more detailed physical model.

In experiments, only the autocorrelation functions from those measurements showing a stable average fluorescence intensity were used to calculate a correlation time. Figure 7.1A shows autocorrelation functions obtained for **PPE-L** in 0.03 μM, 3.0 μM, 80.0 μM OTAB solutions and the fitting of each by Eqn.7.3. In the presence of 0.03 μM OTAB, which is lower than the molarity of 0.05 μM **PPE-L**, the experimental autocorrelation function was well described by Eqn 7.3 with a correlation time of 573 ± 41 μs. The diffusion coefficient calculated using Eqn 7.5 was $(8.6 \pm 1.2) \times 10^{-7}$ cm^2 s^{-1} and the hydrodynamic radius calculated using Eqn 7.6 was 2.5 ± 0.4 nm. These values were not significantly different from those of **PPE-L** in deionized water. In the presence of 3.0 μM OTAB, which is 60 times higher than the molarity of

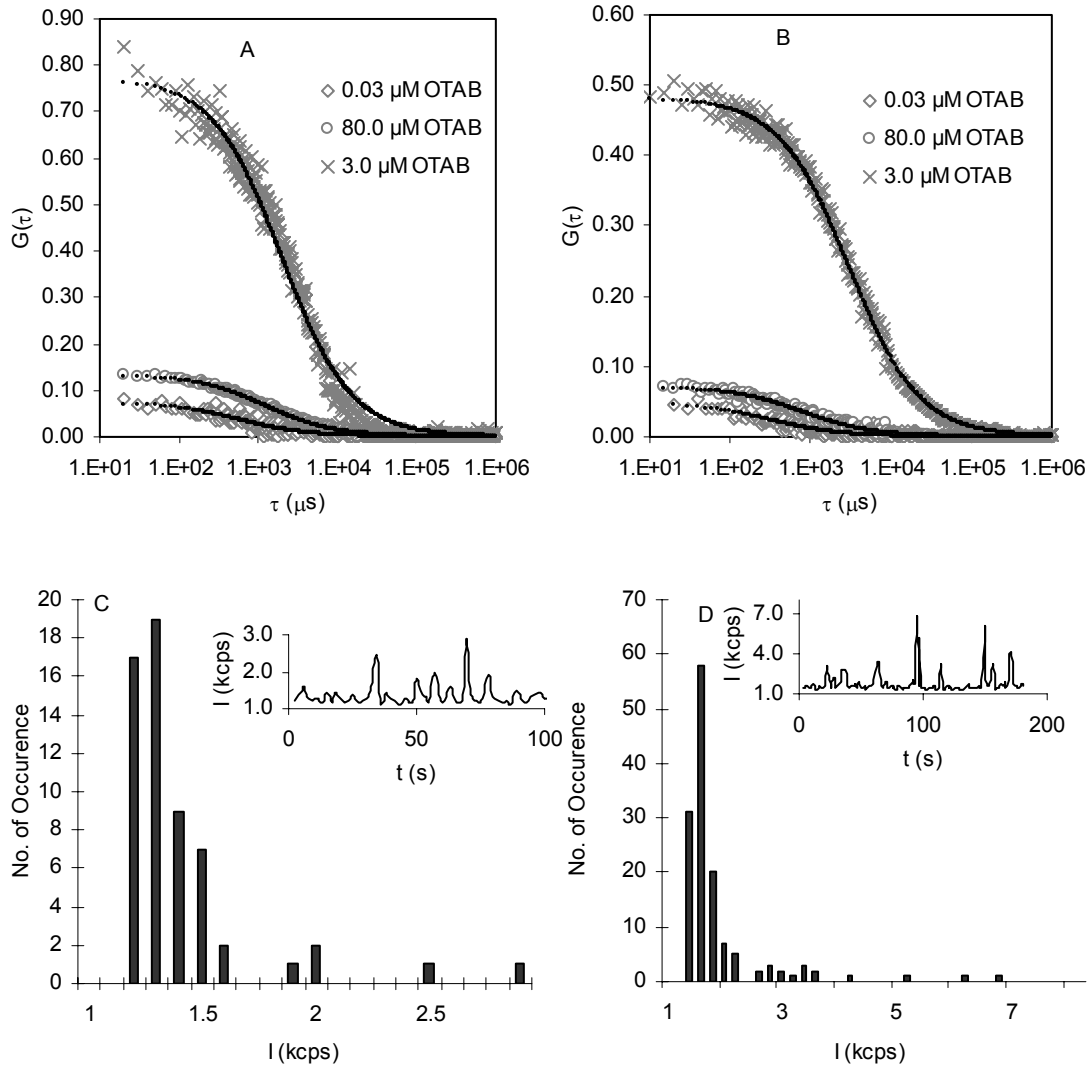

Figure 7. 1 A) Autocorrelation functions of 2.8 $\times 10^{-5}$ mg/ml **PPE-L** in three different solution conditions; B) Autocorrelation functions of 2.1 $\times 10^{-5}$ mg/ml **PPE-H** in three different solution conditions; C) The photon counting rate histogram of 2.8 $\times 10^{-5}$ mg/ml **PPE-L** in 1.0 μM OTAB aqueous solution; D) The photon counting rate histogram of 2.1 $\times 10^{-5}$ mg/ml **PPE-H** in 1.0 μM OTAB aqueous solution, insets are the time trajectory of the photon counting rate.

PPE-L, the experimental autocorrelation function yielded a correlation time of 2040 ± 43 μs. The corresponding diffusion coefficient was (1.9 ± 0.5) × 10^{-7} cm^2 s^{-1} and the hydrodynamic radius was 12.6 ± 4.5 nm. Under these solution conditions, the fitting quality was poor at the tail of the autocorrelation function and parallel measurements gave a wide distribution of correlation times indicating that a wide range of particle sizes exist. In the presence of 80.0 μM OTAB that was 1600 times higher than the molarity of **PPE-L** 0.05 μM, the experimental autocorrelation function is well fitted by Eqn 7.3 yielding a correlation time of 1254 ± 12 μs. The corresponding diffusion coefficient is (3.10 ± 0.05) × 10^{-7} cm^2 s^{-1} and the hydrodynamic radius is 6.6 ± 0.1 nm.

The autocorrelation functions measured for **PPE-H** in 0.03 μM, 3.0 μM, 80.0 μM OTAB solutions and the fitting of each curve are shown in Figure 7.1B. In the presence of 0.03 μM OTAB, the experimental autocorrelation function is well fitted by Eqn 7.3, yielding a correlation time of 324 ± 25 μs. The diffusion coefficient calculated using Eqn 7.5 is (1.2 ± 0.2) × 10^{-6} cm^2 s^{-1} and the hydrodynamic radius calculated using Eqn 7.6 is 1.7 ± 0.2 nm. These values are not significantly different from those of **PPE-H** in deionized water. In the presence of 3.0 μM OTAB that was 60 times higher than the molarity of **PPE-H**, the fitting to the experimental autocorrelation function yielded a correlation time of 3066 ± 30 μs. The corresponding diffusion coefficient was (1.23 ± 0.04) × 10^{-7} cm^2 s^{-1} and the hydrodynamic radius was 16.4 ± 0.6 nm. Under these solution conditions, the autocorrelation function was well fitted by Eqn 7.3. In the presence of 80.0 μM OTAB that is 1600 times higher than the molarity of **PPE-H** 0.05 μM, the autocorrelation function is well described by Eqn 7.3 with a correlation time of 798 ± 20 μs. The corresponding diffusion coefficient was (4.9 ± 0.2) × 10^{-7} cm^2 s^{-1} and the hydrodynamic radius was 4.1 ± 0.2 nm.

In the OTAB concentration ranges of 0.01 - 0.3 μM and 5.0 - 80 μM, the experimental autocorrelation functions are described well by a single diffusing species and provide highly reproducible fitting parameters. When the OTAB concentration was in the range of 0.3 - 5.0 μM, however, only a few well defined autocorrelation functions were obtained from the FCS trajectories. Often times, the fluorescence time trajectory showed spikes, with a stable baseline, see the insets of the Figure 7.1C and 7.1D for **PPE-L** and **PPE-H** in 1.0 μM OTAB solution. The histograms for these two measurements are shown in Figure 7.1C and 7.1D and suggest that most of the counting history has a narrow distribution of fluorescence events. No autocorrelation function was obtained from these events; they appear as a random background noise. Whenever a spike appeared, an autocorrelation function was obtained. However these autocorrelation functions did not have a well defined shape (such as a magnitude of more than 1, broken or having a sharp peak) and no reliable fitting could be obtained from them. The low probability events in Figure 7.1C and 7.1D are attributed either to particles of different size diffusing through the illumination volume or to the particles of comparable size diffusing through the illumination volume by a different trajectory. The spike was indeed fluorescence rather that scattered excitation light because no such spike or strange autocorrelation function was obtained for a scattering sample (a $BaSO_4$ suspension in DI water). These rare events, fluorescent spikes and ill-shaped autocorrelation functions, are attributed to large particles that pass through the illumination volume in a random trajectory. A diluted suspension of fluorescent beads of 0.1 μm and 2.0 μm in diameter show the same type of behavior.

In summary, for the OTAB concentration ranges of 0.01~0.3 μM and 5.0 ~ 80 μM, the FCS gives rise to reliable measurements and produces information on the diffusion constant and the hydrodynamic radius of the polymer. For the OTAB concentration range of 0.3 ~ 5.0 μM, the

FCS measurement could be used to detect the existence of large particles, but could not provide accurate information on the particle size. The radii reported in this concentration regime should not be taken as accurate values, but rather as an indicator that very large particles are present in solution.

7.3.2 Dependence of Polymer Size on the Concentration of Surfactant

It is known that a negatively charge polyelectrolyte and cationic surfactant form electrostatic complexes (Reference 31 and references therein). In this work, the hydrodynamic radius of **PPE-L**/OTAB and **PPE-H**/OTAB complexes were measured as a function of the concentration of OTAB, which was varied from 0.01 μM to 90 μM, about four orders of magnitude. Because the FCS correlation time changes with solution viscosity, the diffusion constant of Coumarin 334 was measured over this OTAB concentration range also. The diffusion coefficient of the dye showed no dependence on the OTAB concentration, indicating that the viscosity change caused by the presence of up to 90 μM OTAB was negligible. Because of the high sensitivity of FCS, the **PPE-L** and **PPE-H** concentration could be controlled as low as 0.05 μM monomer unit or 0.1 μM side chain charges. Such low concentrations of **PPE-L** and **PPE-H** allowed concentration ratios of OTAB to monomer unit ($C_{OTAB}/C_{monomer}$) up to 1800:1 and the molar ratio of OTAB to the side chain charge of the polymer (C_{OTAB}/C_{charge}) up to 900:1 to be accessed while keeping the OTAB concentration much lower than its critical micelle concentration (CMC) 0.3 mM.[69] Under these conditions both the polymer and the surfactant could be treated as free molecules before mixing, greatly reduced the complexity of the system.

The hydrodynamic radius of **PPE-L**/OTAB and **PPE-H**/OTAB complexes as a function of the molar ratio of OTAB and monomer unit had an "Ω" shape as shown in Figure 7.2A and 7.2B. Three regimes can be identified from these plots.1) A low concentration regime, where the

molarity of OTAB varied from 0.01 μM to 0.3 μM, corresponding to a $C_{OTAB}/C_{monomer}$ range from 0.2 to 6.0 and a C_{OTAB}/C_{charge} range from 0.1 to 3.0. In this regime, the measured R_H shows little dependence on the OTAB concentration and is comparable to the size of the polymer in deionized water. 2) A medium concentration regime, where the molarity of OTAB varies from 0.3 μM to 20 μM, corresponding to a $C_{OTAB}/C_{monomer}$ range from 6 to 400 and a C_{OTAB}/C_{charge} range from 3 to 200. In this regime, the R_H, presumably of PPE/OTAB complexes, first increase and then decrease with increasing OTAB concentration. Near the turning point of the curve where the concentration of OTAB was 1.0 μM, the hydrodynamic radius becomes much larger than 10 times that of PPE in deionized water, too large to be accurately measured by FCS; it is indicated in Figure 7.2A an 7.2B with large error bars. 3) A high concentration regime, where the molarity of OTAB varies from 20 μM to 90 μM, corresponding to a $C_{OTAB}/C_{monomer}$ range from 400 to 1800 and a C_{OTAB}/C_{charge} range from 200 to 900. In this regime, the complexes formed from **PPE-L** and **PPE-H** show a different trend. For **PPE-L**, the polymer of low charge density, the hydrodynamic radius increases with increasing OTAB concentration, whereas for **PPE-H** the polymer of high charge density, the hydrodynamic radius shows little dependence on OTAB concentration.

The large particles detected in PPE/OTAB system can be attributed to the aggregation of water insoluble stoichiometric complexes. However the $C_{OTAB}/C_{monomer}$ where these particles start to appear is 6.0 not a equimolar ratio as suggested in the literature.[31,37] Ionic strength can have multiple effects on the cooperative binding of surfactants to polyelectrolytes, including a reduction of binding strength because of the screening effects but an enhanced hydrophobic binding.[29] The delayed appearance of the stoichiometric complex might arise from the ionic strength created by the counter ions of the polyelectrolyte.[29]

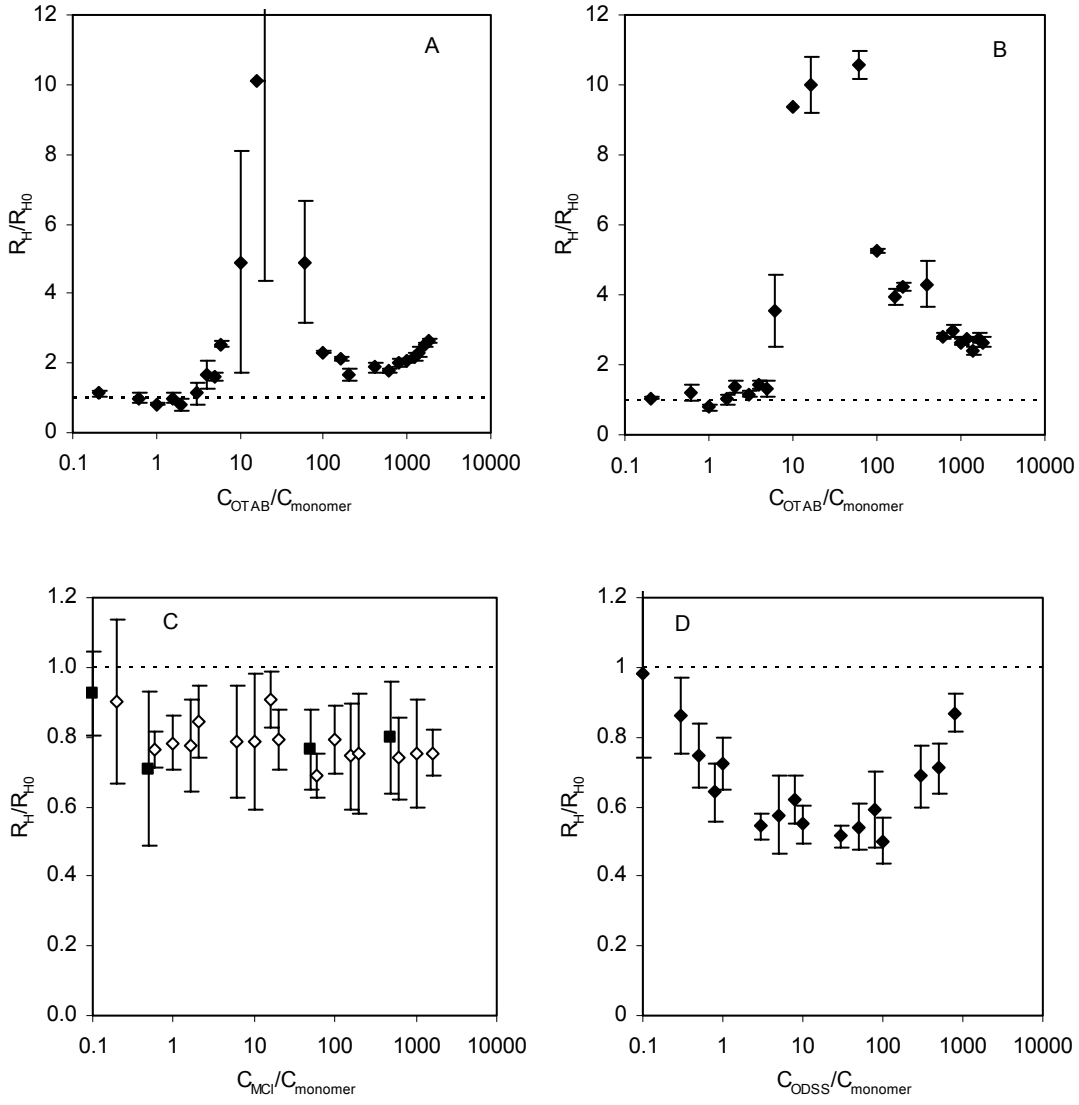

Figure 7. 2 The hydrodynamic radius (R_H) ratio of polymer as a function of solution conditions, R_{H0} represents the hydrodynamic ratio of polymer in deionized water shown in dashed lines in each plot; A)2.8 $\times 10^{-5}$ mg/ml **PPE-L** in OTAB aqueous solutions; B) 2.1 $\times 10^{-5}$ mg/ml **PPE-H** in OTAB aqueous solutions; C) 2.8 $\times 10^{-5}$ mg/ml **PPE-L** in NaCl (solid square)and KCl (blank diamonds) solutions D) 2.8 $\times 10^{-5}$ mg/ml **PPE-L** in ODSS solutions.

As comparison, the hydrodynamic radius of **PPE-L** was measured in NaCl, KCl and the anionic surfactant ODSS solutions. The concentration of these solutions was controlled in the same way as in PPE/OTAB experiments. The results are shown in Figure 7.2C for NaCl and KCl. The presence of a monovalent salt slightly decreases the **PPE-L** size, however the polymer hydrodynamic radius shows little dependence on the concentration of the salt. Figure 7.2D shows the result for ODSS, in which the R_H of **PPE-L** first decreases and then increases as the concentration of ODSS increases. Comparing the behavior shown in Figure 7.2A and 7.2B with that shown in Figure 7.2C and 7.2D, it can be concluded that the "Ω" curves were unique for the PPE/OTAB system.

7.3.3 The Average Number of Molecules

Another parameter, that can be obtained from fitting Eqn. 7.3 to an autocorrelation function is $\overline{N}$, the time average of the number of molecules in the illumination volume determined by $\overline{N} = C \cdot V$, where V is the confocal volume and C is the concentration. $\overline{N}$ is plotted in Figure 7.3A as a function of surfactant concentration. In contrast to the "Ω" shaped hydrodynamic radius curves in Figure 7.2A and 7.2B, the $\overline{N}$ curves are vertically inverted and have a "v" shape. These curves can also be divided into three regimes according to those found in Figure 7.2A and 7.2B. In the low OTAB concentration regime the average number of particles shows little dependence on the surfacant concentration and was comparable to that of the polymer in deionized water. In the medium OTAB concentration regime, the number of particles sharply decreases with the increase of the surfactant concentration to a value that is almost zero and then increases with the increase of the OTAB concentration. The turning point, where few particles are detected, has a concentration around 1.0 μM; exactly the same value where very large

particles are detected in solution. The lower particle number and larger particle size correlation suggests an aggregation and even precipitation of PPE/OTAB complexes.

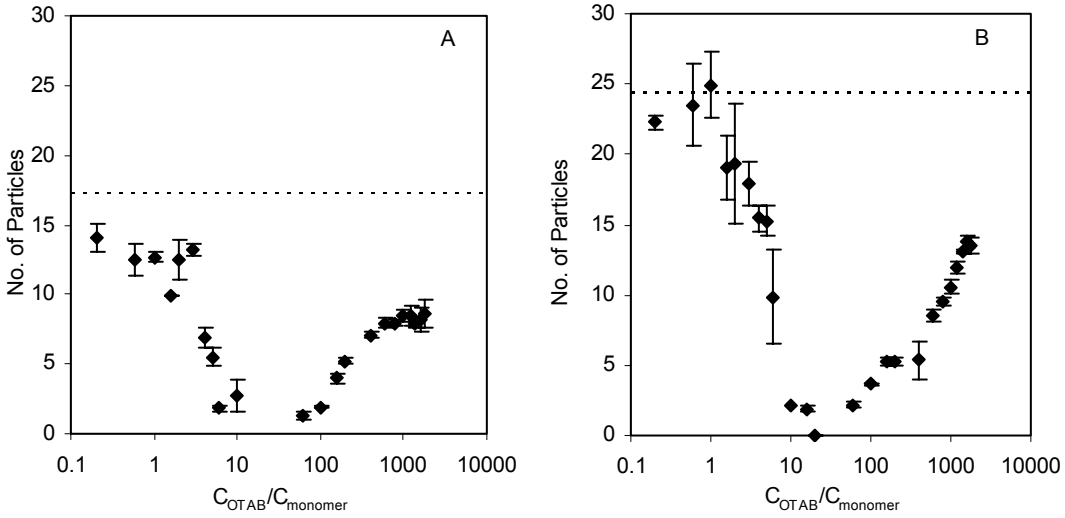

Figure 7. 3 The average number of particles as a function of solution conditions, A) 2.8 $\times 10^{-5}$ mg/ml **PPE-L** in OTAB aqueous solutions; B) 2.1 $\times 10^{-5}$ mg/ml **PPE-H** in OTAB aqueous solutions.

In the high OTAB concentration regime, the complex formed from **PPE-L** and **PPE-H** show different trends. For **PPE-L**, the polymer of low charge density, the number of **PPE-L**/OTAB particles reaches a plateau while the size of the complex increases with an increase of OTAB concentration (Figure 7.2A and 7.3A). For **PPE-H**, the polymer of high charge density, the number of **PPE-H**/OTAB particles increases with the increase of OTAB concentration while the complex size shows little dependence on OTAB concentration (Figure 7.2B and 7.3B).

7.3.4 The Fluorescence Intensity as a Function of Concentration of Surfactant

In the long time limit, the concentration dependence of the intensity yields information on the effective fluorescence efficiency. In the FCS measurement, the power of the diode laser and other features of the instrumental configuration were kept the same for all of the measurements. Each experiment lasted for hundreds of seconds. The time scale for a PPE/OTAB complex diffusing in and out of the illumination volume is on the order of microseconds, estimated with $d = \sqrt{4Dt}$, taking a measured value for the diffusion coefficient D and the size of illumination spot ω_{xy} for d. According to Equation 7.7, the average fluorescence intensity is proportional to the product of concentration and the effective fluorescence efficiency. This relationship can be intuitively understood by realizing that even though a slow diffusing species stays in the illumination volume for a longer time and is excited more times, the frequency in which it passes through the excitation volume is less; a fast diffusing species stays in the illumination volume for a shorter time, but it can enter the detection volume more frequently. If the experimental duration is much longer than the diffusion time scale, the magnitude of diffusion coefficient has no effect on the total number of fluorescence photons.

In Figure 7.4, the average fluorescence intensity is plotted versus the average number of particles in the excitation volume for the solutions at low OTAB concentration and at high OTAB concentration; not near 1.0 μM. Panel A is for **PPE-L**/OTAB and panel B is for **PPE-H**/OTAB. For each plot, the intensity and the particle number show two distinct correlations. All of the points corresponding to solutions having OTAB concentration from 0 μM to 0.5 μM fall onto a shallower linear curve, suggesting a comparatively lower fluorescence efficiency. All of the points corresponding to solutions have OTAB concentration from 3.0 μM to 90.0 μM fall onto a sharp rising curve, suggesting higher fluorescence efficiency. Because the instrument

conditions were kept the same for all of the experiments, the contrast in the effective fluorescence efficiency indicates a dramatic change in the polymer fluorescence quantum yield. When the OTAB concentration is in the range from 3.0 μM to 90.0 μM, the curve for **PPE-L** is superlinear, suggesting a continuing modification of **PPE-L** fluorescence yield by OTAB molecules. Under the same conditions, the curve for **PPE-H** is linear and has a slope that is 2.7 times higher than that in deionized water, suggesting an increase of fluorescence efficiency.

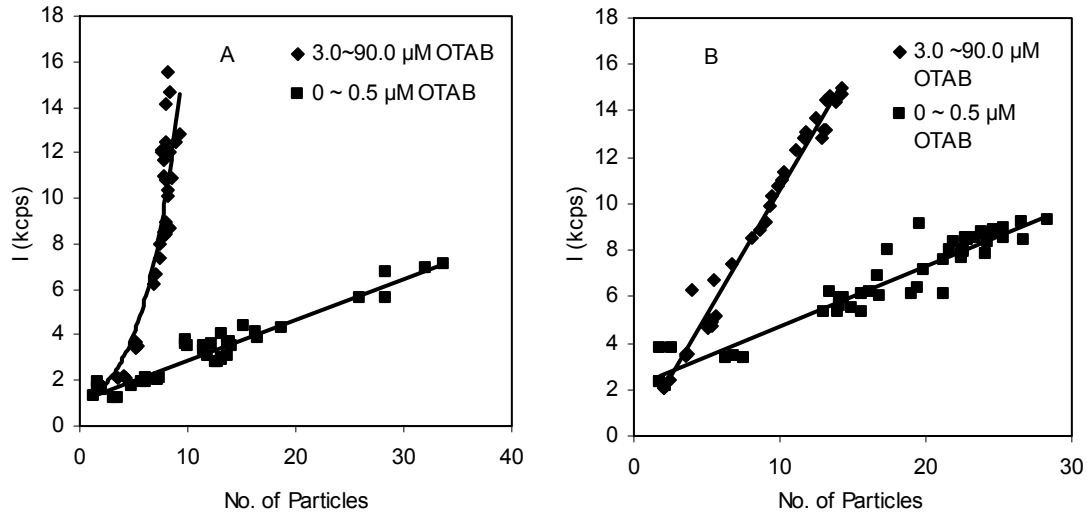

Figure 7. 4 The correlation between the average fluorescence intensity and the average number of particles obtained in FCS measurements, A) 2.8×10^{-5} mg/ml **PPE-L** in OTAB aqueous solutions; B) 2.1×10^{-5} mg/ml **PPE-H** in OTAB aqueous solutions.

7.3.5 The Emission and Excitation Spectra

To understand the behavior shown in Figure 7.4, the steady state emission spectra of **PPE-L** and **PPE-H** were measured for the solution used for the FCS measurements. The spectra of 2.8×10^{-5} mg/ml **PPE-L** in deionized water and in 80 μM OTAB aqueous solution are shown in Figure 7.5A. Those for 2.8×10^{-5} mg/ml **PPE-H** in deionized water and in 90 μM OTAB aqueous

solutions are shown in Figure 7.5B. These spectra are normalized to the same height. **PPE-L** in 80 μM OTAB aqueous solution has a peak intensity about 15 times larger than that of **PPE-L** in deionized water, and **PPE-H** in 90 μM OTAB aqueous solution has a peak intensity of 5 times larger than that of **PPE-H** in deionized water. The quantum yield reported for **PPE-L** in deionized water is 0.05 and that for **PPE-L** in 50 μM OTAB solution is 0.15. A shorter life time was reported for **PPE-L** in OTAB solution.[28] The quantum yield of **PPE-H** is 0.026 measured in deionized water and 0.042 measured in 50 μM OTAB solution. For **PPE-H**, the fluorescence lifetime for was found to be similar in deionized water (570 ps) and in OTAB solutions(446 ps). As shown in panel A, the emission spectrum of **PPE-L** in deionized water shows a peak at 436 nm and a shoulder at 508 nm, with a FWHM of 73 nm. These spectra for **PPE-L** in deionized water are consistent mostly with a single strand species, but a small amount of aggregation.[28] The emission spectrum for **PPE-L** 80 μM OTAB aqueous solution shows a peak at 450 nm, with a FWHM of 36 nm. Panel B shows a broad symmetric emission spectrum with a peak at 490 nm with a FWHM of 109 nm for **PPE-H** in deionized water. The emission spectrum for **PPE-H** in 80 μM OTAB aqueous solution shows a peak at 450 nm, with a FWHM of 36 nm.

To summarize, at high concentration of OTAB ($C_{OTAB}/C_{monomer}$ up to 1600:1 and 1800:1), the emission spectra of **PPE-L** and **PPE-H** are red shifted (14 nm for **PPE-L** and 16 nm for **PPE-H**) and are narrower (by about two times) than those observed in deionized water. In addition, the fluorescence quantum yields for the two polymers in OTAB solution are increased over that in water.

The excitation spectra of **PPE-L** and **PPE-H** were measured and are shown in Figure 7.5C and 7.5D. Consistent with the dominant fluorescence feature of single strand **PPE-L** in dilute aqueous solution, no spectral signature of the aggregation is obvious in the excitation

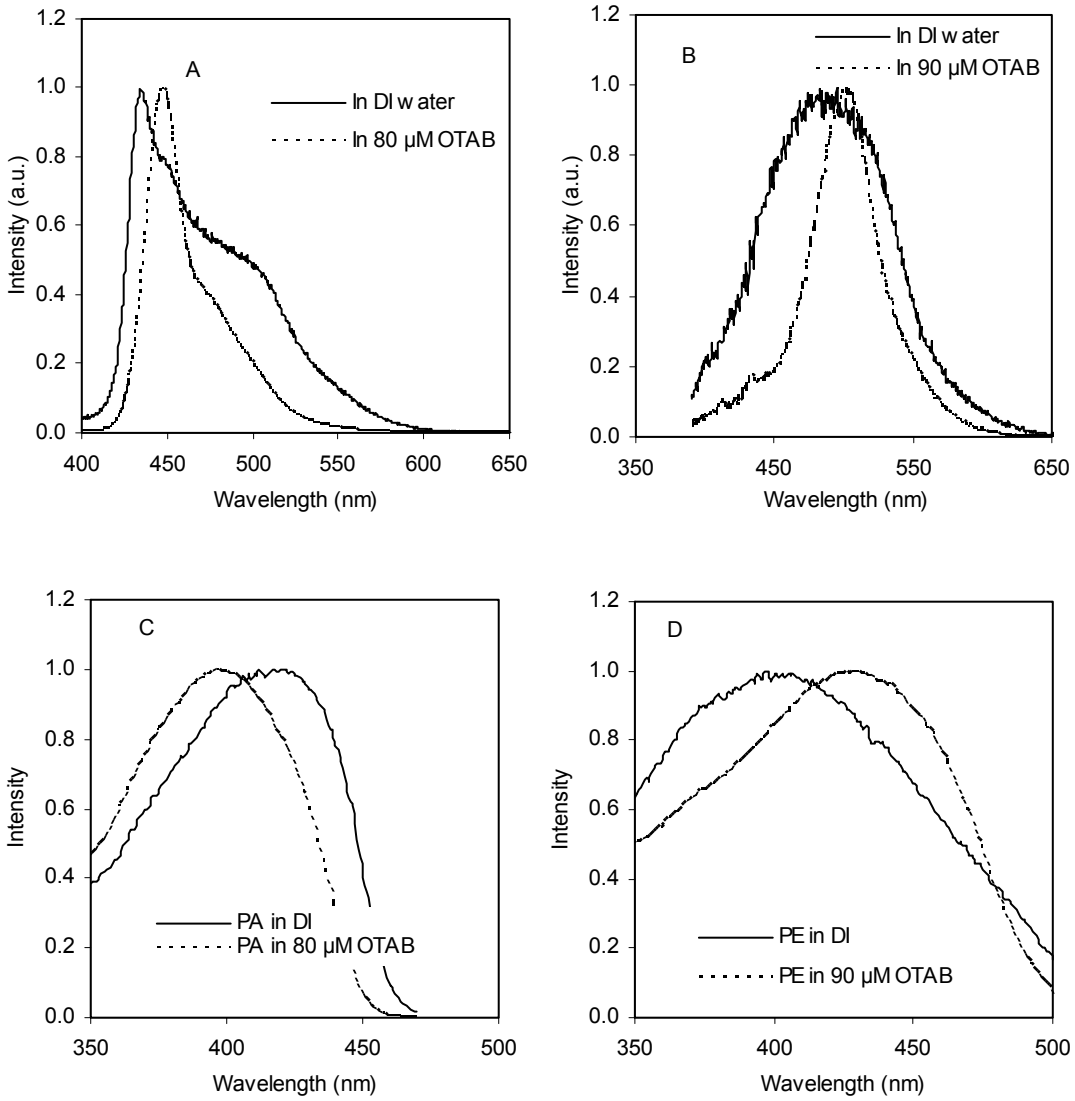

Figure 7. 5 The emission spectra of A) 2.8 $\times 10^{-5}$ mg/ml PPE-L; B) 2.1 $\times 10^{-5}$ mg/ml **PPE-H**. The excitation spectra of C)2.8 $\times 10^{-5}$ mg/ml **PPE-L**; D) 2.1 $\times 10^{-5}$ mg/ml **PPE-H**.

spectrum (Figure 7.5C). In the presence of 80 μM OTAB, the excitation spectrum is blue shifted, but are otherwise similar. For **PPE-H**, the excitation spectrum in 90 μM OTAB solution is red shift with respected to that in deionized water.

Previous ζ-potential studies show that the surface charge of **PPE-L** was inverted in the presence of excess of OTAB.[28] The mobility and ζ-potential for **PPE-H** was measured in deionized water and in 50 μM OTAB solution, a condition that is the same as that previously reported for **PPE-L**. The ζ-potential for **PPE-H** in deionized water is -28 ± 2 mV and the mobility is -1.7 ± 0.7. In OTAB solution the ζ-potential is 53 ± 1 mV and the mobility is 3.95 ± 0.08.

7.4 Discussions

The hydrodynamic properties of complexes formed by OTAB with two PPE-SO_3^- polymers, containing different side-chain charge density, below the critical micelle concentration have been directly measured with FCS. The hydrodynamic radius, the number of detected molecules and the effective fluorescence efficiency data consistently suggest that PPE/OTAB complexes fall into three catagories depending on the C_{OTAB} /$C_{monomer}$ ratio. They are single-strand substoichiometric complexes (Figure 7.6a), multiple-strand clusters (Figure 7.6b and 7.6c) and single-strand superstoichiometric complexes (Figure 7.6d and 7.6e).

The formation of the soluble substoichiometric complexes has long been known for flexible polyelectrolytes.[29,31,34] Polymer and surfactant molecules are fastened together by the electrostatic interactions between opposite charges. When C_{OTAB} /$C_{monomer}$ < 6, the complexes have a size comparable with the polymer in deionized water are single strand substoichiometric complexes between PPE-SO_3^- and OTAB. The structures are represented by Figure 7.6a and the charges that are not neutralized make this complex soluble in water. The surfactant chain in these

complexes may not be fully extended therefore there is no obvious increase in hydrodynamic radius as expected for the fully extended surfactant chains.

When there is sufficient surfactant, all the charges from the polyelectrolyte will be neutralized and the stoichiometric complex will form by both the electrostatic interactions between opposite charges and the hydrophobic interactions between parallel alkyl chains.[29,31,34] This complex is not soluble in water and tends to aggregate into larger assemblies and precipitate. This accounts for the huge particles and significant heterogeneity found when C_{OTAB} /$C_{monomer}$ > 6. The structure of these kinds of large particles is represented by Figure 7.6b, which is extendable in three dimensions. The stoichiometric complexes are usually synthesized by mixing surfactant and polyions in equal molar amount (calculated based on the number of charge).[31,47,48] Accordingly, in our case, large particles should have be observed when the ratio C_{OTAB} /$C_{monomer}$ equals to 2.0 not 6.0. The delay is attributed to screening of the electrostatic interaction by the counter ions from the polymer.[29] The structure represented by Figure 7.6b is in agreement with the structure proposed by Thünemann *et.al* who has used small- and wide-angle X-ray scattering to study the solid state structure of precipitates prepared by mixing the aqueous solutions of PPE-COO^- and cationic surfactants at the stoichiometric ratio.[47,48]

From the structure of the solid state stoichiometric complexes as shown in Figure 7.6b, the large but soluble particles that appear in the higher concentration part of the intermediate regime can be inferred to have a structure like that shown in Figure 7.6c, where the cluster of stoichiometric chains have a boundary layer of OTAB molecules with their charged head groups facing water, rather than the 3-D extendable structure show in Figure 7.6b. Because of the outer layer of OTAB molecules, the clusters are soluble in water and the charge polarity of the particle should be inverted with respect to that of pure PPE-SO_3^- in deionized water. This charge

inversion was verified by the zeta potential measurements [28] where the values for PPE-SO_3^- in deionized water and in 50 μM OTAB solutions show opposite signs. Further increase of the OTAB concentration decreases the number of stoichiometric chains in the structure c, reflected by the decreasing trend in the higher concentration part of the intermediate OTAB concentration regime. This trend is conserved until only one stoichiometric chain is left in structure c and leads to structure d.

Depending on the charge density of the polymer, the fate of structure d is different. In the case of **PPE-L** whose charge density is low, the size of the particle increases as C_{OTAB} /$C_{monomer}$ increases from 400 to 1800 while the number of particles is constant, which indicates a continuous modification of the structure d and a final structure like that of e. This causes a supralinear growth of fluorescence intensity versus the number of particles curve (Figure 7.4A). As in the case of **PPE-H** whose charge density is two times larger than that of **PPE-L**, the size of the particle remains constant but the number of particle in the solution increases while C_{OTAB} /$C_{monomer}$ increases from 400 to 1800. The linear fluorescence intensity versus the number of particles curve suggests that the complexes of **PPE-H** in this regime have the same composition.

The change of particle size with the increase of C_{OTAB} /$C_{monomer}$ in the whole tested OTAB concentration range can be understood by the continuous change in the stoichiometric ratio in the chemically and physically stable complexes. From structure a to structure e, the stoichiometric ratio of the complexes, if calculated based on the number of charges from OTAB and PPE-SO_3^-, evolves from < 1 : 1 (a) to 1 : 1 (b) to between 1 : 1 and 2: 1 (c) to 2 : 1 (d) to > 2 : 1.

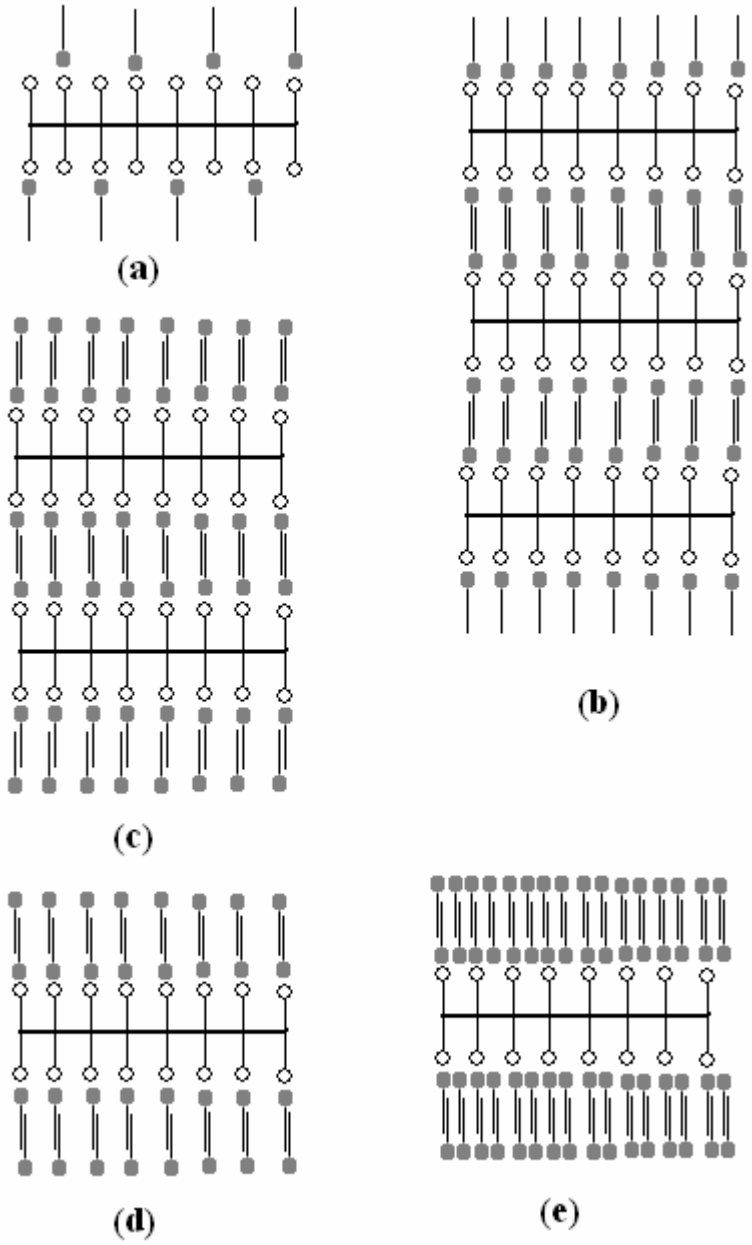

Figure 7. 6 The cartoon showing the possible structures of **PPE-L**/OTAB and **PPE-H**/OTAB complexes

The charge density of **PPE-H** is two times larger than that of **PPE-L** (see Scheme 7.1). However the hydrodynamic radius of **PPE-L**/OTAB and **PPE-H**/OTAB complexes as a function of OTAB concentration are generally similar, but show some difference in the high concentration regime, see Figure 7.2 and Figure 7.3. In the high concentration regime, the hydrodynamic radius of **PPE-L**/OTAB complexes increases while the average number of complexes detected in the excitation volume is constant as the OTAB concentration increases. In contrast, the hydrodynamic radius of **PPE-H**/OTAB complexes are constant while the average number of particles in the excitation volume increases as the OTAB concentration increases. The different trends can be understood from the difference in charge density of **PPE-L** and **PPE-H** and the structures shown in Figure 7.6. In the case of **PPE-L**, the charge density is low, so that the hydrophobic interaction holding multiple chains together in structure b and c is smaller. Hence, it is easier to break the complexes into structure d than for the case of **PPE-H**. When the OTAB concentration is increased, more OTAB pairs can insert into the space between side chains of **PPE-L** of structure d and form structure e to optimize the hydrophobic interactions between OTAB molecules. Therefore the complex's hydrodynamic radius increases in the high concentration regime. In the case of **PPE-H**, the hydrophobic interaction is stronger, and it is more difficult to break the structure d from large complexes of structure b and c, hence the number of complexes with the same hydrodynamic radius increase more gradually as the OTAB concentration increases.

Burrow *et. al.*[71] studied the fluorescence of anionic poly[1,4-phenylene-[9,9-bis(4-phenoxy-butylsulfonate)]fluorene-2,7-diyl]copolymer (PBS-PFP) as a function of cationic surfactant concentration and identified three surfactant concentration regimes.[71] In the low concentration regime, $< 2 \times 10^{-6}$ M, the fluorescence is quenched. In a wide intermediate

concentration regime, from 2×10^{-6} to 10^{-3} M, the fluorescence intensity remains constant. In the third regime where the surfactant concentration is above 10^{-3} M, the CMC, the fluorescence is enhanced and spherical aggregates of the complexes were detected. The difference in the fluorescence intensity indicates that polyelectrolyte/surfactant complexes are intrinsically different in these three regimes. The triple-phasic behavior is consistent with the findings on the size of the complexes in this paper.

The conformation of the complexes of flexible conjugated polyions with oppositely charged surfactant or radom coil nonfluorescent polyions have been extensively studied and the three component phase diagram has worked out[29,72]. The general picture is that with increase of the concentration of surfactant, the complexes evolve from substoichiometric complexes to stoichiometric complexes and finally to the encapsulation of polyions by micelles above the CMC.[43,72-75] This picture predicts the detection of structure a and b, but not other structures. Our results contrast with this standard picture in two aspects. First, these results show that a distribution of soluble complex structures evolves with the stoichiometric ratio from 1 : 1 to > 2 : 1. Second the OTAB concentrations in this study are far below the CMC[69] and CAC.[29] The complex structures of c, d and e are not the result of the pre-existing micelle or vesicle structures. It appears that the C_{OTAB} /$C_{monomer}$ ratio is a dominant factor for the composition of the complexes. The contrast between these findings from PPE-SO_3^- and those from random coil polyelectrolyte suggests that the rigidity of the polymer backbone plays an important role in determining the conformation between polyions and surfactant.

Different effects of surfactant on the fluorescence of PPE have been reported in the literature.[50-52] With the help of the structures proposed in Figure 7.6, the following prediction can be made. In the low OTAB concentration regime, the fluorescence intensity will first increase

because binding of the surfactant breaks or loosens the PPE aggregate. Near the right boundary of this regime the fluorescence quenches because of the precipitation of the PPE polymers. This prediction is consistent with the studies reported by Yu *et. al.*.[50] On the higher OTAB concentration side of the intermediate regime, the fluorescence intensity increases again with increase of the OTAB because of the dissolution of the precipitate and formation of particles having structure c. Experimental results of this kind have been reported by Kaur *et. al.*.[28] It is expected that this enhancement of the fluorescence intensity will stop when all of the PPE chains have the structure of d or e. However this is difficult to observe using steady state fluorescence measurements, because such a method needs a comparatively high concentration and the available highest C_{OTAB} /$C_{monomer}$ is limited by the CMC[69] and CAC[29].

For both **PPE-L** and **PPE-H**, the complex size shows a strong dependence on the charge ratio C_{OTAB}/C_{charge}. The uniform particle size can only be achieved when C_{OTAB}/C_{charge} is in the range of 0.1 to 6.0 where substoichiometric complexes are formed, and when C_{OTAB}/C_{charge} is over 100, multiple chains of PPE exist in the complex with a size decreasing with increasing of C_{OTAB}/C_{charge}. It is interesting to compare these observations to those found for DNA/lipid complexes. In the case of DNA/lipid complexes, the optimized transfection condition has a charge ratio in the range of 0.3-5.0 and DNA particles of 100-700 nm size have been observed by electron microscopy.[59,76] Our data suggests that it is highly possible that insufficient lipid charge causes the heterogeneity of DNA/lipid complexes which increases the uptake barrier for DNA delivery.

7.5 Conclusion

It is shown in this paper that FCS is a powerful tool for studying the interactions between surfactant and fluorescent polyelectrolyte. It yields valuable information that is not accessible by

traditional methods. It is found that even in a concentration far lower than the CMC and CAC of OTAB, the PPE-SO_3^-/OTAB complexes exist in a series of structures that have different size, chemical composition, and conformation depending on the comparative concentration of polyelectrolyte and surfactant. This complicated situation indicates that the rigidity of the polymer backbone plays an important role in determining the conformation between polyions and surfactant and the ratio C_{OTAB} /$C_{monomer}$ might be a dominant factor for the composition of the complexes. With the help of the structures inferred from the FCS studies, the contradictory effects of surfactant reported on the PPE fluorescence can be explained by a unified picture. The PPE-SO_3^- represents the type of polyelectrolytes with rigid backbone, including dsDNA. Our results have important implications in the field of gene delivery.

7.6 Acknowledgements

I would like to thank Dr. Matthew Shtrahman of University of Pittsburgh for his generous help with the FCS instrument. The work is supported by National Science Foundation (CHE-0415457).

References

(1) Zhou, C. Z.; Liu, T.; Xu, J. M.; Chen, Z. K. *Macromolecules* **2003**, *36*, 1457-1464.

(2) Wilson, J. N.; Bunz, U. H. F. *J. Am. Chem. Soc* **2005**, *127*, 4124-4125.

(3) Skotheim, T. E.; Elsenbaumer, R. L.; Reyolds, J. R. *Eds. Handbook of Conducting Polymers* **1998**, *Marcel Decker: New York.*

(4) Rothberg, L. J.; Yan, M.; Galvin, M. E.; Kwock, E. W.; Miller, T. M.; Papadimitrakopoulos, F. *Synthetic Metals* **1996**, *80*, 41-58.

(5) Perahia, D.; Traiphol, R.; Bunz, U. H. F.; *Macromolecules* **2001**, *34*, 151-155.

(6) Levitsky, I. A.; Kim, J.; Swager, T. M. *J. Am. Chem. Soc* **1999**, 1466-1472.

(7) Jones, R. M.; Bergstedt, T. S.; McBranch, D. W.; Whitten, D. G. *J. Am. Chem. Soc* **2001**, *123*, 6726-7.

(8) Bunz, U. H. F.; Imhof, J. M.; Bly, R. K.; Bangcuyo, C. G.; Rozanski, L.; Bout, D. A. V. *Macromolecules* **2005**, *38*, 5892-5896.

(9) Thomas, S. W.; Joly, G. D.; Swager, T. M. *Chem. Rev.* **2007**.

(10) Schanze, K. S.; Pinto, M. R. *Proc. Nat. Aca. Sci.* **2004**, *101*, 7505-7510.

(11) Rininsland, F.; Xia, W.; Wittenburg, S.; Shi, X.; Stankewicz, C.; Achyuthan, K.; McBranch, D.; Whitten, D. *Proc. Nat. Acad. Sci.* **2004**, *101*, 15295-15300.

(12) McQuade, D. T.; Pullen, A. E.; Swager, T. M. *Chem Rev* **2000**, *100*, 2537-74.

(13) Liu, M.; Kaur, P.; Waldeck, D. H.; Xue, C.; Liu, H. *Langmuir* **2005**, *21*, 1687-1690.

(14) Kim, I.-B.; Dunkhorst, A.; Gilbert, J.; Bunz, U. H. F. *Macromolecules* **2005**, *38*, 4560-4562.

(15) Heeger, A. J.; Diaz-Garcia., M. A. *Curr. Opin. Solid State Mater.* **1983**, *3*, 16.

(16) Harrison, B. S.; M.B.;, R.; Reyolds, J. R.; Scahnze, K. S., , . *J.Am. Chem. Soc.* **2000**, *122*, 8561.

(17) Gaylord, B. S.; Heeger, A. J.; Bazan, G. C. *Proc. Nat. Acad. Sci.* **2002**, *99*, 10954-10957.

(18) Haskins-Glusac, K.; Pinto, M. R.; Tan, C.; Schanze, K. S. *J. Am. Chem. Soc.* **2004**, *126*, 14964-14971.

(19) Chu, Q.; Pang, Y.; Ding, L.; Karasz, F. E. *Macromolecules* **2002**, *35*, 7569-7574.

(20) Chu, Q.; Pang, Y. *Macromolecules,* **2003**, *36*, 4614-4618.

(21) Tan, C.; Pinto, M. R.; Schanze, K. S. *Chem Comm.* **2002**, 446-447.

(22) Jiang, H.; Zhao, X.; Schanze, K. S. *Langmuir* **2006**, *22*, 5541-5543.

(23) Jenekhe, S. A.; Osaheni, J. A. *Science* **1994**, *265*, 765-768.

(24) Sariciftci, N. S.; Smilowitz, L.; Heeger, A. J.; Wudl, F. *Science* **1992**, *258*, 1474-1476.

(25) Cotts, P. M.; Swager, T. M.; Zhou, Q. *Macromolecules* **1996**, *29*, 7323-7328.

(26) Halkyard, C. E.; Rampey, M. E.; Kloppenburg, L.; Studer-Martinez, S. L.; Bunz, U. H. F. *Macromolecules* **1998**, *31*, 8655-8659.

(27) Fiesel, R.; Halkyard, C. E.; Rampey, M. E.; Kloppenburg, L.; Studer-Martinez, S. L.; Scherf, U.; Bunz, U. H. F. *Macromol.r Rapid Comm.* **1999**, *20*, 107-111.

(28) Kaur, P.; Yue, H.; Wu, M.; Liu, M.; Treece, J.; Waldeck, D. H.; Xue, C.; Liu, H. *J. Phys. Chem. B* **2007**.

(29) Kogej, K.; Skerjane, J. In *Physical Chemistry of Polyelectrolytes*; Radeva, T., Ed.; Mercel Dekker, Inc.: New York, Basel, 2001, p 793-827.

(30) Goddard, E. D. *J. Coll. & Interf. Sci.* **2002**, *256*, 228-235.

(31) MacKnight, W. J.; Ponomarenko, E. A.; Tirrell, D. A. *Acc. Chem. Res* **1998**, *31*, 781-788.

(32) La Mesa, C. *J.f Coll. & Interf. Sci.* **2005**, *286*, 148-157.

(33) Macdonald, P. M. *Coll. & Surf. A* **1999**, *147*, 115-131.

(34) Tam, K. C.; Wyn-Jones, E. *Chem. Soc. Rev.* **2006**, *35*, 693-709.

(35) Goddard, E. D. *Coll. & Surf.* **1986**, *19*, 255-300.

(36) Yeh, F.; Sokolov, E. L.; Walter, T.; Chu, B. *Langmuir* **1998**, *14*, 4350-4358.

(37) Bakeev, K. N.; Shu, Y. M.; Zezin, A. B.; Kabanov, V. A.; Lezov, A. V.; Mel'nikov, A. B.; Kolomiets, I. P.; Rjumtsev, E. I.; MacKnight, W. J. *Macromolecules* **1996**, *29*, 1320-1325.

(38) Morishima, Y.; Mizusaki, M.; Yoshida, K.; Dubin, P. L. *Coll. & Surf.* **1999**, *147*, 149-159.

(39) Chen, L.; McBranch, D. W.; Wang, H.-L.; Helgeson, R.; Wudl, F.; Whitten, D. G. *Proc. Natl. Acad. Sci.* **1999**, *96*, 12287-12292.

(40) Chen, L.; Xu, S.; McBranch, D.; Whitten, D. *J. Am. Chem. Soc.* **2000**, *122*, 9302-9303.

(41) Fan, C.; Plaxco, K. W.; Heeger, A. J. *J. Am. Chem. Soc.* **2002**, *124*, 5642-5643.

(42) Gaylord, B. S.; Wang, S.; Heeger, A. J.; Bazan, G. C. *J. Am. Chem. Soc.* **2001**, *123*, 6417-6418.

(43) Wang, D.; Moses, D.; Bazan, G. C.; Heeger, A. J.; Lal, J. *J.Macromol. Sci.* **2001**, *A38*, 1175-1189.

(44) Ho, H.-A.; Boissinot, M.; Bergeron, M. G.; Corbeil, G.; Dore, K.; Boudreau, D.; Leclerc, M. *Angewandte Chemie Internatl. Ed.* **2002**, *41*, 1548-1551.

(45) Gaylord, B. S.; Heeger, A. J.; Bazan, G. C. *J. Am. Chem. Soc.* **2003**, *125*, 896-900.

(46) Tapia Maria, J.; Burrows Hugh, D.; Knaapila, M.; Monkman Andrew, P.; Arroyo, A.; Pradhan, S.; Scherf, U.; Pinazo, A.; Perez, L.; Moran, C. *Langmuir* **2006**, *22*, 10170-4.

(47) Thunemann, A. F.; Ruppelt, D. *Langmuir* **2001**, *17*, 5098-5102.

(48) Thunemann, A., F. *Adv. Mater.* **1999**, *11*, 127-130.

(49) Clark, A. P. Z.; Shen, K.-F.; Rubin Yves, F.; Tolbert Sarah, H. *Nano letters* **2005**, *5*, 1647-52.

(50) Yu, M. H.; Gan, H. Y.; He, F.; Tang, Y. L.; Zheng, D. G.; Wang, S.; Li, Y. L. *Chinese Chem. Lett.* **2006**, *17*, 671-674.

(51) Wosnick, J. H.; Mello, C. M.; Swager, T. M. *J. Am. Chem. Soc* **2005**, *127*, 3400-3405.

(52) Lavigne, J. J.; Broughton, D. L.; Wilson, J. N.; Erdogan, B.; Bunz, U. H. F. *Macromolecules* **2003**, *36*, 7409-7412.

(53) Godfrey, J. E.; Eisenberg, H. *Biophys. Chem.* **1976**, *5*, 301-8.

(54) Godfrey, J. E. *Biophys. Chem.* **1976**, *5*, 285-99.

(55) Duzgunes, N.; de Ilarduya, C. T.; Simoes, S.; Zhdanov, R. I.; Konopka, K.; de Lima, M. C. P. *Curr. Med. Chem.* **2003**, *10*, 1213.

(56) Hirko, A.; Fuxing Tang, A.; Hughes, J. A. *Curr. Med. Chem.* **2003**, *10*, 1185.

(57) Nakanishi, H.; Tsuchiya, K.; Okubo, T.; Sakai, H.; Abe, M. *Langmuir* **2007**, *23*, 345-347.

(58) Pedroso de Lima, M. C.; Neves, S.; Filipe, A.; Duzgunes, N.; Simoes, S. *Curr. Med. Chem.* **2003**, *10*, 1221-1231.

(59) Zabner, J.; Fasbender, A. J.; Moninger, T.; Poellinger, K. A.; Welsh, M. J. *J. Biol. Chem.* **1995**, *270*, 18997-19007.

(60) Bastardo, L. A.; Garamus, V. M.; Bergstroem, M.; Claesson, P. M. *J. Phys. Chem. B* **2005**, *109*, 167-174.

(61) Lapitsky, Y.; Parikh, M.; Kaler, E. W. *J. Phys. Chem. B* **2007**, *ASAP Article, DOI: 10,102/jp0678958*.

(62) Zhao-chang Fan; Shan, L.; Goldsteen, B. Z.; Guddat, L. W.; Thakur, A.; Landolfi, N. F.; Edmundson, M. S. C. M. V. C. Q. P. A. R. A. B. *J. Mol. Recogn.* **1999**, *12*, 19-32.

(63) Adjimatera, N.; Kral, T.; Hof, M.; Blagbrough, I. S. *Pharm.l Res.* **2006**, *23*, 1564-1573.

(64) Koppel, D. E. *phys. Rev. A* **1974**, *10*, 1938-1945.

(65) Magde, D.; Elson, E.; Webb, W. W. *Phys. Rev. Lett.* **1972**, *29*, 705-708.

(66) *Fluorescence Correlation Spectroscopy, Theory and Applications*; Rigler, R.; Elson, E. S., Eds.; Springer, 2001.

(67) Pristinski, D.; Kozlovskaya, V.; Sukhishvili, S. A. *J. Chem. Phys.* **2005**, *122*.

(68) Van Rompaey, E.; Sanders, N.; De Smedt, S. C.; Demeester, J.; Van Craenenbroeck, E.; Engelborghs, Y. *Macromolecules* **2000**, *33*, 8280-8288.

(69) Lu, J. R.; Simister, E. A.; Thomas, R. K.; Penfold, J. *J. Phys. Chem. B* **1993**, *97*, 6024-6033.

(70) Culbertson, C. T.; Jacobson, S. C.; Ramsey, J. M. *Talanta* **2002**, *56*, 365-373.

(71) Burrows, H. D.; Tapia, M. J.; Silva, C. L.; Pais, A. A. C. C.; Fonseca, S. M.; Pina, J.; Seixas de Melo, J.; Wang, Y.; Marques, E. F.; Knaapila, M.; Monkman, A. P.; Garamus, V. M.; Pradhan, S.; Scherf, U. *J. Phys. Chem. B* **2007**, *111*, 4401-4410.

(72) Galant, C.; Amiel, C.; Wintgens, V.; Sebille, B.; Auvray, L. *Langmuir* **2002**, *18*, 9687-9695.

(73) Li, Y.; Xu, R.; Couderc, S.; Bloor, D. M.; Warr, J.; Penfold, J.; Holzwarth, J. F.; Wyn-Jones, E. *Langmuir* **2001**, *17*, 5657-5665.

(74) Claesson, P. M.; Bergstroem, M.; Dedinaite, A.; Kjellin, M.; Legrand, J.-F.; Grillo, I. *J. Phys. Chem. B* **2000**, *104*, 11689-11694.

(75) Tapia, M., J.; Burrows , H., D.; Knaapila, M.; Monkman Andrew, P.; Arroyo, A.; Pradhan, S.; Scherf, U.; Pinazo, A.; Perez, L.; Moran, C. *Langmuir* **2006**, *22*, 10170-4.

(76) Gershon, H.; Ghirlando, R.; Guttman, S. B.; Minsky, A. *Biochemistry* **1993**, *32*, 7143-7151.

CONCLUSION

Surface interactions are involved in many biological phenomena including protein/protein docking. Since the interactions between proteins are essential for electron transfer, the understanding of how ionic strength changes modify protein formal potentials is important. Many studies have shown that electrostatically adsorbed cytochrome *c*/HOOC-SAM/Au composite electrodes appear to be a useful model system for illustrating how changes in protein binding affect its function. The investigations reported in chapter 2 show that adsorption of cytochrome *c* onto negatively charged surfaces alters the electrostatic and redox thermodynamic properties of the protein significantly. This dramatic change is illustrated by an inversion in the slope of formal potential versus f(I) relative to solution cytochrome *c*. The inversion of slope, however, is not observed for cytochrome *c* immobilized on a neutral electrode surface, through dative bonding of the protein to pyridine terminated SAMs. The major causes of the inverted slope are attributed to a change in the effective surface charge of the protein upon immobilization to negative surfaces and differential adsorption of the two redox forms of the protein on negative surfaces. The final contributor to the electrostatic picture is the specifically binding ions. It thus seems that the models that have been used to understand ionic strength effects on solution cytochrome *c* are appropriate for adsorbed cytochrome *c* with the recognition that upon binding the protein can be converted from having a net positive to a net negative surface charge. The importance of this conclusion arises from cytochrome *c*'s function in the mitochondria where it electrostatically binds to the inner mitochondrial membrane and subsequently participates in electron transfer. Further investigations which better establish the

correspondence between SAM modified electrodes and physiological binding conditions, in particular the change in differential adsorption under varying ionic strength conditions, are warranted.

The effect of ionic strength on the electron transfer rate of surface immobilized cytochrome *c* shows that the interaction between cytochrome *c* and the negatively charged surface of carboxylic acid-terminated SAMs has an electrostatic nature. On this surface, the thermodynamically stable geometry of cytochrome *c* is also an electron transfer favorable one, which results in an electron transfer rate that monotonically decreases with increase of the ionic strength. The in homogeneities observed in these studies experimentally support the notion that a range of adsorbate geometries are being probed, analogous to the dynamic docking model for generic protein-protein interactions.

The temperature, overpotential, distance and viscosity dependencies of the electron transfer rate of cytochrome *c* immobilized on PyC_n/C_{n-1} SAMs give a picture consistent with a nonadiabatic reaction at long distances and an increasingly solvent / protein friction controlled mechanism for the thinner films. The mechanism change can be understood using the Zusman formulation and is linked to the increase in electronic coupling and the slowing of the polarization relaxation with the decreasing film thickness. The overpotential dependence of the rate constant at short distances is consistent with this interpretation and discounts conformational gating as a possible mechanism. In contrast, the measured rates on short carboxyl-terminated monolayers show no variation with the increasing driving force, and can be regarded as a typical signature of a gated mechanism. The present results and interpretation suggest that the “unusual” distance dependence of the heterogeneous electron transfer rate that has been found for different

proteins immobilized on metals by a variety of methods is in fact not unusual and may occur generally – driven by the large electronic couplings and large electric field strengths.

On mixed carboxyl/hydroxyl SAM surfaces, cytochrome *c* has a faster ET rate constant than on pure carboxylic acid SAMs. In both the mixed carboxylic/hydroxyl SAM acid system and pyridine/alkane SAM, the electron transfer rate constant of cytochrome *c* increases systematically as the surface content of the diluent molecules increases. When the chain length of diluent molecule decreases, the electron transfer rate increases, especially at a high surface content of diluent molecule where the electron transfer rate constant has a value that is comparable with those collected on pure carboxylic acid-terminated SAM having the same chain length as the diluent molecule. The diluent dependent electron transfer kinetics unambiguously show that electron tunnels through the diluent molecules.

Fluorescence correlation spectroscopy was used to reveal how the hydrodynamic properties of the complexes between poly (phenylethynylene) based polyelectrolytes (PPE-SO_3^-) and octadecyl trimethylammoniumbromide (OTAB) evolve with surfactant concentration. This study shows that FCS is a power tool for studying the interactions between surfactant and polyelectrolyte. It yields valuable information that is not accessible to other traditional methods. It is found that even in a concentration far lower than the CMC and CAC of OTAB, the PPE-SO_3^-/OTAB complexes exist in a series of structures having different size, chemical composition and conformation depending on the comparative concentration of polyelectrolyte and surfactant. These findings indicate that the rigidity of the polymer backbone plays an important role in determining the conformation between polyions and surfactant and the ratio C_{OTAB} /$C_{monomer}$ might be a dominant factor for the composition of the complexes. With the help of the structures inferred from the FCS studies, the contradictory effects of surfactant reported on the PPE

fluorescence can be explained within a unified picture. The PPE-SO_3^- represents the type of polyelectrolytes with rigid backbone, including dsDNA. Our results have important implication in the field of gene delivery.